INAUGURAL - DISSERTATION

zur

Erlangung der Doktorwürde

der

Naturwissenschaftlich-Mathematischen

Gesamtfakultät

der

Ruprecht-Karls-Universität

Heidelberg

Vorgelegt von

Dipl. Chem. Agatha Anna Korytowski

geboren in Ruda Śląska, Polen

Tag der mündlichen Prüfung: 22.01.2016

Dissertation

submitted to the
Combined Faculty of Natural Sciences and Mathematics
Heidelberg University, Germany
for the degree of

Doctor of Natural Sciences (Dr. rer. nat.)

Presented by
Dipl. Chem. Agatha Anna Korytowski
Born in Ruda Śląska, Polen

Oral examination: January 22th, 2016

Influence of Lipid Oxidization on Structures and Functions of Biological Membranes

Referees:

Prof. Dr. Motomu Tanaka,

Prof. Dr. Reiner Dahint

Summary

The primary aim of this thesis is to clarify how the structures and functions of biological membranes are influenced by the oxidative damage mediated by free radicals. As a precisely defined model systems, artificially reconstituted lipid membranes (Langmuir monolayers, vesicles, supported membranes, multilamellar membranes) incorporating two oxidized phospholipids bearing aldehyde or carboxyl groups at the end of truncated *sn*-2 acyl chains were fabricated. By the combination of various experimental methods, the generic impact of chain oxidization on physical characteristics of membranes (e.g. lateral cooperativity, fine-structures perpendicular to membrane planes, electrostatics) and the specific interactions of oxidized phospholipids with EO6 peptides and acute immune response proteins was investigated.

In the first step, the influence of oxidized phospholipids (OxPL) on the thermodynamics and electrostatics were investigated using Langmuir film balance at the air-water interface. The pressure-area (π-A) isotherms and surface potential ($\Delta\psi$-A) measurements implied that both OxPLs lead to a decrease in the isothermal compression modulus. In fact, surface potential measurements suggest changes in the orientation of oxidized moieties that decrease the lateral cooperativity. Further increase in the fraction of oxidized lipids resulted in the loss of molecules into bulk water, which seems consistent with the destabilization of cell membranes under oxidative stresses.

In the second step, the impact of lipid oxidization on the electrostatics of membranes was examined by the combination of high-energy specular X-ray reflectivity (XRR) and grazing-incidence X-ray fluorescence (GIXF). The scattering length density profiles reconstructed from XRR results suggested that both OxPL leads to membrane thinning, which seems plausible from the decrease in the lateral cooperativity suggested by Langmuir isotherms. GIXF offers an unique possibility to localize specific target elements within Å accuracy, suggesting that the binding affinity ($Ca^{2+} > Cs^{+} > K^{+}$) could be interpreted in terms of the solvation entropy (Hofmeister series). Further, the impact of oxidization on the vertical structural ordering of vertically stacked membrane models was investigated by off-specular neutron scattering. A decreased lamellar periodicity d indicated that incorporation of OxPL into the membrane displace water molecules from the inter-membrane region due to the reorientation of oxidized moieties.

In the third step, the combination of experimental techniques was utilized to shed light on specific interactions of OxPLs with peptides and proteins; C-reactive protein that is characteristic for the acute immune responses and monoclonal antibody EO6 to oxidized lipids. Following the fundamental characterization of membrane-protein interactions using isothermal titration calorimetry (ITC) and dynamic light scattering (DLS) of vesicle suspensions, in addition to XRR, GIXF, off-specular neutron scattering, dual waveguide polarization interferometry (DPI) was used to monitor the changes in thickness, refractive index, and the optical anisotropy (birefringence) of lipid membranes simultane-

ously. Furthermore, the specific binding of EO6 was verified from the fluorescence imaging of glioblastoma multiforme cells undergoing apoptosis, where a clear accumulation of OxPLs could be identified in apoptotic blebs.

The obtained results demonstrated that the combination of well defined membrane models and unique physical techniques is a powerful tool to shed a new quantitative light on the generic and specific impacts of lipid oxidization on the lateral cooperativity, vertical fine-structures, electrostatics, and specific interactions in inflammation and apoptosis.

Zusammenfassung

Das Ziel dieser Arbeit war es, den Einfluss von oxidativen Beschädigungen, die durch freie Radikale hervorgerufen werden, auf die Struktur und Funktion biologischer Membranen aufzuklären. Als exakt definierte Modellsysteme wurden Lipidmembranen unterschiedlicher Art hergestellt (Lipidmonolagen, Vesikel, trägergestützte Membranen und vertikal gestapelte Membranmultilagen), die zwei Typen von oxidierten Phospholipiden (OxPL), die entweder eine Aldehyd- oder eine Carboxylgruppe am Ende der *sn*-2 Acylkette tragen, beinhalten. Mit Hilfe einer Kombination verschiedener experimenteller Verfahren konnten die hervorgerufenen Effekte der Oxidation der Kohlenstoffketten auf die physikalischen Eigenschaften der Membranen (z.B. laterale Kooperativtät, Feinstruktur senkrecht zur Membran, Elektrostatik) und die spezifischen Wechselwirkungen von oxidierten Phospholipiden mit dem EO6 Peptid und einem akuten Protein der immunologischen Abwehrreaktion ermittelt werden.

Als Erstes wurden die Auswirkungen oxidierter Phospholipide (OxPL) auf die Thermodynamik und Elektrostatik von Lipidmonolagen an der Wasser-Luft Grenzfläche mittels einer Langmuir-Filmwaage untersucht. Die Ergebnisse der Langmuir-Isothermen und des Oberflächenpotentials implizierten, dass beide oxidierten Phospholipide zu einem sinkenden Kompressionsmodulus führen. Den Messungen des Oberflächenpotentials zufolge basiert die sinkende laterale Kooperativität auf der Veränderung der Orientierung der oxidativen, funktionellen Gruppen. Die Erhöhung des Anteils an OxPL führte zum Verlust von Lipidmolekülen von der Wasser-Luft Grenzfläche in die wässrige Phase, was im Einklang mit der Destabilisierung der Zellmembran unter oxidativem Stress steht.

Im zweiten Schritt wurden die Auswirkungen der Lipidoxidation auf die Elektrostatik von Membranen unter Verwendung einer Kombination von hoch-energetischer, spekularer Röntgenreflektometrie (XRR) mit Röntgenfluoreszenz unter streifendem Einfall (GIXF) untersucht. Die rekonstruierten Profile der Streulängendichte aus den XRR Ergebnissen deuteten darauf hin, dass beide OxPL zu einer Verdünnung der Membran führen, was im plausiblen Zusammenhang mit der Abnahme der lateralen Kooperativität steht, die durch die Langmuir-Isothermen suggeriert wurde. GIXF bietet eine einzigartige Möglichkeit, die elementspezifische räumliche Anordnung in der Größenordnung von Ångström zu bestimmen. Die Ergebnisse wiesen darauf hin, dass die Bindungsaffinität der Ionen ($Ca^{2+} > Cs^{+} > K^{+}$) im Hinblick auf die Solvatationsentropie (Hofmeister-Reihe) interpretiert werden kann. Ferner wurde die Auswirkung der Oxidation auf die strukturelle Anordnung von vertikal gestapelten Membranmodellen durch nicht-spekuläre Neutronenstreuung untersucht. Die Verringerung des lamellaren Abstandes zwischen den Membranen durch Erhöhung des OxPL Anteils zeigte, dass die Veränderung der Orientierung der oxidativen Gruppen zu einer Verdrängung von Wassermolekülen aus dem Zwischenmembranbereich führt.

Im dritten Schritt, wurde eine Kombination von experimentellen Techniken verwendet, um über die spezifische Wechselwirkung von OxPL mit Peptiden und Proteinen Aufschluss zu geben; einmal mit dem C-reaktiven Protein (CRP), welches charakteristisch für die akute immunologische Abwehr ist, und außerdem mit dem monoklonalen Antikörper EO6 gegen oxidierte Lipide. Nach der grundlegenden Charakterisierung der Membran-Protein Wechselwirkungen unter Verwendung von isothermer Titrationskalorimetrie (ITC) und dynamischer Lichtstreuung (DLS) von Vesikelsuspensionen, wurde zudem XRR, GIXF, nicht-spekuläre Neutronenstreuung und Dualpolarisationsinterferometrie (DPI) verwendet, um die Änderungen in den Parametern Dicke, Brechungsindex und optischer Anisotropie gleichzeitig zu überprüfen. Ferner wurde die spezifische Bindung von EO6 mittels Fluoreszenzmikroskopie von apoptotischen Gehirntumorzellen (Glioblastoma multiforme) verifiziert, was auf eine Akkumulation von OxPLs in apoptotischen Bläschen zurückzuführen ist.

Die erhaltenen Ergebnisse zeigten, dass die Kombination von exakt definierten Membranmodellen mit einzigartigen, physikalischen Messmethoden ein mächtiges Werkzeug ist, um quantitative Aufschlüsse über allgemeine und spezifische Wirkungen der Lipidoxidation auf die laterale Kooperativität, vertikale Feinstruktur und Elektrostatik sowie über die spezifische Wechselwirkungen bei Entzündungen und Apoptose zu erlangen.

Acknowledgments

I would like to thank

Prof. Dr. Motomu Tanaka for his kind supervision and the opportunity to work on fascinating projects in an excellent scientific environment. His stimulating suggestions and encouragement were more than inspiring.

PD Dr. Peter van Hoogevest as well as the **Phospholipid research center** and **Lipoid GmbH** for financial support, supply of compounds and scientific exchange during my PhD.

Prof. Dr. Wolfgang Stremmel for the great collaboration on the mucin project.

Dr. Ali Makky for fruitful collaboration on the oxidized phospholipid project during his time in our group.

Dr. Wasim Abuillan for scientific discussions and supervision in tough scientific topics. His endless patients and explanations were more than a great help during my PhD.

Dr. Stefan Kaufmann and **Dr. Cornelia Monzel** for giving me a good understanding for the handling of proteins, cells and microscopes.

Dr. Nataliya Frenkel, Dr. Alexandra Burk and **Victoria Frank** for open ears, experience exchange and the arrangement of traditions in our group.

Federico Amadei and **Maryam Eshrati** for a cheerful time in the office, lab and other places.

Dr. Andrea Guimero from Sinning group for help with the ITC.

Dr. Akihisa Yamamoto (Kyoto University), **Dr. Bruno Deme** (ILL) and **Dr. Oleg Konovalov** (ESRF) for introduction into the world of scattering.

Ms. Gabriele Fabry for management of financial issues and for solving irresolvable problems.

All colleagues of the Tanaka group for an overall great time, fruitful collaborations and discussions and humorous time in Grenoble.

Special thanks go to **my family** for endless support during all the time.

Table of Contents

Abbreviations

A	Area per molecule
A_2	Second virial coefficient
°C	Degree celsius
c	Concentration
$CaCl_2$	calcium chloride
CD95L	CD95-Ligand
CRP	C-reactive protein
$<d>$	Average distance
D	Diffusion coefficient
DLS	Dynamic light scattering
DOPC	1,2-di-(9Z-octadecenoyl)-*sn*-glycero-3-phosphocholine
DOPG	1,2-di-(9Z-octadecenoyl)-*sn*-glycero-3-phospho-(1'-*rac*-glycerol)
DOTAP	1,2-di-(9Z-octadecenoyl)-3-trimethylammonium-propane
DPI	Dual Polarization Interferometry
DPPC	Dipalmitoylphosphatidylcholine
E	Electric field
EDTA	Ethylenediaminetetraacetic acid
EtOH	Ethanol
GBM	Glioblastoma multiforme
GIXF	Grazing-incidence X-ray fluorescence
h	Hour(s)
H_2O	Water
H_2O_2	Hydrogen peroxide
HBS	Hepes buffered saline
Hepes	4-(2-hydroxyethyl)-1-piperazineethanesulfonic acid
ITC	Isothermal titration calorimetry
KCl	Potassium chloride
KOH	Potassium hydroxide
L_C	Liquid condensed phase
LDL	Low density lipoproteins
L_e	Liquid expanded phase
LPC	Lysophosphatidylcholine
MDa	Mega Dalton

mg	Milligram(s)
ml	Milliliter(s)
min	Minute(s)
mM	Millimolar
mol%	Mole percent
M_w	Molecular weight
n	Binding stoichiometry
NaCl	Sodium chloride
NaOH	Sodium hydroxide
NH_4OH	Aqueous solution of ammonia
nm	Nanometer(s)
NMR	Nuclear magnetic resonance
OPPC	1-oleoyl-2-palmitoyl-*sn*-glycero-3-phosphocholine
OxLDL	Oxidized low density lipoproteins
OxPL	Oxidized phospholipid
PC	Phosphorylcholine
Pdl	Polydispersity index
PL	Phospholipid
PazePC	1-palmitoyl-2-azelaoyl-*sn*-glycero-3-phosphocholine
POPC	1-palmitoyl-2-oleoyl-*sn*-glycero-3-phosphocholine
PoxnoPC	1-palmitoyl-2-(9'-oxo-nonanoyl)-*sn*-glycero-3-phosphocholine
QCM-D	Quartz crystal microbalance with dissipation monitoring
r	Radius
R_H	Hydrodynamic radius
RT	Room temperature
ROS	Reactive oxygen species
s	Second(s)
SLD	Scattering length density
SLS	Static light scattering
SOPC	1-stearoyl-2-oleoyl-*sn*-glycero-3-phosphocholine
SUV	Small unilamellar vesicles
T	Temperature
T_m	Main transition temperature
Tris	Tris(hydroxymethyl)aminomethane

vol%	Volume percent
w%	Weight percent
X%	Mole percent of a compound X
XRR	X-ray reflectivity
γ	Surface tension
Δ	Delta
ΔD	Shift in dissipation (as measured by QCM-D)
Δf	Shift in resonance frequency (as measured by QCM-D)
ΔG	Gibbs energy change
ΔH	Enthalpy change
ΔH_d	Heat of dilution
ΔS	Entropy change
ΔT	Temperature difference
ε	Dielectric permittivity
ζ	Zeta potential
η	Viscosity
κ	Compressional modulus
λ	Wavelength
μ_e	Electrophoretic mobility
µl	Microlit
µM	Micromolar
μ_n	Surface dipole moment
π	Surface pressure
ρ	(Electron) density
σ	Roughness
ϕ	Volume fraction
ψ	Monolayer surface potential

1 Introduction

Cell membranes are crucial components of all living organisms. Biological membranes define the boundaries between interior and exterior of cells and sustain their structural integrity. They are involved in the control and execution of a great variety of biochemical processes by the confinement of reactions in two-dimensional spaces [1, 2, 3]. The lipid bilayer is the structural core of all biomembranes, which was classically described in a simple form by Singer and Nicholson's fluid mosaic model [4]: the lipid bilayer can be treated as a two dimensional diffusion barrier and structural matrix, which embeds active molecules, peripheral and integral membrane proteins as well as covalently linked complex carbohydrates (Figure 1.1). Although the modern pictures of cell membrane architectures include more complex features, such as rafts and caveolin, the fluidity of lipid membranes plays crucial roles in determining its lateral organizations and functional states of a cell [1]. Perturbation of the membrane structures modifies not only the physico-chemical properties of membranes but also their functions in a variety of biological processes, such as transport of ions and enzymatic activities [2, 5].

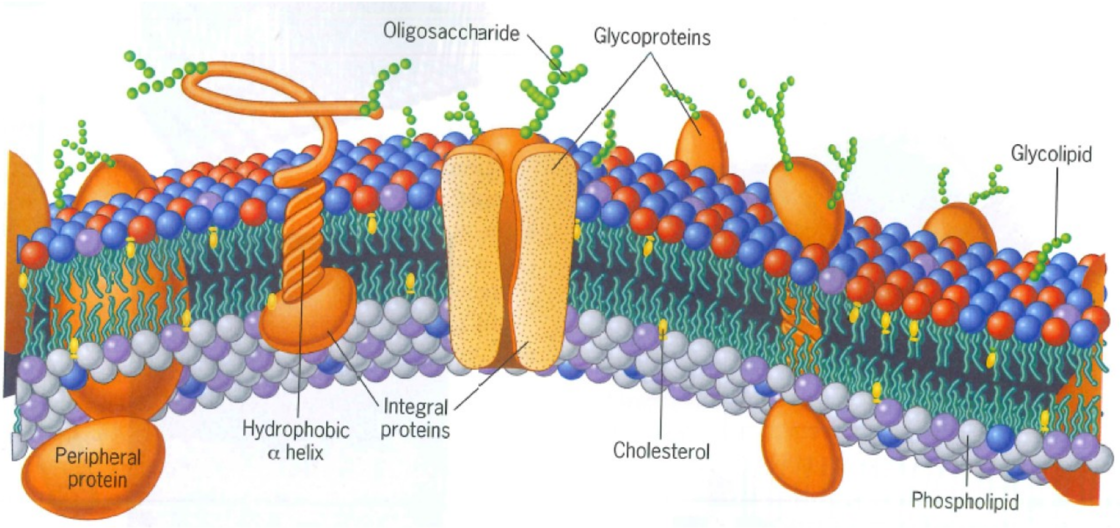

Figure 1.1 Sketch of a cell membrane, consisting of a lipid bilayer, membrane proteins and carbohydrates [6].

Looking into molecular components, phospholipids such as 1-palmitoyl-2-oleoyl-*sn*-glycero-3-phosphocholine (POPC) represent one of the most abundant lipids in mammalian membranes. Their unsaturated lipid chains are prone to oxidative damage at the location of the carbon-carbon double bonds. Among these oxidization products, PazePC and PoxnoPC are two stable lipid oxidization products bearing carboxyl and carbonyl groups respectively at the end of their truncated *sn*-2 chains (Figure 1.2).

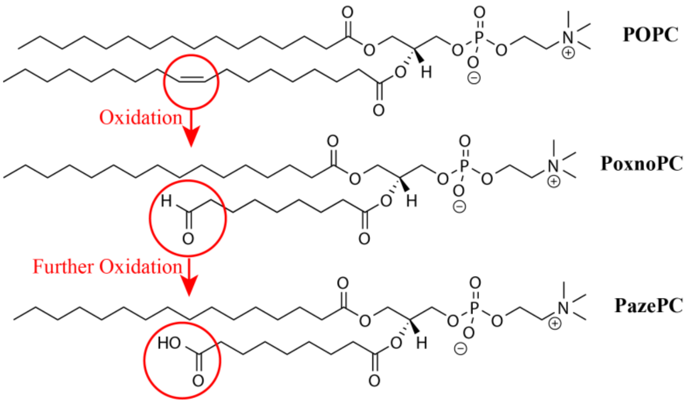

Figure 1.2 Oxidization of POPC forming OxPL species such as PoxnoPC and PazePC.

Phospholipid oxidization can be mediated via enzymes, but it can also result from cellular metabolism and mitochondrial respiration. Another source is the reaction of lipids with free radicals present in various tissues such as inflammation and phagocytosis of virus- or bacteria-infected cells [7, 8]. As a result of the attack by free radicals a large and diverse array of oxidation products is generated [9].

One consequence of oxidization is the introduction of polar functional groups into the lipid structure which is expected to have pronounced effects on the membrane biophysical properties [10]: The polarity profile and the overall lipid organization is altered, because the oxidatively modified chains can adopt the so-called extended conformation [11], where the chains remain no longer in the hydrocarbon chain region, but protruding into the aqueous phase [12]. Recent molecular dynamics simulations by Khandelia *et al.* suggests that a large free energy penalty of embedding a charged carboxyl group of PazePC in the hydrophobic core of a lipid bilayer is the reason for the reorientation of the oxidized chain into the aqueous phase [13].

Recent studies demonstrated that the presence of OxPL plays a role in the pathogenesis of several diseases [14, 15, 16, 17]. PoxnoPC leads to Finnish type familial amyloidosis (FAF), a neurodegenerative disease by accelerating the fibrillation of a core amyloidogenic segment of gelsolin [18]. PazePC has been detected in LDL particles and has been implicated in the genesis of atherosclerosis. Both OxPL often accompany each other in their biological environment and have been found in atherosclerotic lesions as well as on the surface of apoptotic cells [19, 20]. In fact, oxidatively modified lipids can promote apoptosis and necrosis [19] and accelerate neurodegenerative diseases such as Alzheimer's disease [21].

Although several studies have demonstrated the presence of OxPL in many pathological states, there is no systematic study that unravels how lipid oxidization influences the fine-structures and electrostatics of cell membranes. Eventually, the induced changes in the structure and mechanics of membranes, may affect the membrane protein function that may result in the onset or progression of diseases.

The primary aim of this study is to study the impact of OxPL by modelling the surface of apoptotic cells to unravel changes in (i) the mechanics of biological membranes due to oxidatively modified lipid–lipid interaction, (ii) specific lipid–ion interaction representing the interaction between the cell and the electrolyte, and (iii) lipid–protein interaction which can be altered by the lipid environment (Figure 1.3).

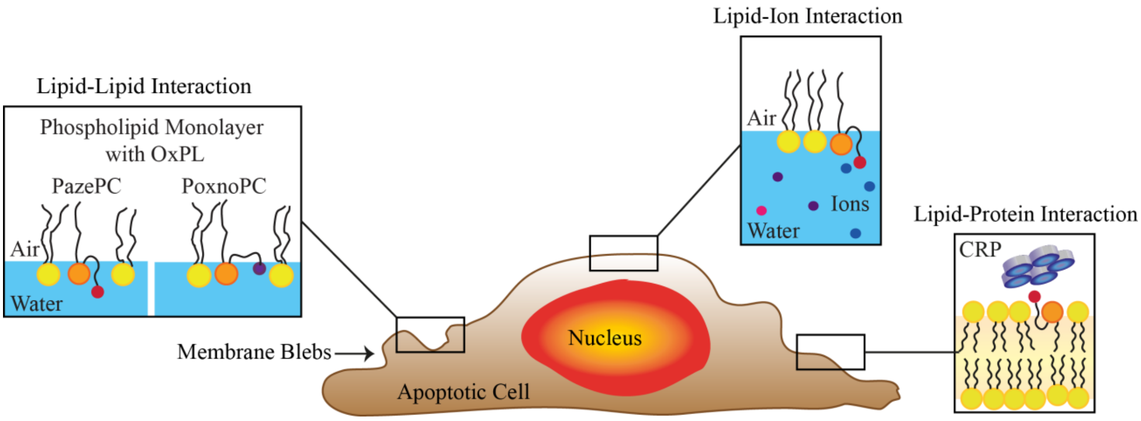

Figure 1.3 The impact of oxidized phospholipids (OxPL) on the structure and electrostatics of the membrane and the altered interaction with the surrounding environment such as ions and proteins.

In this study, the surface of the apoptotic cell was modelled by different planar model cell membranes, such as lipid monolayer at the air-water interface, solid-supported lipid bilayer membrane at the solid-liquid interface, lipid vesicles or stacks of mulitlamellar membranes. Membrane models serve as precisely defined models of biological membranes which can be subjected to many physical techniques to quantitatively determine many physical membrane properties.

In chapter 4, the generic impact of chain oxidization on physical characteristics of membranes (e.g. lateral cooperativity, fine-structures perpendicular to membrane planes, electrostatics) was studied by the combination of various experimental methods. In the first step, the influence of lipid oxidization on the thermodynamics and electrostatics were investigated using Langmuir film balance at the air-water interface. A quantitative determination of induced changes in thermodynamic properties such as compression modulus (κ) and Gibb's free energy (ΔG^{exc}) was obtained by pressure-area (π-A) isotherms. The surface potential ($\Delta\psi$-A) technique was used complementary to gain insight into the changes in the orientation of oxidized moieties. In the second step, the impact of lipid oxidization on the structures and electrostatics of membranes was examined by the combination of specular X-ray reflectivity (XRR) and grazing-incidence X-ray fluorescence (GIXF). Systematic variation of the membrane composition unraveled quantitative changes in the thickness, roughness and electron density of the lipid monolayers as a function of molar fraction of two types of OxPL (PazePC and PoxnoPC). Simultaneous GIXF measurements determined quantitatively the element-specific density profiles of monovalent (K^+ or Cs^+) and divalent ions (Ca^{2+}) in the vicinity of the interface in the presence and absence of both OxPL with high spatial accuracy (± 5 Å) (Figure 1.4).

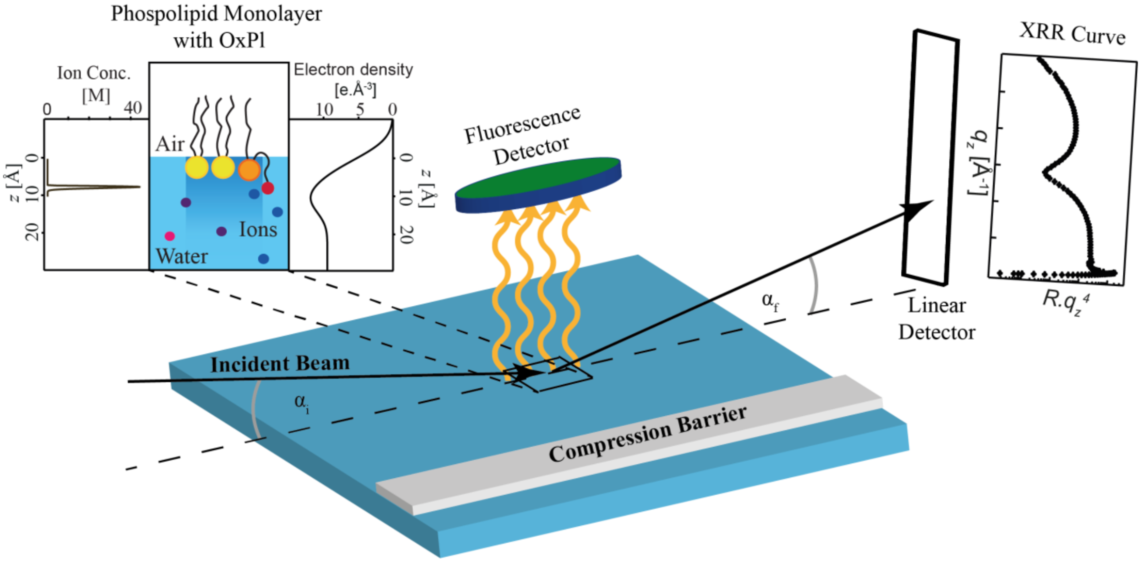

Figure 1.4 Experimental setup and scattering geometry used for XRR and GIXF together with the experimental XRR curve (right) and the reconstructed ion concentration profile (left).

Further, the impact of oxidization on the vertical structural ordering of vertically stacked membrane models was investigated by off-specular neutron scattering.

In chapter 5, a systematic characterization of the specific interactions of peptides and proteins with membranes incorporating OxPLs were performed by a wide combination of experimental techniques. In the first step, the interaction of the acute immune response C-reactive protein (CRP) with lipid membranes in the presence and absence of OxPL was studied using different membrane model systems such as liposomes, solid-supported membranes, lipid monolayers and lamellar mulitlayers. To discriminate the affinity strength of CRP to liposomes as a function of membrane composition, different methods were employed: Dynamic light scattering (DLS) was used to determine the adsorption in terms of liposome size changes as a function of membrane composition and protein concentration, and isothermal titration calorimetry (ITC) was utilized to obtain thermodynamic parameters which quantitatively discriminated the interaction strength dependent on the membrane composition.

Moreover, alterations in fine-structures of membranes perpendicular to the plane of membranes due to CRP interaction were studied by high-energy specular X-ray reflectivity measured at the solid-liquid and air-water interface. XRR provided fine-structural information upon the interaction with CRP in a Ca^{2+} dependent manner. In addition, the impact of CRP on the vertical structure of membrane multilayers was studied by off-specular neutron scattering. In combination with the obtained changes in chain packing (in terms of refractive index and birefringence) by dual polarization interferometry (DPI) a binding model of CRP to lipid membranes was created.

In the second step, the specific interaction of the host defense antibody EO6 to OxPL was investigated on glioblastoma multiforme (GBM) cells undergoing apoptosis by fluorescence microscopy to verify the presence of oxidative species in apoptotic lesions. Therefore, *in vitro* model systems of a cell surface were utilized where the intramolecular distance of the apoptosis inducing ligand CD95L could be regulated within nm accuracy. Furthermore, the specific interaction of EO6 to OxPL was studied in lipid membranes incorporating OxPL as supported membrane model systems of apoptotic cells by surface tension and quartz crystal microbalance with dissipation monitoring (QCM-D).

Details of the results are presented in the following chapters.

2 Theoretical Background

2.1 Principles of X-Ray Scattering

Since the discovery of X-rays in 1895 by Wilhelm Conrad Röntgen [22], they have played a crucial role in the research of condensed matter. From 1923, when Compton described the total reflection of X-rays from stratified, solid substrates with smooth surfaces [23], XRR was discovered as a surface-sensitive technique. Its characteristics in terms of wavelength and energy make X-rays a powerful, non-destructive tool to investigate the structural characterization of layered structures at molecular length scales (Å-resolution) [24].

2.1.1 Basic Principles

X-ray radiation propagates as an oscillating electric and magnetic field. When X-ray hits any type of matter, the electric field of the incident wave and the charge or the magnetic field of the wave and the magnetic momentum (spin) interact with each other. When X-ray **interacts with matter**, the following scenarios can occur (Figure 2.1): **1) elastic**, **2) inelastic scattering** (Compton scattering) or **3) absorption** (photoelectric absorption, fluorescent X-ray emission and Auger electron emission), and **4) diffraction** defined by Bragg´s Law for diffraction from crystal lattice. In X-ray scattering experiments, X-rays are elastically scattered by the electrons within the atom. Elastic scattering provides information about the structure and the arrangement of atoms within the sample. Inelastic scattering gives information about the movement of the atoms (vibrations), while adsorption can be used to study fine structures, type and the environment of atoms.

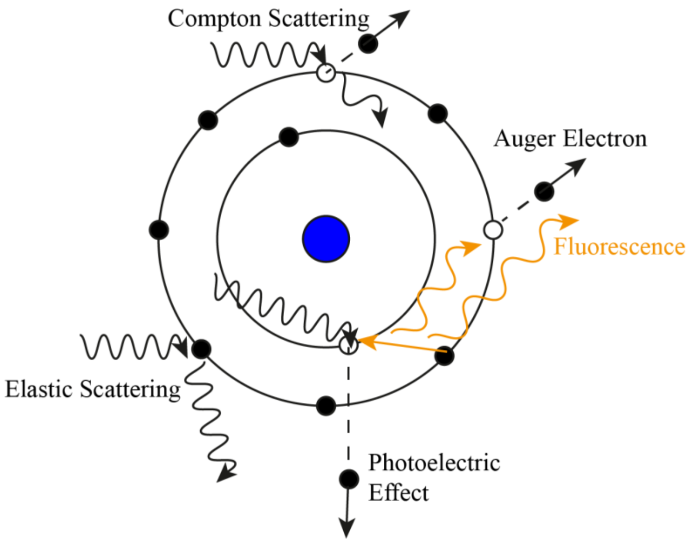

Figure 2.1 Illustration of the main possible interactions between X-rays and atoms.

In X-ray reflectivity (XRR), the reflected intensity R of an incident X-ray beam is measured as a function of the incidence angel α_i. The reflectivity is measured below and above the critical angle and includes the interference from X-rays which penetrates into the sample and scatters at different sample layers. XRR determines the layer thickness, roughness and the electron density profile along the surface normal of thin single or multilayer systems [25]. Its high surface-sensitivity is based on the refractive index n of materials, which is smaller than unity in the wavelength region of X-rays. As a result, X-rays undergo total reflection at small incidence angles followed by a steep decay of the reflected intensity at higher angles. In general, X-rays can be refracted and reflected at interfaces with different electron densities at the boundary between e.g. gas and vacuum and solid or liquid matter.

When investigating a sample at the length scale large compared to atomic structures, the sample can be described in terms of continuous media. The atomic structure can be neglected and the refraction is described by complex **refractive index**, given by:

$$n = 1 - \delta + i\beta, \tag{2.1}$$

where δ and β are the real and imaginary part of the refractive index, respectively. The real part δ describes the strength of interaction between material and radiation and is related to the electron density ρ_e [e/Å^3] and the classical radius of the electron ($r_e = 2.82 \times 10^{-5}$ Å) and the wavelength λ, as given by:

$$\delta = \frac{2\pi\rho_e r_e}{k^2} = \frac{\lambda^2\rho_e r_e}{2\pi} = \frac{\lambda^2(SLD)}{2\pi}, \tag{2.2}$$

where k is the wave vector of the X-ray radiation, given by $k = 2\pi/\lambda$.

The imaginary part of the refractive index depends on the adsorption coefficient μ of X-ray radiation in a material [26]:

$$\beta = \frac{\lambda\mu}{4\pi} \tag{2.3}$$

For X-rays in general, δ has typical values in the range of ~ 10^{-5} and β is in the range of ~ 10^{-8} for most biological matter [26]. Thus, β can be ignored without introducing significant errors. Therefore, the refractive index in X-ray region is slightly less than one for any material and it is equal to unity in vacuum or air.

2.1.2 Specular X-ray Reflectivity (XRR)

When X-rays interacts with a **single smooth interface** between two media with refractive indices of n_1 and n_2, the incident beam can be reflected (Figure 2.2a, black arrow) and refracted (blue arrow).

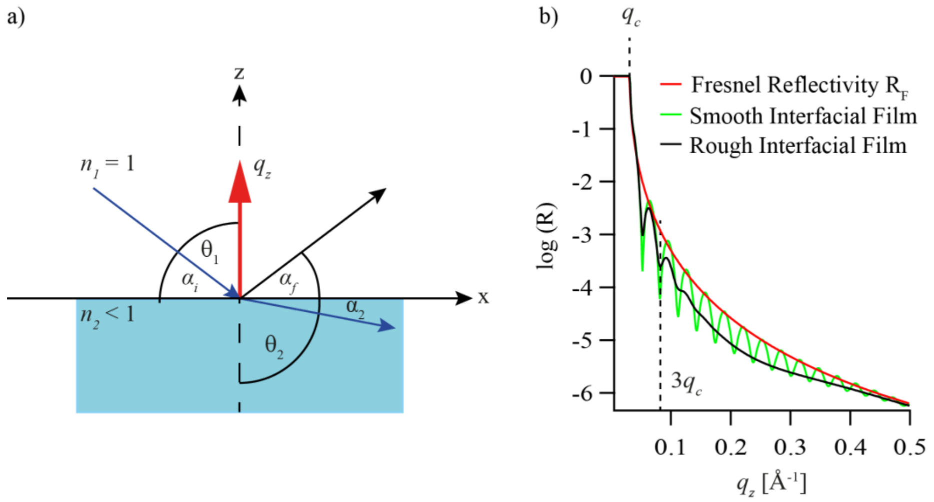

Figure 2.2 (a) Illustration of the reflection (black arrow) and refraction (blue arrow) of the incident beam in the x-z plane including the angles and the refractive indices for calculation of the critical angle of total reflection. (b) Examples of reflectivity profiles for the Fresnel reflectivity (red), a smooth (green) and a rough (black) thin polymer film with a thickness of 200 nm.

The angle of refraction is described by **Snell's law** as:

$$\frac{sin\Theta_1}{sin\Theta_2} = \frac{n_2}{n_1} = \frac{v_1}{v_2}, \qquad (2.4)$$

with the angle θ_1 of the incoming ray and the refractive index n_1 and the angle θ_2 of the outgoing ray and the refractive index n_2. The refractive index n_i is the speed of light in vacuum c_0 divided by the speed of light v_i in matter.

Total external reflection occurs for angles θ_1, when the angle θ_2 reaches 90°, which corresponds to $\sin\theta_2 = 1$. If the X-ray comes from vacuum, $n_1 = 1$. So the critical angle θ_c is given as $\theta_c = \sin^{-1} n_2$. Because n_2 is only slightly below one, the possible maximum angle for total external reflection is close to 90°. For X-rays total external reflection occurs only under grazing incidence. As a consequence, it is common to measure the reflection angles as angles α between the incoming X-ray and the mirror surface. Then the **critical angle** α_c is given as: $cos\alpha_c = n_2$. With a Taylor expansion of the cosine, α_c can be written as:

$$\alpha_c \approx \sqrt{2\delta} \approx \sqrt{\frac{\lambda^2 \rho_e r_0}{\pi}} \qquad (2.5)$$

At the end, the critical angle is defined by the electron density of the material and the wavelength of the X-ray.

Above the critical angle, both refraction and reflection occurs. This leads to an exponential decrease of reflectivity R, based on the **Fresnel** equations. The reflectivity profile can be given as a function of the varying incidence angle or the wave vector transfer q_z (perpendicular to the surface):

$$q_z = \frac{4\pi}{\lambda} \sin \alpha_i \tag{2.6}$$

If the momentum transfer is large compared to q_c, the reflectivity can be approximated to:

$$R_F(q_z) = \frac{q_c^4}{16 q_z^4} \tag{2.7}$$

This last equation gives general information about the shape of the reflectivity curve, where the reflectivity decreases steeply at $q_z > q_c$, while the total external reflection can be seen as a plateau at $q_z < q_c$. Furthermore, the reflectivity decreases by $1/q_z^4$ by power law when $q_z > 3\ q_c$.

If X-rays interfere with structures which contain one or several layers with different electron densities, the mathematical description of the reflectivity profile cannot be described by Fresnel equation anymore. The **kinematical theory** defines that the multiple reflections and refractions are negligible small in a system, which consists of homogenous layers with sharp interfaces [26]. Here the reflectivity can be obtained by the sum of the reflectivity for each layer in respect to the different phase factors. The kinematical theory is valid for smooth surfaces, where only specular reflection occurs, and at higher angles ($q_z > 3q_z$). Thus, the description of the reflectivity fails near the critical angle α_c and for rough surfaces.

For a rough interface, the **Born approximation** describes the interference of scattered rays. Assuming that the incident beam intensity is unperturbed, the scattered intensity can be described by the Fourier transform of the electron density distribution across the interface. The ratio of actual reflected intensity and the Fresnel reflectivity from ideal interfaces is a function of the absolute square of the Fourier transformation of the electron density gradient across the sample surface normalized to the substrate electron density, and is given by the **Master formula**:

$$R(q_z) \propto \frac{1}{{q_z}^4} \left| \int_{-\infty}^{\infty} \left(\frac{d\rho}{dz}\right) e^{-iq_z z} dz \right|^2, \tag{2.8}$$

which is valid only in the high q-range. For smooth interfaces between two mediums this equation is simplified to equation 2.7. The Born approximation is the common used model for the interpretation of scattering experiments. However, it is invalid in case of multiple reflections and refractions in the vicinity of the critical angle.

Parratt introduced in 1954 a recursive method which improved the description of the reflectivity profile in the small q-range [27]. In contrast to the signal from single interface, at stratified interfaces multiple reflections and refractions at different interfaces occur. If multiple reflections interfere with each other, the reflectivity profile shows an oscillation pattern and deep minima, known as the **Kiessig fringes**. The distance between the minima in the oscillation pattern is related to the film thickness d given by:

$$d = \frac{2\pi}{\Delta q_z} \tag{2.9}$$

The limit of detection of film thickness is dependent on the q_z maximum ($d_{min} \approx q_{z\text{-}max}$). There, high brilliancy, flux and focus of the beam are factors influencing q_z.

In case of **rough interfaces**, an additional diffuse component of the reflectivity occurs (off-specular reflectivity) and the reflectivity decreases more steeper (Figure 2.2b, black), resulting in a loss of information. If the roughness is small relative to the layer thickness, the effect of roughness on the Fresnel reflectivity can be modified within the Born approximation to an extended Fresnel coefficient by the introduction of an idealized uncorrelated roughness given by:

$$R(q_z) = R_F(q_z) * e^{-2\sigma^2 q_z^2}, \tag{2.10}$$

where σ is the root mean square (r.m.s.) roughness and characterized by a mean standard deviation of the layer thickness $\sigma = \sqrt{\langle d^2 \rangle}$.

In **stratified layers** multiple reflections from each interfaces (also back- and forth reflections) and the interference of the reflected and transmitted waves occur. The **Parratt formalism** is a fully dynamical description of the scattering processes and is the most widely used method in calculating the reflectivity from stratified layers. **Abelès matrix** method is an equivalent formalism which is based on layer matrices [28]. In these two methods, the film is described by a **slab model**, which represents different slabs of homogenous electron density ρ_i, thickness d_i and roughness $\sigma_i < d_i$ for each assumed layer. For N-layers between two homogenous bulk mediums the relation among the incident electric field E_0^+, reflected E_0^- and transmitted E_{N+1}^- amplitudes can be described (Figure 2.3) according to Abelès by:

$$\begin{pmatrix} E_0^+ \\ E_0^- \end{pmatrix} = \frac{C_1 C_2 \ldots C_{N+1}}{t_1^F t_2^F \ldots t_{N+1}^F} \begin{pmatrix} E_{N+1}^+ \\ 0 \end{pmatrix}, \tag{2.11}$$

where C_{j+1} is the propagation matrix given by:

$$C_{j+1} = \begin{pmatrix} \exp(-ik_{zj}d_j) & \mathrm{r}_{\mathrm{j-1}}\exp(-ik_{zj}d_j) \\ \mathrm{r}_{\mathrm{j-1}}\exp(ik_{zj}d_j) & \exp(ik_{zj}d_j) \end{pmatrix}, \tag{2.12}$$

where t_j^F is the Fresnel transmission coefficient and r_j the Fresnel reflection coefficient.

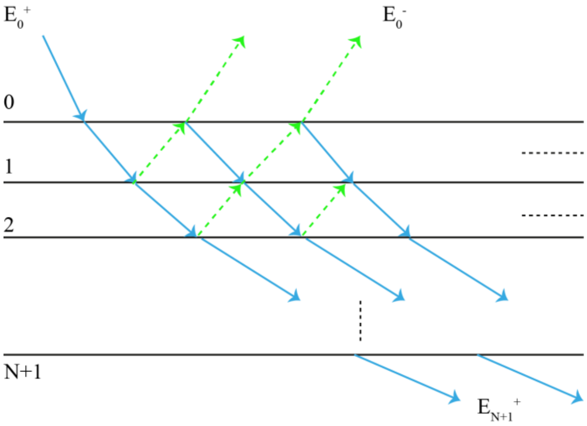

Figure 2.3 Illustration of the multiple reflections and refractions at interfaces of stratified films.

With the propagation matrices expressed as:

$$C_1 C_2 \dots C_{N+1} = \begin{pmatrix} a & b \\ c & d \end{pmatrix} \tag{2.13}$$

the reflectivity can be given by:

$$R = |r|^2 = \left|\frac{E_0^-}{E_0^+}\right|^2 = \left|\frac{c}{a}\right|^2 \tag{2.14}$$

If the condition $\sigma_i < d_i$ is not fulfilled, it is possible to use Abelès matrix or Parratt formula to calculate the reflectivity for any system. Then the system can be divided into equally thick layers, while the total film thickness is obtained from the Fourier transform of the reflectivity curve as a starting point. The only parameters which must be refined are the electron density of each layer and eventually one overall roughness which describe the effective interfacial roughness.

2.1.3 Grazing Incidence X-ray Fluorescence (GIXF)

When X-rays interact with matter, characteristic X-ray fluorescence lines can be emitted dependent on the chemical element. These lines can be used to identify elements within the sample. The intensity of emitted fluorescence depends on its absorption cross-section, which is the atomic number in the X-ray region. The **penetration depth** of the evanescent field under grazing incidence depends on the angle of incidence given by Snell's law for the relation of angle of refraction and a given incident angle [25, 29]:

$$\Lambda(\alpha_i) = \frac{\lambda}{\sqrt{8}\pi}\left[\sqrt{(\alpha_i^2-\alpha_c^2)^2+4\beta^2}-(\alpha_i^2-\alpha_c^2)\right]^{-\frac{1}{2}}, \tag{2.15}$$

with β as the imaginary part of the refractive index (equation 2.1). At incident angles α_i above the critical angle of total reflection α_c the penetration depth into water subphase is about a few micrometers, while below the critical angle, the X-rays penetrate about 46 Å and increases rapidly close the critical angle. The **fluorescence intensity** $I_i^f(\alpha)$ from an element i at the depth z at the air-water interface depends on the angle of incidence α of the X-ray beam:

$$I_i^f(\alpha) = S\int_0^\infty I^{ill}(z,\alpha) * c_i(z) * \exp(-z/L_i)\,dz, \tag{2.16}$$

with S as a constant that can be scaled out by normalization to the fluorescence signal from the corresponding blank buffer, $ci(z)$ as the concentration of element i, and L_i as the attenuation length of water at the characteristic fluorescence line, e.g. $\mathrm{L_{K\,K\alpha}}$ = 68.14 µm, $\mathrm{L_{Ca\,K\alpha}}$ = 93.71 µm and $L_{\mathrm{Cs\,L\alpha}}$ = 146.69 µm.

The illumination profile $I^{ill}(z,\alpha)$ is the most crucial part which can be determined by the matrix propagation technique [30] using slabs model, yielding the electron density and the thicknesses of each slab from XRR analysis [31]. Here, the **concentration profile** of the ion species condensed at the phosphocholine head group of a lipid monolayer can be analyzed using an asymmetric Gaussian profile [32]:

$$c_i(z) = c_0 + c_{max}\frac{\sqrt{\mathrm{e}}(z-z_{\mathrm{HC}})}{z_{\max}}\exp\left(-\frac{(z-z_{\mathrm{HC}})^2}{2z_{\max}^2}\right), \tag{2.17}$$

where c_0 is the bulk concentration, z_{HC} the hydrocarbon chain-phosphocholine head interface, c_{max} the maximum ion concentration, and z_{max} its peak position. Thus, c_{max} and z_{max} are the only two fitting parameters in the fitting procedure. The analysis can be refined with the Levenberg-Marquardt nonlinear least square optimization [33], yielding the ion concentration profile along the z-axis.

2.1.4 Off-Specular (Diffuse) Scattering

Off-specular or diffuse scattering occurs if an interface has a topological roughness, which leads to non-mirror-like scattering. Here the total intensity is described by a function of q_z and $q_\parallel$. It can be expressed by the scattering function $S(q_z, q_\parallel)$, which is defined in terms of incident flux and the slid angle of detection [34]:

$$I(q_z, q_\parallel) \propto \frac{1}{q_z^2} S(q_z, q_\parallel) \tag{2.18}$$

The diffuse scattering from a rough interface is determined by the characteristics of the topological roughness. Here the scattering function can be expressed in terms of the height-height correlation C of the interface by [25]:

$$C(x, y) \coloneqq \langle u(x_0 - x, y_0 - y) * u(x_0, y_0) \rangle_{x_0, y_0} \tag{2.19}$$

The topological root mean square (rms) roughness σ of an interface is also defined by a height-height correlation function:

$$\sigma \coloneqq \sqrt{\langle u^2 \rangle} = \sqrt{C(0,0)} \tag{2.20}$$

In case of vertically stacked membranes, a statistical, time-averaged description of the fluctuation is described by the membrane correlation function. Within the approach of a continuum model, the total free energy of the membrane multilayers can be described with the discrete smectic Hamiltonian H [35]:

$$H = \int_0^A d^2r \sum_{n=1}^{N-1} \left(\frac{B}{2d} (u_{n+1} - u_n)^2 + \frac{\kappa}{2} \left(\nabla_{xy}^2 u_n \right)^2 \right), \tag{2.21}$$

where N is the total number of membranes, d their equilibrium periodicity and A the area occupied by the set of multilayers. At any time, each point of a membrane can be defined in x and y coordinates and is displaced from the average membrane z-position by an increment $u_n(x, y)$ due to thermal fluctuations (Figure 2.4a).

The scattering from a set of stratisfied interfaces with correlated roughnesses can be described by the scattering function S within the first Born approximation (that assumes that scattering is weak compared to the incident billumination) as:

$$S(q_z, q_\parallel) \propto \frac{1}{q_z^2} \sum_{n,m=0}^{N} e^{-(1/2) q_z^2 (\sigma_n^2 + \sigma_m^2)} \Delta\rho_n \Delta\rho_m e^{-i q_z (z_n - z_m)} * \int_{-\infty}^{\infty} e^{q_z^2 C_{nm}(r)} e^{-i q_\parallel r} dr, \tag{2.22}$$

where N is the total number of membranes, $\Delta\rho_n$ is the step in scattering length density across the nth interface and C_{nm} is the cross-correlation function between the nth and the mth interface.

If multilayers have constant membrane periodicity, the scattering function can be simplified to:

$$S(q_z, q_\parallel) \propto \frac{e^{-q_z^2\sigma^2}}{q_z^2} N + 2\left[\sum_{k=1}^{N}(N-k)\cos\,(kq_z\,d) * \int_{-\infty}^{\infty} e^{q_z^2 C_k(r)} e^{-iq_\parallel r} dr\right] \qquad (2.23)$$

Within this system, the vertical compression is characterized by the compression modulus B while bending is characterized by the membrane bending modulus κ. Mechanical parameters can be characterized uniquely by the Caillé parameter η and the de Gennes parameter λ of smectic liquid crystals by (Figure 2.4b):

$$\eta = \frac{\pi k_B T}{2d^2\sqrt{\kappa B/d}},\ \text{Caillé parameter} \qquad (2.24)$$

$$\lambda = \sqrt{\frac{\kappa}{Bd}},\ \text{de Gennes parameter} \qquad (2.25)$$

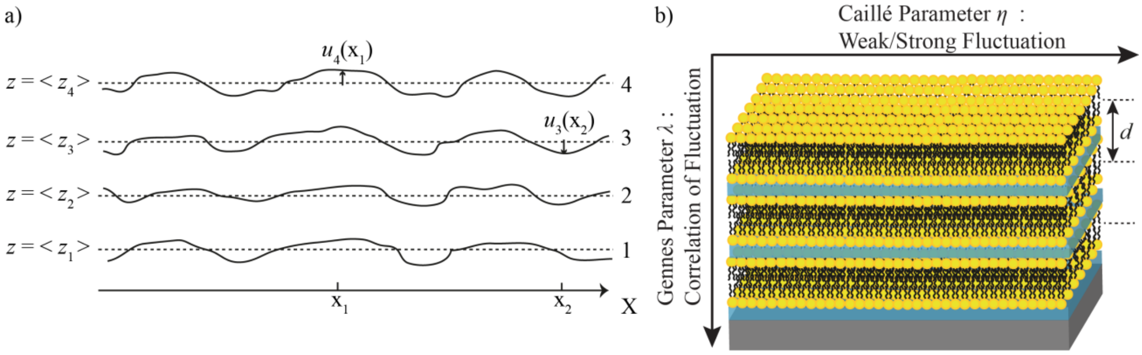

Figure 2.4 (a) Parameterization of a set of stratified rough layers. (b) Properties of membrane fluctuations described by Caillé and de Gennes parameter.

A high Caillé parameter η corresponds to a "soft" system with strong fluctuations and a high amplitude. The de Gennes parameter λ implies the stiffness of a system and if the bending modulus is rather dominant (high λ values) or the compression modulus (low λ values). Moreover, it determines how strongly the fluctuations of a layer are correlated with its neighbors, depending on the wavelength: small λ values imply a weak transmission depth of the displacement, whereas high λ values mean that short wavelength are damped more strongly than long wavelength.

3 Materials and Methods

3.1 Materials

3.1.1 Chemicals

Deionized water (DI water, resistance $R > 18\ \text{M}\Omega\text{cm}^{-1}$) was purified by a Millipore system (Molsheim, France). The chemicals for the buffers were purchased from Roth (Karlsruhe, Germany), except for EDTA which was purchased from Fluka (Buchs, Switzerland) and KCl coming from AppliChem (Darmstadt, Germany). Gibco® PBS tablets were purchased from Life Technologies GmbH (Frankfurt, Germany).

3.1.2 Buffers

For all aqueous solutions double deionized water a Millipore station (Millipore, Molsheim, France) was used, with a specific resistance of $\rho > 18\ \text{M}\Omega\text{cm}$. For the conducted experiments the following buffers were prepared:

- Hepes-buffer:150 mM NaCl, 10 mM Hepes, 0.1 mM EDTA at pH 7.4.
- Hepes-buffer with 2 mM $CaCl_2$: 150 mM KCl, 10 mM Hepes, 2 mM $CaCl_2$ at pH 7.4.
- K^+-buffer: 150 mM KCl, 10 mM Hepes, 0.1mM EDTA at pH 7.4.
- Cs^+-buffer: 150 mM CsCl, 10 mM Hepes at pH 7.4.
- Ca^{2+}-buffer: 50 mM $CaCl_2$, 10 mM Hepes, at pH 7.4.
- CRP-buffer: 100 mM NaCl, 10 mM Tris-HCl, 5 mM $CaCl_2$ at pH 8.0.
- PBS-buffer: Gibco® PBS tablet with 150 mM NaCl, 10 mM phosphate at pH 7.3-7.5.

3.1.3 Phospholipids

The lipids 1-palmitoyl-2-oleoyl-*sn*-glycero-3-phosphocholine (**POPC**, MW = 760.08 g/mol), 1-oleoyl-2-palmitoyl-*sn*-glycero-3-phosphocholine (**OPPC,** MW = 760.08 g/mol), 1-stearoyl-2-oleoyl-*sn*-glycero-3-phosphocholine (**SOPC**, MW = 788.13 g/mol), 1,2-dioleoyl-*sn*-glycero-3-phosphocholine (**DOPC**, MW = 786.11 g/mol), 1,2-di-(9Z-octadecenoyl)-*sn*-glycero-3-phosphoethanolamine (**DOPE**, MW = 698.54 g/mol), 1,2-dioleoyl-3-trimethylammonium-propane (chloride salt) (**DOTAP**, MW = 760.08 g/mol), 1,2-dioleoyl-*sn*-glycero-3-phospho-(1'-*rac*-glycerol) (sodium salt) (**DOPG**, MW = 796.52 g/mol), 1-palmitoyl-2-azelaoyl-*sn*-glycero-3-phosphocholine (**PazePC,** MW = 665.84 g/mol), 1-palmitoyl-2-(9'-oxo-nonanoyl)-*sn*-glycero-3-phosphocholine (**PoxnoPC,** MW = 649.84 g/mol) and **Cholesterol** (99% pure, MW = 386.65

g/mol) were purchased from Avanti Polar Lipids (Alabaster, AL, USA) and 1,2-dipalmitoyl-*sn*-glycero-3-phosphocholine (**DPPC,** MW = 734.04 g/mol), Soya-PC (**Lipoid S100**, $\overline{\mathrm{MW}}$ = 780 g/mol) and Soya-LPC (**Lipoid S LPC80**, $\overline{MW}$ = 555 g/mol) were generous gifts from Lipoid (Ludwigshafen, Germany) (Figure 3.1). The stock solutions of lipid mixtures at the final concentration of 1 mg/ml were prepared in chloroform:methanol (9:1 v/v) and stored at -20 °C. The purity of the OxPL lipids was verified by thin layer chromatography on silica gel coated plates from Machery-Nagel (Düren, Germany), using chloroform:methanol:water: ammonia (65:20:2:2, v/v) as the eluent. No impurities were detected upon examination of the plates after potassium permanganate staining.

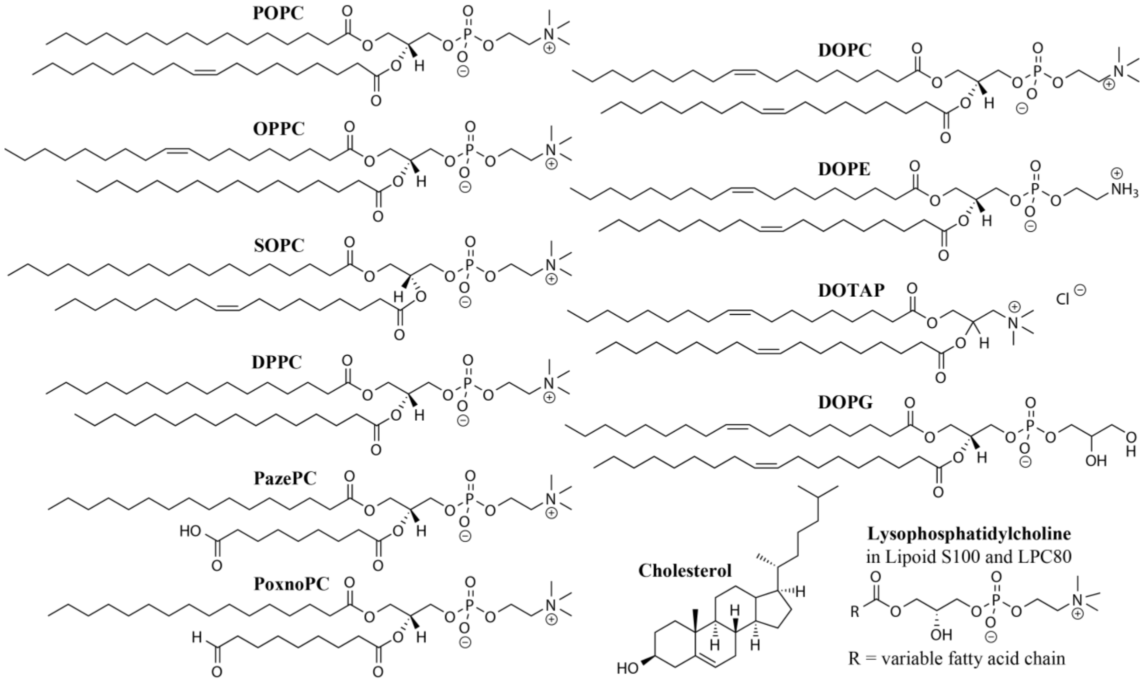

Figure 3.1 Chemical structure of the lipids used in this study.

3.1.4 Proteins

The C-reactive protein (**CRP**) was purchased from Hölzel Diagnostica (Cologne, Germany) or Sigma-Aldrich (Munich, Germany) and diluted in CRP-buffer for experiments. Prior to use, CRP diameter was checked by DLS and SDS-Page (12%) to secure that the pentameric form is present (Figure 3.2). **EO6** monoclonal antibody (mice) was purchased from Avanti Polar Lipids (Alabaster, USA) and stored undiluted. For experiments it was diluted in PBS-buffer. **Secondary antibody** (anti-mouse produced in goat) labeled with TRITC was purchased from Sigma-Aldrich (Munich, Germany) and stored undiluted at -20 °C. **Mucin 2** and **mucin 3** from porcine stomach were generous gift from Prof. Stremmel (Heidelberg, Germany). It can be purchased from Sigma-Aldrich (Munich, Germany). Both crystalline proteins were dissolved in Hepes-buffer.

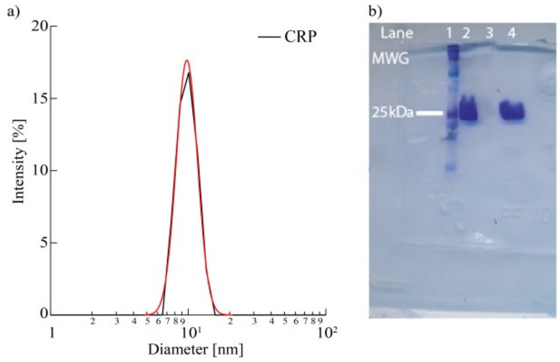

Figure 3.2 (a) DLS measurements show that hydrated CRP has a diameter of d_{CRP} ~ 10 nm with a FWHM ~ 4 nm, (b) while SDS Page (12%) exhibit a molecular weight of ~ 24 kDa and a purity of ~ 99% (lane 2 and 4).

3.1.5 Cell experiments – Solvents and Chemicals

Glioblastoma multiforme cells from patients (**GBM10, GBM39, GBM60**) were kindly provided by the group of Prof. A. Martin-Villalba (DKFZ, Heidelberg, Germany). **EO6** mouse monoclonal antibody [(IgM) Anti-(Oxidized Phospholipid)] was purchased from Avanti Polar Lipids (Alabama, USA). **Neutravidin**, a 60 kDa deglycosylated avidin molecule was purchased from Invitrogen (Karlsruhe, Germany). The apoptosis signaling ligand **hsCD95L** was custom designed by Apogenix GmbH (Heidelberg, Germany). Cell staining of unfixed cells was done with **PKH67** according to the manufacture instructions (Sigma Aldrich, Munich, Germany), a green fluorescent dye (λ_{ex} = 490 nm, λ_{em} = 502 nm). Cell staining of fixed cells was done with **anti-mouse IgG** (whole moleculae)**-TRITC** antibody goat (Sigma Aldrich, Munich, Germany), a orange fluorescent dye (λ_{ex} = 557 nm, λ_{em} = 576 nm). Cell nuclei were DNA stained with

Hoechst dye (λ_{ex} = 340 nm, λ_{em} = 460 nm) which was a kind gift from Patrick Horn from the group of Prof. A. Ho (Heidelberg, Germany). **Mowiol® 4-88** (Sigma Aldrich, Munich, Germany) was freshly prepared according to the manufactures protocol and stored at -20 °C.

3.2 Methods: Substrate Preparation, Instrumental Methods and Experimental Protocols

Unless otherwise mentioned, all used substrates were cleaned by modified RCA protocol as described elsewhere [36]. The **RCA cleaning procedure** consists of repeated steps of sonication of the substrates for three minutes in acetone, ethanol, methanol and H_2O each. Afterwards they were sonicated in a freshly prepared mixture consisting of 5:1:1 (v/v/v) H_2O:NH_4OH (30%):H_2O_2 (30%) for the same time and then heated up for another 30 minutes at 60 °C. Finally they were rinsed 10 times with H_2O, dried at 70 °C and stored in a vacuum chamber over night.

3.2.1 Preparation Protocols

3.2.1.1 Preparation of Small Unilamellar Vesicles (SUV)

Small unilamellar vesicles (**SUV**s) of lipids were prepared as follows: Phospholipid stock solutions in chloroform/methanol (9:1, v/v) were mixed in a desired ratio and the solvents were evaporated either with method (i) or (ii) dependent on the amount of vesicle solution needed: (i) using the rotary evaporator for 2 h under reduced pressure or (ii) under a nitrogen stream, followed by a removal of any traces of solvent in the vacuum chamber over night.

The resulting dry lipid film was rehydrated in filtered and degassed buffer solution to obtain a desired final lipid concentration. The suspension was mixed by vortexing for several minutes. To obtain SUVs, two different methods were used in dependence of the experimental technique used afterwards: the lipid suspension was either gained by (iii) using an extruder (min. 31 cycles) with a polycarbonate membrane (Avestin, Mannheim, Germany) with a pore size of 50 nm or (iv) sonication for 45 min with a titanium tip sonicator S3000 (Misonix, Farmingdale, NY, U.S.A.) followed by a centrifugation at 10000 rpm at 4 °C for 15 min to remove any residual titanium particles from the tip sonicator. At the end the supernatant was transferred into a new clean tube.

3.2.2 Instrumental Methods and Experimental Protocols

3.2.2.1 Langmuir Film Balance

Surface Pressure Measurements - Principle of the Technique

The Langmuir trough or surface film balance consists of (i) a hydrophobic trough usually manufactured of Teflon (PTFE) to prevent water spilling, (ii) a force sensor for surface tension measurements and (iii) one or two barriers to control the surface area of the monolayer spread at the air-water interface. The force sensor allows the determination of the surface tension by the vertical pull on a wetted Wilhelmy plate hanging through the surface. The Wilhelmy plate is an absolute method in which the forces acting on the plate, usually made of platinum or filter paper, partially immersed in the subphase are measured. Such forces are the downward forces, such as gravity (P) and surface tension (γ), and upward forces, such as buoyancy (A) due to the displacement of water. The net downward force acting on the Wilhelmy plate is given by:

$$F = P + 2\gamma(w + t)\cos\theta - A, \tag{3.1}$$

where w and t (t << w) are the width and the thickness of the plate, respectively, and θ is the contact angle of the liquid with the solid plate. If the plate is completely wetted, the contact angle $\theta = 0$ and $\cos\theta = 1$. In addition, since t << w, the buoyancy term can be neglected yielding:

$$F = P + 2\gamma w \tag{3.2}$$

When the composition of the interface is changed and providing that the plate is maintained in a fixed position, the gravity P stays constant, then:

$$\Delta F = 2w(\gamma_{water} - \gamma_{monolayer}) = 2w\pi, \tag{3.3}$$

where π is the surface pressure.

Usinf the Langmuir trough, information about the structure and physical properties of lipid membranes can be gained by investigating lipid monolayers at the air-water interface as a model system. Indeed, the Langmuir monolayer has been considered since a long time as excellent models to study the interactions in 2D arrangements of amphiphilic molecules as well as models of cell membranes. Such monolayer at the air-water interface presents the unique advantage that density and lipid composition can be precisely controlled via surface tension measurements. Interestingly, the structural properties at the molecular level of the lipid monolayers (thickness, roughness, electron density) can be studied by combining the Langmuir balance to X-ray scattering techniques (XRR, GIXF which are explained in section 3.2.2.2) and optical techniques such as Brewster angle microscopy, fluorescence microscopy and ellipsometry to get more information about the film structure (film thickness, domains size) at different length scales. In addition, the surface is accessible from the aqueous side and can be used for the study of interactions of ions and proteins with the membrane [37, 38] (as utilized in the sections 5.1.4.3, 5.2.2.2 and 7.1.3 in this thesis).

When spreading amphiphilic compounds dissolved in an organic solvent onto an aqueous subphase, an oriented, insoluble monolayer is formed, the so-called Langmuir monolayer [39, 40]. The polar hydrophilic head of the molecules remain in contact with the aqueous phase while the hydrophobic hydrocarbon chains extend into the air. Moving barriers compress or expand the monolayer and hence modify its surface area. If the area is decreased due to compression of the lipid film, the lipid film undergoes a phase transition from a more disordered, liquid expanded phase (L_e-phase) to an ordered, liquid condensed phase (L_c-phase), where the hydrocarbon chains have an ordered configuration (Figure 3.3). This phase transition can be described with the two-dimensional analogue of the three-dimensional van-der-Waals equation, which is valid for the two phases and for a coexistence regime.

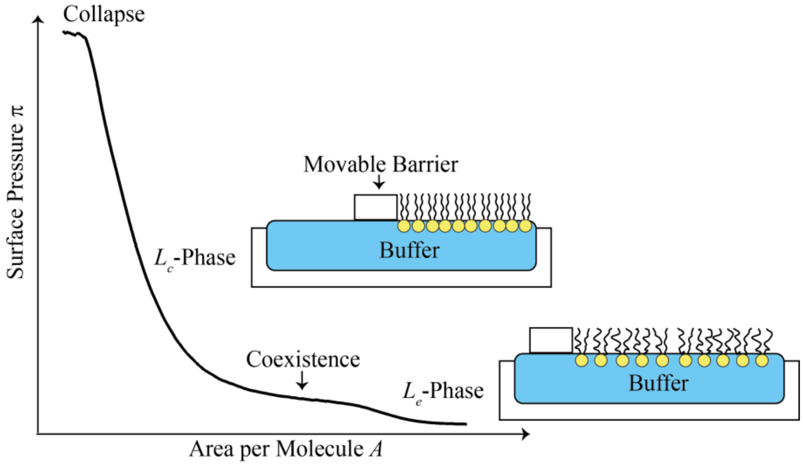

Figure 3.3 Sketch of a Langmuir isotherm showing the Langmuir film balance and how lipids undergo a transition from disordered L_e-phase to ordered L_c-phase upon compression including a plateau region corresponding to the phase coexistence.

While compression, the surface pressure of the lipid film π is monitored as a function of the molecular area A and describes the in-plane interaction of the molecules, confined by two dimensions. The maximum achievable surface pressure is limited by the surface tension of the air-water interface ($\sigma \approx 72$ mN/m), but usually the monolayer collapse is far below that.

From the pressure-area isotherms, thermodynamic properties such as the compressional modulus and Gibb’s free energy can be obtained. The **compressional modulus** κ (the reciprocal of isothermal compressibility Cs) can be used to characterize the actual phase of the lipid monolayer and is calculated according to [41]:

$$\kappa = \frac{1}{C} = -A\left(\frac{\partial \pi}{\partial A}\right)_T \tag{3.4}$$

According to Davies and Rideal values below 12.5 mN/m, in the range of 13 - 50 mN/m, 100 - 250 mN/m and above 250 mN/m account for the gaseous state, the liquid expanded phase, liquid condensed phase and the solid state of a monolayer, respectively [42].

The excess **Gibb´s free energy** can be calculated from *π-A* isotherms by [40, 43]:

$$\Delta G_{12}^{exc} = \int_0^{\pi}\left[A_{12}^{mix} - A_{12}^{ideal}\right] d\pi = \int_0^{\pi}\left[A_{12}^{mix} - \chi A_1 - (1-\chi)A_2\right] d\pi, \tag{3.5}$$

where A_{12}^{mix} is the effective mean molecular area of the mixture, A_1 the area per molecule of pure OxPL, A_2 the area per molecule of pure phospholipid and χ is the mol% of OxPL. If the monolayer is ideally mixed or totally immiscible, ΔG_{12}^{exc} is equal to zero. If ΔG_{12}^{exc} has positive values then the mixture exhibits phase separation, while negative values of ΔG_{12}^{exc} indicates monolayer stability and the mixture has attractive interactions between the components.

In case of an ideal mixture, the **average area per molecule** A_{12} is given as:

$$A_{12}^{ideal} = \chi A_1 - (1-\chi)A_2 \tag{3.6}$$

If the plot of A_{12} against χ of the experimental data deviates from linearity then the mixture is not ideal and the average molecular area is modified by the molecular interactions.

Surface Potential Measurements - Principle of the Technique

Concomitantly to the π-A measurements, the surface dipole potential can be measured to get the electrical properties of the monolayer, which can reveal the conformation and orientation of the monolayer constituents. The surface potential arises from the potential difference occurring between the hydrocarbon tails and the first few water layers near to the lipid head group. Changes in the dipole potential caused by spreading a lipid monolayer at the air-water interface can be estimated from the conductance of hydrophobic ions. Typical phospholipids (PL) give rise to values of ~ 400 mV in monolayers and ~ 280 mV in bilayers [44].

The most widely used method is the vibrating Kelvin probe developed initially for measuring contact potential differences between conducting materials. The setup consists of a metallic plate as sensing electrode located at a short distance above the surface of the aqueous subphase (Figure 3.4).

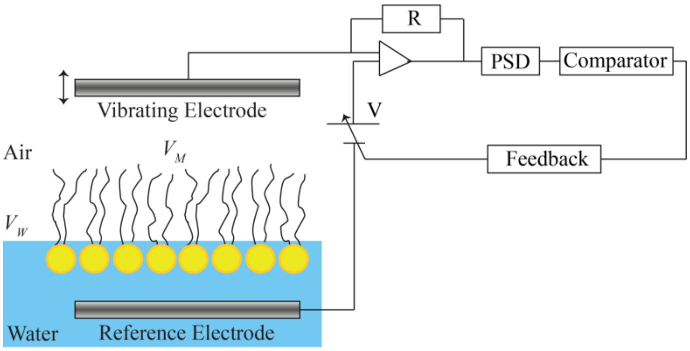

Figure 3.4 Schematic illustration of the experimental setup for surface-potential measurements of monolayers at the air-water interface.

On the bottom of the subphase, there is a reference electrode located. The subphase surface with a potential V (V_W if clean, V_M if covered with a monolayer) charges the air capacitance C, formed between the surface and the vibrating electrode. If the plate vibrates, it modulates the capacitance and causes an alternating current which flows through the high value resistance R, generating an alternating voltage. This voltage can be detected by a phase-sensing detector and passed to a computer. The comparator gives an error signal, which is used to adjust the DC voltage applied to the reference electrode to a value $-V$ which nulls the alternating current (going through R). By measuring V first of the clean subphase and then for the monolayer surface, the surface potential of the monolayer $\Delta V = V_W - V_M$ is readily determined. Therefore, ΔV is a direct measure of microscopic processes occurring in the monolayer.

To gain the molecular dipole moments of molecules forming the monolayer, the **Helmholtz** equation can be used:

$$\Delta V = \frac{\mu_n}{A\varepsilon_0} = \frac{\mu cos\theta}{A\varepsilon\varepsilon_0}, \tag{3.7}$$

where μ_n is the effective molecular moment (directed normally to the subphase surface), A the area occupied by each molecule and ε_0 the permittivity of free space. The molecules with an actual moment of μ can also be described with an angle θ to the subphase normal, where ε is an apparent relative permittivity and accounts for dipole-dipole interaction in the monolayer. Within this model, the monolayer is considered to be a floating monolayer with a formation of a uniform assembly of molecular dipoles which are contributed equally to the polarization with a constant remaining ε.

The monolayer at the air-water interface using the Helmholtz model can be described by the **Vogel and Möbius (VM)** two-layer capacitor model, where it is assumed that there is no difference in the contributions of headgroup and tailgroup moments [45, 46]. This is based on the assumption that the headgroup moment is well-screened by the water subphase so that its contribution to the surface potential can be neglected. Thus, the effective molecular moment can be described as a sum of two terms by:

$$\mu_n = \mu_\alpha + \mu_\omega, \tag{3.8}$$

where μ_α and μ_ω are the distributions of the headgroup and hydrocarbon chain, respectively (Figure 3.5a). In the VM model, μ_α includes hydration effects of the headgroup and effects arising from head-group-subphase interaction such as the contribution from the diffuse double-layer. However, the combination of effects from both, headgroup region and the diffuse double layer, might complicate the interpretation of values quoted for the headgroup moments.

Therefore, **Demchak and Fort (DF)** introduced a three-layer capacitor model which treats the underlying water subphase to the surface potential independently [47] (Figure 3.5b).

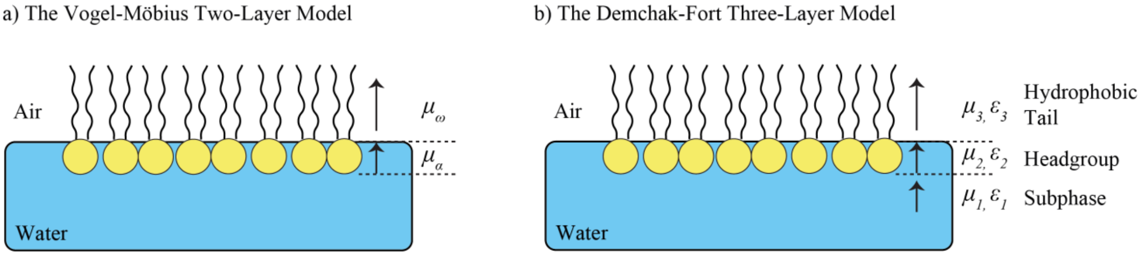
a) The Vogel-Möbius Two-Layer Model

b) The Demchak-Fort Three-Layer Model

Figure 3.5 Schematic illustration of the (a) Vogel-Möbius (VM) two-layer capacitor model and (b) the Demchak-Fort (DF) three-layer model of a monolayer at the air-water interface.

In the DF model, each layer is described with a local relative permittivity ε_i which leads to a modification in the Helmholtz equation to:

$$\Delta V = \frac{1}{A\varepsilon_0}\left[\frac{\mu_1}{\varepsilon_1} + \frac{\mu_2}{\varepsilon_2} + \frac{\mu_3}{\varepsilon_3}\right], \tag{3.9}$$

where μ_1/ε_1 is the contribution from any polarization or change in orientation of water molecules due to the presence of the monolayer, μ_2/ε_2 is the contribution from dipoles of the hydrophilic head group and μ_3/ε_3 is the contribution from the hydrophobic tail region. The contribution of the subphase is assumed to be constant for all unionized close-packed insoluble monolayers. The introduction of ε_2 and ε_3 enables the description of inter- and intra-molecular dipole-dipole interactions in the monolayer as well as hydration effects of the headgroup.

However, calculations based on both models, DF and VM, can be easily compared, since:

$$\mu_\alpha = \left[\frac{\mu_1}{\varepsilon_1} + \frac{\mu_2}{\varepsilon_2} + A\varepsilon_0\psi_0\right] \tag{3.10}$$

and

$$\mu_\omega = \frac{\mu_3}{\varepsilon_3}, \tag{3.11}$$

where A is the molecular area and ψ_0 is the potential across the double-layer. The double-layer potential ψ_0 can be obtained by solving the non-linear Poisson-Boltzmann equation which yields the **Gouy-Chapman** equation by:

$$\psi_0 = \frac{2kT}{e}\sin h^{-1}\left[\frac{\sigma}{(5.88*10^{-7}c\varepsilon T)^{1/2}}\right], \tag{3.12}$$

where k is the Boltzmann's constant, T the absolute temperature, e the electronic charge, σ the surface charge density, c the ionic concentration and ε the relative permittivity of the electrolyte ($\varepsilon \sim 80$ for aqueous subphases).

Although these models are limited due to their strong assumptions, which might lead to discrepancies to experimentally obtained results, they are a powerful tool to model the interaction at the air-water interface of membrane-related biological processes.

Experimental Protocols

The **surface pressure-area isotherms** were obtained using different Teflon Langmuir troughs with a pressure sensor coupled to a Wilhelmy plate made of filter paper (Nima-LB total trough area A = 345 cm^2, total volume V = 575 ml; KSV-LB total trough area A = 243 cm^2, total volume V = 185 ml). The total trough was filled with buffer and the lipids dissolved in chloroform (c = 1.0 mg/ml) were gently spread onto the buffer subphase at RT (19 ± 1 °C) using a Hamilton microsyringe. Prior to compression, 20 min was allowed for the complete evaporation of the solvent. The barrier speed of the instrument was set at 4 cm^2/min while the surface pressure of the film was measured.

In the study of the interaction between phospholipids (DOPC, DOPE, DOTAP, DOPG) and mucin (mucin 2 and mucin 3), the lipids dissolved in chloroform (c = 1.0 mg/ml) were spreaded onto Hepes-buffer subphase. After 10 min of evaporation, the mucin solution (20 µl of 0.5 mg/ml) was injected under the barrier. After an incubation time of 1 h the barriers speed was set at 7.5 cm^2/min for film compression.

For **surface potential** measurements a Kibron balance (µ Trough S, Kibron, Helsinki, Finland) equipped with a Precision Plus trough was used to simultaneously measure π-A and $\Delta\psi$-A isotherms, using the features of the control software (FilmWare 3.57, Kibron). Total trough area was A = 135 cm^2 with a total volume of V = 20 ml. The surface pressure π was measured using a Wilhelmy wire hanging from a high precision microbalance. The monolayer dipole potential ψ was measured using the vibrating plate method.

To investigate the lipid-peptide interaction of EO6 antibody and CRP with phospholipid monolayers **surface tension** measurements were measured with the above mentioned Kibron balance. After deposition the lipids gently onto the buffer and let the solvent evaporate for 15 min, the film was compressed to a desired surface pressure and left for 15 min to equilibrate. Then the surface tension was measured with time. If surface tension was stable, the peptide was injected into the subphase and the difference in surface tension was recorded.

3.2.2.2 XRR and GIXF

Experimental Protocols

Specular X-ray Reflectivity (XRR) and **Grazing Incidence X-ray Fluorescence (GIXF)** experiments were carried out at the beamline ID10B of the European Synchrotron Radiation Facility (ESRF, Grenoble) with the experimental setup shown in Figure 3.6.

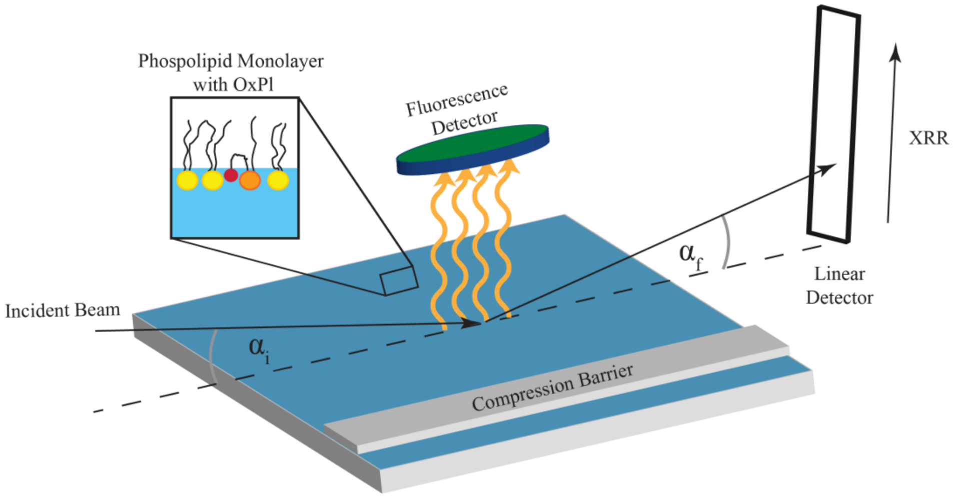

Figure 3.6 The experimental setup and the scattering geometry used for XRR and GIXF at the air-water interface.

There the model systems of (i) pure OPPC (control), (ii) PazePC/OPPC (0.1), (iii) PoxnoPC/OPPC (0.1) (iv) pure PazePC and (v) pure PoxnoPC at the air-water interface were in the focus of interest. As OPPC is the enantiomer of POPC and the investigations focused on the change in physical properties of the membrane due to (1) the presence of OxPL and (2) the presence of different cations, it was assumed that there will be no differences in behavior due to different stereochemistry of phospholipids. For experiments, monolayers were prepared by spreading the lipid solution onto the following subphases: (a) K^+-buffer, (b) Ca^{2+}-buffer and (c) Cs^+-buffer. Prior to compression, 20 min was allowed for the complete evaporation of the solvent. The lipid monolaye was compressed to the surface pressure of π = 20 mN/m which coincide with an area per lipid molecule in the range of $A \approx 65$ - 110 Å^2, depending on the lipid mixture used.

The samples were irradiated with a monochromatic synchrotron beam either with an energy of 8 keV (λ = 1.55 Å), 9 keV (λ = 1.37 Å) or 14 keV (λ = 0.89 Å). The film balance was kept in a He atmosphere to minimize the scattering of the fluorescence emission by air as well as to minimize the radiation damage. **XRR** was measured with a linear detector (Vantec-1, Bruker AXS, USA). After subtraction of the diffuse intensity background (at $\alpha_f \neq \alpha_i$), the specular reflectivity was analyzed using the Parratt formalism [27] with a genetic minimization algorithm implemented in the Motofit software package [48].

GIXF measurements were carried out at incident angles α_i below and above the critical angle of total reflection α_c. X-ray fluorescence signals from the chemical elements in the illuminated volume were recorded with an energy sensitive detector (Vortex, SII NanoTechnology, USA) and normalized by the detector counting efficiency. The emissions from K K_α, Ca K_α or Cs L_α lines were extracted using a multiple-Gaussian peak fitting routine in a self-written code (Igor Pro, WaveMetrics, Portland, USA). To compensate systematic differences between the experiments, the recorded fluorescence intensities were normalized by the elastically scattered beam intensity. The fluorescence signals in the presence of monolayers were normalized by the signals from the corresponding blank buffer, and are plotted as a function of momentum transfer perpendicular to the interface**.** This procedure eliminates artifacts arising from the experimental geometry such as the size of beam footprint and the fluorescence detector aperture [32].

3.2.2.3 Fluid Chamber (XRR)

High-energy specular X-ray reflectivity measurements were performed at a sealed X-ray tube (D8 Advance, Bruker, Germany), operating with Mo Kα radiation (E = 17.48 keV, λ = 0.0709 nm) at the KIT (inhouse instrument, Karlsruhe, Campus Nord, Germany). The incident beam was collimated by various slits, reducing the beam size to 200 µm in the scattering plane. Automatic attenuator settings were used to avoid radiation damage. In addition, each measurement was completed in approximately 3 h. For sample preparation freshly cleaned silicon wafers with native oxide (24 mm x 9 mm) were inserted into a self-manufactured Teflon fluid chamber with Kapton windows which was inspired by the work of Miller *et al.* and Novakova *et al.* [49, 50] (Figure 3.7).

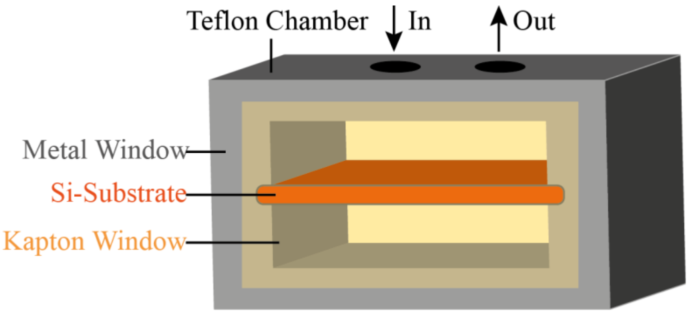

Figure 3.7 A schematic representation of the self-manufactured Teflon fluid chamber. At both sides X-ray can pass through the Kapton windows. On the upper side, the samples can be injected through the injection holes.

The **membranes** were directly prepared in the fluid chamber by injecting 2 ml of a liposome solution with a concentration of 1 mg/ml. After 2 h incubation time at 37 °C, the chamber was rinsed 10 times with buffer to wash away excess liposomes and a reflectivity measurement of the solid-supported membrane at RT was performed. For **protein** experiments, CRP (1 ml of 25 µg/ml) was added to the fluid chamber and incubated for 2 h at 37 °C. The momentum transfer perpendicular to the membrane plane is given as a function of the angle of incidence α_i given by equation (2.6). For each measurement point, the reflectivity was corrected for the beam footprint and for the beam intensity with the help of an in-beam monitor. The data were fitted using the Parratt formalism [27, 51] with a genetic minimization algorithm implemented in the Motofit software package [48].

3.2.2.4 Off-Specular Neutron Scattering

Neutron scattering experiments were carried out at D16 of the Institut Laue-Langevin (ILL, Grenoble, France). Figure 3.8 shows (a) the geometry of the experiment and (b) the scattering intensity as a function of Γ and Ω.

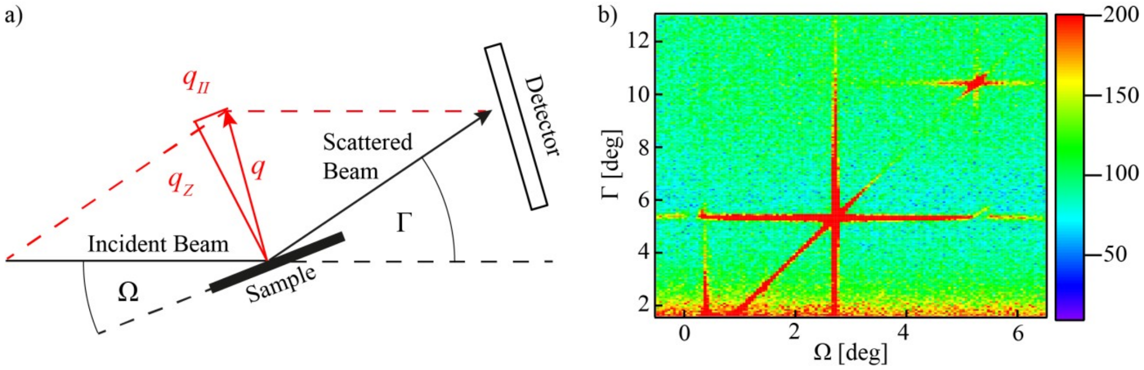

Figure 3.8 (a) Geomtery of the scattering experiment and (b) the scattering intensity from POPC multilayers as a function of Γ and Ω, measured at 37 °C and ~ 33% relative humidity. The diagonal line corresponds to a specular condition (Γ = 2Ω), while the horizontal stripes resulting from the sample periodicity are known as Bragg sheets. From geometrical considerations, the angular coordinates Γ and Ω can be translated into the reciprocal space coordinates q_z and $q_{||}$ (equations 3.11, 3.12).

A monochromatic (Δλ/λ = 1%) neutron beam of λ = 4.51 Å hits the sample through an aluminum windows of the sample chamber, whereas the incident angle Ω (i.e., the angle between the incident beam and the sample plane) is adjusted by a rotation stage. The intensity of the scattered beam is recorded by a two-dimensional position-sensitive ^{3}He detector with 128 x 128 channels with a pixel size of 3 mm. The sample-to-detector-distance was set to 953 mm. Γ denotes the angle between the scattered and the incident beam. The beam, focused to the sample in the vertical plane, had a horizontal width of 3 mm and was 25 mm in height at the sample position. For each measurement at an angle Ω, the detector readout was normalized to the intensity of the incident beam (via an in-beam monitor), the channel sensitivity, and the illuminated sample area. Subsequently, the two-dimensional detector readout was integrated in the vertical direction, which resulted in an one-dimensional intensity projection as a function of the horizontal detector channel position (corresponding to Γ). Thus, one Ω -scan yielded the recorded intensity as a function of Γ and Ω. The datasets in angular coordinates can be transformed into the reciprocal space using following equations:

$$q_z = \frac{2\pi}{\lambda}[\sin(\Gamma - \Omega) + \sin(\Omega)], \qquad (3.13)$$

$$q_{\parallel} = \frac{2\pi}{\lambda}[\cos(\Gamma - \Omega) - \cos(\Omega)]. \qquad (3.14)$$

Here, q_z and $q_{\parallel}$ are the scattering vector components perpendicular and parallel to the sample plane (see Figure 3.8a).

In case of many periodically arranged interfaces, the interference of reflected waves gives a high reflection intensity, which is known as Bragg peaks (Figure 3.8b). Here, the position of the peak maxima q_z^{max} are located periodically along q_z:

$$q_z^{max} = \frac{2m\pi}{d}, m = 1,2, \ldots \qquad (3.15)$$

Sample Preparation

The solid-supported membrane multilayers were prepared by the deposition of a 1.5 ml portion of lipid mixtures dissolved in 7:3 (v/v) mixtures of $CHCl_3$ and CH_3OH at a total concentration of 1 mg/ml. To study the influence of OxPL on the membrane, lipid membranes that contained two different molar fractions of either PazePC or PoxnoPC (10 mol% and 20 mol%) as well as pure OxPL and pure POPC membranes (control) were prepared. For the study of the interaction of CRP with solid-supported membrane multilayers, liposomes of POPC with and without incorporating 20 mol% of either PazePC or PoxnoPC were prepared. CRP was added to final concentrations of (2.9 µM, 1.5 µM and 0.8 µM) and left for incubation of 1 d at RT in CRP-buffer prior to deposition onto the Si substrates.

Si substrates with native oxide (Si-Mat, Landsberg/Lech, Germany) were cut into rectangular shape (55 mm x 25 mm) and cleaned by RCA method. The wafers were stored at 70 °C for 3 h, and subsequently in a vacuum chamber overnight to remove the residual solvent. The average number of membranes in the stacks could be roughly estimated to be in the order of several hundred from the amount of solution and the coated area.

To achieve the maximum contrast in scattering length density between hydrated region and hydrocarbon chains, Hepes-buffer (10 mM Hepes, 150 mM KCl, 2 mM $CaCl_2$ at pH 8) was prepared with D_2O (Euriso-Top, Saint-Aubin, France).

For the scattering measurements in humidified air, a climate chamber provided by the ILL was used, which allows for the precise regulation of both sample temperature and relative humidity (RH) (i.e., the osmotic pressure exerted to the sample) [52]. To ensure the equilibration, the sample was kept at each temperature and humidity condition for at least 1 h before the measurement. The samples were measured at 37 °C at two different relative humidity (RH) conditions (low RH $\approx$ 33% and high RH > 95%) and in buffer conditions. For low and high RH, the sample cell reservoir was filled with D_2O. For experiments in bulk buffer conditions, a self-built liquid cell was used (Figure 3.9). Two Si wafers, with one coated with the membrane and moistened by a small amount of D_2O buffer, were mounted together facing each other and separated by small glass slide pieces (thickness: 0.13 mm). The capillary force confines a thin layer of aqueous buffer between the two wafers. During measurements, the entire liquid cell was kept inside the climate chamber at controlled temperature and high RH (> 95%) to minimize the evaporation of water.

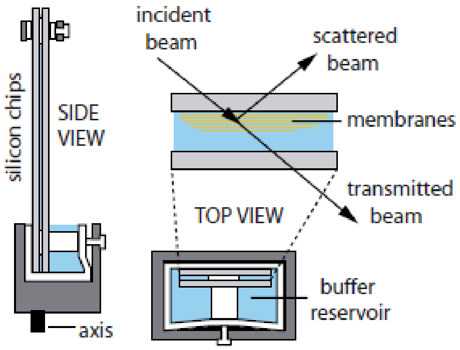

Figure 3.9 Sketch of the self-developed liquid cell (adopted from [53]). The solid-supported membrane multilayers are immersed in a thin layer of bulk between the two silicon wafers. The neutron beam hits the sample through the silicon support.

3.2.2.5 Static-, Dynamic Light Scattering (SLS, DLS) and Zeta(ζ) Potential

Principle of the Techniques

Overview. The most used techniques based on light scattering are the static light scattering (SLS) and dynamic light scattering (DLS). SLS involves the measurement of the time-averaged intensity in the time-scale of seconds, while DLS measurements involve light scattering intensity fluctuation in the time-scale of microseconds, in order to obtain a meaningful autocorrelation function. In general, SLS can determine the molecular weight M_w of proteins or peptide aggregation in solution in the typical range of 1 kDa to 20 MDa. The aggregation monitored by SLS gives rise to stoichiometry data in direct relation to the calculated M_w. With DLS particle hydrodynamic diameter and size distribution of molecules or aggregates can be determined. The zeta(ζ) potential determination is based on the measurement of the electrophoretic mobility of the charged particle in the presence of an electrical field by a combination of laser Doppler velocimetry and phase analysis light scattering. The ζ potential gives a number for the surface charge of the molecule and gives qualitative information about the stability of the system. Particles with a high charged surface tend to repulse the particles of the same charge, whereas particles with a charge close to zero tend to aggregate and cause flocculation due to interparticle interaction. Consequently, in the study of membrane interaction DLS and SLS techniques are very sensitive to changes in shape and size, the aggregation or peptide-induced aggregation of lipid vesicles, while the ζ potential detects altered electrophoretic mobility, when charged peptides interact with charged vesicles.

Static light scattering SLS uses the time-average intensity of the sample in a long time-scale relative to molecular diffusion (seconds to minutes). The molecular weight M_W and the second Virial coefficient (A_2) can be determined through the **Zimm method**:

$$\frac{KC}{R_\Theta} = \frac{1}{M_W P(\Theta)} + 2A_2 C, \qquad (3.16)$$

where C is the concentration of the scattering particle, K the optical constant, A_2 the second Virial coefficient, N_A the Avogadro's number and R_θ an angle dependent shape factor (Rayleigh ratio). They can be defined as:

$$K = \frac{2\pi^2}{\lambda_0^4 N_A}\left(n_0 \frac{dn}{dC}\right)^2, R_\theta = \frac{I_A n_0^2}{I_R n_R^2} R_R \text{ and } P(\theta)^{-1} = \left(1 + \frac{q^2 R_g^2}{3}\right), \qquad (3.17)$$

where I_R is the reference scattering intensity, I_A the residual intensity of the solute, n_0 the solvent refractive index, n_R the reference refractive index, λ_0 the vacuum wavelength of the incident light, dn/dC the refractive index increment, R_R the Rayleigh ratio of the reference, $P(\theta)$ the intraparticle structure factor, θ the angle at which is being measured, R_R the radius of gyration and

q, the scattering vector. The shape factor is important for large particles since it arises from coherent interferences between light scattered from different points of the particle, but can be neglected for particles that are much smaller than the wavelength of the irradiated light. Under this condition the Rayleigh expression can be simplified to equation 3.18. In the Zimm method, M_w can be determined by extrapolation of the scattering intensity both to zero angel (equation 3.18) and infinite dilution (equation 3.19):

$$\frac{KC}{R_\Theta} = \frac{1}{M_W} + 2A_2C \tag{3.18}$$

$$\frac{KC}{R_\Theta} = \frac{1}{M_W P(\Theta)}, \tag{3.19}$$

where A_2 describes the interparticle interactions. Stable scattering particles (monomers) in solution show positive values, while negative values indicate a tendency to aggregation. A_2 is calculated by the slope of equation 3.18. In the simpler **Debye method**, the intensity is measured at different concentrations but not at different scattering angles. By the consideration of ideal solvent conditions, M_W and A_2, but not R_g can be determined.

With the help of the **Dynamic Light Scattering** (**DLS**) technique size and polydispersity index (*PdI*) of measured substances can be determined. Particles, emulsions and molecules in suspension undergo random walk, known as the Brownian motion. This is the motion induced by the bombardment by solvent molecules that themselves are moving due to their thermal energy. In this situation the probability density function is given by the formula [54]:

$$P(r,t|0,0) = (4\pi Dt)^{-3/2} exp(-r^2/4Dt), \tag{3.20}$$

where D is the diffusion constant. When assuming that the particles used in the experiment are spherical particles with a small diameter compared to the molecular dimensions, the **Stoke-Einstein relation** can be applied which gives the diffusion constant [54]:

$$D = \frac{k_B T}{6\pi\eta r}, \tag{3.21}$$

where r is the radius of the particels, k_B is the Boltzmann constant, T is the temperature in Kelvin degrees and η is the viscosity of the solvent. Since from the light scattering it is possible to obtain information about the position of the particles, the formula above determines the radius of the particels.

When particles are illuminated with a laser, the intensity of the scattered light fluctuates at a rate that is dependent upon the size of the particle, since smaller particles can move more quickly than big particles. These fluctuations are based on the Doppler shift, since the wavelength of the incoming light is changed because of the Brownian motion. This change is related to the size of the particle. Computing these intensity fluctuations yields the intensity autocorrelation function which allows for the determination of the velocity of the Brownian motion and hence the particle size using the Stokes-Einstein relationship. The diameter measured in dynamic light scattering is the hydrodynamic radius given by a translational diffusion coefficient. The translational diffusion coefficient refers to how the particle diffuses within the fluid and depends on the size of the particle core, as well as on the surface structure, concentration and type of ions in the medium. Any inconsistency in size, shape and mass distribution of the sample can be determined with the polydispersity index (*PdI*).

The **zeta(ζ) potential** of a particle is the overall potential that the particle acquires in a particular medium. The ζ potential is commonly used to characterize the physical properties of colloids and liposomes to establish their suitability for a range of applications. Liposomes, for example, are often used as drug delivery vehicles due to their ability to incorporate water-soluble materials in their aqueous volume or oil soluble materials in the lipid bilayer [55]. They can be designed for different applications by controlling their lipid composition or modifying their surfaces by conjugation of antibodies or peptides [56]. In a suspension charged liposomes attract ions to their surface. These ions form a layer coating the surface known as the Stern layer (Figure 3.10).

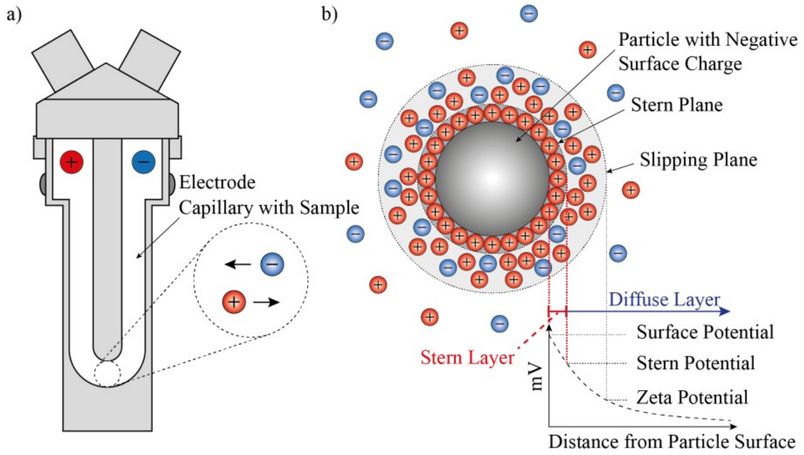

Figure 3.10 Schematic illustration of (a) the folded capillary cell and (b) the electric double layer that surrounds a particle in aqueous medium. The potential at the shear plane is known as the ζ potential.

Outside the Stern layer, there is a diffuse layer, where ions move more freely. If a particle moves in the presence of an electrical field, a shear plane forms within the diffuse layer and the ions within this boundary move with the particle, while the ions further away from the particle do not move with it. The electric potential which exists at this boundary is the ζ potential [57].

During the ζ potential measurement a voltage is applied across a pair of electrodes at each end of a measuring cell. The charged particles are attracted to the oppositely charged electrodes and move towards them. This movement is opposed by viscous forces that act on the particle. Finally, the particle reaches a constant velocity at equilibrium, which can be measured and expressed as the electrophoretic mobility. By measuring the electrophoretic mobility the ζ potential can be determined with the Smoluchowski equation using **Henry's function**, which is given as [58]:

$$\mu = \frac{v}{E} = \frac{2\varepsilon\xi f(kR)}{3\eta}, \tag{3.22}$$

where v is the constant velocity, E the electric field, ζ the zeta(ζ)-potential, μ the electrophoretic mobility, ε the dielectric permittivity of solution, η the viscosity and $f(kR)$ the Henry's coefficient. The factor $f(kR)$ counts for the ratio between the particle radius R, and the inverse thickness of the double layer, $1/k$. When the particle is much smaller than the double layer, then $f(kR) = 1$ (Hückel limit), while when the particle is much larger than the double layer, as is the case when the ionic strength is high, then $f(kR) = 1.5$ (Smoluchowsky limit). In aqueous electrolyte solutions ($> 10^{-3}$ M) the electrical double layer is much smaller than the particle's radius ($kR >> 1$) and the function $f(kR)$ approaches 1.5. Thus the **Smoluchowski approximation** applies and the ζ potential is simplified to:

$$\zeta = \frac{\mu\eta}{\varepsilon} \tag{3.23}$$

In the intermediate region between Smoluchowski and Hückel extremes, Henry's function can have values between 1 and 1.5 depending on the particle size and the nature of the electrolytic solution [59, 60]. Thus, the ζ potential makes it possible to estimate the membrane surface potential which depends on the adsorption or insertion of charged molecules in the lipid bilayer.

Experimental Protocols

DLS, SLS and ζ potential measurements were performed at 20 °C in Hepes- or CRP-buffer using a Malvern Zetasizer Nano ZS (Malvern Instruments Ltd., UK) with a backscattering detection at a constant 173° scattering angle, equipped with a He-Ne laser (λ_{em} = 632.8 nm) at 20 °C.

DLS experiments were carried out in disposable semi-micro cuvettes (Plastibrand, Wertheim, Germany). For each size measurement 3 scans (100 - 500 runs each) with a sample volume of 400 µl and an initial equilibration time of 2 min at 20 °C were performed using different modes of the instrument ("general purpose mode" for liposomes and the "protein analysis" mode for proteins) under automatically optimized conditions. The raw data were analyzed as distribution by intensity [%] with Igor PRO (WaveMetrics, Portland, USA) software using a lognormal function which is given as $f\ (x, K) = K_0 + K_1 * \exp -[ln\ (x/K_2)/K_3]^{\,2}$, yielding the position of the maximum and the full width at half maximum (FWHM).

In the study about the interaction between lipid liposomes and proteins, the protein was added quickly to the liposome solution, then the cuvette was placed into the instrument and DLS was measured at least over 60 min at 25 °C. In the mucin study 100 µl of mucin solution (10 mg/ml of mucin 2 and 0.8 mg/ml of mucin 3) was added to 300 µl of liposome solution (DOPC, DOPE) yielding final concentrations of 0.75 mM of liposomes and 1 µM of mucin. For a comparison of the interaction between both mucin types, the endconcentration of mucins were kept constant in respect to the obtained molecular masses. In a control measurement, mucin 3 was used as a 10 mg/ml solution (yielding an endconcentration of 12.5 µM). In the CRP study, CRP was added to liposome solutions giving final concentrations of 0.75 mM of liposomes and 0.1 µM, 0.5 µM, 0.8 µM or 2.9 µM of CRP.

SLS experiments for the determination of the molar masses of mucin 2 and mucin 3 were performed in a square glass cuvette 8G (Malvern Instruments Ltd., UK) using 800 µl samples at different concentrations and automatically optimized conditions. The average scattering intensity from the different concentrations was thus recorded. Samples were analysed using the Malvern supplied “molecular weight” operating procedure, the light being detected at an angle of 173° and a temperature of 25 °C in automatic duration mode. Scattering from a water reference (Malvern Instruments Ltd., UK) and the buffer alone were recorded as part of the procedure. Between measurements the cuvette had to be cleaned with water and force-dried using a nitrogen stream. The complete Debye-Plot was measured 3 times and the resulting data were then analyzed with OriginPro (OriginLab, Northampton, USA) using linear fitting options.

Zeta(ζ) potential measurements were carried out in Malvern Zetasizer folded capillary cells DTS 1060 (Malvern Instruments Ltd., UK). For each sample the instrument performed 3 scans (100 - 500 runs each), with an initial equilibration time of 2 min at 20 °C and a constant voltage of 150 mV running on auto mode. When mucin samples were used, they were filtered through a polycarbon filter (with a diameter of 50 nm for mucin 2 and 200 nm for mucin 3) prior the measurements to split the monomeric form from the aggregates. Values for viscosity, refractive index and dielectric constant were chosen from the manufacturers database in case of Hepes-buffer (viscosity 1.0021 cP, RI 1.330 and dielectric constant 80.4) as well as for proteins and liposomes (RI 1.450 - 1.460). The ζ potential was analyzed with the Malvern Zetasizer software calculated from the mobility measurements automatically by the instrument utilizing the Smoluchowski equation [58] and only used if the software deemed the result quality as good.

3.2.2.6 Dual Polarization Interferometry (DPI)

Principle of the Technique

The Dual Polarization Interferometry (DPI) is a versatile analytical technique for the biophysical characterization of membrane systems and their associated proteins. It can be applied to the study of liposome adsorption at the solid-liquid interface and the subsequent effects of OxPL on the lipid membrane as well as the adsorption of proteins on lipid membranes.

The measuring chip consists of a sensitive structure on the surface and a hidden reference structure inside (Figure 3.11a). These structures have a core region with higher refractive index and adjacent cladding regions with lower refractive index, which defines the boundaries. If the angle of the incident light source is greater than the critical angle, the light become internally reflected within the waveguide with an evanescent field beyond the waveguide boundaries. This evanescent field has a thickness of a few hundred nanometers and its intensity decays exponentially with respect to the distance from the waveguide surface. The propagation velocity of the light is determined by reflection angle, dimensions of the waveguide and the phase change at the boundaries [61]. The output from both (sensing and reference) waveguide interfere with each other and form Young's interference pattern with alternating levels of polarization of the light (Figure 3.11a).

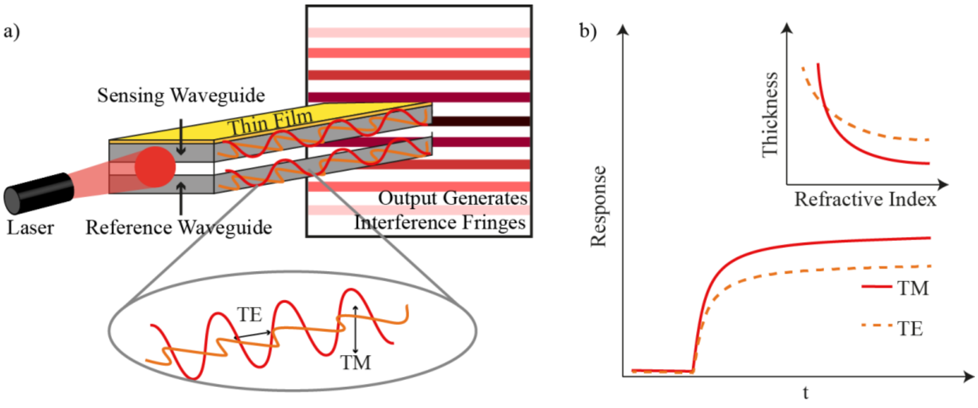

Figure 3.11 (a) Schematic assembly of the DPI with its waveguide structure including the transverse magnetic (TM) and transverse electric (TE) polarization modes. The output from both (sensing and reference) waveguides generate fringes which are modified if a thin biological layer is applied. (b) TM and TE responses are solved by Maxwell's equations and the results are superimposed to find an intersection point, which yields the exact layer properties (thickness and refractive index).

When polarized laser light is sent through the waveguide, the light is split into two equal beams that travel through both the upper and lower waveguides [62]. At the end of the waveguide, the two beams interact with each other and form Young's interference pattern on a photodiode array. If a thin layer is immobilized on the surface of the upper waveguide, the optical properties are modified: the optical path length is affected by the change in refractive index within the evanescent field, whereas the light in the lower waveguide does not experience such influence and therefore progresses at a constant velocity [63]. This causes a relative phase shift in the interference patterns representing the relative phase position of the light coming from the sensing waveguide and the reference waveguide at the output face of the two waveguides. The excitation of the chip with two orthogonal polarizations mode gives two separate measurements of fringe shifts.

As its name implies DPI uses the change in the polarization of the light within the waveguide. These two types of waveguide illumination are the transverse magnetic (TM) and the transverse electric (TE) polarized modes. In both cases, the evanescent field magnitude and its decay profile differ for the two polarization modes. The TE mode evanescent field profile is more closely confined to the surface of the waveguide than the TM mode. As a result, the TE mode is more sensitive to changes occurring close to the waveguide surface. However, the TM evanescent field is larger, so the uniform change in the bulk refractive index will affect TM more than TE. The ratio TE/TM of the responses determines the differences in the layer density. For a dense thin film TE/TM ratio is larger than 1, whereas a diffuse and thick film has a TE/TM ratio lower than 1. To calculate the thickness and the refractive index corresponding to the layer condition, Maxwell's equations must be solved for both, TM and TE. The results are superimposed to find an intersection point, which shows the resulting thickness and the refractive index of the layer (Figure 3.11b).

The parameters refractive index n and thickness d for an adsorbed isotropic single layer are fitted to the measured phase changes with a minimization algorithm [61, 64]. The anisotropy of the layer is considered by an additional parameter, the birefringence ($\Delta n = n_0 - n_e$), which describes the difference between the refractive index perpendicular n_0 and parallel to the surface n_e. For supported membranes, Δn gives the ordering of alkyl chains [65, 66]. The optical birefringence is high for fully aligned/ordered and low for disordered alkyl chains within a solid-supported membrane. The analysis is performed by fixing one of the parameters refractive index n, thickness d or birefringence Δn to determine the other two.

The advantage of this technique is that it reveals in real-time high-resolution data on thickness d, refractive index n and birefringence Δn, which allows for a clear understanding of the molecular mechanisms involved in lipid bilayer formation and subsequent interactions. In contrast to QCM-D, the change in the mass measured by DPI complementary yields the change in the mass of dry components.

Experimental Protocols

Measurements were performed at T = (25 ± 0.1) °C with the *AnaLigh*t® BIO200 (Farfield Group Ltd., Salford, UK) using a dual slap waveguide made of a 4 layers PECVD Silicon Oxynitride (SiO_xN_y) (22 mm x 6 mm) (*AnaChip*®) illuminated with an alternating polarized He-Ne laser beam (λ_{em} = 632.8 nm).

Calibration and linearization of the system was performed either before or after the experiment: Firstly, the sensor was calibrated with an ethanol/water solution (80% w/w) at 50 µL/min to determine the refractive index of the chip. Secondly, it was calibrated with water at 50 µL/min to obtain the refractive index of the bulk. Thirdly, the linearization was implemented with an ethanol:water solution (80% w/w) at 25 µL/min to get the defects in the fringe image which cause periodic errors in the phase measurement. For the **measurement** the sample (450 µL) was added at 10 µL/min to the buffer flow over the surface of the AnaChip® until a stabile bilayer was formed. For the DPI measurements involving the C-reactive protein (CRP), CRP with a concentration of 50 µg/ml (400 µL) was injected at 10 µL/min to the buffer flow over the bilayer surface (concentration estimated according to Hammond *et al.* who used 10 µg/ml ≈ 100 nM) [67]. After the incubation of 20 min, the sample was rinsed at the same flow rate.

3.2.2.7 Isothermal Titration Calorimetry (ITC)

Principle of the Technique

With the help of isothermal titration calorimetry (ITC) the thermodynamic parameters of molecule interactions can be determined. Typical studied systems are protein-substrate interactions, the formation of protein-protein complexes and protein-lipid binding [68]. The advantages of this measurement technique especially in biochemical experiments are the facts that no labeling is needed, there is no molecular weight limit and the optical clarity is not important [69].

In the experiment the heat generated or absorbed can be measured directly when molecules interact in terms of changes in enthalpy ΔH, as well as the binding stoichiometry n and the binding constant K_b. In the simplest and most common case only one ligand is binding to a macromolecule (n = 1). The dissociation constant K_d is then given as an equilibrium constant by the following relationship:

$$K_d = \frac{1}{K_b} = \frac{[L][M]}{[ML]}, \tag{3.24}$$

where $[L]$ is the concentration at the equilibrium of the free ligand, $[M]$ the concentration of the macromolecule and $[ML]$ the concentration of the ligand-macromolecule complex. The Gibbs energy ΔG and entropy ΔS changes can be determined using the following equation:

$$\Delta G = RTlnK_d = \Delta H - T\Delta S \tag{3.25}$$

The instrument consists of two small identical adiabatic cells which are connected to a heater. The sample cell is filled with the macromolecule solution and the reference cell contains water. The temperature in both cells is the same and higher than the temperature of the adiabatic jacket. Therefore both cells have to be heated using a well-known heating current to keep the temperature constant. The ligand can be injected into the sample cell with the help of a syringe, which is filled with the ligand solution and arranged onto the sample cell (Figure 3.12a). After each injection the ligand and the macromolecule interact with each other either in an endo- or exothermic way. The heating power for the sample cell is then adapted (decreased in an exothermic reaction and increased in an endothermic reaction) to maintain the temperature difference between sample and reference cell to be zero. The observed change in heating power is plotted against the time and the quantity of heat of each injection can be obtained by integration of the corresponding peak. To determine the thermodynamic parameters, the resulting quantity of heat per mole of injectant is plotted against the molar ratio $[L]/[M]$ (Figure 3.12b).

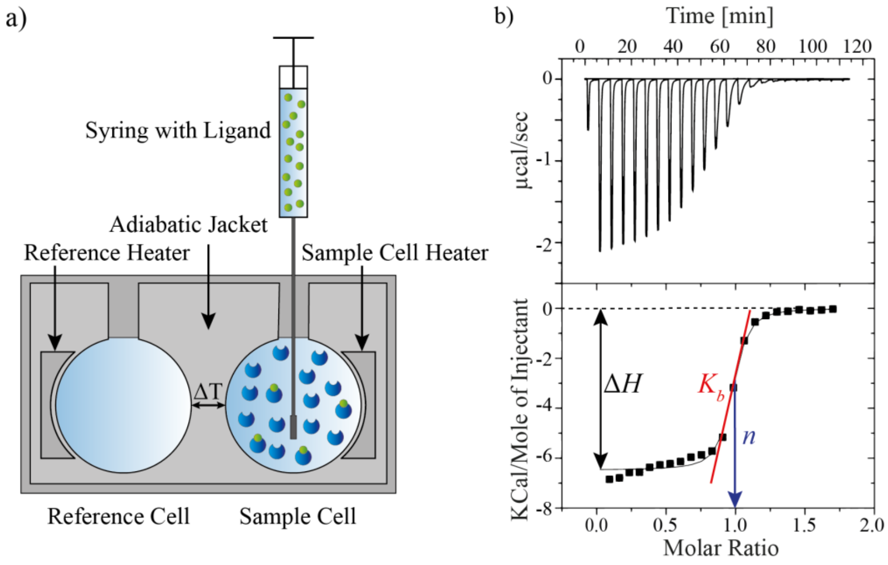

Figure 3.12 (a) Schematic illustration of an ITC instrument during an experiment with a macromolecule (blue) in the sample cell and the ligand (green) in the syringe. (b) Calibration measurement of 0.1 mM $CaCl_2$ (syringe) with 1 mM EDTA (sample cell) and how to obtain the enthalpy change ΔH (black arrow), the binding stoichiometry n (blue arrow) and the binding constant K_b (red line).

Experimental Protocols

ITC measurements were performed using a MicroCal VP-ITC (Malvern, United Kingdom). As **cleaning** procedure the reference cell was filled with degassed water once a week and the sample cell was cleaned according to manufacturers advice (H_2O, Decon 5%, H_2O, EtOH, H_2O, followed by a rinse with buffer). For **calibration** measurement, a 1 mM EDTA solution was loaded into the sample cell and a 0.1 mM $CaCl_2$ solution was loaded into the syringe (both in Hepes-buffer). The measurement was carried out at 25 °C and with a reference power of 10 µcal/sec. The volume of the first injection was 3 µl followed by injections of 10 µl.

In the studies of **lipid-protein interactions**, both, liposome and protein solutions were checked via DLS and degassed shortly before usage. In the experiments dealing with the **mucin protein**, concentration of the small unilamellar liposomes was varied between 200 µM and 50 µM for DOPC liposomes and 50 µM for DOPE and DOPC liposomes which were doped with 20 mol% of DOPG and DOTAP while the mucin (mucin 2 and mucin 3) concentration was kept constant (10 mg/ml). The mucin sample was filled into the sample cell (1.4 ml) while the liposomes were loaded into the injection syringe (~ 0.8 ml). All experiments were carried out at 25 °C and with a reference power of 5 µcal/sec. The initial delay was set to 300 sec and the spacing between the 23 injections was 330 sec. The volume of the first injection was 3 µl followed by injections of

10 µl for the 50 µM liposome solutions and 5 µl for the 200 µM liposome solution, respectively. The heat of dilution was determined in a reference measurement by injecting a 50 µM DOPC/DOPG (20 mol%) solution into Hepes-buffer and it was subtracted from the raw data (~ 1.7 kcal/mol). In the experiments dealing with **CRP**, the liposome solution (1 mM) was filled into the sample cell and CRP (0.5 mg/ml = 4.45 µM) was filled into the syringe. The same settings as in the mucin study were used. The heat of dilution was measured by injecting CRP-buffer into the liposome solution and subtracted from the data (~ 2.0 kcal/mol). The data were analyzed with the provided MicroCal ITC Origin software.

3.2.2.8 Quartz Crystal Microbalance with Dissipation Monitoring (QCM-D)

Principle of the Technique

Quartz crystal microbalance (QCM) is an electro-mechanical method that allows for the real time detection of mass adsorption processes on a solid substrate with a resolution down to 2 ng/cm². This technique is based on the piezoelectricity of quartz which was first discovered by Curie in 1880 [70]. The experimental setup consists of an AT-cut quartz crystal which is covered from both sides with two gold electrodes. The application of an alternating current (AC) voltage causes the shear deformation of the piezoelectric quartz crystal. The frequency of the AC voltage excites the resonance frequency of the quartz crystal f_0. This resonance frequency is given by:

$$f_0 = \frac{v_Q}{2d}, \tag{3.26}$$

where d corresponds to the thickness of the quartz crystal and v_Q describes the velocity of shear waves in the quartz. When the electric field is cut off, the oscillation curve dampened. Fitting the decay of the damping curve provides information on both, the resonance frequency f, of the crystal and the degree of damping, the dissipative losses D. The changes in both Δf and ΔD are the parameters which are acquired during a measurement. The dissipation change provides valuable information about the morphology of the adsorbed film [71]. Qualitatively, a low dissipation indicates a rather rigid layer, while a high dissipation is attributed to soft films. If the adsorbed film is sufficiently thin, rigid and homogenous, the mass uptake Δm is directly proportional to the frequency change Δf_n of the oscillating sensor crystal, as theoretically predicted by **Sauerbrey** in 1959 [72]:

$$\Delta m = -C\frac{\Delta f_n}{n}, \tag{3.27}$$

where C is the mass sensitivity constant (for commercially available quartz crystals: $C = 17.7$ ng/cm² Hz at $f_n = 5$ MHz), and n the overtone number.

In contrast to rigid films, the adsorption of biological materials from aqueous solution leads to a contribution of viscoelastic deformation which is not negligible. Water is coupled to the adsorbed film and if the mass is determined by the Sauerbrey equation, the resulting mass typically exceeds the biomolecular mass of the film [73]. In liquid, the resonance frequency is different than in vacuum or in air. The resonance frequency in liquid is dependent on the density and viscosity of the liquid and moreover, both these properties change with temperature. In addition, dissipational losses occur in liquid which makes the oscillation damp more quickly. Thus, adsorption of a viscoelastic overlayer shifts the resonance frequency to a smaller value and increases the dissipation factor D [74, 75]. D is related to the Q factor and describes the ratio of stored and dissipated energy in the system:

$$D = \frac{1}{Q} = \frac{E_{dissipated}}{2\pi E_{stored}} = \frac{1}{\pi f_0 \tau}, \tag{3.28}$$

where Q is a quality factor, $E_{dissipated}$ is the energy dissipated during one oscillation cycle, E_{stored} is the mechanical energy stored in the oscillator and τ is the decay time constant of the oscillation. The QCM-D considers the energy losses which are represented in the dissipation factor D by exciting intermittently the crystal and measuring the decay of the oscillations as a function of time.

Many proteins, however, are not homogenous or not rigid. The soft adlayer will not fully couple with the induced shear movement of the crystal, which leads to an increase in dissipation ΔD. If the ratio $\Delta D/\Delta f$ exceeds $0.2\text{x}10^{-6}$ Hz^{-1} as a rule of thumb, the mass estimation according to Sauerbrey cannot be applied. For the viscoelastic properties of the bulk and of adsorbed films the more advanced viscoelastic Voigt-Voinova model [76, 77, 78] must be applied, which relates properties like thickness, density, viscoelastic properties (shear modulus and shear viscosity) to the measured parameters Δf and ΔD.

Experimental Protocols

QCM-D measurements were performed with a QCM-D E4 (Q-Sense, Gothenburg, Sweden). The system was operated in flow mode, with a continuous liquid flow of typically 10 µl/min being delivered by a peristaltic pump. Resonance frequency and dissipation were measured at 6 harmonics simultaneously (n = 3, 5 ... 13), corresponding to frequencies of $f_n \approx 15$, 25 …65 MHz. For simplicity, only changes in dissipation and normalized frequency, $\Delta f = \Delta f_n/n$, of the 7th overtone (n = 7, i.e., ~ 35 MHz) are presented, if not otherwise mentioned.

SUV suspensions were deposited on AT-cut SiO_2-coated quartz crystals with a fundamental frequency of 5 MHz for ~ 10 min, followed by rinsing with buffer for 15 min. After confirming the membrane formation, protein solutions [c (CRP) = 50 µg/ml; c (EO6) = 10 µg/ml] were injected for 10 min and allowed to adsorb for another 20 min. Finally, the crystal was washed with buffer for 15 min. The peristaltic pump for liquid flow was set to 100 µL/min, and the temperature was stabilized at (T = 25 ± 0.1) °C.

3.2.2.9 Cell Experiments

Substrate and Liquid Chamber

For cell experiments, microscopic glass slides (25 x 75 mm^2) from Gerhard Menzel GmbH (Braunschweig, Germany) were cleaned following the standard RCA cleaning protocol [36] and sealed to bottomless plastic fluidic channels (μ-Slide VI$^{0.4}$) from Ibidi (Martinsried, Germany) using Sylgard® silicone elastomer as bonding agent purchased from Dow Corning Corporation (Michigan, USA), which was degassed 10 min in an desiccator.

Deposition of Supported Membranes

Solid-supported membranes were prepared by vesicles fusion [79]. Briefly, vesicle suspensions consisting of either pure DOPC or DOPC doped with **0.5 mol% biotin-DOPE** (1 mg/ml) were injected onto the substrates and incubated for 1 h at 37 °C to form a solid-supported membrane. After extensive rinsing with water, **neutravidin** (100 μg/mL) was added and incubated for 30 min at 37 °C. After removing excess neutravidin, hs**CD95L** (2 μg/ml) was incubated for 1 h at RT. Finally, excess proteins were removed by rinsing extensively with cell culture medium prior to the cell adhesion experiments, and the samples were equilibrated at 37 °C. The average intermolecular distance $< d >$ between hs**CD95L** can be estimated from the molar fraction χ of lipid anchors by inserting the area of a lipid in the membrane $A_{lipid} \sim 65$ Å^2 [80, 81] in the following equation:

$$< d > = \sqrt{\frac{A_{lipid}}{\chi}} \tag{3.29}$$

Cell Fixation and Staining

One portion of the cell sample was stained with **PKH67** (Sigma Aldrich, Munich, Germany) according to the manufacture instructions. Briefly, the PKH67 dye solution was added to the in diluents resupended cell pellet. After an incubation time of 2 min at RT, medium with additionally 1% BSA was added to the cells. After 1 min, the suspension was centrifuged and resupsended in medium, which was repeated 5 times. At a desired point in time (15 min, 25 min, 30 min, 1 h, 2 h) the cells were fixed using a **PFA 4%** PBS solution which was incubated for 15 min at 37 °C. After a PBS rinse, any unspecific binding was blocked with a 0.1 mg/ml **BSA** PBS solution which was incubated for 45 min at 37 °C. To this solution, **EO6** monoclonal antibody was added to a final concentration of 10 μg/ml and incubated for 45 min at 37 °C. After a PBS rinse, cells were stained with the secondary antibody **anti-mouse IgG-TRITC** used at a final concentration of 10 μg/ml and incubated for 45 min at 37 °C. Then the channels were rinsed with PBS and DNA was stained with **Hoechst** dye used at a final concentration of

0.0025 µg/ml and incubated for 45 min at 37 °C. After a PBS-buffer rinse, **Mowiol® 4-88** as a polymerization aid, which keeps the fluorescence stable, when held in dark and at 4 °C, was filled into the whole channel.

Microscopy

Image acquisition by phase contrast and fluorescence microscopy was performed on an Axiovert 200 inverted microscope (Carl Zeiss AG, Oberkochen, Germany) equipped with a PlanNeofluar 63 x/1.25 Antiflex oil-immersion objective and a PlanApochromat 100 x/1.4 objective. Confocal microscopy and **z stacks** of fixed and stained cells were performed with a Nikon eclipse Ti microscope (100 x oil objective) in the Nikon imaging center (Heidelberg, Germany).

4 Influence of Lipid Oxidization on the Structure of Membranes

4.1 Impact of OxPL on Phospholipid Monolayers in the Presence of Monovalent (K^+, Cs^+) and Divalent (Ca^{2+}) Cations

To clarify systematically how structures and functions of biological membranes are influenced by the oxidative damage mediated by free radicals, precisely defined Langmuir monolayers were utilized as model systems to study their properties with a combination of experimental techniques.

In the first step in this section, the impact of OxPL in the presence of different monovalent (K^+ or Cs^+) or divalent (Ca^{2+}) ions were investigated by pressure-area (π-A) isotherms of OPPC/OxPL monolayers. Isotherms were recorded for mixtures of OPPC with three molar fractions of OxPLs (5%, 10%, 20%) in order to extract thermodynamic properties such as the compressional modulus κ and the Gibb´s free energy energy ΔG^{exc} (for more details see section 3.2.2.1).

In the second step, the molecular behavior during compression was investigated by surface potential measurements of phospholipid monolayers OPPC/OxPL in the presence of K^+ and Ca^{2+} ions to assess the orientation of the oxidized moieties of OxPL at the air-water interface (for more details see section 3.2.2.1).

Finally, the impact of OxPL on the fine structures of lipid monolayers were investigated by X-ray reflectivity (XRR) and Gracing incidence X-ray fluorescence (GIXF) of OPPC/OxPL monolayers on buffers containing either monovalent (K^+, Cs^+) or divalent (Ca^{2+}) ions (section 3.2.2.2). The combination of both techniques (XRR and GIXF, ESRF) in the systematic variation of the membrane composition unravels the influence of phospholipid oxidization on the fine-structures of membranes (thickness, roughness and electron density) and determine qualitatively the element-specific density profiles of ions (K^+, Cs^+ or Ca^{2+}) near the membrane surface in the presence and absence of both OxPL with high spatial accuracy (± 5 Å).

4.1.1 Impact of OxPL on Thermodynamic Properties of Phospholipid Monolayers in the Presence of Monovalent (K^+, Cs^+) and Divalent (Ca^{2+}) Cations

The monolayer study focuses on the changes in pressure-area (π-A) isotherms, compression modulus (κ) and Gibb's free energy (ΔG^{exc}) induced by incorporation of OxPL (either PazePC or PoxnoPC), in different molar fractions (5%, 10%, 20%) into OPPC monolayers (Section 3.2.2.1). To investigate the effect of ions on the lipid systems, experiments were performed on buffers containing monovalent (K^+ or Cs^+) or divalent (Ca^{2+}) ions. Figure 4.1 shows the obtained pressure-area (π-A) isotherms on (I) K^+-buffer, (II) Ca^{2+}-buffer and on (III) Cs^+-buffer, together with the (a) compressional modulus κ and (b) the mean molecular area per one lipid at different mol% of PazePC and the calculated Gibb's free energy (ΔG^{exc}) as an inset on each buffer. Figure 4.2 represents the corresponding data for OPPC monolayers with different mol% of PoxnoPC.

From the analysis of the pressure-area (π-A) isotherms the following can be concluded:

(i) Values of the compressional modulus κ are less than 100 mN/m in the entire surface pressure range indicating that all monolayers are in the liquid expanded phase L_e.

(ii) Values of the compressional modulus κ in general decrease with increasing content of OxPL indicating that the lipids become less packed by increasing the fraction of OxPLs in the membrane.

(iii) In the diagrams of the average area per molecule versus the content of OxPL a deciation from linearity was observed in most cases, which suggests that monolayers from two components do not exhibit ideal mixing.

(iv) Gibbs free energies ΔG^{exc} show negative values for all monolayers indicating that monolayers with two lipid components have less repulsive interactions compared to the pure components. It is found that mostly the monolayers incorporating 5 mol% OxPL have the most stable state.

(v) Gibbs free energies ΔG^{exc} values in case of monolayers containing PazePC are less than those containing PoxnoPC, suggesting that the former monolayers are more stable then the later.

(vi) Values for Gibbs free energies ΔG^{exc} and compressional modulus κ in case of monolayers with PazePC on K^+-buffer are less/larger than the corresponding ones on Cs^+-buffer indicating that these monolayers are less stable on Cs^+-buffer.

(I) K$^+$-buffer

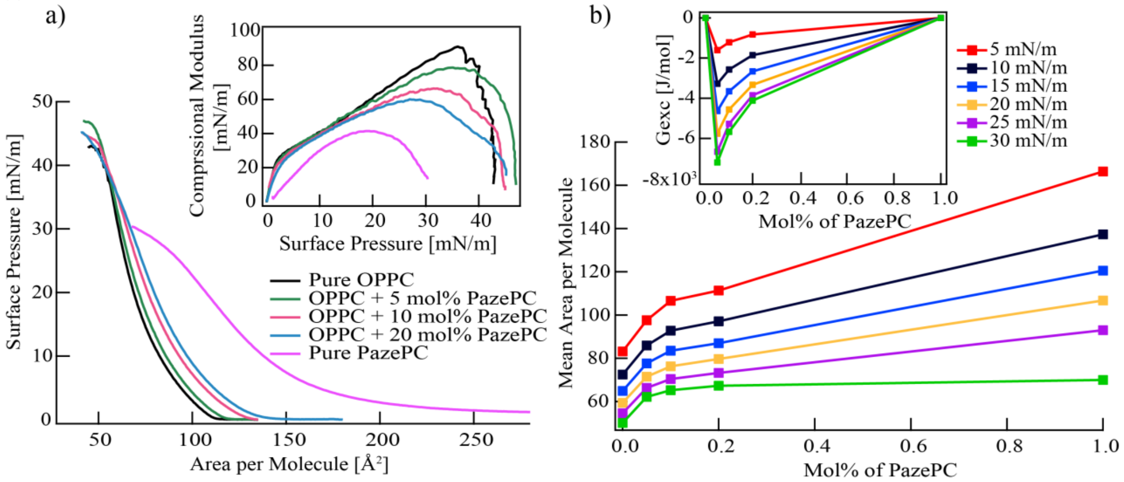

(II) Ca^{2+}-buffer

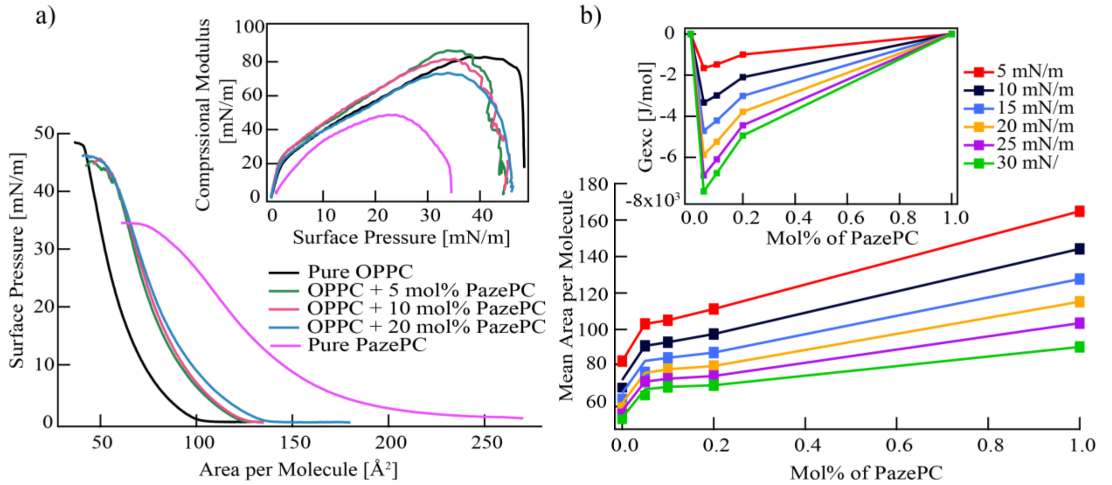

(III) Cs$^+$-buffer

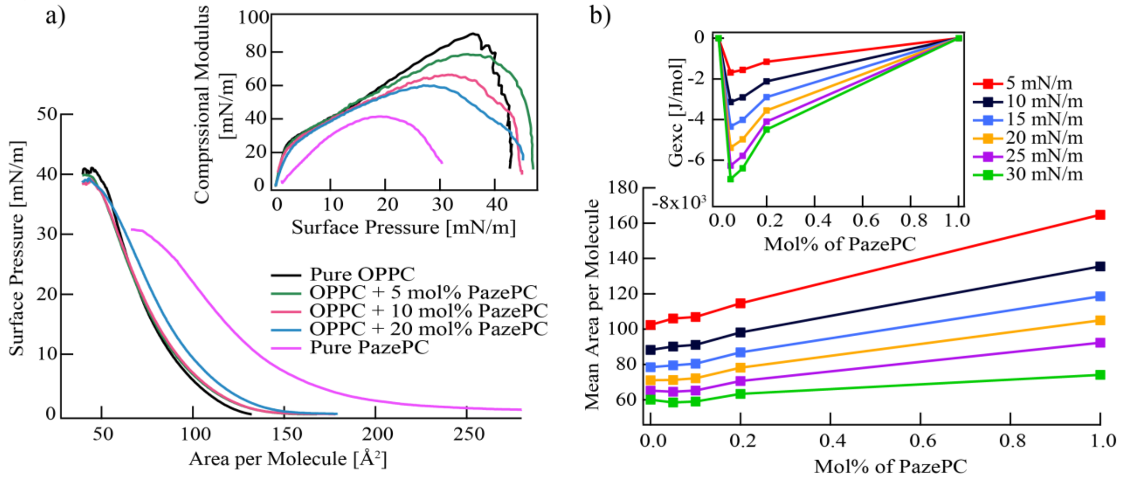

Figure 4.1 (a) Pressure-area (π-A) isotherms of the lipid monolayers (OPPC/PazePC) on (I) K$^+$-buffer, (II) Ca^{2+}-buffer and on (III) Cs$^+$-buffer. The corresponding compressional modulus κ is presented in the inset. (b) The mean molecular area per one lipid molecule at different surface pressures plotted versus the mol% of PazePC. The calculated Gibbs free energies ΔG^{exc} at the corresponding surface pressures are shown in the inset for each buffer.

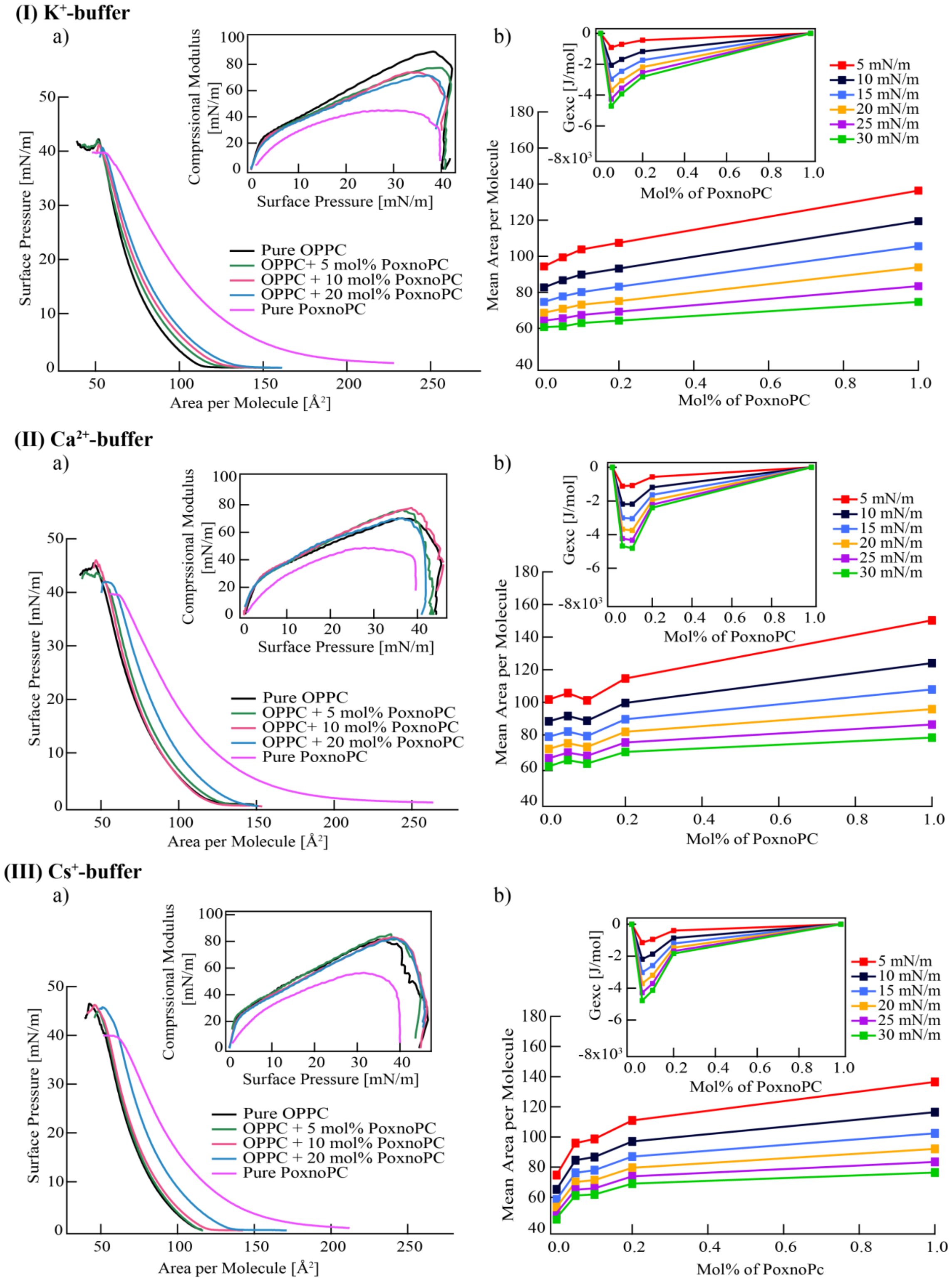

Figure 4.2 (a) Pressure-area isotherms (π-A) of the lipid monolyers (OPPC/PoxnoPC) on (I) K^+-buffer, (II) Ca^{2+}-buffer and on (III) Cs^+-buffer. The corresponding compressional modulus κ is presented in the inset. (b) The mean molecular area per one lipid molecule at different surface pressures plotted versus the mol% of PoxnoPC. The calculated Gibbs free energies ΔG^{exc} at the corresponding surface pressures are shown in the inset for each buffer.

In addition, for all isotherms the area per molecule at 20 mN/m was extracted to calculate the lateral concentration of ions of interest in the following GIXF sections (Table 4.1).

Table 4.1 Overview of the area per molecule for each monolayer on each buffer at the surface pressure of 20 mN/m.

OPPC/PazePC at 20 mN/m	**Ca^{2+}**	**K^+**	**Cs^+**
	Area per molecule [Å²]		
OPPC	60.0	68.7	71.1
OPPC + 5% PazePC	76.5	71.4	71.3
OPPC + 10% PazePC	78.3	76.6	72.3
OPPC + 20% PazePC	80.3	79.6	78.2
PazePC	115.2	106.7	105.1
OPPC/PoxnoPC at 20 mN/m	**Ca^{2+}**	**K^+**	**Cs^+**
	Area per molecule [Å²]		
OPPC	60.0	68.7	71.1
OPPC + 5% PoxnoPC	74.8	71.3	70.3
OPPC + 10% PoxnoPC	76.4	73.2	71.4
OPPC + 20% PoxnoPC	81.9	75.6	80.0
PoxnoPC	95.1	93.9	92.1

4.1.2 Impact of Reorientation of Oxidized Moieties in Phospholipid Monolayers in the Presence of Monovalent (K^+) and Divalent (Ca^{2+}) Ions

Since the Langmuir isotherms of both pure OxPL (PazePC and PoxnoPC) do not reach similar molecular areas near the collapse pressure of monolayers as those of the matrix phospholipid (OPPC) (section 4.1.1), it indicates that OxPL do not have the similar packing density than OPPC. Such result could be related to the presence of the oxidized moiety (carbonyl or carboxyl) at the air-water interface in the vicinity of the polar headgroup. In order, to assess the orientation of the oxidized moieties at the air-water interface, surface potential measurements of pure phospholipids and their mixtures with OPPC were performed. To do so, the molecular behavior of phospholipid monolayers at the air-water interface and their phase changes during compression were studied by surface potential measurements of pure OPPC, PazePC and PoxnoPC monolayers as well as of incorporated OPPC monolayers with different molar ratios (5 mol%, 10 mol%, 20 mol%) of OxPL (either PazePC or PoxnoPC) on K^+- and Ca^{2+}-buffer (section 3.2.2.1). Figure 4.3 shows the surface potential results for OPPC/PazePC monolayers on (a) K^+-buffer and (c) Ca^{2+}-buffer and the corresponding results for OPPC/PoxnoPC monolayers on (b) K^+-buffer and (d) Ca^{2+}-buffer.

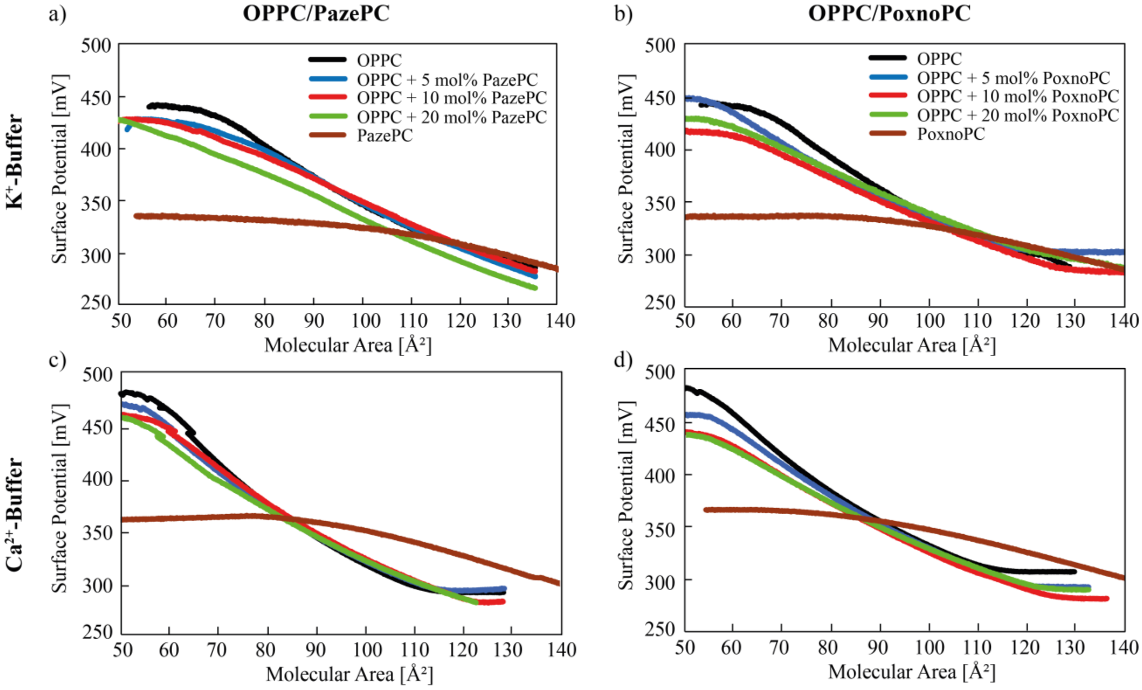

Figure 4.3 Surface potential measurements of OPPC/PazePC monolayers on (a) K^+-buffer and (b) Ca^{2+}-buffer and the corresponding results for OPPC/PoxnoPC monolayers (c, d).

The surface potential measurements of pure OPPC, OxPL and their mixtures on both buffer conditions showed similar tendencies. Indeed, compared to pure OPPC and OPPC/OxPLs mixtures, pure PazePC and PoxnoPC showed higher surface potential values at the molecular areas between 130 - 115 Å^2 on K$^+$-buffer and between 130 - 90 Å^2 on Ca^{2+}-buffer. Then, from these molecular areas the ΔV values of pure PazePC and PoxnoPC become stable and independent on the molecular area (Figure 4.4), indicating thus a packing density dependent on the reorientation of the component of dipole moment vector perpendicular to the monolayer plane μ_n, yielding nearly constant surface dipole potentials during film compression.

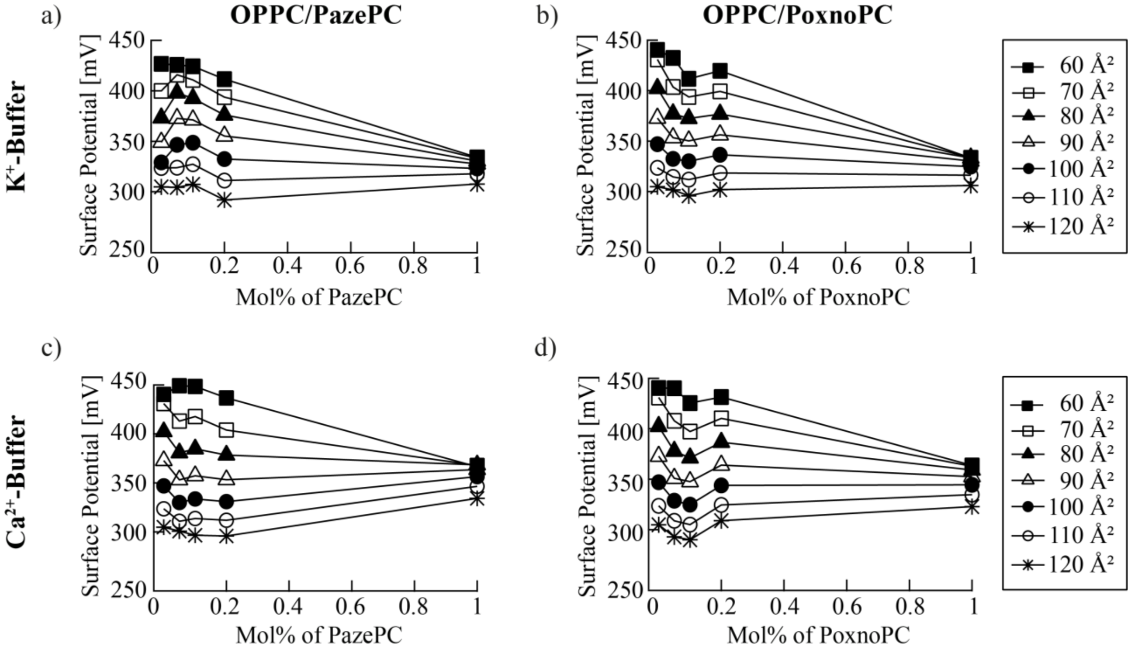

Figure 4.4 Overview of the surface potential ΔV at different molecular areas (60 Å^2 – 120 Å^2) as a function of OxPL content on K$^+$-buffer (a, b) and Ca^{2+}-buffer (c, d), respectively.

In order to gain a better understanding on the normal components of the dipole moments of the terminal CH$_3$ group of the acyl chain, a floating monolayer with a uniform assembly with equally contributed molecular dipoles with a constant ε ($\varepsilon = 1$ for unionized monolayers) is assumed. Thus, the effective molecular momentum μ_n normal to the subphase can be obtained using the Helmholtz equation, given as:

$$\Delta V = \frac{\mu_n}{A\varepsilon_0}, \tag{4.1}$$

where A is the area occupied by each molecule and ε_0 the permittivity of free space. Table 4.2 shows the surface potential ΔV_{70} at a molecular area of 70 Å² for each OPPC/OxPL membrane on K$^+$-buffer and Ca^{2+}-buffer together with the calculated results for the effective molecular momentum μ_n.

Table 4.2 Surface potential ΔV_{70} at 70 Å² for each OPPC/OxPL membrane on K$^+$-buffer and Ca^{2+}-buffer including the effective molecular momentum μ_n normal to the surface calculated according to the Helmholtz equation (4.1).

	OPPC/PazePC		**OPPC/PoxnoPC**	
K$^+$-buffer	ΔV_{70} [mV]	μ_n [mD]	ΔV_{70} [mV]	μ_n [mD]
OPPC	431	799	431	799
OPPC + 5 mol% OxPL	416	771	404	749
OPPC + 10 mol% OxPL	411	762	394	730
OPPC + 20 mol% OxPL	394	730	399	741
PazePC	330	618	333	618
Ca^{2+}-buffer	ΔV_{70} [mV]	μ_n [mD]	ΔV_{70} [mV]	μ_n [mD]
OPPC	431	799	431	799
OPPC + 5 mol% OxPL	413	766	410	760
OPPC + 10 mol% OxPL	418	775	397	737
OPPC + 20 mol% OxPL	404	772	395	733
PazePC	368	682	363	673

The results obtained from the Helmholtz equation can be summarized as follows:

(i) Both OxPL, PoxnoPC and PazePC, show approximately the same surface potential ΔV_{70} (and thus normal momentum μ_n) of ~ 330 mV on K$^+$-buffer and ~ 365 mV on Ca^{2+}-buffer. In addition, their surface potential ΔV_{70} at the same molecular area is lower than that of OPPC which could be related to the extended conformation of the alkyl chain bearing the oxidized moieties (carboxyl or carbonyl).

(ii) The incorporation of OxPL into the OPPC monolayer reduces the surface potential ΔV_{70} by 15 – 35 mV as well as the surface dipole moment μ_n normal to the air-water interface.

(iii) Most OPPC/OxPL monolayers show comparable ΔV_{70} values on Ca^{2+}-buffer at 70 Å² as on K$^+$-buffer. However, the pure OxPL and the OPPC membrane incorporated with 20 mol% PazePC show higher ΔV_{70} values by ~ 20 – 30 mV and thus a higher normal momentum on Ca^{2+}-buffer than on K$^+$-buffer.

In the next step, in order to get better insights on the contribution of oxidized moieties as well as the extended conformation of OxPLs on the surface potential measurements the Demchak-Fort (DF) three-layer capacitor model was aplied for the monolayer [47] (see section 3.2.2.1). Indeed, using the Demchak-Fort three-layer capacitor model, the surface potential ΔV is related to the normal component of group dipole moments of aliphatic molecules forming monolayers at the air-water interface. According to this model, the monolayer surface potential results from the contribution of the dipole moments, of (i) terminal CH_3 group, (ii) the polar head group (PC), and (iii) water molecules reoriented and polarized by the monolayer (Figure 4.5). To take the local polarizabilities of the medium surrounding the dipoles into account, a different effective dielectric constant (ε_i), is assigned to each layer. In addition, when the monolayer is ionized, an electric double-layer is expected to be formed that contributes to the surface potential, with the double-layer potential ψ_0.

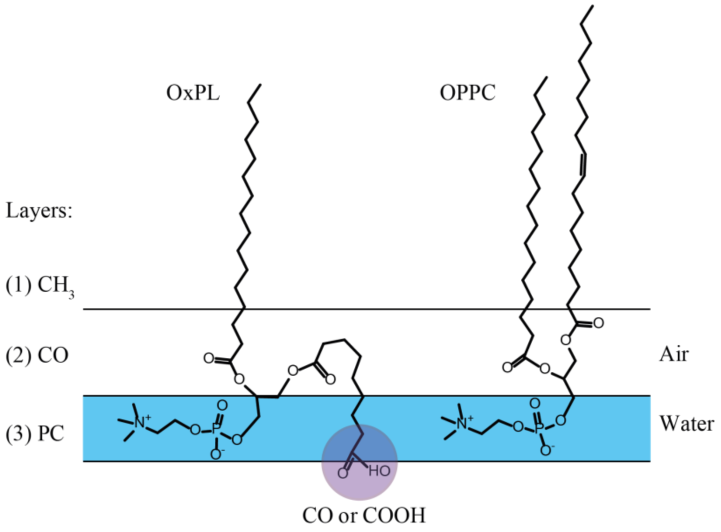

Figure 4.5 Schematic illustration of the molecular structure of the monolayer divided into three parts according to the Demchak-Fort (DF) model.

Applying the Demchak-Fort approach, the surface potential for monolayers of OPPC, PazePC and PoxnoPC can be written, respectively, as follows:

$$\Delta V_{OPPC} = \frac{1}{A\varepsilon_0}\left[2\frac{\mu_{CH3}}{\varepsilon_{CH3}} + 2\frac{\mu_{CO}}{\varepsilon_{CO}} + \frac{\mu_{PC}}{\varepsilon_{PC}} + \frac{\mu_{H2O}}{\varepsilon_{H2O}}\right] + \psi_0, \tag{4.2}$$

$$\Delta V_{PazePC} = \frac{1}{A\varepsilon_0}\left[\frac{\mu_{CH3}}{\varepsilon_{CH3}} + 2\frac{\mu_{CO}}{\varepsilon_{CO}} + \frac{\mu_{PC}}{\varepsilon_{PC}} + \frac{\mu_{COOH}}{\varepsilon_{COOH}} + \frac{\mu_{H2O}}{\varepsilon_{H2O}}\right] + \psi_0, \tag{4.3}$$

where ε_0 is the permittivity of vacuum, A_i is the area per molecule, ε_{CH3}, ε_{CO}, ε_{PC}, and ε_{COOH} are the normal components of the dipole moments of the terminal CH_3 group of the acyl chain, the carbonyl (CO) group, the phosphatidylcholine (PC) headgroup, and the carboxyl group (COOH) of PazePC, respectively. The term $\mu_{H2O}/\varepsilon_{H2O}$ was added to account the reorientation and polarization of water molecules induced by the phospholipid monolayer as described by Tsukanova *et al.* [82].

Assuming, that for a given temperature T, pH and molecular area the contributions of $\mu_{CH3}/\varepsilon_{CH3}$, $\mu_{PC}/\varepsilon_{PC}$, $\mu_{H20}/\varepsilon_{H20}$ and $\mu_{CO}/\varepsilon_{CO}$ of PazePC to the surface potential ΔV are identical to those of OPPC monolayer, the decrease in ΔV of PazePC compared to OPPC would arise from the looping of the oxidized chain toward the buffer subphase:

$$\Delta V_{OPPC} - \Delta V_{PazePC} = \frac{1}{A\varepsilon_0}\left[\frac{\mu_{CH3}}{\varepsilon_{CH3}} - \frac{\mu_{COOH}}{\varepsilon_{COOH}}\right] + \psi_0' \tag{4.4}$$

The resulting difference is ~ 63 mV and ~ 80 mV on Ca^{2+}- and K^{+}-buffer, respectively. Such value is in the same order of the corresponding surface potential of terminal CH_3 group (63 mV) reported by Taylor *et al.* [83]. However, the calculated values must be treated with caution, since the values used for μ and ε were taken from literature sources, ignoring possible hydration effects on the headgroup/functional group and the reorientation of water molecules. Such result would indicate that the carboxyl group (COOH) of PazePC does not contribute to ΔV but to a difference in ψ_0' which shows that the functional group lies parallel to the interface. However, the difference in ψ_0' cannot be seen here, as it is assumed that μ_{CH3} is the same in both, OPPC and OxPL.

Following the same reasoning for PoxnoPC, the resulting difference ΔV on Ca^{2+}- and K^{+}-buffer are ~ 68 mV and ~ 98 mV, respectively. As in the case of PazePC, the difference of 68 mV could be related to the looping of the oxidized acyl chain toward the buffer subphase. However, in the presence of K^{+}-buffer the difference of ΔV is higher, although the possibility for the double layer potential to alter the monolayer potential is excluded since polar headgroups of OPPC and PoxnoPC are in their zwitterionic form at the studied pH.

However, it should be noticed that the combination of surface potential measurements, the theory of Demchak-Fort (DF) three-layer model and the calculation of the contribution of layers according to the molecular structure is a challenge. Therefore, the aim of such analysis was to extract a rough estimation of the contribution of the oxidized chain on the normal component of the phospholipids dipole moment. A more valuable calculation could be done, if (1) a quantitative theory relating microscopic properties to macroscopic measurements of ΔV is developed, and (2) experimental techniques are improved which have a spatial resolution comparable with molecular dimensions to provide new experimental data for testing new developments in molecular dynamics calculations.

4.1.3 Impact of OxPL on Phospholipid Monolayers in the Presence of Monovalent K^+ Ions

In this section, the impact of OxPLs on the fine-structures of OPPC phospholipid monolayers in the presence of K^+ ions were studied by X-ray reflectivity (XRR, ESRF) (see section 2.1.2). Thus, induced changes by oxidative stress in thickness d, electron density ρ and roughness σ of phospholipid monolayers were obtained in high spatial accuracy. Phospholipid monolayers were used as well defined model systems and studied after compression to the surface pressure of $\pi = 20$ mN/m which coincide with an area per lipid molecule in the range of $A \approx 65 - 110$ Å^2 (Table 4.1), depending on the lipid mixture used.

Figure 4.6a/c shows the XRR curves of pure OPPC monolayer (black), OPPC monolayers doped with 10 mol% of PazePC/PoxnoPC (green), and pure PazePC/PoxnoPC monolayers (blue) on K^+-buffer. The solid red line in each panel represents the best matching fits to the experimental data gained from a two slap model (for hydrocarbon chains and choline head group, each). The reconstructed electron density (ρ) profiles along the z-axis are also shown in Figure 4.6b/d. The thickness d, electron density ρ, and root mean square (rms) roughness σ of each interface are summarized in Table 4.3.

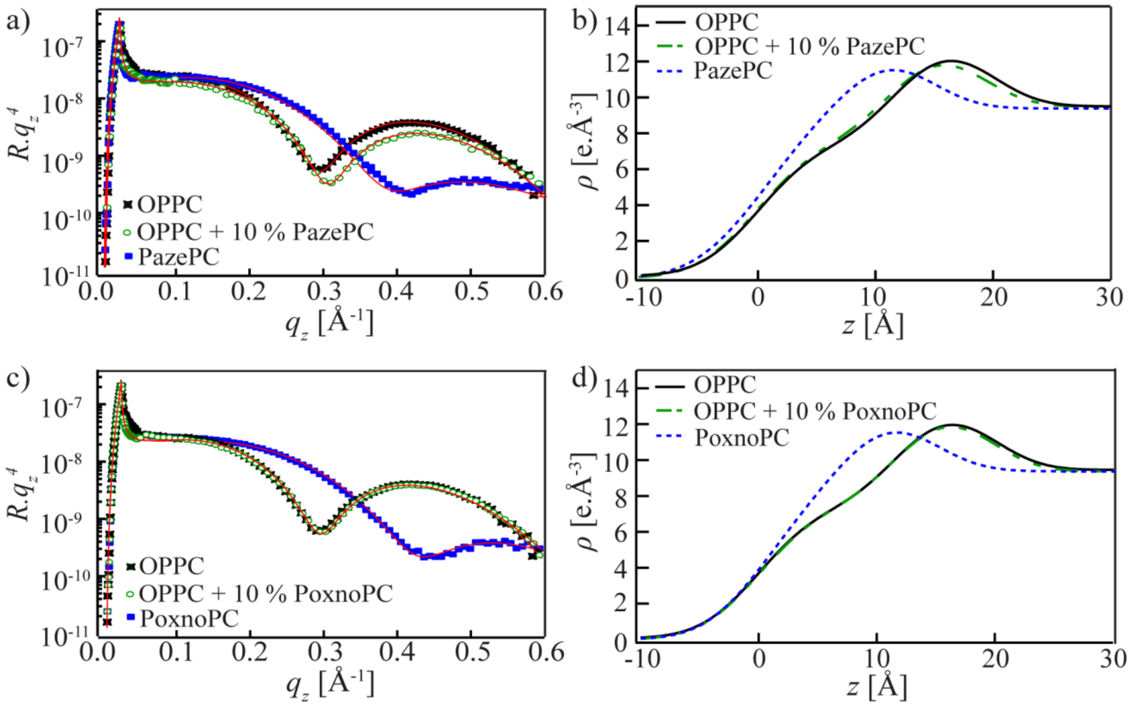

Figure 4.6 (a) XRR curves for OPPC (black), OPPC with 10 mol% PazePC (green) and pure PazePC (blue) on K^+-buffer together with the best fits to the experimental results (solid red line), and (b) the reconstructed electron density profiles along the z-axis (perpendicular to the interface). The corresponding XRR and the electron density profiles from PoxnoPC systems are presented in (c) and (d), respectively.

The hydrocarbon chain of pure OPPC has a thickness of d_A = 11.7 Å with ρ_A = 0.262 e Å^{-3}. The ρ_A value is lower than those of saturated hydrocarbon chains ρ_A = 0.32 - 0.33 e Å^{-3} [84, 85], while the total thickness of the monolayer (19.6 Å) seems fully consistent with one half of the values reported for the corresponding bilayers, 19.5 Å [86]. The quality of the fit can be validated when comparing the average number of electrons per one phospholipid molecule calculated from the fit (440 e$^-$) with the one calculated from the chemical formula of OPPC (420 e$^-$).

Table 4.3 Thickness *d*, electron density *ρ*, and roughness *σ* corresponding to best fits of the XRR data of OPPC/OxPL monolayers on K$^+$ buffer at 20 mN/m.

OPPC			
	d [Å]	ρ [e × Å^{-3}]	σ [Å]
Hydrocarbon chain	11.7	0.262	4.0
Choline head	7.9	0.465	3.4
Buffer	∞	0.335	3.3
OPPC + 10 mol% PazePC 1)			
	d [Å]	ρ [e × Å^{-3}]	σ [Å]
Hydrocarbon chain	11.4	0.263	4.1
Choline head	7.4	0.460	3.6
Buffer	∞	0.335	3.2
PazePC 1)			
	d [Å]	ρ [e × Å^{-3}]	σ [Å]
Hydrocarbon chain	7.7	0.322	4.5
Choline head	6.6	0.454	3.5
Buffer	∞	0.335	3.3
OPPC + 10 mol% PoxnoPC			
	d [Å]	ρ [e × Å^{-3}]	σ [Å]
Hydrocarbon chain	11.7	0.263	4.0
Choline head	7.5	0.465	3.5
Buffer	∞	0.335	3.3
PoxnoPC			
	d [Å]	ρ [e × Å^{-3}]	σ [Å]
Hydrocarbon chain	7.4	0.295	4.1
Choline head	6.6	0.460	3.6
Buffer	∞	0.335	3.2

1) The membranes containing PazePC were less stable than those containing PoxnoPC.

It is notable that the hydrocarbon chains of both PazePC and PoxnoPC monolayers are about 4 Å thinner compared to that of OPPC monolayer recorded at the same surface pressure. The smaller values found for the hydrocarbon chain layer thickness can be interpreted in terms of reorientation of the oxidized chains towards the aqueous phase [87], followed by an increase in the mean molecular area. This increase in molecular area was observed with an increased molar fraction of OxPL in the former section of the monolayer study (section 4.1.1.). It leads to an increase in the electron density of hydrocarbon chain ($\Delta\rho = 10 - 20\%$) as well as the interface roughness.

The disturbance to the chain orders reported here, are consistent with previous MD simulations of DOPC and POPC mixed with mono-oxidized acyl chain bearing an aldehyde group [88] as well as in MD simulations with PLPC mixed with an aldehyde group [89] where the tendency of the OxPL tails to bent towards the water interface leads to an increase in the average area per lipid and a decrease in bilayer thickness with higher content of OxPL. In addition, the experimental finding from the fluorescence film balance (Sabbatini) shows film expansion of monolayers with increasing content of OxPL and a solubilization of the OxPL into the aqueous phase at high film compression [87]. However, when PazePC/PoxnoPC were incorporated into OPPC with 10 mol% (Figure 4.6a/c, green), the thickness, the roughness of each interface and the electron density of hydrocarbon chain layers showed no remarkable difference of the corresponding values from pure OPPC, suggesting that the incorporation of OxPL at 10 mol% leads to no remarkable change in the vertical fine-structures of phospholipid membranes.

4.1.4 Density Profiles of K^+ Ions in the Presence/Absence of OxPL

The combination of XRR and Gracing incidence X-ray fluorescence (GIXF) in the systematic variation of the membrane composition enables the qualitatively determination of element-specific density profiles of ions near the membrane surface (for more details see section 2.1.3). Modelling the membrane surface in the presence and absence of OxPL, the specific lipid–ion interaction, which represents the interaction between the cell and the electrolyte, can be studied in high spatial accuracy.

Normalized K K_α fluorescence intensities were fitted for each monolayer (Figure 4.7a) OPPC/PazePC and (b) OPPC/PoxnoPC on K^+-buffer. The fluorescence signals of K K_α are close to unity, which indicated that K^+ ions are weakly interacting with all phospholipids. Although the slightly lower fluorescence signals at $q_z < q_c$ compared to unity seem to suggest a depletion of K^+ ions near the interface, the reconstructed ion concentration profiles in this case were equal to the bulk values.

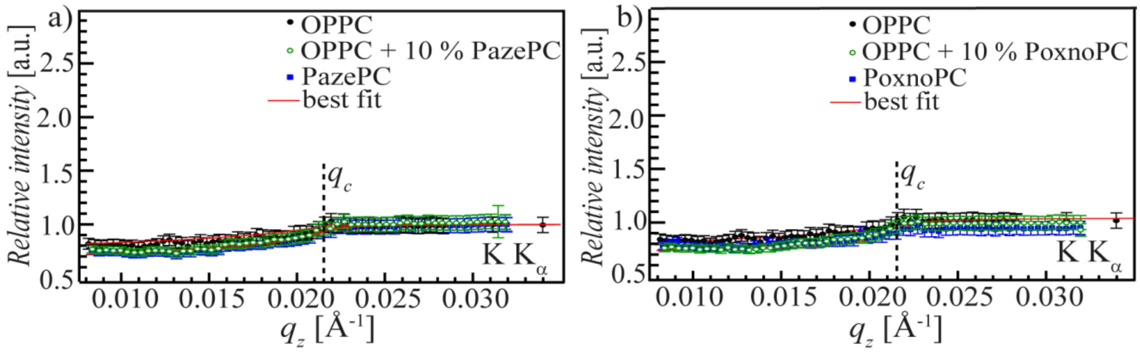

Figure 4.7 (a) Fluorescence intensities of K Kα as a function of q_z for OPPC (black), OPPC with 10 mol% PazePC (green) and pure PazePC (blue) on K^+-buffer together with the best fits (solid red line). The corresponding fluorescence intensities from OPPC/PoxnoPC systems are presented in (b), respectively.

4.1.5 Impact of OxPL on Phospholipid Monolayers in the Presence of Divalent Ca^{2+} Ions

The obtained XRR curves of OPPC/OxPL monolayers on Ca^{2+}-buffer together with the best fits (red lines) are shown in Figure 4.8. The parameters corresponding to the best fit results are summarized in Table 4.4.

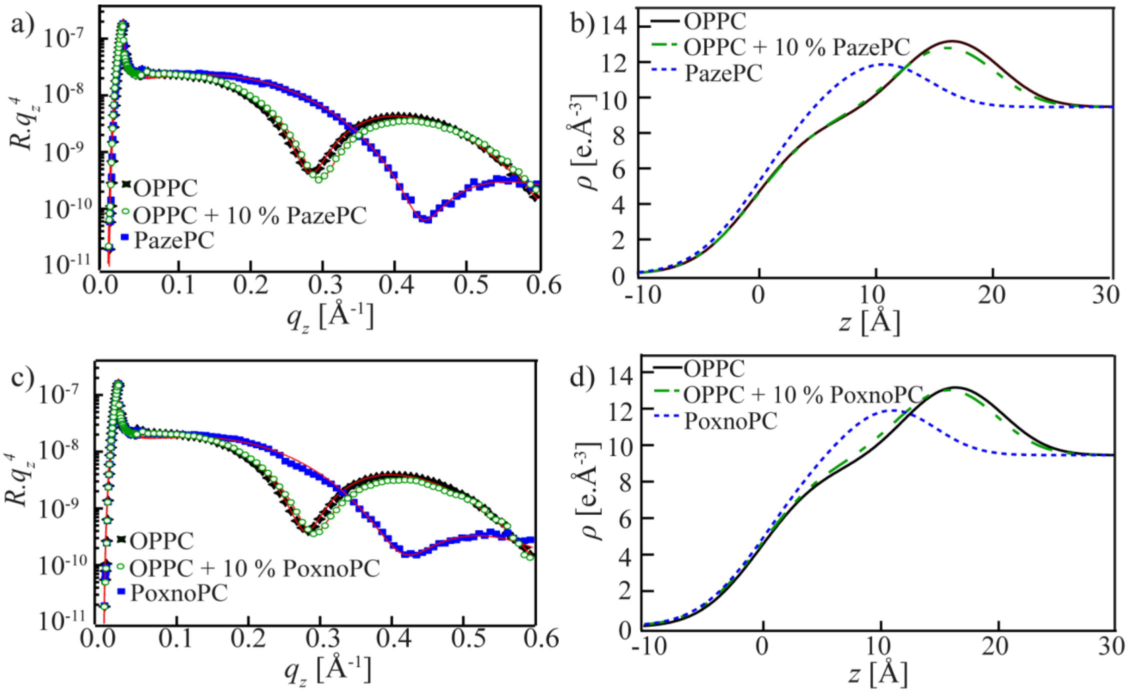

Figure 4.8 (a) XRR curves for OPPC (black), OPPC with 10 mol% PazePC (green) and pure PazePC (blue) on Ca^{2+}-buffer together with the best fits to the experimental results (solid red line), and (b) the reconstructed electron density profiles along the *z*-axis (perpendicular to the interface). The corresponding XRR and the electron density profiles from PoxnoPC systems are presented in (c) and (d), respectively.

The OPPC monolayer on Ca^{2+}-buffer shows similar structural parameters to those on K^+-buffer, suggesting that Ca^{2+} ions do not alter the structure of OPPC membranes. The incorporation of 10 mol% OxPL (PazePC or PoxnoPC) did not result in any remarkable change in thickness, electron density, and roughness of each interface. This leads to the conclusion that the structural integrity of OPPC membranes was not disturbed by the oxidization of hydrocarbon chains up to 10 mol%.

On the one hand, monolayers of pure PazePC and pure PoxnoPC on Ca^{2+}-buffer found to be thinner than OPPC monolayers; $\Delta d_A \sim -4.6$ Å for hydrocarbon chains and $\Delta d_H = -1.8$ Å for head groups, which follows the same tendency found on K^+-buffer. But on the other hand, the PazePC and PoxnoPC monolayers on Ca^{2+}-buffer possess much larger electron densities for head group and hydrocarbon chain regions compared to that on K$^+$-buffer. These findings suggest one of the following **two scenarios**: **(1)** either lipid molecules are laterally compacted on Ca^{2+}-buffer, or **(2)** Ca^{2+} ions are enriched at the interface.

Table 4.4 Thickness d, electron density ρ, and roughness σ corresponding to best fits of the XRR of OPPC/OxPL monolayers on Ca^{2+}-buffer measured at 20 mN/m.

OPPC			
	d [Å]	**ρ [e × Å^{-3}]**	**σ [Å]**
Hydrocarbon chain	12.4	0.317	4.1
Choline head	8.0	0.510	3.3
Buffer	∞	0.335	3.2
OPPC + 10 mol% PazePC			
	d [Å]	**ρ [e × Å^{-3}]**	**σ [Å]**
Hydrocarbon chain	12.0	0.318	4.3
Choline head	7.6	0.496	3.4
Buffer	∞	0.335	3.2
PazePC			
	d [Å]	ρ [e × Å^{-3}]	σ [Å]
Hydrocarbon chain	7.6	0.352	4.3
Choline head	6.3	0.478	3.4
Buffer	∞	0.335	3.2
OPPC + 10 mol% PoxnoPC			
	d [Å]	ρ [e × Å^{-3}]	σ [Å]
Hydrocarbon chain	12.0	0.319	4.3
Choline head	7.8	0.502	3.5
Buffer	∞	0.335	3.2
PoxnoPC			
	d [Å]	ρ [e × Å^{-3}]	σ [Å]
Hydrocarbon chain	7.9	0.333	4.3
Choline head	6.2	0.473	3.6
Buffer	∞	0.335	3.2

With the help of obtained information from the monolayer study (section 4.1.1), the first scenario can easily be excluded, because the difference in area per lipid molecule at π = 20 mN/m between K$^+$-buffer and Ca^{2+}-buffer is below 7% and the lateral compressibility is almost identical. In contrast, the obtained XRR results with a remarkable increase in the electron density in the slab of PazePC head groups support the second scenario. In addition, a cross-linking of lipids by Ca^{2+} ions can be suggested, as the average number of electrons per one PazePC molecule calculated from the fit on Ca^{2+}-buffer (N_e = 625 e$^-$) was much larger than the value calculated from the chemical formula (N_e = 364 e$^-$). The enhanced lateral cooperativity in lipid monolayers in the presence of Ca^{2+} seems to be qualitatively in good agreement with the previous studies using ^{2}H NMR [90], grazing incidence X-ray diffraction and Monte Carlo simulations [91], dilational rheology [92] and atomistic MD simulations [90, 93, 94].

4.1.6 Density Profiles of Ca^{2+} Ions in the Presence/Absence of OxPL

To support the suggested scenario (2) of the condensation of Ca^{2+} ions at interfaces, the density profiles of Ca^{2+} ions using GIXF for OPPC (black), OPPC with 10 mol% PazePC (green) and pure PazePC (blue) (Figure 4.8a) were measured including the reconstructed ion concentration profiles normal to the monolayer surfaces (Figure 4.9b). The corresponding results for OPPC/PoxnoPC monolayers are presented in Figure 4.9c and 4.9d, respectively.

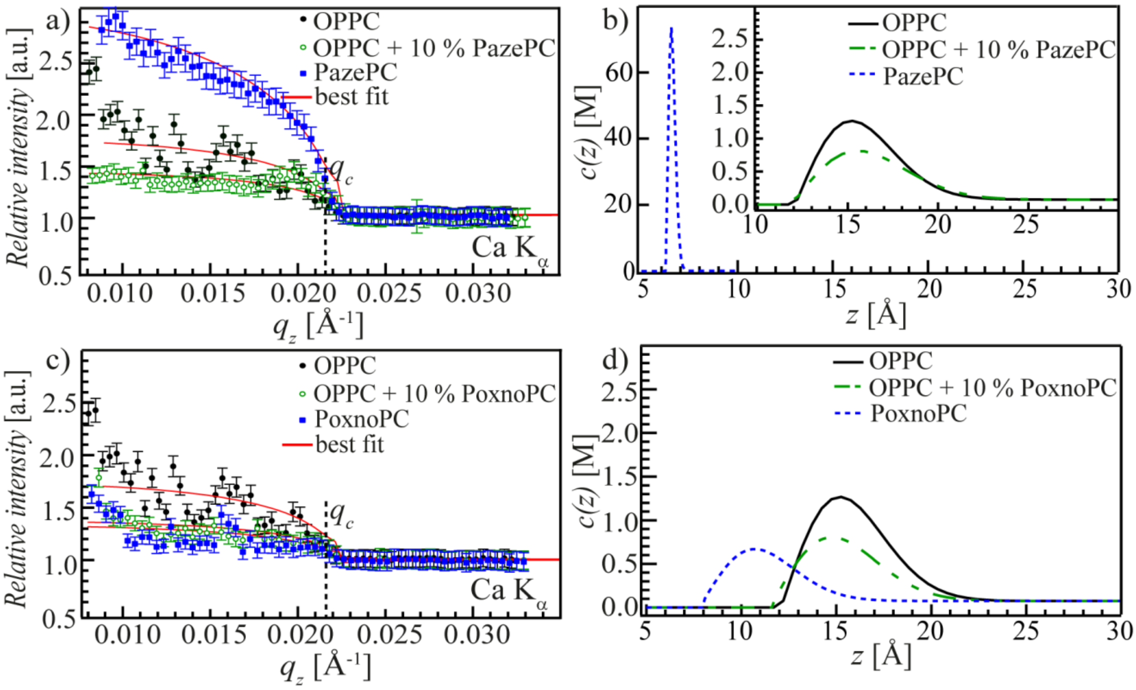

Figure 4.9 (a) Fluorescence intensities of Ca K_α as a function of q_z for OPPC (black), OPPC with 10 mol% PazePC (green) and pure PazePC (blue) on Ca^{2+}-buffer together with the best fits (solid red line) and (b) the reconstructed electron density profiles along the *z*-axis (perpendicular to the interface). The corresponding XRR and the electron density profiles from PoxnoPC systems are presented in (c) and (d), respectively.

As shown in Figure 4.9 the fluorescence signals at $q_z < q_c$ for all OPPC/PoxnoPC and OPPC/PazePC monolayers is higher than the bulk level (at $q_z > q_c$). This supports the scenario (2) of an accumulation of Ca^{2+} ions on the membrane surface, which is consistent with the modification in electron densities found by XRR results. Table 4.5 shows the parameters obtained from the best fit. There, z gives the position of the maximum concentration of Ca^{2+} ions with the definition of the interface between air and hydrocarbon chains to be at $z = 0$.

Table 4.5 Position of the maximum concentration z, ion lateral concentration c_L and number of ions per lipid N of OPPC/OxPL monolayers on Ca^{2+}-buffer.

	z [Å]	**c_L [ions/cm^2][10^{13}]**	**N [ions/lipid]**
OPPC	15.3	4.1	0.26
OPPC + 10 mol% PazePC	15.3	2.9	0.24
PazePC	6.6	19.0	2.1
OPPC + 10 mol% PoxnoPC	14.8	2.8	0.20
PoxnoPC	10.7	2.1	0.20

For OPPC (black) the positions of the maximum concentration is located at $z_{\max} = 15.3$ Å (head group region). The Ca^{2+} ions located there show a surface concentration of 4.1×10^{13} ions/cm^2. This means, that $N = 0.26 \times Ca^{2+}$ ion is coupled to one OPPC molecule, i.e. $1 \times Ca^{2+}$ ion is coupled to ~ 4 × OPPC molecules. The incorporation of 10 mol% of PazePC/PoxnoPC (green) as well as pure PoxnoPC monolayer (blue) does not cause any remarkable change in the density profiles of Ca^{2+} near the interface. In contrast, in a pure PazePC monolayer a remarkable enhancement of Ca K_α signals below q_c is visible. The condensation of Ca^{2+} ions in the vicinity of interface show the lateral Ca^{2+} ion concentration of $c_L = 19 \times 10^{13}$ ions/cm^2. This value is 10 times larger than for pure OPPC and gives the number of $N = 2.1$ Ca^{2+} ions per lipid molecule. The founding that Ca^{2+} can bind to around four lipid head groups or form lipid/ion clusters [95], indicates that the enrichment of Ca^{2+} ions at the head group region can be explained by the high attractive interaction of the Ca^{2+} ions with the negatively charged carboxyl group of PazePC, which is reorientated into the aqueous phase as reported from MD simulations by Khandelia *et al.* [13].

4.1.7 Impact of OxPL on Phospholipid Monolayers in the Presence of Monovalent Cs^+ Ions

To investigate if the size of monovalent ions has a different influence on the monolayers, they were deposited on Cs^+-buffer. Figure 4.10a/b represents the XRR curves of OPPC/OxPL monolayers together with the best fits to the reflectivity curves (red lines). The obtained thickness d, electron density ρ, and root mean square (rms) roughness σ of each interface are summarized in Table 4.6.

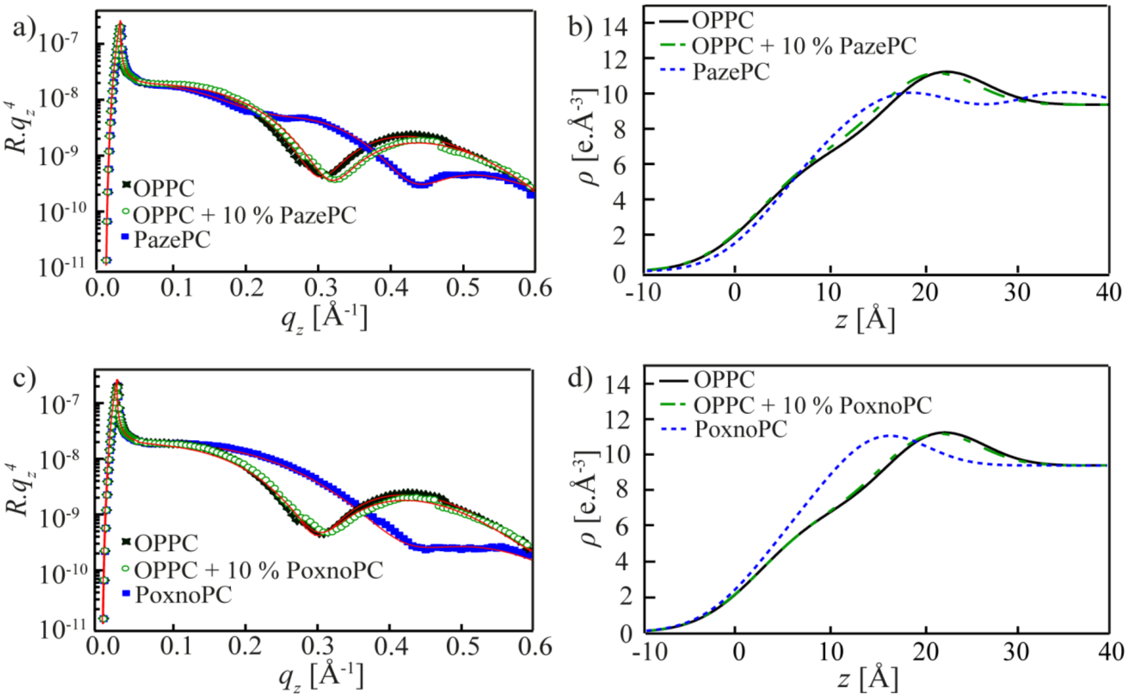

Figure 4.10 (a) XRR curves for OPPC (black), OPPC with 10 mol% PazePC (green) and pure PazePC (blue) on Cs^+-buffer together with the best fits to the experimental results (solid red line), and (b) the reconstructed electron density profiles along the z-axis (perpendicular to the interface). The corresponding XRR and the electron density profiles from PoxnoPC systems are presented in (c) and (d), respectively.

In comparison to the obtained results on K^+-buffer, here on Cs^+-buffer the thickness and electron density values obtained for OPPC monolayers in the presence and absence of OxPL are slightly but distinctly smaller. Pure PoxnoPC exhibits no distinguishable differences, which is consistent with the lateral compressibility modulus showing no notable differences as well. On the other hand for negatively charged PazePC the packing of molecules becomes weaker by replacing K^+ ions by the bulkier Cs^+ ions, which seems to be in qualitative agreement with MD simulations of Jurkiewicz *et al.* on lipid bilayers, suggesting that the thickness of a bilayer in 1M CsCl is distinctly thinner than those in 1M KCl and NaCl, especially for membranes incorporating negatively charged phosphatidylserine (PS) [95]. Consequently, the difference in membrane fine-structures detected by XRR (in the presence of Cs^+ and K^+) suggests that electrostatics of charged PazePC membranes is influenced not only by valence numbers but also by the species of ions.

Pure PazePC monolayers were less stable on Cs^+-buffer due to the weaker lateral packing. This is why the matching fit to the XRR results was achieved by a 4-slab model. It is assumed that aggregates of PazePC molecules are formed underneath the PazePC monolayer, which was previously reported by Sabatini *et al.* [96].

Table 4.6 Thickness *d*, electron density *ρ*, and roughness *σ* corresponding to best fits of the XRR of OPPC/OxPL monolayers on Cs^+-buffer measured at 20 mN/m.

OPPC			
	d [Å]	*ρ* [e × $Å^{-3}$]	*σ* [Å]
Hydrocarbon chain	11.3	0.253	4.4
Choline head	7.3	0.437	3.4
Buffer	∞	0.335	3.2
OPPC + 10 mol% PazePC			
	d [Å]	*ρ* [e × $Å^{-3}$]	*σ* [Å]
Hydrocarbon chain	10.7	0.260	4.4
Choline head	7.1	0.436	3.4
Buffer	∞	0.335	3.2
PazePC [2)]			
	d [Å]	*ρ* [e × $Å^{-3}$]	*σ* [Å]
Hydrocarbon chain	6.6	0.302	3.9
Choline head	5.8	0.384	4.1
Buffer	∞	0.335	3.3
OPPC + 10 mol% PoxnoPC			
	d [Å]	*ρ* [e × $Å^{-3}$]	*σ* [Å]
Hydrocarbon chain	10.9	0.253	4.4
Choline head	7.2	0.437	3.4
Buffer	∞	0.335	3.2
PoxnoPC			
	d [Å]	*ρ* [e × $Å^{-3}$]	*σ* [Å]
Hydrocarbon chain	7.0	0.287	4.4
Choline head	6.5	0.451	3.3
Buffer	∞	0.335	3.2

[2)] Values for the PazePC monolayer from a 4-slab model.

4.1.8 Density Profiles of Cs^+ Ions in the Presence/Absence of OxPL

Figure 4.11a shows the normalized Cs L_α fluorescence intensities of all monolayers on Cs^+-buffer together with the best fit results (red lines). The corresponding results for OPPC/PoxnoPC monolayers are presented in Figure 4.11b.

The fluorescence intensities of OPPC (Figure 4.11, black) and OPPC doped with 10 mol% PazePC (Figure 4.11a, green) show no sign of ion condensation near the interface, like the case of monolayers on K^+-buffer (section 4.1.4). On the other hand, the signal from pure PazePC monolayer (Figure 4.11a, blue) is 1.5 times larger than the bulk signal.

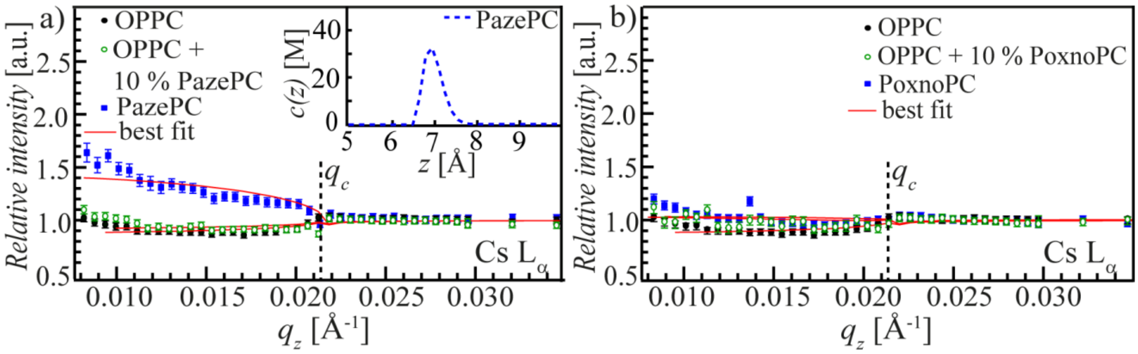

Figure 4.11 (a) Fluorescence intensities of Cs L_α as a function of q_z for OPPC (black), OPPC with 10 mol% PazePC (green) and pure PazePC (blue) on Cs^+-buffer together with the best fits (solid red line). The corresponding results for OPPC/PoxnoPC systems are presented in (b) respectively.

The extracted concentration maximum for pure PazePC is located at z = 7.0 Å (Figure 4.11a, inset) and the lateral concentration of Cs^+ ions was found to be $c_L = 1.09\times10^{14}$ ions/cm^2. Calculations with the area per molecule of A = 105 Å^2 from pressure-area isotherms (section 4.1.1, Table 4.1) leads to the number of Cs^+ ions per one PazePC molecule to be $N = 1.2$. Consequently the binding stoichiometry of Cs^+ and PazePC is almost 1 : 1, i.e. Cs^+ does not cross-link PazePC molecules. This value is one half of PazePC on Ca^{2+}-buffer (N = 2.1). Namely, if one considers the valency, the binding affinity of PazePC to Cs^+ is 4 times weaker than the binding to Ca^{2+}.

4.1.9 Impact of Charges and Ions on Head Group Geometry

The effect of enhancement in case of Cs^+ ions in contrast to K^+ ions can be understood with specific ion effects i.e. charge, size, charge distribution and polarization based on the Hofmeister series for both monovalent ions. In case of PazePC there are three oxygen atoms attracting the cations: the carboxylate, the phosphate group in the phosphocholine (PC) head group and the carbonyl. Comparing these three possible binding positions from MD simulations, the binding with the carbonyl group (*sn*-2 > *sn*-1) is prevailing [97]. The carbonyl groups can form complexes by carbonyl-cation-carbonyl interactions. K^+ ions predominantly form complexes with three (or four) lipid molecules, while Cs^+ ions form mostly complexes with two lipid molecules [97]. Interestingly, Haverd and Warr found in flotation experiments for carboxylic groups that for the selectivity of anionic surfactants the discrimination between alkali metal ions at the air-water interface is difficult while for phosphate groups the selectivity order $K^+ < Cs^+$ is distinguishable [98]. In addition, binding is affected by the tilt of the P-N angle which depends on the ion type present in the subphase and some present charge in the phospholipid [94, 99]. Negative charges decrease the P-N angle as well as small, hard ions like K^+. Consequently in case of K^+ ions, P-N angle is small and there are high repulsive interactions with the tert-amino cations N^+. Cs^+ ions on the other hand increases the P-N tilt angle, making all three possible binding partners easier to reach (Figure 4.12).

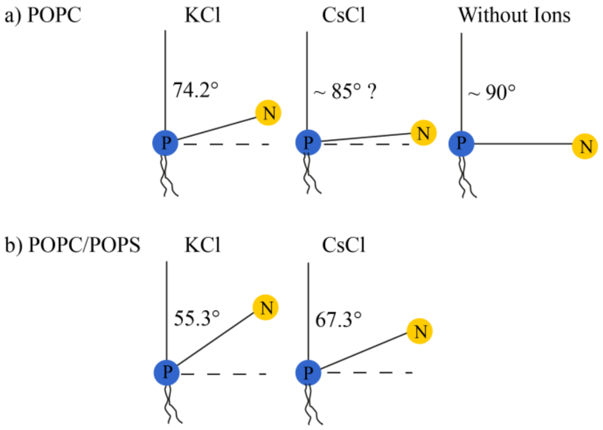

Figure 4.12 Different P-N tilt angles of phosphocholine (PC) head groups dependent on the present ions in zwitterionic POPC and anionic systems POPC/POPS [94, 99].

Another point is polarity and binding length: In comparison to K^+ ions, Cs^+ is a larger, polar cation and its binding length is larger. Thus, approaching towards the binding sides of phospholipids (PL) and accumulation near the PC head group with a flatter P-N angle is more attractive to Cs^+ ions. Therefore, the enrichment of Cs^+ ions on the PazePC membranes is expected to be more than K^+ ions which is consistent with our finding. Interestingly, it seems to be necessary that negative charges in the PL are present forming enough attracting forces for Cs^+ ions, because neither the 10 mol% mixtures nor pure PoxnoPC did show an enhancement of Cs^+ ions.

4.2 Impact of OxPL on Intermembrane Interactions of Membrane Multilayers

The model system of vertically stacked membranes represents a simplified model for the cell-cell interaction. Their advantage is, that the highly oriented multilayer stacks offer unique experimental possibilities to study interactions in lipid bilayer systems, both with and without membrane proteins. In off-specular scattering experiments, the high degree of structural orientation allows a precise distinction between the normal q_z, and the lateral component $q_{\shortparallel}$ of the scattering vector. Thus, it is suitable to study the lateral and vertical structure of the bilayers.

The influence of oxidization on the structural ordering and mechanical properties of membrane models was investigated using neutron scattering techniques (ILL, Grenoble) on solid-supported phospholipid multilayers (POPC) which were incorporated with different molar fractions (10%, 20%) of OxPL, either PazePC or PoxnoPC, under various relative humidity conditions (low relative humidity (RH) ~ 33%, high RH~ 96%, bulk condition) at 37 °C (see section 3.2.2.4).

The lamellar periodicity d of the multilayers can be obtained from the specular signals. In the first step, the lamellar periodicity d was calculated from the gap Δq_z between two neighboring Bragg peaks given as:

$$d = \frac{2\pi}{\Delta q_z} \tag{4.5}$$

In the second step, the vertical correlation length Λ was calculated from the half width at half maximum (HWHM) of the Gaussian fit according to:

$$\Lambda = \frac{2\pi}{HWHM} \tag{4.6}$$

Figure 4.13 demonstrates the specular signals of POPC incorporated with different molar fraction of OxPL at various relative humidity conditions, including the position of Bragg peaks highlighted with black arrows. The results for the spacing of the multilayer stacks d are presented in Table 4.7.

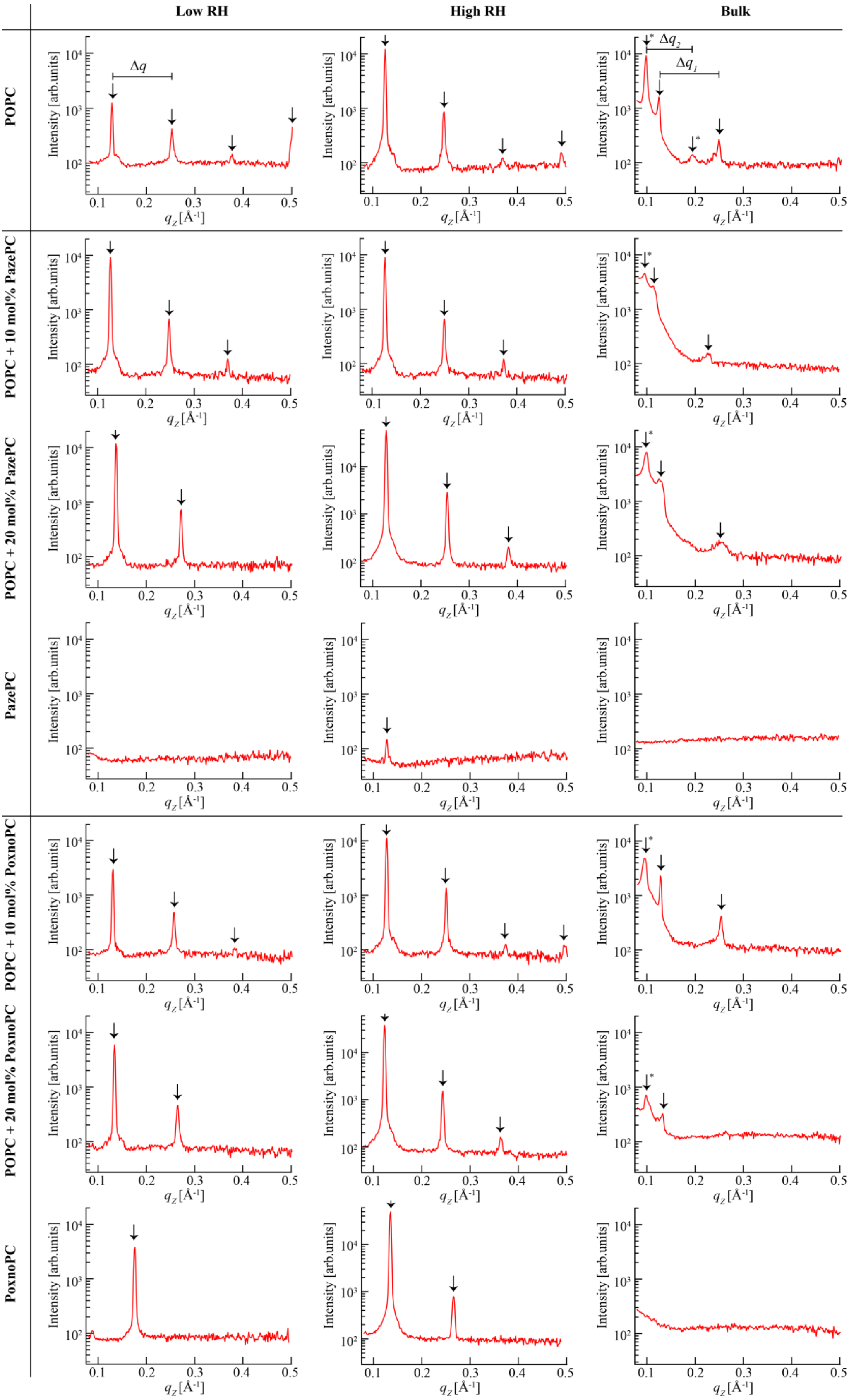

Figure 4.13 Specular signals of POPC multilayers with or without incorporation of OxPL, either PazePC or PoxnoPC, at different molar ratios (10% and 20%) and relative humidity conditions (RH) at 37 °C. The position of the Bragg peaks is highlighted with black arrows. The stars indicate that the Bragg peaks appeared due to the presence of a second phase.

Table 4.7 Lamellar periodicity *d* of POPC multilayers with or without incorporation of OxPL, either PazePC or PoxnoPC, at different molar ratios (10% and 20%) and relative humidities (RH) at 37 °C. In the bulk condition, Hepes-buffer with 2 mM $CaCl_2$ was prepared with D_2O.

	Lamellar Periodicity *d* [Å]			
	Low RH (~ 33%)	**High RH (~ 96%)**	**Bulk (D_2O)**	
POPC	**49.8**	**50.6**	**49.9**	**63.2**
10% PazePC	47.2	50.0	56.2	67.4
20% PazePC	45.7	48.8	49.6	63.3
PazePC	-	48.9	-	-
10% PoxnoPC	48.4	50.6	49.0	63.2
20% PoxnoPC	46.9	50.0	47.6	65.3
PoxnoPC	35.5	50.2	-	63.3

Changes in the specular signal due to the experimental conditions or membrane compositions reflect the impact of hydration and OxPL on the vertical order of membranes. The results of specular signals and the obtained lamellar periodicity *d* lead to the explanation of the experimental results as follows:

(i) At high RH, the repetition length is increased due to a higher hydration state of multilayers. The lamellar periodicity *d* of pure POPC membranes in fluid L_α phase at low RH (~ 50 Å) is in good agreement with reported values at comparable conditions [100].

(ii) At high RH, all membrane systems show the best ordered state, as the number of Bragg peaks is the highest.

(iii) The incorporation of 10 mol% OxPL demonstrates clearly, that PazePC induces a less ordered state than PoxnoPC, as the number of Bragg peaks is less in case of PazePC in both conditions at low RH and high RH. However, the incorporation of 20 mol% OxPL reveals that both OxPL, PazePC and PoxnoPC, shows similar ordered states, as both systems have the same number of Bragg peaks in both conditions at low RH and high RH.

(iv) In bulk conditions both pure OxPL exhibit a lower stability of multilayers than pure POPC with or without the incorporation of OxPL, since no Bragg peaks are observed. Thus, the presence of OxPL lead to an unbinding transition, where membranes repel each other.

(v) In bulk conditions, the coexistence of two different phases can be observed for the systems of pure POPC with and without the incorporation of OxPL. The lamellar periodicity d_1 ~ 50 Å (Table 4.7 bulk condition, left column) represents the membrane distance in fluid L_α phase [100]. The coexistence of a second phase exhibits a lamellar periodicity of d_2 ~ 63 Å (Table 4.7 bulk condition, right column) which is in good agreement with previous results reported by Schneck *et al.* for DPPC membranes in L_α

phase in the presence of 2 mM Ca^{2+} ions (d ~ 69 Å) [101]. The increase in lamellar distance can be explained by the reduction of electrostatic interactions between two membranes by the dielectric constant of water ($\varepsilon_{H2O} \approx 80$) due to the high hydration and the screening of electrostatic interactions due to the ionic strength of present divalent Ca^{2+} ions.

Table 4.8 summarizes the vertical correlation length Λ of each multilayer system at different relative humidity conditions which was calculated according to equation 4.6. The results demonstrate, that the vertical correlation length Λ (e.g. at high RH) is higher for the phospholipid mixtures than for the pure phospholipid systems which is consistent to the results obtained from the free energy calculation of isotherms, where the mixtures were found to be more stable than the pure components (section 4.1.1).

Table 4.8 Vertical correlation length Λ of POPC multilayers with or without incorporation of both OxPL, PazePC or PoxnoPC, at different molar ratios (10% and 20%) and relative humidities (RH) at 37 °C. In the bulk condition, Hepes-buffer with 2 mM $CaCl_2$ was prepared with D_2O.

	Vertical Correlation Length Λ [Å]			
	Low RH (~ 33%)	**High RH (~ 96%)**	**Bulk (D_2O)**	
POPC	**939**	**902**	**622**	**714**
10% PazePC	943	991	525	379
20% PazePC	905	970	365	433
PazePC	-	766	-	-
10% PoxnoPC	1001	970	366	865
20% PoxnoPC	941	985	439	1326
PoxnoPC	736	776	-	

The off-specular neutron scattering study gave insight into the impact of OxPL on the vertical structure of membrane multilayers. An increase in vertical correlation length Λ in addition to a decrease in the lamellar periodicity d was observed when OxPL were incorporated into POPC membranes at low and high RH. This can be explained by a reduction in the water content of the head group region while the thickness of the head group region is decreased in the presence of OxPL as supported by the XRR study. This is consistent with previous studies, where the truncated *sn*-2 chain of PoxnoPC was found to be near the hydrated head group region, while the *sn*-2 chain of PazePC is reoriented into the aqueous phase, which can displace some water from this area [89, 102].

4.3 Summary

In the first step, the impact of lipid oxidization on the thermodydnamics and electrostatics of lipid monolayer was investigated by pressure-area (π-A) isotherms and surface potential ($\Delta\psi$-A) measurements (sections 4.1.1, 4.1.2). The pressure-area (π-A) isotherms demonstrated that the incorporation of OxPL into the phospholipid monolayer led to a decreased packing order and a non-ideal mixing behavior, while the lipids remained in the liquid expanded phase L_e. In addition, monolayers containing PazePC were found to be less stable on Cs^+-buffer. The surface potential results revealed that at the same molecular area (70 Å²), both pure OxPL decreased the surface potentials $\Delta V_{70} \sim 330$ mV on K^+-buffer, and ~ 365 mV on Ca^{2+}-buffer corresponding to a decrease in the surface dipole moment μ_n normal to the air-water interface by ~ 200 mD, which was obtained using the Helmholtz equation (3.7). These results suggested the reorientation of the terminal oxidatively moieties of the *sn*-2 hydrocarbon chain into the vicinity of the polar headgroup region, which was supported by the combination of surface potential measurements with the theory of Demchak-Fort (DF) three-layer capacitor model. This model enabled the assumption of the contribution of the extended conformation of the alkyl chain bearing the oxidized moieties (carboxyl or carbonyl) to the normal components of the phospholipid dipole moment. PazePC showed a resulting difference in surface potential of $\Delta V \sim 63$ mV on Ca^{2+}-buffer, and $\Delta V \sim 80$ mV on K^+-buffer, while PoxnoPC showed $\Delta V \sim 68$ mV on Ca^{2+}-buffer, and $\Delta V \sim 98$ mV on K^+-buffer, respectively, which was found to be in the same order of the corresponding surface potential of terminal CH_3 group (63 mV) reported by Taylor *et al.* [83]

In the second step, the electrostatics of membranes under oxidative stress was examined by the combination of high-energy specular X-ray reflectivity (XRR) and grazing-incidence X-ray fluorescence (GIXF) of OPPC monolayers incorporated with different molar fractions (5%, 10%, 20%) of both oxidized phospholipids (OxPL), PazePC or PoxnoPC, on different buffers (K^+-buffer, Ca^{2+}-buffer and Cs^+-buffer) (sections 4.1.1 - 4.1.2). The XRR results demonstrated that both pure OxPL formed thinner monolayers than pure OPPC on different buffers, which was more pronounced for PazePC. However, the incorporation of 10 mol% OxPL did not result in any remarkable change in thickness, electron density, and roughness of each interface. Density profiles of monovalent/divalent ions near the membrane surface were gained by GIXF for each phospholipid composition. In general, strong specific effects of cations on mixed OPPC/OxPL monolayers were observed. For example, the thickness and stability of PazePC monolayers on Cs^+-buffer were distinctly less than those on K^+-buffer. Moreover GIXF results demonstrated, a clear enrichment of Cs^+ ions in the vicinity of PazePC membranes, while K^+ ions showed no sign of enrichment. The presence of Ca^{2+} cations showed (1) an accumulation of Ca^{2+} ions near the head groups and (2) an increased thicknesses and increased electron densities of both, hydrocarbon chains and choline head groups. PazePC with its carboxylic group pointing into the subphase showed the highest accumulation of Ca^{2+} ions in the polar head group regions, yielding $N = 2.1$ Ca^{2+} ions per PazePC lipid. If the sequence of binding affinity from the Hofmeister series ($Ca^{2+} > K^{+} > Cs^{+}$) [95, 103] is compared to the results mentioned here, the GIXF results suggest a slightly different trend ($Ca^{2+} > Cs^{+} > K^{+}$). This finding seems qualitatively consistent with obtained XRR results, where PazePC monolayer on Cs^{+}-buffer was thinner than that on K^{+}-buffer.

In the third step, the impact of oxidization on the inter-membrane interactions, stacks of planar membranes on solid supports was investigated by off-specular neutron scattering measured at different relative humidities (RH) (section 4.1.9). It was found that the incorporation of OxPL into the membrane can displace water molecules from the inter-membrane region due to the reorientation of oxidized moieties which was shown by a decrease in the lamellar periodicity ($\Delta d \sim 2 - 4$ Å) and by an increased vertical correlation length ($\Delta\Lambda \sim 70 - 90$ Å). In case of pure OxPL membranes, a more distinct increase in vertical correlation length was found ($\Delta\Lambda_{\mathrm{PoxnoPC}} \sim$ 126 Å and $\Delta\Lambda_{\mathrm{PazePC}} \sim$ 136 Å) indicating a lower stability of OxPL membrane multilayers which is in good agreement with the results suggested by Langmuir isotherms (section 4.1.1).

5 The Interaction between Phospholipids and Proteins

5.1 C-reactive protein (CRP)

C-reactive protein (CRP) is an acute phase reactant plasma protein and plays a crucial role in the immune response. In case of tissue injury, infection or inflammation, CRP binds in the presence of Ca^{2+} ions to phosphocholine (PC) expressed on the surface of dead or dying cells in order to activate metabolic, scavenging and host defense functions [104]. Since CRP possesses recognition patterns (analogous to scavenger receptors) and host defense functions, it plays possibly a role in pathogenesis and diseases. Furthermore, a relation between increased CRP production and coronary heart diseases is of special interest. Future coronary events can be predicted based on increased CRP level, even if they have been considered as normal before [105]. Plasma CRP is produced by hepatocytes in which its synthesis is regulated by transcriptional control of cytokines [106]. However, as the production of CRP is only one part of the nonspecific acute-phase response to most forms of inflammation, infection and tissue damage, the interpretation of CRP values in diagnostics is reliable only in full knowledge of all other clinical and pathological results [105].

CRP protein belongs to the pentraxin family and has a pentameric form of five identical, nonglycosylated polypeptide subunits (Figure 5.1a).

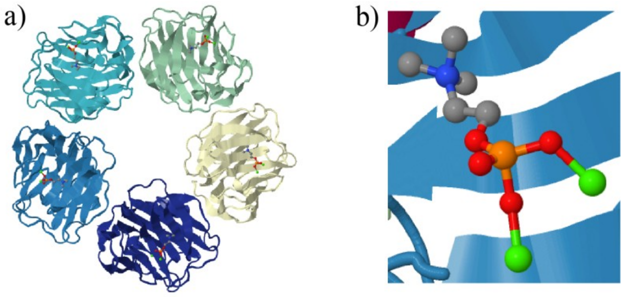

Figure 5.1 (a) Ribbon diagram of the crystal structure showing the ligand-binding site of each protomer together with five phosphocholine molecules. (b) Each PC can bind through two oxygens (red) of its phosphate group to the ligand-binding pocket over two Ca^{2+} ions (green) [104].

Each subunit is composed of 206 amino acids with a molecular mass of ~ 23 kDa. The pentameric form has a diameter of ~ 9 nm and a thickness of ~ 3 nm [104]. High-resolution X-ray analysis revealed that each CRP subunit consists of two-layered *ß* sheet with a flattened jellyroll topology. On this concave face there are furrows, following the curvature of the subunits which have a negatively charged inner part [104]. Describing the binding of CRP to PC, Thompson *et al.* proposed that two Ca^{2+} ions are bound to each of the five charged subunits of CRP by protein side chains via electrostatic interaction. Moreover, one molecule of PC is turned towards the shallow surface pocket on each subunit, interacting with the two protein-bound Ca^{2+} ions via the phosphate group and with the side chain glutamic acid via the positively charged quaternary nitrogen of the choline moiety (Figure 5.1b) [104].

Chang *et al*. observed that CRP binds in a calcium-dependent manner to both oxidized low density lipoproteins (OxLDL) and apoptotic cells through specifically recognition of the PC ligand of OxPL [107]. CRP does not bind to PC of native low density lipoproteins (LDL), nonoxidized phosphatidylcholine or OxPL without the PC head group. Previous studies suggested that the local disordering of PC groups is necessary for the binding of CRP to the PC head group [108]. These structural changes can be caused by mild oxidation of unsaturated hydrocarbon chains in the membrane [107]. By incorporating chemically pre-oxidized OxPL into artificial membrane models, Sabatini *et al.* demonstrated that the lipid oxidization enhances the binding of antibacterial proteins [109].

The consequences of CRP binding to oxidized phosphatidylcholine have not yet been investigated. Recently, there is a considerable evidence that such OxPL are proinflammatory and proatherogenic [107]. A high level of CRP is strongly related to atherosclerosis and myocardial infarction. Toward an effective therapy for such severe diseases, understanding the binding mechanism of CRP and its affinity to these oxidized molecules will open possibilities to control its concentration and probably reducing its harmful concentration that leads to those severe diseases.

The affinity of CRP to bind to phosphocholines may be important for host defense [110] and handling of autologous constituents including necrotic [111] and apoptotic cells [112]. Better understanding of the pathways of apoptosis and their regulation would allow access to novel therapeutic target areas for instance cardiovascular disease [113]. Therefore the research on CRP, including the study of its molecular structure-function relationships is practically important in medical and pharmaceutical applications.

In this section, the interaction between CRP and phsopholipids (PL) with and without the incorporation of OxPL is studied using cell model systems in combination with different physical techniques. Here, experiments were performed using (i) **liposomes** with DLS and ITC, (ii) **solid-supported membranes** with high energy specular X-ray reflectivity (inhouse instrument, Karlsruhe), DPI and QCM-D, (iii) **phospholipid monolayers** with surface tension and specular X-ray reflectivity (ESRF, Grenoble) measurements and (iv) **membrane multilayers** with off-specular neutron scattering (ILL; Grenoble).

5.1.1 The Interaction of CRP with Phospholipid Liposomes

5.1.1.1 Adsorption Effects of CRP on Liposome Sizes

To investigate the influence of oxidization on the interaction of CRP with phospholipids, POPC liposomes were prepared with and without 20 mol% of OxPL (PazePC or PoxnoPC, see section 3.2.1.1). Then CRP was added to the liposome solutions to reach the desired final concentrations (2.9 µM, 0.8 µM, 0.5 µM and 0.1 µM). Finally, the changes in size distributions were monitored over 90 min by dynamic light scattering (DLS).

In the following paragraphs, the changes in size distribution of POPC/PazePC liposomes during the incubation of CRP at various concentrations are monitored.

Figure 5.2 presents the DLS results of the interaction of CRP (2.9 µM) with POPC/PazePC (20 mol%) liposomes (a) within 60 min and (b) after 60 min of incubation. A distinct shift of the size distribution to larger diameters as well as the broadening of the distribution can be clearly observed just right after the addition of CRP to the liposome solution (Table 5.1). In addition, big particles are formed ($d \sim 1000$ nm) and their number rises with time. After 60 min of incubation, less distinct changes in size distributions could be observed (Figure 5.2b), accompanied by the formation of even bigger aggregates ($d \sim 7000$ nm).

Table 5.1 Peak position and FWHM of the size distributions of POPC/PazePC (20 mol%) liposomes with CRP (2.9 µM) within the first 60 min of incubation, compared to pure liposomes (at t = 0 min).

POPC/PazePC + CRP (2.9 µM)		
Time	**Diameter [nm]**	**FWHM [nm]**
0	**94**	**79**
1	223	153
3	239	145
5	283	148
60	315	142

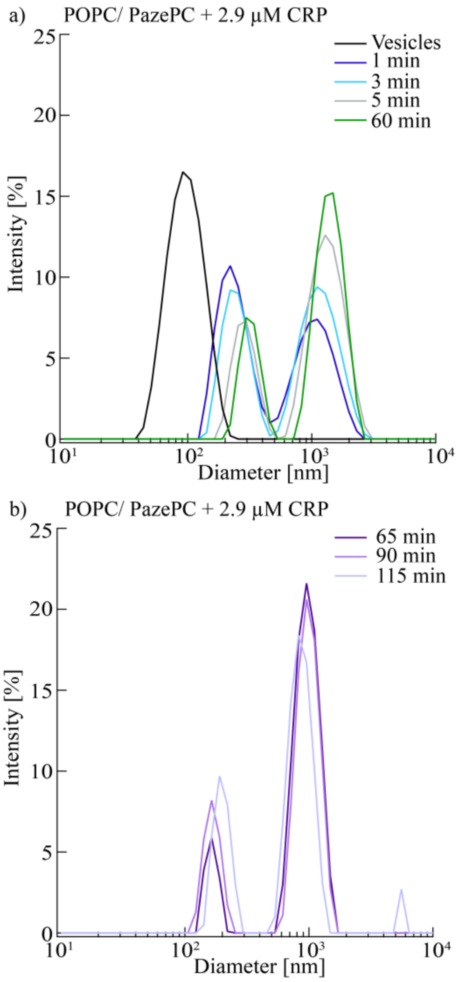

Figure 5.2 Changes in size distributions of POPC/PazePC (20 mol%) liposomes (black) after the addition of CRP (2.9 µM) (a) within the first 60 min and (b) after 60 min of incubation.

The interaction of CRP with POPC/PazePC (20 mol%) liposomes is strong even with a lower CRP concentration (0.8 µM). Two different size distributions are formed right after the addition of CRP (Figure 5.3), showing stable values for the diameter at the maximum position (*d* ~ 50 nm) within 5 min (Table 5.2). The FWHM of the distribution (FWHM ~ 60 nm) is stable over time, while the FWHM of the second distribution increases continuously (Table 5.2, right). This indicates the formation of further CRP-liposome-intermediates with time.

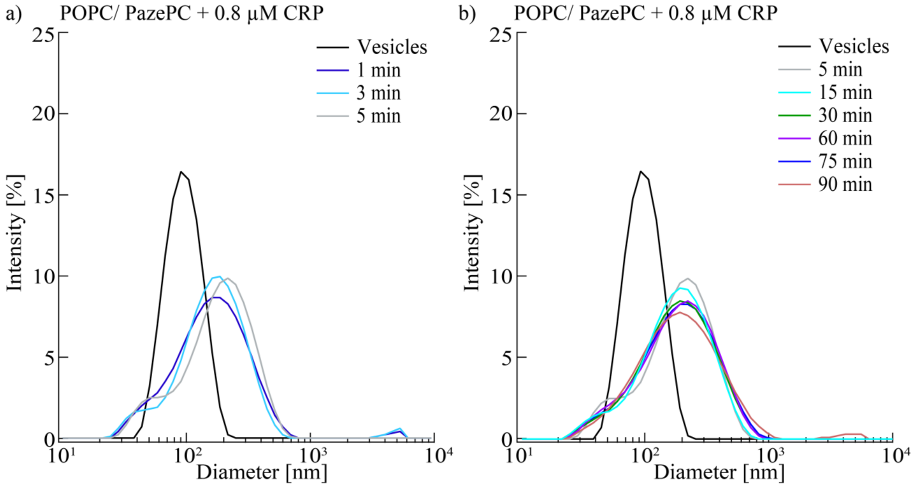

Figure 5.3 Changes in size distributions of CRP (0.8 µM) with POPC/PazePC (20 mol%) liposomes (black) (a) within 5 min and (b) within 90 min of incubation.

Table 5.2 Peak position and FWHM of the size distributions of POPC/PazePC (20 mol%) liposomes with CRP (0.8 µM) within 90 min of incubation, with respect to pure liposomes (at t = 0 min).

	POPC/PazePC + CRP (0.8 µM)			
	Peak 1		**Peak 2**	
Time [min]	**Diameter [nm]**	**FWHM [nm]**	**Diameter [nm]**	**FWHM [nm]**
0	**95**	**81**	**-**	**-**
5	56	53	215	268
15	51	63	197	278
30	53	65	200	318
60	56	64	213	325
75	55	65	206	331
90	58	67	194	360

Figure 5.4 shows the DLS results of the long term experiment of the interaction of CRP (0.5 μM) with POPC/PazePC (20 mol%) liposomes (a) in the first 60 min and (b) after 60 min. Within the first 60 min no changes can be observed. After 90 min the maximum position of the size distribution and the FWHM started to increase continuously (Table 5.3), resulting in the formation of big aggregates (*d* ~ 150 nm) after 150 min of incubation time.

Table 5.3 Peak position and FWHM of the size distributions of POPC/PazePC (20 mol%) liposomes with CRP (0.5 μM) over 260 min, with respect to pure liposomes (at t = 0 min).

POPC/PazePC + CRP (0.5 μM)		
Time [min]	**Diameter**	**FWHM [nm]**
0	**86**	**95**
5	87	93
15	87	90
30	85	82
60	87	86
75	87	95
90	93	112
115	127	147
150	131	162
170	141	178
200	149	204
260	156	222

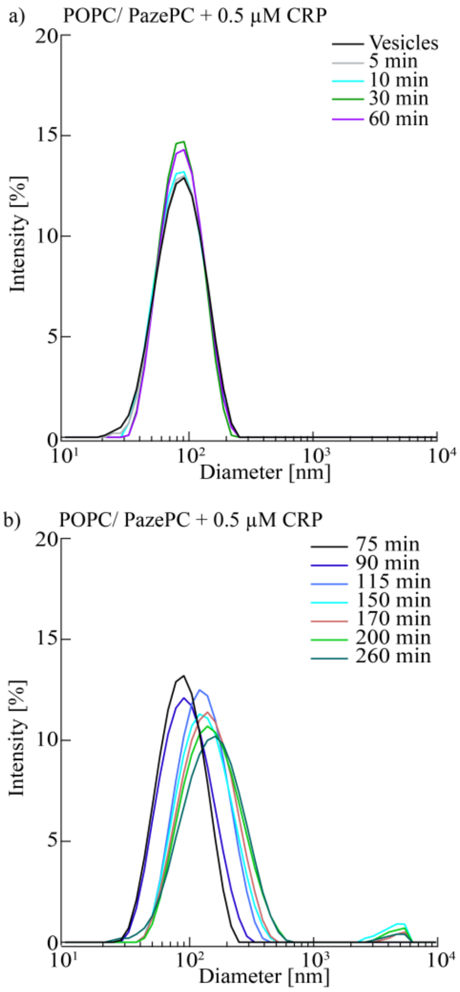

Figure 5.4 Changes in size distributions of POPC/PazePC (20 mol%) liposomes after the addition of CRP (0.5 μM) (a) within the first 60 min and (b) between 60 min and 260 min.

Figure 5.5 presents the DLS results of the long term experiment of the interaction of CRP (0.1 µM) with POPC/PazePC (20 mol%) liposomes over 360 min. The obtained fitting results (Table 5.4) reveal an increase in FWHM of ~ 10 nm after 360 min, which corresponds to a very weak interaction.

Table 5.4 Peak position and FWHM of the size distributions of POPC/PazePC (20 mol%) liposomes with CRP (0.1 µM) over 360 min, with respect to pure liposomes (at t = 0 min).

POPC/PazePC + CRP (0.1 µM)		
Time [min]	**Diameter [nm]**	**FWHM [nm]**
0	**81**	**73**
30	83	74
60	82	81
90	83	80
120	84	85
155	85	81
220	87	88
270	85	86
360	85	84

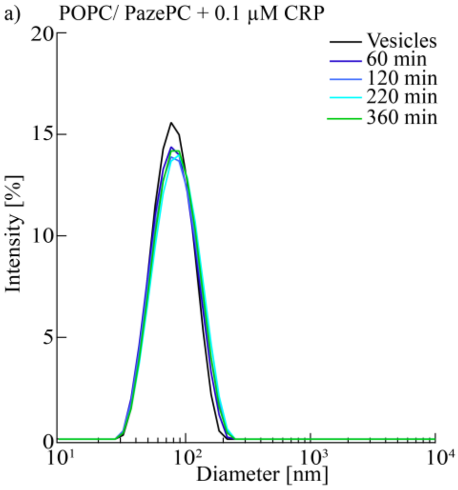

Figure 5.5 Changes in size distributions of POPC/PazePC (20 mol%) liposomes (black) after the addition of CRP (0.1 µM) in a long term experiment over 360 min.

Interaction of CRP with POPC/PoxnoPC Liposomes

In the following paragraphs, the changes in size distributions of POPC/PoxnoPC liposomes during the incubation of CRP at various concentrations are presented.

The DLS results show a clear shift of the maximum position of the size distribution to bigger diameters and a broadening of the distribution within the first 10 min (Figure 5.6a). In addition, big particles are formed (*d* ~ 4500 nm) right after the addition of CRP (2.9 μM) to the liposome solution. After 10 min the position of the size distribution remained stable while the FWHM of both size distributions increased gradually (Table 5.5).

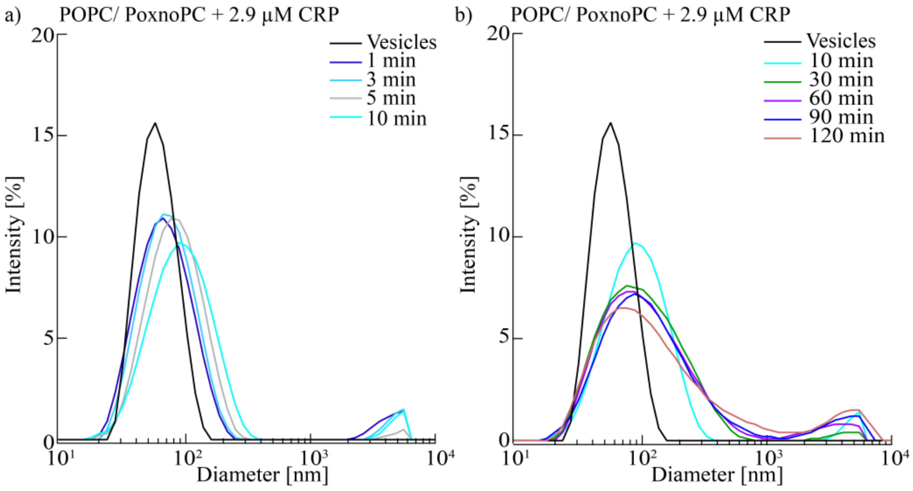

Figure 5.6 Changes in size distributions of POPC/PoxnoPC (20 mol%) liposomes (black) after the addition of CRP (2.9 μM) (a) in the first 10 min and (b) within 120 min of incubation.

Table 5.5 Peak position and FWHM of the size distributions of POPC/PoxnoPC (20 mol%) liposomes with CRP (2.9 μM) within 120 min, with respect to pure liposomes (at t = 0 min).

	POPC/PoxnoPC + CRP (2.9 μM)			
	Peak 1		**Peak 2**	
Time [min]	**Diameter [nm]**	**FWHM [nm]**	**Diameter [nm]**	**FWHM [nm]**
0	**59**	**53**	**-**	**-**
5	83	105	5149	1719
10	93	133	5021	1799
30	96	180	4352	2615
60	96	191	3496	3618
90	100	196	4167	3694
120	93	204	4311	4348

Figure 5.7 represents the DLS results of the interaction of CRP (0.8 µM) with POPC/PoxnoPC (20 mol%) liposomes (a) in the first 10 min and (b) over 120 min. The obtained fitting results (Table 5.6) reveal that the biggest changes in maximum position of size distributions happened within the first 10 min while the FWHM of both distributions increased continuously.

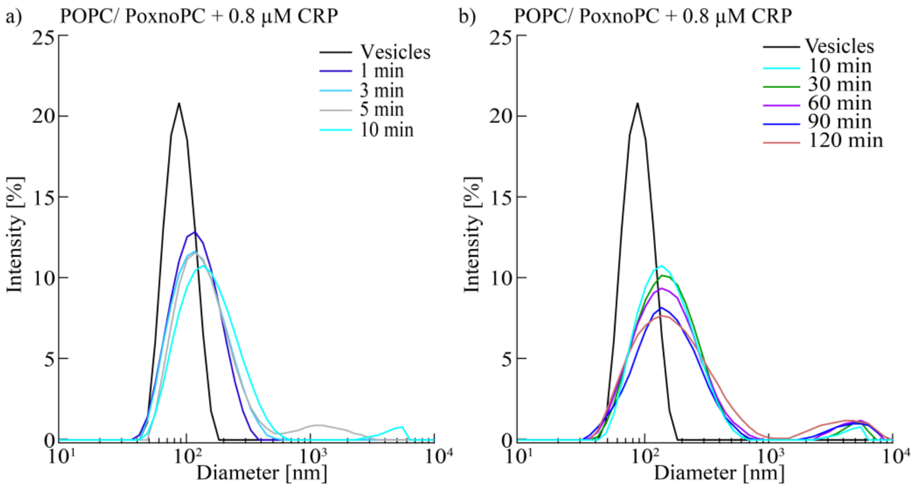

Figure 5.7 Changes in size distributions of POPC/PoxnoPC (20 mol%) liposomes (black) after the addition of CRP (0.8 µM) (a) in the first 10 min and (b) within 120 min of incubation.

Table 5.6 Peak position and FWHM of the size distributions of POPC/PoxnoPC (20 mol%) liposomes with CRP (0.8 µM) within 120 min of incubation, with respect to pure liposomes (at t = 0 min).

	POPC/PoxnoPC + CRP (0.8 µM)			
	Peak 1		**Peak 2**	
Time [min]	**Diameter [nm]**	**FWHM [nm]**	**Diameter [nm]**	**FWHM [nm]**
0	**91**	**61**	**-**	**-**
5	132	151	1162	1432
10	148	196	4758	2148
30	153	215	4969	2490
60	149	225	4870	3708
90	153	226	4711	4344
120	156	282	4075	4803

After 120 min the size distribution is shifted by ~ 60 nm to larger diameters and FWHM is increased by 220 nm. In comparison to the interaction of CRP with PazePC doped liposomes, PazePC shows more pronounced changes on the size distributions (shift by ~ 120 nm and FWHM increase by ~ 280 nm) indicating a stronger interaction with CRP. However, different liposome-protein products are formed with PoxnoPC, which is indicated by the more heterogeneous distribution at larger diameter values.

Figure 5.8 shows the DLS results of the interaction of POPC/PoxnoPC (20 mol%) liposomes with CRP ((a) 0.5 µM and (b) 0.1 µM) over 160 min. The obtained fitting results are presented in Table 5.7. In both experiments almost no changes on the size distributions was detected.

Comparing this PoxnoPC result with the PazePC result at the concentration of 0.5 µM, the different interaction strength of the used OxPL with CRP becomes obvious: After 90 min an interaction in case of PazePC was detected by DLS (p.81), while PoxnoPC did not show any changes in size distribution over 160 min.

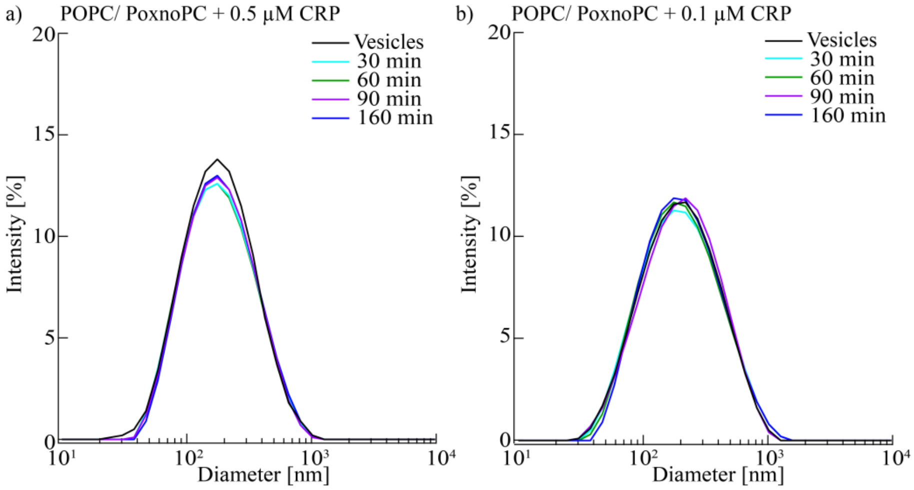

Figure 5.8 Changes in size distributions of POPC/PoxnoPC (20 mol%) liposomes (black) with CRP (0.5 µM (a) and 0.1 µM (b)) over 160 min of incubation. No changes on the size distributions of liposomes with CRP are observed.

Table 5.7 Peak position and FWHM of the size distributions of POPC/PoxnoPC (20 mol%) liposomes with CRP (0.5 µM, left and 0.1 µM, right) over 160 min of incubation, with respect to pure liposomes (at t = 0 min).

	POPC/PoxnoPC			
	+ CRP (0.5 µM)		**+ CRP (0.1 µM)**	
Time [min]	**Diameter [nm]**	**FWHM [nm]**	**Diameter [nm]**	**FWHM [nm]**
0	**68**	**74**	**74**	**91**
30	68	77	73	93
60	68	77	73	90
90	69	76	75	92
160	69	76	73	89

Interaction of CRP with POPC Liposomes

In the following, changes in size distributions of POPC liposomes during the incubation of CRP at various concentrations are presented as control experiments.

Figure 5.9 presents the DLS results of the interaction of POPC liposomes with CRP at the highest concentrations used in this study ((a) 2.9 µM and (b) 0.8 µM) over 145 min. The obtained fitting results are presented in Table 5.8. At 2.9 µM CRP, the broadening of the peak was only about ~ 10 nm implying a weak interaction.

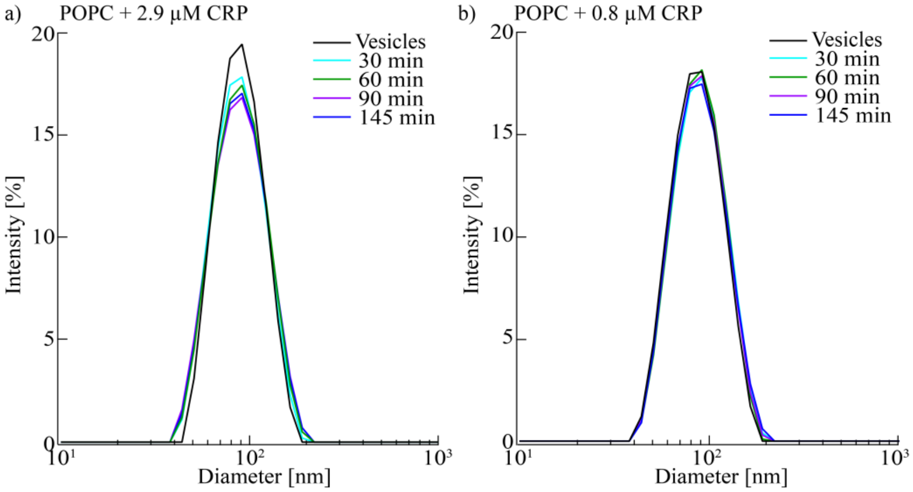

Figure 5.9 Changes in size distributions of POPC liposomes (black) with CRP ((a) 2.9 µM and (b) 0.8 µM) over 145 min of incubation. No interaction between the POPC liposomes and CRP are observed at these concentrations.

Table 5.8 Peak position and FWHM of the size distributions of POPC liposomes with CRP (2.9 µM, left and 0.8 µM, right) over 145 min of incubation, with respect to pure liposomes (at t = 0 min).

	POPC			
	+ CRP (2.9 µM)		**+ CRP (0.8 µM)**	
Time [min]	**Diameter [nm]**	**FWHM [nm]**	**Diameter [nm]**	**FWHM [nm]**
0	**88**	**63**	**86**	**65**
30	87	68	88	70
60	88	71	88	68
90	88	73	87	68
145	88	74	87	69

5.1.1.2 Summary of the DLS Results

By studying the interaction of liposomes (with and without incorporated OxPL) with CRP using DLS, it was shown that the interaction strength clearly depends on both, the type of OxPL and CRP concentrations (Table 5.9). Thus, the following conclusions can be made:

(i) The interaction of CRP with liposomes containing OxPL was stronger than with pure POPC. Comparing the two OxPL, PazePC showed a stronger interaction with CRP, resulting in the following order of the interaction strength:

PazePC > PoxnoPC > POPC

(ii) It can be assumed that different OxPL interact with CRP in a different mode. In case of PazePC, reproducible size distributions exhibited the same features, while in case of PoxnoPC the size distributions exhibited nonreproducible multi-populations.

Table 5.9 Overview of the interaction strength for all phospholipid liposomes with CRP at different concentrations reflected in changes in size distributions.

	Interaction		
c_{end} (CRP) [µM]	**PazePC (20 mol%)**	**PoxnoPC (20 mol%)**	**Pure POPC**
2.9	Large Changes	Large Changes	Small Changes
0.8	Large Changes	Large Changes	Not Detectable
0.5	Intermediate	Not Detectable	-
0.1	Small Changes	Not Detectable	-

The overall results obtained by DLS measurements suggest that OxPLs are necessary in the interaction of CRP with phospholipid membranes.

5.1.1.3 Thermodynamic Properties of CRP Interaction with Phospholipid Liposomes

To investigate the thermodynamic aspects and the influence of OxPL on the interaction between CRP and phospholipid liposomes, isothermal titration calorimetry (ITC) measurements were performed (Figure 5.10). In the experiments the CRP solution was stepwise titrated into the liposome solution of POPC or POPC doped with 20 mol% of OxPL (either PazePC or PoxnoPC) and the released heat was measured (section 3.2.2.7). The fit of the raw data yields the changes in enthalpy (ΔH) (in respect to the heat of dilution (ΔH_d)), the binding constant K_b, the change in entropy ΔS as well as the binding stoichiometry n.

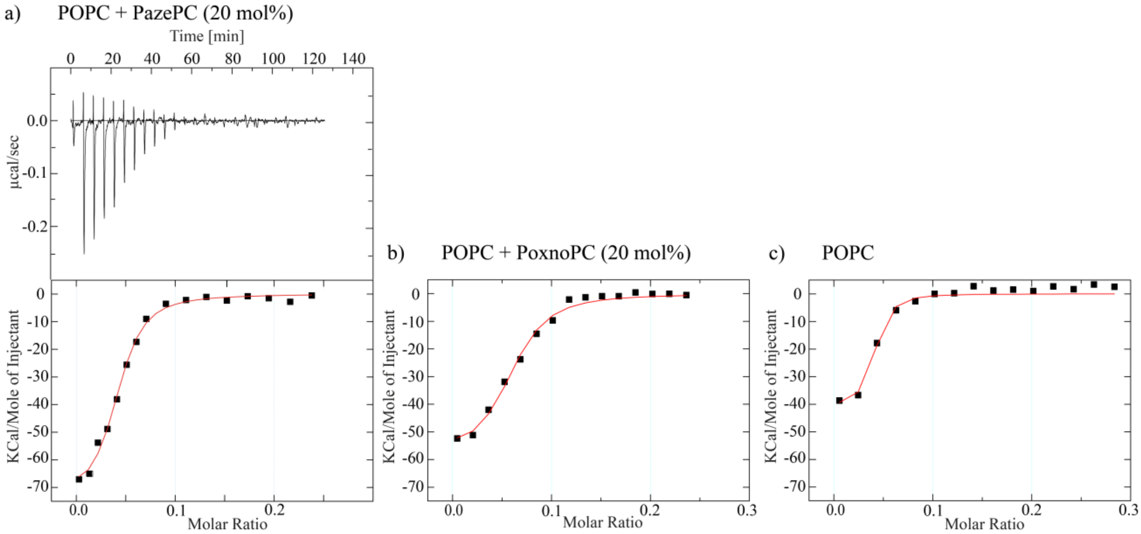

Figure 5.10 ITC measurement and the resulting graphs including the fitting results (red) of CRP with (a) POPC + PazePC (20 mol%), (b) POPC + PoxnoPC (20 mol%) and (c) pure POPC.

Table 5.10 Obtained results from ITC measurements of CRP with POPC liposomes with (a) PazePC (20 mol%) or (b) PoxnoPC (20 mol%) and (c) pure POPC liposomes.

CRP +	**ΔH [kcal/mol]**	**K_b [L/mol]**	**ΔS [cal/(mol*K)]**	**n**
a) PazePC	-73.7 ± 2.5	(7.45 ± 1.51)E+7	-211	(4.1 ± 0.1)E-2
b) PoxnoPC	-57.4 ± 2.9	(6.36 ± 1.02)E+7	-257	(5.7 ± 2.0)E-2
c) POPC	-41.5 ± 2.0	(10.2 ± 2.54)E+7	-105	(3.4 ± 0.2)E-2

The calculated average enthalpy change (ΔH) for PazePC is (-73.7 ± 2.5) kcal/mol and shows the highest released heat in the interaction with CRP compared to the other liposome compositions. These obtained results suggest for the strength of interaction with CRP the following trend:

PazePC > PoxnoPC > POPC,

which agrees well with the DLS results found in the previous section.

5.1.2 The Interaction of CRP with Phospholipid Multilayers

5.1.2.1 The Impact of CRP on the Structural Ordering of Phospholipid Multilayers

The influence of CRP on the structure and mechanics of solid-supported phospholipid multilayers (POPC) with or without incorporation of 20 mol% of OxPL, either PazePC or PoxnoPC, was investigated by off-specular neutron scattering (ILL, Grenoble) under various relative humidity conditions (low relative humidity (RH) ~ 33%, high RH~ 96%, bulk condition) and different CRP concentrations (2.9 µM, 1.5 µM and 0.8 µM) at 37 °C (see section 3.2.2.4 for more details).

The lamellar periodicity *d* of the multilayers was obtained from the Bragg peak positions defined by the Gaussian fit along the specular profile (Table 5.11). Changes in the specular signal due to the experimental conditions or membrane compositions reflect the impact of hydration and interaction of CRP with the membranes on the vertical order of membranes.

Table 5.11 Lamellar spacing *d* of POPC multilayers with or without incorporation of 20 mol% of either PazePC or PoxnoPC at different CRP concentrations and relative humidities (RH) at 37 °C with respect to the membranes before CRP incubation (grey, bold).

	Lamellar Spacing *d* [Å]			
	Low RH (~ 33%)	**High RH (~ 96%)**	**Bulk (D_2O)**	
POPC	**49.8**	**50.6**	**49.9**	**63.2**
+ CRP (2.9 µM)	52.2	-	-	-
+ CRP (1.5 µM)	56.7	-	-	-
+ CRP (0.8 µM)	51.1	-	-	-
+ 20 mol% PazePC	**45.7**	**48.8**	**49.6**	**63.3**
+ CRP (2.9 µM)	53.0	-	55.7	-
+ CRP (1.5 µM)	50.2	-	-	-
+ CRP (0.8 µM)	50.6	-	-	-
+ 20 mol% PoxnoPC	**46.9**	**50.0**	**47.6**	**65.3**
+ CRP (2.9 µM)	68.0	64.6	48.3	55.3
+ CRP (1.5 µM)	67.6	-	49.9	65.4
+ CRP (0.8 µM)	67.1	-	-	66.8

The obtained results demonstrate that CRP decreases the vertical ordering structure of membrane multilayers at all given CRP concentrations (Table 5.11). Since the first Bragg Peak was observed neither at high RH nor at bulk condition for most samples, the samples measured at low RH was the most stable condition and considered here as the condition for extracting the structural changes. When 20 mol% of OxPL was incorporated into the membrane, CRP leads to a higher increase in the lamellar spacing *d* than pure POPC (Δ*d* ~ 3 Å), which is more pronounced for PoxnoPC (Δ*d* ~ 21 Å) than for PazePC (Δ*d* ~ 6 Å).

Although the binding mechanism between CRP and lipid membranes incorporating OxPL is unknown at the moment, it is likely that the accessibility of the PC head group plays a crucial role. MD simulations of Khandelia and Mouritsen predicted the orientation of the polar *sn*-acyl chain of PazePC to point towards the water phase, while the truncated chain of PoxnoPC points out to the hydrophobic/hydrophilic interface [13]. In contrast to PazePC, it was reported that PoxnoPC causes intercalation of peptides into a phospholipid mono- or bilayer [114]. Therefore, it is assumed that, on the one hand, PoxnoPC creates a high disorder where PoxnoPC lipids meet non-oxidized PL, which in turn creates more space for CRP to intercalate easily into the membrane and interact with the more accessible PC head group. On the other hand, it is assumed that CRP binds on top of PazePC incorporated membranes.

CRP has a doughnut shape with a diameter of ~ 9 nm and a thickness of ~ 3 nm. Thus, the intercalation of CRP into the PoxnoPC incorporated membranes may lead to different randomly tilted angles normal to the membrane plane creating thicker layer in average (Figure 5.11b). In contrast to this, CRP with a parallel conformation in case of PazePC incorporated memebranes exhibits smaller inter-membrane distances (Figure 5.11a).

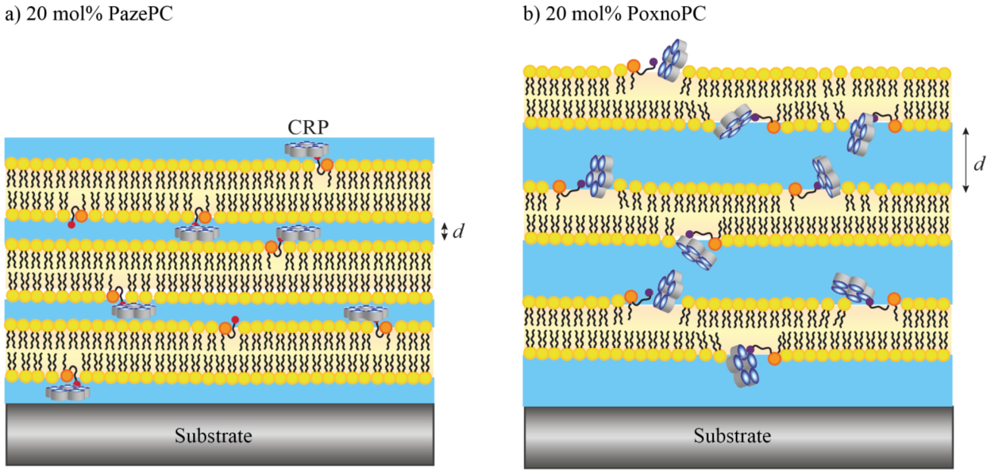

Figure 5.11 Schematic illustration of the interaction of CRP with 20 mol% of (a) PazePC or (b) PoxnoPC incorporated membrane multilayers.

Unfortunately, strong Bragg sheets were not obtained in any experiments. Thus, data analysis of mechanical properties was not possible. However, some changes in vertical structure of membrane multilayers due to CRP interaction were observed by off-specular neutron scattering which led to the assumption of a possible scenario of interaction of CRP with the multilayer stacks (Figure 5.11). These changes were found not to be CRP concentration dependent, since the lowest concentration of 0.8 µM reached already the saturation and induced comparable changes as the highest concentration of 2.9 µM.

5.1.3 Interaction of CRP with Solid-Supported Membranes

5.1.3.1 Characterization of Structural Changes of Phospholipid Membranes Induced by CRP Studied by Dual Polarization Interferometry (DPI) in Real--Time

To gain further insights into changes on structures of supported membranes caused by the incubation of CRP dual polarization interferometry (DPI) measurements were performed. Therefore, solid-supported membranes were prepared (SOPC, DPPC), which where doped with 20 mol% of OxPL (either PazePC or PoxnoPC) and the change in the phase as a function of time was detected (section 3.2.2.6). The first set of experiments was performed with SOPC as a matrix lipid, because it is in liquid phase (L_e) at room temperature (RT) (with a melting temperature of 6 °C). The second set of experiments was performed with DPPC as a matrix lipid, because it is in gel phase (L_β) at RT (with a main phase transition temperature of 42 °C). DPPC is more densely packed and exhibits an area per molecule of approximately 50 Å^2. The DPI technique yields the thickness d, the refractive index n, the change in the mass density Δm (of dry components) and the birefringence $\Delta n = n_0 - n_e$, which is the ratio between the refractive index perpendicular and parallel to the beam direction. In case of supported membranes, Δn can be used as a measure for the ordering of alkyl chains [48, 115].

Interaction of CRP with SOPC/OxPL Membranes

Figure 5.12 shows the raw phase data of (a) a pure SOPC membrane and a SOPC membrane incorporating (b) 20 mol% PazePC and (c) PoxnoPC before and after the injection of CRP.

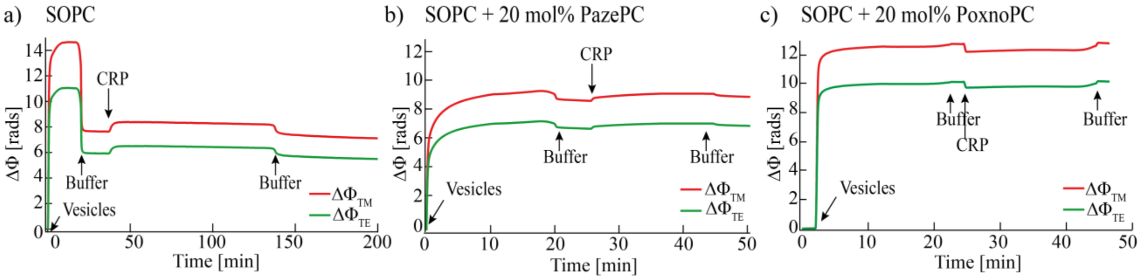

Figure 5.12 Real-time phase changes in TM and TE waveguide modes $\Delta\Phi_{\mathrm{TM}}$ (red) and $\Delta\Phi_{\mathrm{TE}}$ (green) during membrane formation of (a) pure SOPC and SOPC incorporating (b) 20 mol% PazePC and (c) 20 mol% PoxnoPC, and injection of CRP.

After rinsing with buffer the final phase level ($\Delta\phi_{\mathrm{TM}}^{\mathrm{SOPC}} \approx 8$ rads, $\Delta\phi_{\mathrm{TE}}^{\mathrm{SOPC}} \approx 6$ rads; $\Delta\phi_{\mathrm{TM}}^{\mathrm{SOPC/PazePC}} \approx 8$ rads, $\Delta\phi_{\mathrm{TE}}^{\mathrm{SOPC/PazePC}} \approx 6$ rads and $\Delta\phi_{\mathrm{TM}}^{\mathrm{SOPC/PoxnoPC}} \approx 12$ rads,

$\Delta\phi_{TE}^{SOPC/PoxnoPC} \approx 9$ rads) was lying above the original level, which suggests the formation of a supported lipid bilayer [65].

When CRP is injected, both systems SOPC and SOPC/PazePC show an increase in phase. In contrast, SOPC/PoxnoPC shows a decrease in phase during CRP injection which indicates a decrease of the refractive index (RI). After rinsing with buffer, the signal came back to the initial level. This indicates on the one hand, that the membranes remain intact even in the presence of OxPL after the interaction with CRP. On the other hand, it shows that the incubation time of 20 min or 100 min was not long enough to establish a dense CRP layer, as it was washed away by the buffer flow easily (Figure 5.12).

Interaction of CRP with DPPC/OxPL Membranes

Figure 5.13 shows the raw phase data of a DPPC membrane incorporating (a) 20 mol% PazePC and (b) 20 mol% PoxnoPC before and after the injection of CRP.

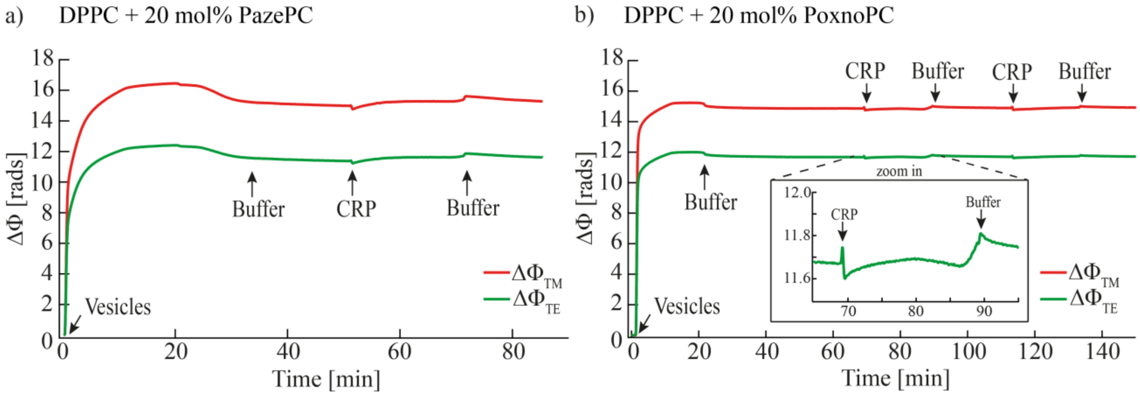

Figure 5.13 Real-time phase changes in TM and TE waveguide modes $\Delta\Phi_{TM}$ (red) and $\Delta\Phi_{TE}$ (green) during membrane formation of DPPC incorporating (a) 20 mol% PazePC and (b) 20 mol% PoxnoPC, and injection of CRP.

After rinsing with buffer the formation of the supported bilayers for both OxPL show the same increase in phase ($\Delta\phi_{TM}^{DPPC/OxPL} \approx 15$ rads, $\Delta\phi_{TE}^{DPPC/OxPL} \approx 11$ rads). When CRP is injected, the matrix lipid DPPC shows the same general trends as SOPC. In case of DPPC/PazePC there is a small increase in the phase after the protein injection, while DPPC/PoxnoPC shows a decrease during the protein injection. The relative changes of the phase after protein injection are slightly smaller than with SOPC, especially in the case of PoxnoPC. Furthermore, there are fluctuations of the phase at the beginning and at the end of the protein injection (Figure 5.13a, b inset).

Binding Model

It is reported that DPPC tends to cause phase separation when it is mixed with other phospholipids [116]. Due to the dense packing between DPPC molecules and the observed increase of phase after CRP injection, it is likely that CRP binds to the phase boundary between DPPC and OxPL. The similarity of the results between the matrix lipids DPPC and SOPC suggests that the binding of CRP to SOPC containing membranes also takes place at the phase boundary between OxPL and SOPC. In addition, it was previously reported, that the extended conformation of oxidative moieties in the acyl chain of OxPL lead to nucleation of extended lipid domains in a lipid bilayer which corresponds to a 2-D analog of a micelle and eventually results in phase separation [117]. At the point where OxPL and non-oxidized PL meet in the membrane, there is a high disorder and therefore more space for CRP to interact easily with the more accessible PL.

Although the binding mechanism between OxPL and CRP is still not well understood, it is likely that the accessibility of the OxPL play a crucial role. The MD simulations of Khandelia and Mouritsen predicted the orientation of functionalized phospholipids in the bilayer. There, the polar *sn*-acyl chain of PazePC is orientated towards the water phase, while the truncated chain of PoxnoPC points out to the hydrophobic/hydrophilic interface [13]. Furthermore, it was reported that PoxnoPC causes an intercalation of peptides into a phospholipid mono- or bilayer while PazePC did not show the same effect [114]. This leads to the explanation of the experimental results as follows (Figure 5.14):

(i) In case of **PazePC** incorporated bilayers, CRP forms a protein layer on top of the bilayer surface (Figure 5.3a).

(ii) In case of **PoxnoPC** incorporated bilayers, the protein is intercalated into the bilayer, and integrates water into the membrane and leads to an increase in the disorder (Figure 5.3b).

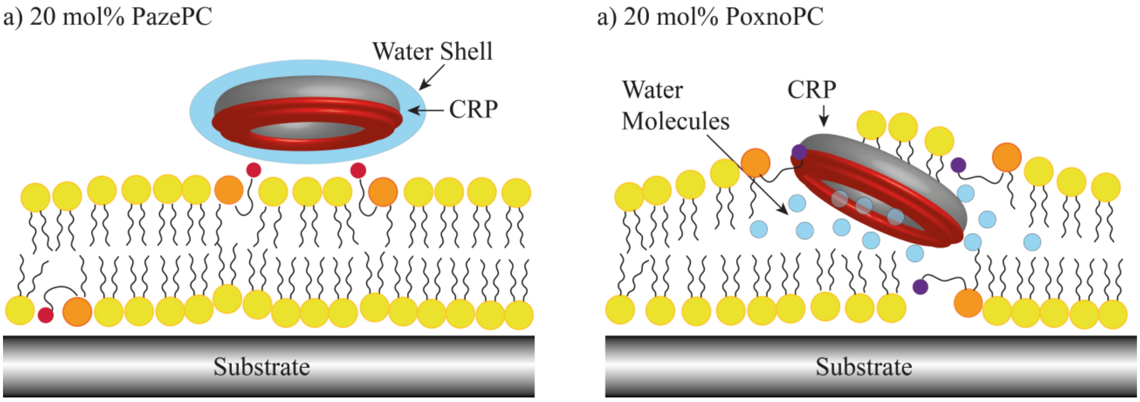

Figure 5.14 Schematic illustration of a possible binding of CRP to a phospholipid bilayer doped with 20 mol% of either (a) PazePC or (b) PoxnoPC.

Quantifying the Interaction of CRP with Solid-Supported Membranes

In this part, the binding of CRP to the lipid bilayers is characterized by parameters as thickness d, refractive index η, birefringence, density ρ and mass m of the lipid bilayer and the protein layer. Initially some assumptions and boundary limits have to be set.

(i) Dry CRP protein has (by means of Pymol) a diameter of 9.3 nm and a thickness of 3.3 nm. In aqueous environment the protein is surrounded by a water shell. Therefore, it is assumed that the hydrated protein has a thickness of 4 - 5 nm.

(ii) Depending on the coverage of the protein on the bilayer the refractive index of the protein layer can take values between 1.33 (η_{water}) and 1.46 (η_{dry}, dry protein). The relation between the measured refractive index and the volume fraction ϕ, which is a scale for the coverage, is given as:

$$\eta = \eta_{dry}\phi_{prot} + \eta_{water}(1 - \phi_{prot}) \tag{5.1}$$

The maximum of the volume fraction can reach a value of 0.70. This value corresponds to a hexagonal packing of circular disks on a surface.

The most crucial assumption is the **choice of model** for each system. In case of a bilayer functionalized with PazePC, CRP is bound on top of the bilayer. This system is regarded as a **two-slab model**. The intercalation of CRP into the PoxnoPC functionalized bilayer leads to an intercalation of water molecules and increases the disorder of the membrane. Here, the system is treated as an **one-slab model**.

Incorporation of PazePC

The **fitting procedure** for the systems doped with **PazePC** as **two-slab model** was carried out as described in the following. For the fitting of the bilayer the refractive index η of the bilayer is set as constant to 1.49 as described by Leblanc *et al.*[118] while the others parameters are fitted as free parameters. In the next step, the protein layer was fitted by setting the refractive index η of the protein layer to be free while fixing thicknesses d and birefringences at various values within a reasonable margin. Additionally, from the total refractive index of the protein layer, the volume fraction ϕ was calculated (Table 5.12).

Assuming a thickness d for CRP layer to be within the margin of 4 nm and 5 nm, the refractive index of the protein (η = 1.34) was found to be close to the refractive index of water (η_{water} = 1.33). The calculated volume fraction ϕ of 8% shows that only a small amount of CRP binds to the bilayer. This result is supported by the obtained mass and lateral density values for the CRP layer.

Table 5.12 The best fit parameters for the DPI raw data for both systems (a) SOPC and (b) DPPC incorporating 20 mol% PazePC and the binding of CRP to the bilayers assuming two different thicknesses *d* of hydrated protein (c - f). Bolt values are fixed in the fitting procedure.

Layer	*d* [Å]	η	Δm_{DPI}	$\Delta\rho$ [g/cm^3]	ϕ
a) SOPC	44	**1.49**	490	1.11	-
b) DPPC	49	**1.49**	575	1.17	-
c) CRP (SOPC)	**40**	1.34	6	0.02	8%
d) CRP (DPPC)	**40**	1.34	7	0.02	8%
e) CRP (SOPC)	**50**	1.34	6	0.01	8%
f) CRP (DPPC)	**50**	1.34	7	0.01	8%

For the effect of packing density for membranes doped with 20 mol% PazePC, it can be concluded, that the binding of CRP to the lipid bilayers is comparable for both matrix lipids SOPC and DPPC. The refractive index η, density ρ and volume fraction ϕ show almost identical results (Table 5.12), with small deviations in the mass. It can be concluded, that for CRP binding the high dense packing of DPPC does not show a different effect than SOPC, when 20 mol% PazePC is incorporated.

Incorporation of PoxnoPC

In the **fitting procedure** for the systems doped with **PoxnoPC**, the system is treated with an **one-slab model** with the protein intercalated into the membrane. The fitting procedure for the bilayer is the same as described before. For the fitting of η (CRP + bilayer), the thickness of the slab is fixed with values representing the bilayer thickness including the assumed thicknesses *d* for the hydrated CRP (in the range of *d* = 30 – 50 Å) (Table 5.13 c - f).

For the binding mechanism of CRP, the increased thickness *d* of the slab results in a decrease of the values for refractive index η, mass *m* and density ρ confirming the hypothesis that water molecules are also intercorporated into the bilayer. Possible interpretation for the higher thickness *d* is that the packing of lipid molecules becomes less and the distance between the bilayer lipids gets larger due to some disorder caused by the incorporation of CRP combined by water molecules (Figure 5.14b). This disorder is probed by the birefringence which follows the trend that the smaller the thickness *d* of the slab, the higher the birefringence. Moreover, the refractive index of the lipid bilayer is 1.49 and that of dry protein is 1.46, thus according to equation (5.1) the expected refractive index should lie between these two values. Since this is not the case, the measured refractive index of $\eta \sim 1.42$ (Table 5.13) indicates either the presence of molecules with lower refreactive index (i.e water, $\eta = 1.33$) within the membrane or the presence of a disordered membrane with defects. In contrast to the systems doped with 20 mol% PazePC, the volume fraction ϕ cannot be calculated here, because the refractive index η depends on the amount of protein, water and the bilayer lipids.

Table 5.13 The best fit parameters for the DPI raw data for both systems (a) SOPC and (b) DPPC incorporating 20 mol% PoxnoPC and the binding of CRP to the bilayers assuming different thicknesses *d* for incorporating protein into the bilayer (c - h). Bolt values are fixed in the fitting procedure.

Layer	***d* [Å]**	***η***	***Birefringence***	**Δm_{DPI}**	**$\Delta\rho$ [g/cm^3]**
a) SOPC	44	**1.49**	0.000	498	1.13
b) DPPC	49	**1.49**	0.000	872	1.17
c) CRP (SOPC)	**74**	1.42	0.004	326	0.50
d) CRP (DPPC)	**79**	1.44	0.008	395	0.57
e) CRP (SOPC)	**84**	1.41	0.002	316	0.43
f) CRP (DPPC)	**89**	1.42	0.005	397	0.50
g) CRP (SOPC)	**94**	1.40	0.001	318	0.38
h) CRP (DPPC)	**99**	1.41	0.004	399	0.48

For the effect of packing density, the solid-supported membranes of SOPC and DPPC incorporating 20 mol% PoxnoPC show significant differences for CRP binding. The SOPC system provides overall smaller values for bilayer thickness *d*, refractive index η, mass *m* and density ρ. First, the denser packing of the DPPC bilayer leads to a larger thickness *d*, mass *m* and density ρ than in the SOPC bilayer. Second, the relative change between the refractive index of bilayer and CRP + bilayer is smaller with DPPC than with SOPC. This leads to the assumption of a smaller amount of CRP intercalated into the membrane in case of DPPC. Less CRP inside the membrane implicates less incorporated water and less disorder in the membrane. The birefringence for DPPC is twice as large as for SOPC, which can be explained by the higher ordered lipids in the DPPC system which may be less affected by the protein intercalation than the less ordered system SOPC.

5.1.3.2 Characterization of Changes in Viscoelasticity of Phospholipid Membranes Induced by CRP Interaction

In order to assess the adsorption kinetics of interaction of CRP onto lipid membranes in the presence and absence of OxPL, solid-supported membranes were prepared via *in situ* vesicle fusion onto hydrophilic SiO_2-coated quartz crystals using QCM-D (for more details see section 3.2.2.8). Liposomes were composed of OPPC incorporated with 10 mol% OxPL (PoxnoPC, PazePC).

Formation of Solid-Supported Membranes

In the first step, the injection of liposomes suspension (0.2 mM) induces a decrease in the frequency and a simultaneous increase in the dissipation du to the adsorption of intact liposomes on the quartz crystal until a critical density is reached (Figure 5.15).

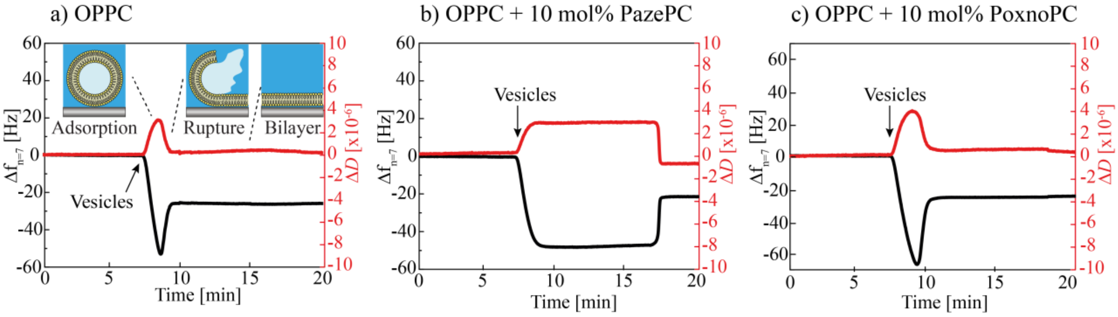

Figure 5.15 Changes in resonant frequency Δf (black) and dissipation ΔD_7 (red) monitored at 35 MHz ($n = 7$) during formation of solid-supported membranes on SiO_2 substrates of (a) pure OPPC membrane, (b) OPPC/PazePC membrane, and (c) OPPC/PoxnoPC.

The critical density of liposomes corresponds to the minimum in frequency shift (~ -53 Hz for OPPC, ~ -48 Hz for OPPC/PazePC, ~ -67 Hz for OPPC/PoxnoPC) and the maximum in dissipation (3.10×10^{-6} for OPPC, 2.73×10^{-6} OPPC/PazePC, -0.63×10^{-6} OPPC/PoxnoPC) caused by maximal liposome adsorption. Once a critical surface density is reached, the fusion of liposomes by formation of planar membranes could be detected by an increase in Δf_7 and a decrease in ΔD_7, due to the release of the intravesicular water. Finally, both Δf_7 and ΔD_7 reach saturation levels at $\Delta f_7 \sim -24 \pm 3$ Hz and $\Delta D \sim 0.06 \times 10^{-6}$ upon rinsing with buffer (Table 5.14), demonstrating the formation of a stable solid-supported membrane [119].

The incorporation of OxPL into OPPC liposomes alters significantly their rupture process compared to pure OPPC. The incorporation of 10 mol% PazePC results in a maximal change resonance frequency Δf_{max} ($\Delta f_{max} = -48$ Hz) which is comparable to pure OPPC. In contrast, in case of the matrix lipid POPC, it was reprted by A. Makky *et al.* that the liposomes containing OxPL were able to rupture at lower surface coverage [102]. During liposome injection this maximal change resonance frequency and thus the surface coverage were stayed constant for 10 min until the liposome ruptured. This might be caused by the contained Ca^{2+} ions in the buffer, which screens the repulsive interaction between the negatively charged PazePC lipids. The slight negative dissipation for the POPC/PazePC bilayer is most likely due to a baseline shift. OPPC/PoxnoPC liposomes show the highest maximal change resonance frequency Δf_{max} (Δf_{max} = -67 Hz) and maximal dissipation during liposome injection. Nevertheless, the resonant frequency values after the membrane formation were comparable in the presence and absence of OxPL.

Table 5.14 Maximal change in resonant frequency Δf_{max}, the difference in frequency Δf_{mem} and energy dissipation ΔD_{mem} before and after membrane formation monitored by QCM-D.

Liposome Composition	**Δf_{max} [Hz]**	**Δf_{mem} [Hz]**	**ΔD_{mem} [$\times 10^{-6}$]**
OPPC	-53.7	-26.3	0.27
+ PazePC 10 mol%	-48.1	-21.3	-0.63
+ PoxnoPC 10 mol%	-67.3	-25.8	0.55

The Interaction of CRP with Solid-Supported Membranes

In the second step, CRP was injected (c = 50 µg/ml) for 5 min onto the solid-supported membranes, followed by 20 min of incubation time (Figure 5.16) in order to monitor the interaction kinetics of CRP with the membrane. However, a binding of CRP was not detected neither in the presence nor in the absence of OxPL as there was no remarkable change in both Δf_7 ($\Delta f_{change} < 2$ Hz) and ΔD_7 observed.

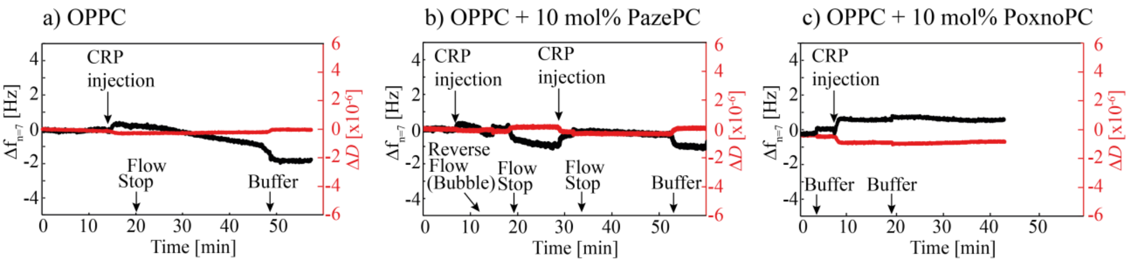

Figure 5.16 Changes in resonant frequency Δf_7 (black) and dissipation ΔD_7 (red) monitored at 35 MHz ($n = 7$) during the injection of CRP onto (a) pure OPPC membrane, (b) OPPC/PazePC membrane, and (c) OPPC/PoxnoPC. For none of the membranes, a binding of CRP was detected.

The results indicated that the membranes remain intact after the addition of CRP solution. However, the incubation time of 20 min or 40 min was not sufficient enough to establish a detectable and stable CRP layer, as it could be washed away by the buffer flow easily (Figure 5.16b).

5.1.3.3 Characterization of Changes in Fine-Structures of Solid-Supported Membranes Induced by CRP

The study of interaction of CRP with solid-supported membranes was extended towards analysis of the fine-structural changes upon CRP injection using high-energy specular X-ray reflectivity (XRR) at a high energy (17.48 keV) (section 3.2.2.3). There, solid-supported membranes incorporated with 20 mol% OxPL were prepared to investigate the differences of interaction with CRP.

CRP Interaction with PazePC Incorporated Membrane

Figure 5.17 displays the XRR experimental data of supported membranes of an SOPC membrane doped with 20 mol% PazePC before (black) and after (red) the incubation with CRP, together with the best fit results to the experimental results (solid lines) and the reconstructed scattering length density (*SLD*) profile (inset). The fitting of the curves was accomplished with a 5-slab model, with the slabs representing outer head groups, alkyl chains, inner head groups, water reservoir, and SiO_2, respectively.

The interaction of CRP with the membrane doped with 20 mol% PazePC leads to an increase in scattering length density (*SLD*) at the outer head groups and an increase in roughness in both, alkyl chains and outer head groups (Table 5.15).

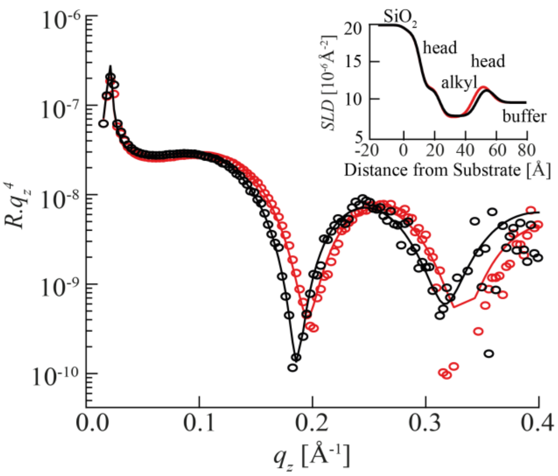

Figure 5.17 XRR results of a SOPC + 20 mol% PazePC membrane in the absence (black) and presence (red) of 145 µM CRP. The solid lines represent the best model fits to the data. The scattering length density (*SLD*) profiles corresponding to the best fit results are presented in the insets.

Table 5.15 The best fit parameters ($\chi^2 \leq 0.05$) from the XRR results of SOPC + 20 mol% PazePC membrane in the absence and presence of CRP.

	Without CRP			**With CRP**		
SOPC	*d* [Å]	*SLD* [10^{-6} Å^{-2}]	*σ* [Å]	*d* [Å]	*SLD* [10^{-6} Å^{-2}]	*σ* [Å]
Outer headgroup	11.2	11.5	4.1	10.4	12.5	4.6
Alkyl chain	24.1	7.7	3.9	22.2	7.6	4.8
Inner headgroup	9.3	11.5	3.3	9.3	11.5	3.2
Water	3.1	9.5	3.5	3.1	9.5	3.4
SiO_2	10.0	18.7	3.2	10.1	18.6	3.2

CRP Interaction with PoxnoPC Incorporated Membrane

Figure 5.18 shows the XRR experimental data of POPC supported membranes doped with 20 mol% PoxnoPC before (black) and after (red) the incubation with 145 µM CRP for 2 h at 37 °C, together with the best fit results to the experimental results (solid lines). The scattering length density profile (inset) shows a modification in the alkyl chain region after the incubation with CRP. The modifications on the *SLD* profiles before and after addition of CRP are more pronounced than for the PazePC incorporated membrane. The experimental errors are within the symbol size. The fitting of the curves was accomplished with a 5-slab model, with the slabs representing outer head groups, alkyl chains, inner head groups, water reservoir, and SiO_2, respectively.

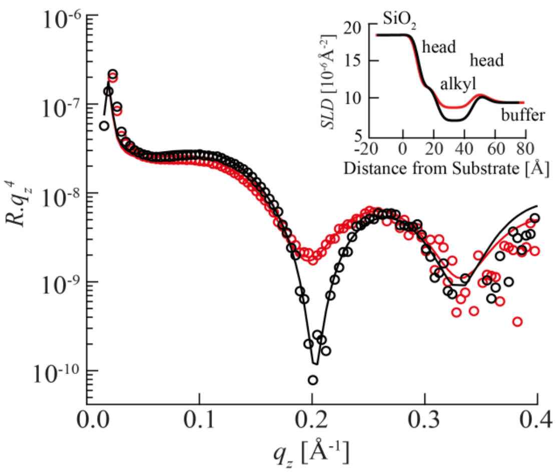

Figure 5.18 XRR results of a POPC + 20 mol% PoxnoPC membrane in the absence (black) and presence (red) of 145 µM CRP together with the best fit (solid line). The scattering length density (*SLD*) profiles corresponding to the best fit results are presented in the insets.

Table 5.16 The best fit parameters ($\chi^2 \leq 0.09$) for the XRR results for a POPC + 20 mol% PoxnoPC membrane in the absence and presence of CRP.

	Without CRP			**With CRP**		
POPC	*d* [Å]	*SLD* [10^{-6} Å^{-2}]	*σ* [Å]	*d* [Å]	*SLD* [10^{-6} Å^{-2}]	*σ* [Å]
Outer headgroup	9.5	10.6	4.1	9.8	11.0	5.9
Alkyl chain	23.4	7.0	3.7	23.9	8.8	3.8
Inner headgroup	8.4	12.0	3.5	8.4	11.9	3.5
Water	3.1	9.5	3.4	3.1	9.5	3.4
SiO_2	10.0	18.7	3.2	10.1	18.6	3.2

The global shape of curves indicates, upon CRP incubation there are no shift of the minima towards smaller q_z values. This means that the total thickness of the system remained unchanged. Thus, an additional dense CRP layer can be excluded. These results lead to the conclusion, that CRP changes the structure of the existing POPC/PoxnoPC membrane by either incorporation or by the formation of a very loose CRP layer. In addition, these results demonstrate that CRP does not destroy the structural integrity of membranes but just forms small defects by incorporation which can be seen in the increased roughness of the outer headgroup region.

5.1.4 Interaction of CRP with Phopholipid Monolayers

5.1.4.1 Concept of Complex Phospholipid Compositions

As reported by Volanakis, lysophosphatidylcholine (LPC) is by far the most effective surfactant in promoting the binding of CRP to PC liposomes[108]. To mimic the system of Volanakis, Soja-LPC (Lipoid S LPC80) was investigated as a mixture with Soja-PC (Lipoid S100) and further mixed with 20 mol% POPC or PazePC. In addition, it was reported by Ji *et al*. that CRP binds to low density lipoproteins (LDL), which have a free cholesterol ratio of 9% - 48% (depending on the LDL used)[120]. Therefore, lipid mixtures were incorporated with 20 mol% cholesterol. Table 5.17 gives an overview of the used monolayer compositions.

Table 5.17 Overview of the two lipid systems POPC (left) and PazePC (right), incorporated with 20 mol% of LPC and cholesterol used for the monolayer study of CRP interaction.

PC: LPC (soja) (4:1)	PC: LPC (soja) (5:1)
Pure POPC	Pure PazePC
POPC + 20 mol% LPC	PazePC + 20 mol% LPC
POPC + 20 mol% cholesterol	PazePC + 20 mol% cholesterol
POPC + 20 mol% cholesterol + 20 mol% LPC	POPC + 20 mol% cholesterol + 20 mol% LPC

The lipid systems were investigated by surface pressure measurements. Surface pressure measurements were performed to study the adsorption of protein into lipid monolayers (section 3.2.2.1). Since the lateral pressure of physiological membrane is about 30 mN/m, the experiments were investigated at a surface tension of 15 – 20 mN/m. After a stable monolayer was formed, 180 nM of CRP were injected into the subphase and the change in surface pressure was monitored with time.

5.1.4.2 Characteristics of Complex Phopholipid Systems

Figure 5.19 shows the surface pressure measurements of (a) the POPC system and (b) PazePC system. In both cases, the incorporation of 20 mol% cholesterol slightly decreased the average area per molecule. In contrast, additional 20 mol% LPC into the lipid mixtures resulted in a very large change in the average area per molecule. However, the collapse pressure and the overall shape of the isotherms did not change significantly.

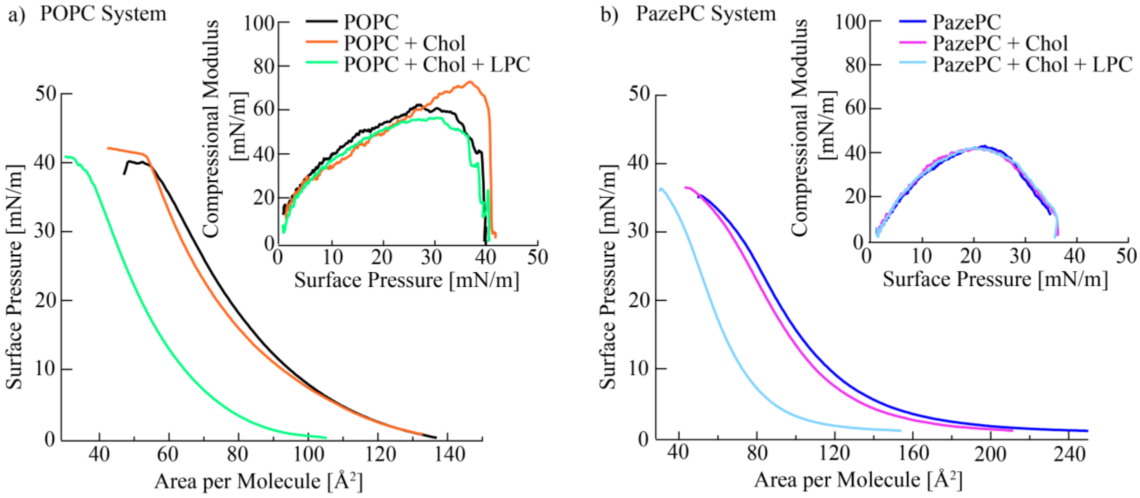

Figure 5.19 Pressure-Area (π-A) isotherms of (a) POPC (black) and (b) PazePC (dark blue) incorporated with 20 mol% of cholesterol (orange, pink) and 20 mol% of each cholesterol and LPC (green, light blue), respectively together with the compressional modulus as insets.

5.1.4.3 Characterization of CRP Adsorption Strength to Phopholipid Monolayers Studied by Surface Tension

In this section surface tension measurements were performed with lipid monolayers represented in Table 5.17 and injected CRP. The data is represented in terms of surface pressure over time.

LPC/PC System

At first the systems LPC/PC (soja) (1:4) and LPC/PC (soja) (1:5) were investigated. Unfortunately, both monolayer compositions were not stable and therefore not suitable for the study of CRP interaction (data not shown). Therefore, in the second step Soja-LPC was used just in a 20 mol% doping ratio with POPC or PazePC.

POPC System

Figure 5.20 shows the surface tension results as a change in surface pressure over time for the different POPC systems with CRP injection which were measured at initial surface pressures of $\pi \sim 15$ mN/m (a, b) and $\pi \sim 20$ mN/m (c, d). These results indicate that CRP does not interact with the pure POPC monolayer but shows small insertion into the POPC monolayers incorporated with 20 mol% of LPC, where an increase of $\Delta\pi \sim 2$ mN/m after 85 min is observed for both initial surface pressures of 15 mN/m and 20 mN/m (Figure 5.20b). The system POPC + 20 mol% cholesterol showed also an increase of surface pressure of $\Delta\pi \sim 2$ mN/m after 80 min of CRP injection (Figure 5.20c).

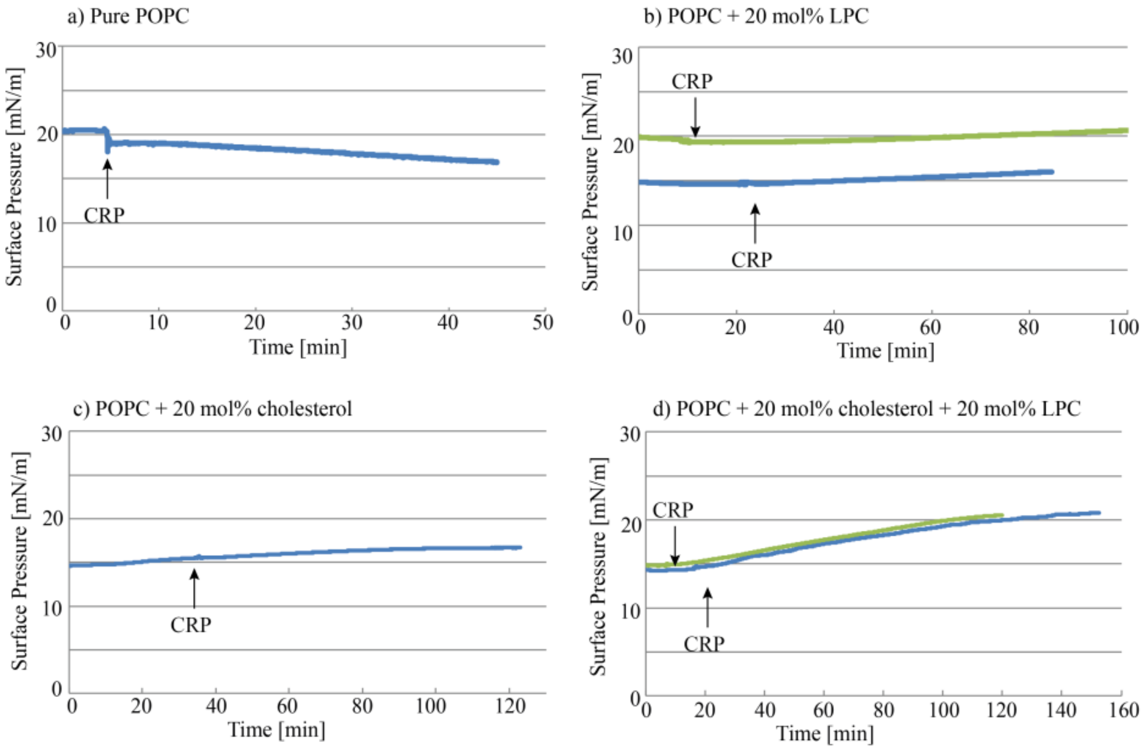

Figure 5.20 Surface pressure measurements of injected CRP under (a) pure POPC, (b) POPC + 20 mol% LPC, (c) POPC+ 20 mol% cholesterol and (d) POPC + 20 mol% cholesterol + 20 mol% LPC monolayer.

However, POPC incorporated with 20 mol% of both cholesterol and LPC showed the highest adsorption of CRP into the lipid monolayer, where the surface pressure increased by $\Delta\pi \sim 5$ mN/m after 80 min. This tendency showed high reproducibility (Figure 5.20 d, blue and green). Here, the addition of cholesterol and LPC surfactant changed the monolayer structure which made the phosphocholine (PC) group to be more accessible for CRP binding.

PazePC System

Figure 5.21 represents the surface pressure results for the PazePC system with CRP where the starting of CRP injection is indicated by arrows. The initial surface pressure of the monolayers was $\pi \sim 15$ mN/m. The used systems showed no increase in surface pressure, but a continuous decrease of surface pressure indicating that PazePC monolayers with and without doping of either LPC or cholesterol are unstable with time. It is likely, that CRP interaction with these systems facilted micelles formation that dissolved into the bulk phase.

In addition a long term measurement (over 12 h) was performed with a higher final concentration of CRP (800 nM) injected underneath PazePC + 35% LPC monolayer (not shown here). Even though, it was not possible to detect any increase in surface pressure after CRP injection.

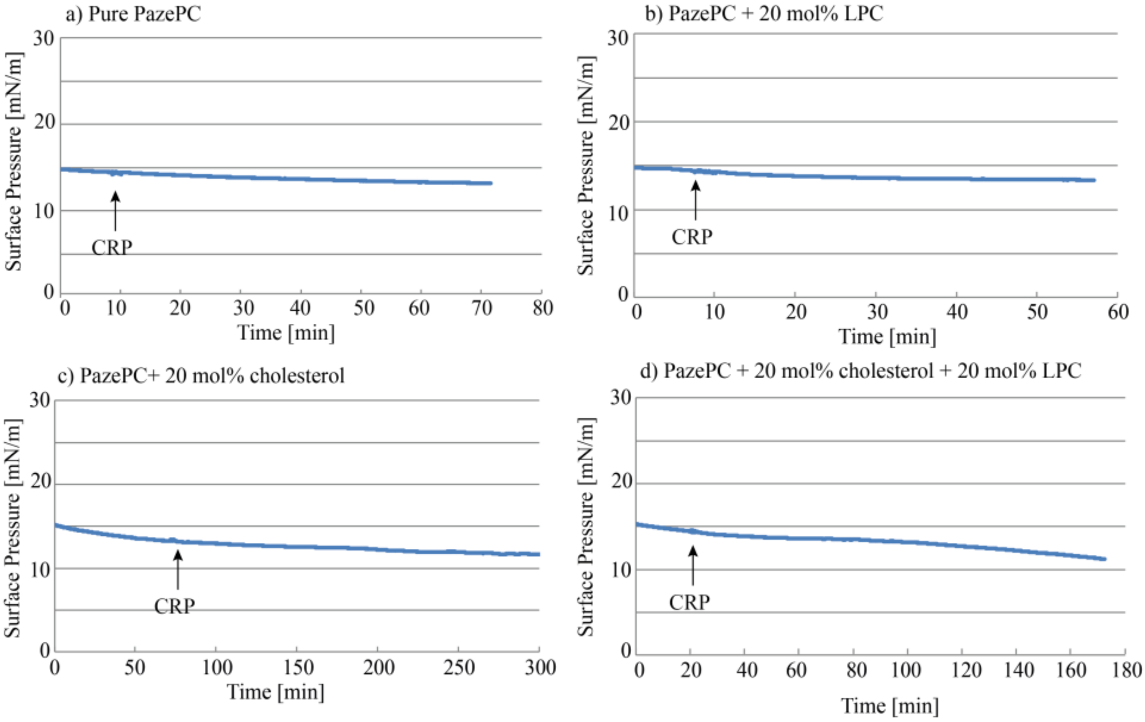

Figure 5.21 Surface pressure measurements of injected CRP under (a) pure PazePC, (b) PazePC + 20 mol% LPC, (c) PazePC+ 20 mol% cholesterol and (d) PazePC + 20 mol% cholesterol + 20 mol% LPC monolayer.

5.1.4.4 Characterization of Changes in Fine-Structures of Phospholipid Monolayers Induced by CRP

Based on the surface pressure measurements in the previous section, specular X-ray reflectivity (XRR) experiments were accordingly planned and performed at the ID10 (Grenoble) (see section 3.2.2.2 for more details). First, the most promising system POPC incorporated with 20 mol% cholesterol and LPC and its interaction with CRP was studied. In the second step, 20 mol% OxPL were incorporated instead of cholesterol to see the effect of OxPLs on the interaction with CRP (180 nM). At the end, the effect of Ca^{2+} onto the binding of CRP with pure PazePC on K^+-buffer and CRP-buffer was studied.

CRP Interaction with LPC Incorporated Systems

Figure 5.22 shows the XRR curves for POPC + 20 mol% cholesterol + 20 mol% LPC (purple), POPC + 20 mol% PazePC + 20 mol% LPC (green) and POPC + 20 mol% PoxnoPC + 20 mol% LPC (orange) together with POPC (black) monolayers used in this study together with the best fit (red). The reconstructed electron density (ρ) profiles along the *z*-axis are also shown in Figure 5.22 (right). The thickness *d*, electron density ρ, and root mean square (rms) roughness σ of each interface are summarized in Table 5.18.

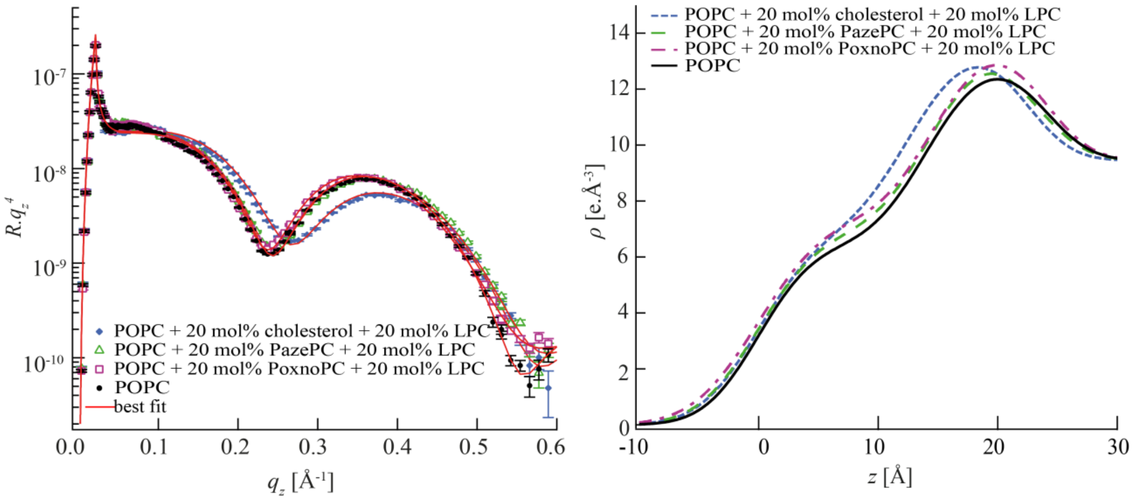

Figure 5.22 XRR curves for POPC + 20 mol% cholesterol + 20 mol% LPC (purple), POPC + 20 mol% PazePC + 20 mol% LPC (green) and POPC + 20 mol% PoxnoPC + 20 mol% LPC (orange) together with POPC (black) on CRP-buffer together with the best fits to the experimental results (solid red line) and the reconstructed electron density profiles along the *z*-axis (perpendicular to the interface).

Table 5.18 Thickness d, electron density ρ, and roughness σ corresponding to best fits of the XRR of POPC monolayers incorporated with 20 mol% LPC, and 20 mol% of either cholesterol or OxPL (PazePC or PoxnoPC).

POPC			
	d [Å]	ρ [e × Å^{-3}]	σ [Å]
Hydrocarbon chain	14.3	0.252	3.8
Choline head	9.9	0.482	3.6
Buffer	∞	0.335	3.2
POPC + 20 mol% cholesterol + 20 mol% LPC			
	d [Å]	ρ [e × Å^{-3}]	σ [Å]
Hydrocarbon chain	12.6	0.242	3.9
Choline head	9.7	0.490	3.9
Buffer	∞	0.335	3.2
POPC + 20 mol% PazePC + 20 mol% LPC			
	d [Å]	ρ [e × Å^{-3}]	σ [Å]
Hydrocarbon chain	14.3	0.246	3.9
Choline head	8.9	0.489	3.7
Buffer	∞	0.335	3.3
POPC + 20 mol% PoxnoPC + 20 mol% LPC			
	d [Å]	ρ [e × Å^{-3}]	σ [Å]
Hydrocarbon chain	14.4	0.258	4.3
Choline head	9.5	0.478	3.5
Buffer	∞	0.335	3.2

It can be concluded from the XRR results, that on the one hand the incorporation of 20 mol% OxPL and LPC does not change the POPC monolayer structural properties significantly. On the other hand, the incorporation of 20 mol% cholesterol, results in a slightly decreased thickness in hydrocarbon chains.

In the second step, CRP was injected into the subphase underneath POPC monolayers incorporated with 20 mol% LPC and either cholesterol or OxPL and incubated for 3 h. Figure 5.23 shows the results for POPC incorporated with (a) cholesterol/LPC and (b) PoxnoPC/LPC monolayers before (black) and after (green) injection of CRP. Unfortunately, no data could be obtained for POPC/PazePC/LPC monolayers due to the misalignment during the measurement.

a) POPC + 20 mol% cholesterol+ 20 mol% LPC

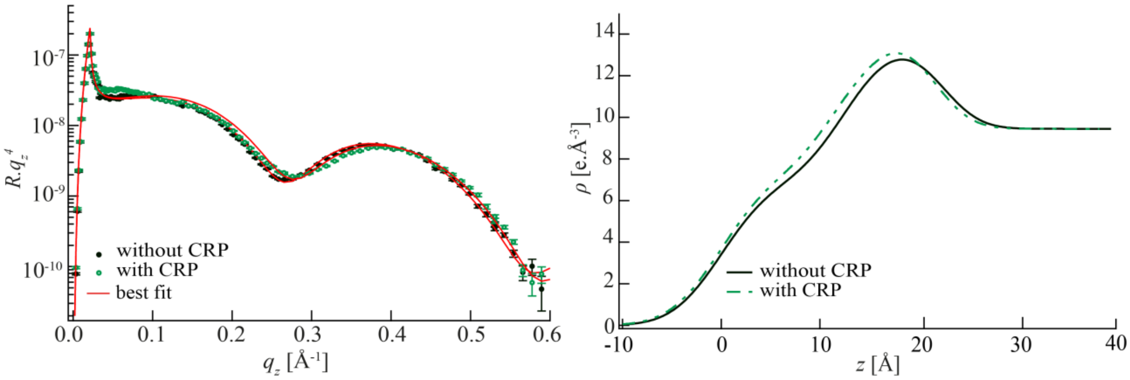

b) POPC + 20 mol% Poxno + 20 mol% LPC

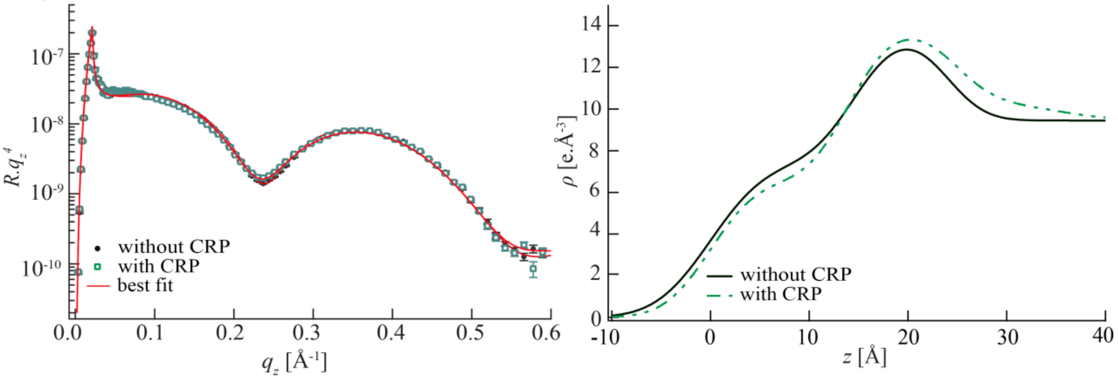

Figure 5.23 XRR curves (left) for POPC systems incorporated with 20 mol% LPC and either (a) 20 mol% cholesterol or (b) 20 mol% PoxnoPC, before (black) and after CRP injection (green) on CRP-buffer together with the best fits to the experimental results (solid red line) and the reconstructed electron density profiles along the *z*-axis (perpendicular to the interface) (right).

The XRR results lead to the conclusion, that the CRP injection does not significantly change the fine-structures of these phospholipid monolayers. Moreover, the GIXF experiments agree well with the XRR experiments as no enhancement of sulfur at the air-water interface could be detected (data not shown here).

Interaction of CRP with PazePC on different Buffers

As reported before by Volanakis [121], CRP binding to PC is Ca^{2+}-dependent. The interaction of CRP with pure PazePC on K^+ containing buffer and Ca^{2+} containing buffer was studied in order to probe the effect of Ca^{2+} on the binding. Figure 5.24 shows the comparison of XRR results of PazePC with CRP on (a) K^+ containing buffer and on (b) Ca^{2+} containing buffer before (black) and after the injection of CRP during 2 h.

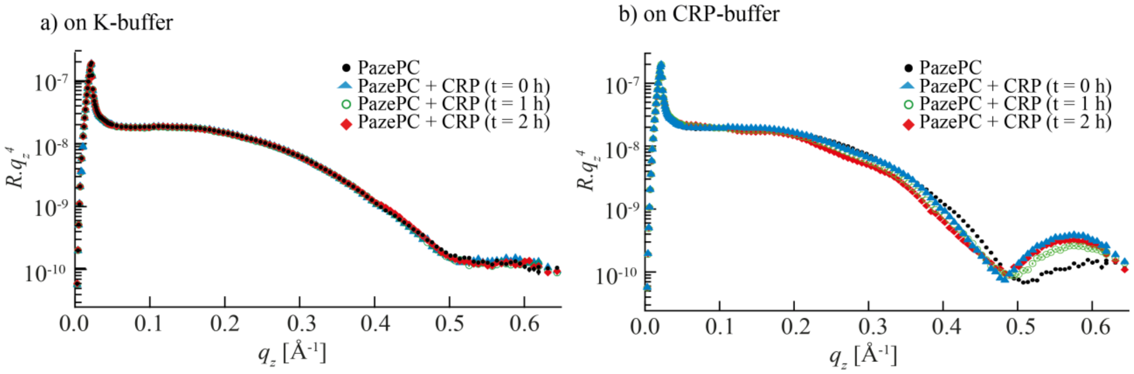

Figure 5.24 XRR results of PazePC before (black) and after CRP injection on (a) K^+ containing buffer and (b) Ca^{2+} containing buffer for different time points.

On the one hand, on K^+-buffer there is no significant change in fine-structures after CRP injection even after 2 h of incubation. On the other hand, on Ca^{2+} containing buffer, the thickness of the monolayer is increased just right after the injection of CRP solution (~ 10 min), which is seen by the shift of the minima to lower q_z values.

Table 5.19 Thickness d, electron density ρ, and roughness σ corresponding to best fits of the XRR of PazePC monolayers before and after CRP injection (1 h) on Ca^{2+} containing buffer. After CRP injection the best fitting results were obtained assuming a 3-slab model with an additional protein layer.

	Without CRP			**With CRP**		
PazePC	d [Å]	ρ [e x Å^{-3}]	σ [Å]	d [Å]	ρ [e x Å^{-3}]	σ [Å]
Hydrocarbon chain	6.3	0.250	3.5	6.4	0.256	3.5
Choline head	6.2	0.455	3.5	6.4	0.457	4.4
CRP layer	-	-	-	**37.8**	**0.345**	**3.5**
Buffer	∞	0.335	3.2	∞	0.335	3.2

The data with injected CRP was fitted with an additional slab accounting for a protein layer. This layer shows a thickness of $d_{CRP} = 38$ Å and leads to an increase in choline head roughness by $\Delta\sigma \sim 1$ Å underlying the assumed binding model of an additional protein layer on top of the lipid monolayer. The thickness of hydrated protein fits well to the thickness obtained by dual polarization interferometry study (see section 5.1.3.1). However, the low electron density ρ can be attributed to a less dense layer of CRP and suggests therefore that the lipid monolayer is not fully covered with CRP proteins.

5.1.5 Summary

In this section the interaction of CRP with membrane models incoprporated either with LPC, cholesterol or OxPL were investigated using (i) **liposomes** with DLS and ITC, (ii) **solid-supported planar bilayers** with DPI, QCM-D and XRR, (iii) **phospholipid monolayers** with surface tension and XRR measurements and (iv) **membrane mulitlayers** with off-specular neutron scattering.

A difference in adsorption and thus the interaction strength of CRP with POPC liposomes with or without the incorporation of 20 mol% OxPL was monitored by DLS and ITC using liposomes as model for cell membranes study. At 0.5 µM CRP concentration only liposomes incorporated with PazePC showed affinity to CRP after 90 min. The ITC results revealed that the enthalpy change was higher in case of PazePC ($\Delta H_{\mathrm{PazePC}}$ = -73.7 kcal/mol) incorporated liposomes than for PoxnoPC ($\Delta H_{\mathrm{PoxnoPC}}$ = -57.4 kcal/mol) or pure POPC (ΔH_{POPC} = -41.5 kcal/mol). Thus, the liposome model studies suggest an interaction strength following the trend: PazePC > PoxnoPC > POPC.

A significant difference in binding mechanism of CRP with membranes (POPC, SOPC or DPPC) incorporated with 20 mol% PazePC or PoxnoPC was suggested by off-specular neutron scattering and DPI measurements. The increase in lamellar spacing d was more pronounced for PoxnoPC (~ 21 Å) than for PazePC (~ 6 Å), which led to the assumption that in case of PoxnoPC, CRP intercalates into the membrane leading to disordered bilayers with the integration of water molecules (hydration of CRP) into the membrane. In contrast, in case of PazePC, CRP adsorbed parallel to the membrane surface via additional electrostatic interactions between the negatively charged carboxylate group and positively residues of CRP.

In addition, the effect of packing density of both matrix lipids (SOPC, DPPC) on CRP binding was studied by DPI. In case of PazePC, the highly dense packing of DPPC did not play a significant role for CRP binding and showed comparable results to the SOPC membrane. In case of PoxnoPC, the relative change of the DPPC bilayer before and after the incubation of CRP was smaller than of SOPC bilayer, leading to the conclusion that in case of DPPC a smaller amount of CRP intercalated into the membrane.

QCM-D was not able to detect CRP binding to the supported membranes incorporated with 10 mol% OxPL.

With High Energy Specular X-ray Reflectivity (XRR) the fine structures of membranes incorporated with 20 mol% OxPL were probed before and after incubation with CRP. For PoxnoPC, an increase in electron density in the alkyl chains by 1.8 10^{-6} Å^{-2} and an increase in roughness of the outer head groups by 1.8 Å was detected, supporting the hypothesis of CRP intercalation into the lipid membrane. In case of incorporation of PazePC into the lipid membrane, the interaction with CRP led to an increase of *SLD* at the outer head group underlining the proposed mechanism of a loose CRP layer on the lipid membrane surface.

In the monolayer study the surface tension results reveal, that the POPC system doped with both 20 mol% lysophosphatidylcholine (LPC) and 20 mol% cholesterol showed the strongest interaction with CRP, where an increase of surface pressure of $\Delta\pi \sim 5$ mN/m could be detected after 90 min. Here, cholesterol and the surfactant LPC disturb the monolayer structure, which is a requirement for CRP interaction (i.e PCs are more accessable by CRP). The isotherms revealed that LPC show a higher influence on the molecular packing than cholesterol. It is noteworthy that none of the PazePC monolayers showed an interaction with CRP. The addition of cholesterol and LPC here, most probably destabilize the PazePC monolayer.

The XRR study of lipid monolayers (i) revealed differences in the fine structure of POPC incorporated with 20 mol% LPC and 20 mol% either of cholesterol or OxPL, (ii) probed the interaction of these model membranes with CRP, as well as (iii) probed the Ca^{2+}-dependent interaction. The incorporation of cholesterol led to a slightly decrease in the thickness of hydrocarbon chains of the lipid monolayers. However, none of the model membranes incorporated with LPC showed a significant change in fine-structures before and after CRP injection. In contrast, the monolayer of pure PazePC showed an additional protein layer with a thickness of $d_{\text{CRP}} = 38$ Å after CRP injection in the presence of Ca^{2+} ions, while in the absence of Ca^{2+} ions (only K^+ containing buffer) no significant changes in fine-structures were detected.

5.2 EO6 Monoclonal Antibody

EO6 is an antibody raised against the PC head group of oxidized low density lipoproteins (OxLDL). OxLDL are ligands for both, EO6 and CRP, and located on epitopes on the surface of apoptotic cells *in vivo* [122]. Previous studies demonstrated that CRP co-localizes with the EO6 epitope in human artherosclerotic lesions [107]. Here, EO6 acts as host defense against the proinflammatory and proatherogenic effects of oxidized lipoproteins. Witztum *et al.* developed the EO6 antibody from murine IgM anti-OxLDL autoantibodies from the spleens of hypercholesterolemic apolipoprotein E-deficient mice. EO6 is structurally and functionally identical to classic T15 anti-PC antibodies that are of B-1 cell origin and are reported to provide optimal protection from virulent pneumococcal infection [123]. As innate host defense, both proteins CRP and EO6 share many common configurational domains of PC. However, PC epitopes do not show an absolute immunological identity as both proteins only compete for 60% in binding to OxLDL [20].

In the following section, the interaction of EO6 monoclonal antibody and OxPL was investigated with the use of both, cell model systems and *in vitro* model systems using surface sensitive techniques such as fluorescence microscopy, QCM-D and surface tension measurements. Especially the host defense action of EO6 against proinflammatory and proatherogenic effects of OxPL is of interest for this study. Therefore, the presence of OxPL in blebs of apoptotic cells was studied using an *in vitro* model of a cell surface, which induced apoptosis by the CD95-Ligand (CD95L).

5.2.1 Study of the Specific Binding of EO6 to OxPL by Immunofluorescence Microscopy of *In Vitro* Model Systems of EO6 with Apoptotic Cells

A supported phospholipid membrane functionalized with CD95-Ligand (CD95L) at a defined lateral density was utilized as *in vitro* model of a cell surface in order to induce apoptosis in cells from glioblastoma multiforme (GBM), which is a malignant primary brain tumor (see section 3.2.2.9). The advantage of the use of supported cell model membranes is to regulate the intermolecular CD95L distance within nm accuracy by the doping ratio of biotinylated lipid anchors. The percentage of DOPE-biotin lipids in the mixture of lipids corresponds to the indicated average lateral distance of CD95L and is given as:

$$< d > = \sqrt{\frac{A_{lipid}}{\chi}},$$

where A_{lipid} is the area of a lipid and χ is the molar fraction of used DOPE-biotin. Previous findings by T. Kaindl, M. Teodorczyk and C. Monzel (Prof. Tanaka group, unpublishes results) demonstrated that the number of cells entering the pathway of apoptosis is a matter of CD95/CD95L density. The apoptotic rates for different cell types (GBM, Pan) are the highest for a specific intermolecular distance of CD95L of 11 nm (χ = 0.5 mol% DOPE-biotin) which was also used in this study. At this optimal distance apoptosis is induced on the single cell level (2D) whereas proliferation is promoted in multilevel cultures (3D) and also *in vivo*.

The progression of cell apoptosis is accompanied with the presence of OxLDL on the cell surface. For example, Chang *et al.* reported the presence of oxidatively modified moieties on the surface of apoptotic cells, which are structurally analogous to moieties on the surface of OxLDL. Moreover, EO6 binds to apoptotic blebs on apoptotic cells [20].

The aim of the study was (1) to detect the interaction of EO6 with apoptotic cells at different stages of apoptosis by fluorescent confocal microscopy and (2) to assess the distribution of OxPL on the cell membrane of apoptotic cells.

For this purpose, solid-supported functionalized with CD95L membranes were prepared (see 3.2.2.9) (Figure 5.25) to induce apoptosis on the patients' cancer cells (GBM). The cells were fixed and stained at different time points in order to detect the binding of EO6 to the cells at different apoptotic stages by confocal fluorescence microscopy.

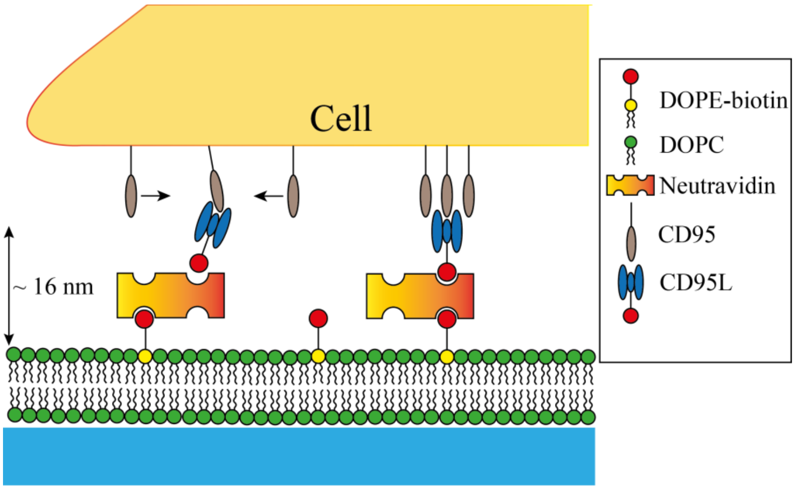

Figure 5.25 Quantitative *in vitro* model system consisting of the supported lipid membrane. The membrane surface is functionalized with CD95L via a biotin/neutravidin linker.

In the first step, the progression of apoptosis was followed by phase contrast microscopy after seeding the living cells onto the *in vitro* model in order to calculate the time-dependent change of fraction of apoptotic cells (Table 5.20). Blebbing and fragmentation of nucleus which can be seen by eye are characteristic signs for cell apoptosis. Cells having blebs or a fragmentation of nucleus, were considered to be apoptotic (Figure 5.26).

Table 5.20 Ratio of apoptotic cells (different cell lines) on supported membranes over time.

Cell line	Time [min]	Ratio of apoptotic cells
GBM10	30	57%
GBM39	30	68%
GBM60	30	73%
GBM10	80	67%
GBM39	100	90%
GBM60	120	89%

It is noteworthy that, after 30 min of cell seeding onto the *in vitro* model more than 50% of the cells were apoptotic in all cell lines. Furthermore, there was a clear increase in the number of apoptotic cells with time and a ratio of approximately 90% was reached after 100 min.

In order to get a more detailed view on (1) the quality of cell probe, and (2) on the early apoptotic state, in the following experiments, data were collected from (1) viable (non-apoptotic) cells on supported planar bilayer without DOPE-biotin (as a negative control), and (2) cells after 15 min of deposition.

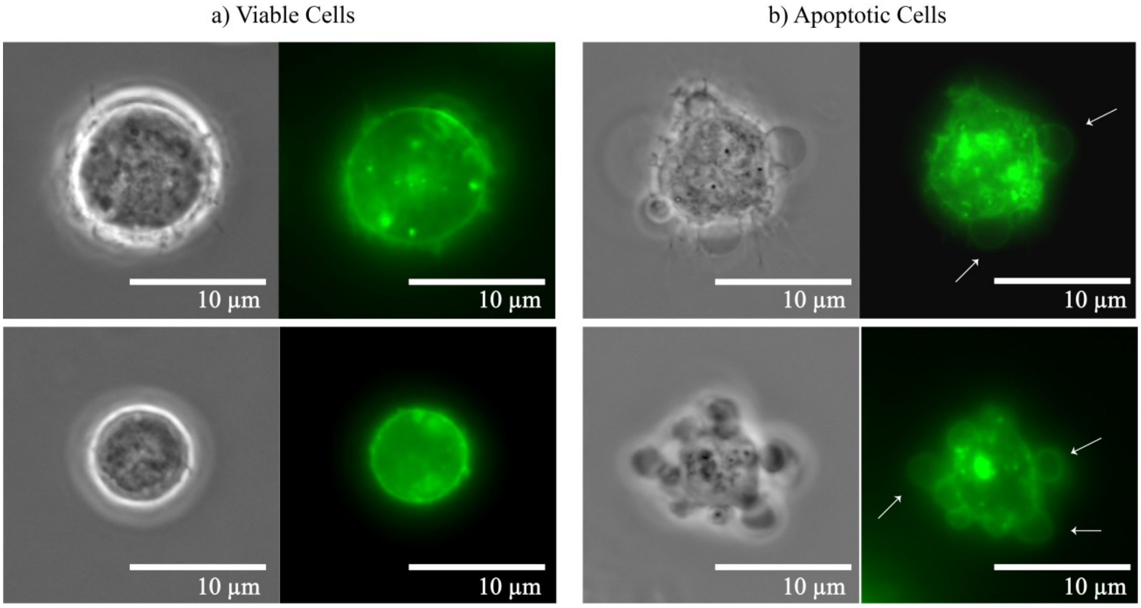

Figure 5.26 Phase contrast images together with images of PKH 67 stained (green) GBM10 cells which are (a) viable and (b) apoptotic (Zeiss, 63 x oil objective). The blebs on the surface of the apoptotic cells are marked with an arrow.

In the second step, the cells were fixed with a 4% PFA solution at given time-points and stained with a secondary antibody (anti-mouse IgG-TRITC) for visualization of bound EO6 and Hoechst dye for visualization of the cell nucleus, followed by a treat with mowiol® to ensure a stable fluorescence. Here, *z*-stacks (which means cross section pictures of the cell in *z* direction) of the fluorescence cells were measured with a confocal microscope in the Nikon imaging center. In Figure 5.27 images of three GBM10 cells in the equatorial plain after 50 min are shown. Here, the nuclei were stained with the Hoechst dye (Figure 5.27a, blue), the binding of EO6 to the cells was visualized with a TRITC conjugated second antibody (Figure 5.27b, red) and the bright-field images (Figure 5.27c) show the blebbing on the surface of the cells. In these images all three cells are in (early) apoptotic stages, because they have blebs on the surface and show hints of fragmentation of the nuclei (Figure 5.27a, Cell 2). From the fluorescence images (Figure 5.27b, red) due to the visible red rim of the cells, it can be assumed that EO6 binds to the surface of the apoptotic cells. Moreover, this rim is not homogenous in terms of fluorescent intensities which indicates that EO6 binds in a punctuate pattern. These results are in good agreement with the study of Huber *et al.* on endothelial cells, where blebs from apoptotic cells contain biologically active OxPL interacting with different EO types. It was also shown there, that these blebs stimulate the adhesion of monocytes which plays an important role in atherogenesis [124].

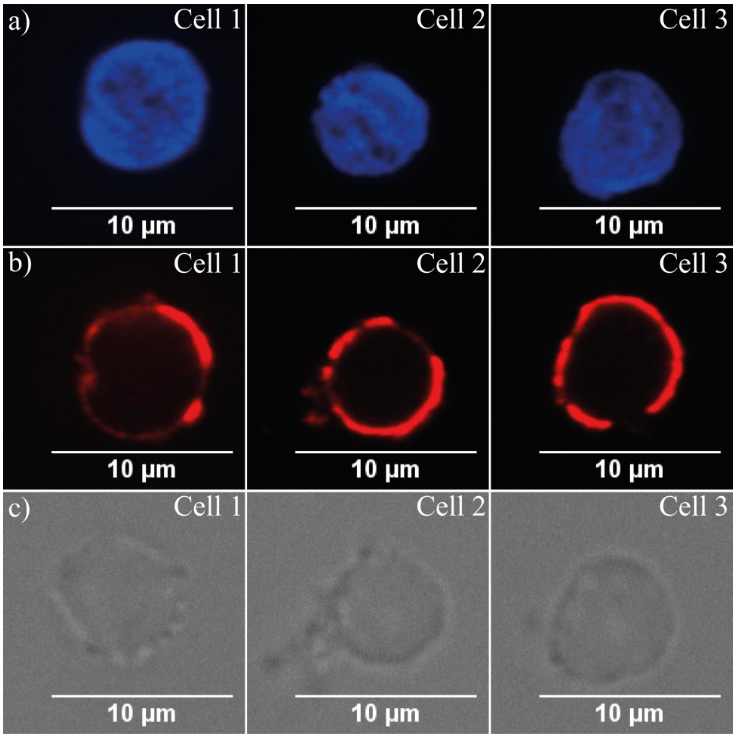

Figure 5.27 Immunofluorescence images of three GBM10 apoptotic cells after 50 min: (a) Nuclei staining with Hoechst dye, (b) secondary-antibody-TRITC staining shows EO6 binding to the surface of the apoptotic cells and (c) bright-field images show the blebbing on the surface of the cells.

5.2.2 Interaction of EO6 with Cell Membrane Models

5.2.2.1 Characterization of Changes in Viscoelasticity of Phospholipid Membranes Induced by EO6 Interaction

In order to assess the mechanism of interaction of EO6 with lipid membranes in the presence and absence of OxPL, supported membranes were prepared via *in situ* liposomes deposition onto hydrophilic SiO_2-coated quartz crystals using quartz crystal microbalance with dissipation monitoring (QCM-D) (section 3.2.2.8). Liposomes were composed either of POPC or POPC doped with 10 mol% OxPL (PoxnoPC, PazePC).

In the first step, the injection of liposomes suspension (0.5 mM) induced a decrease in the frequency Δf_7 and a simultaneous increase in the dissipation ΔD until a critical density of adsorbed intact vesicles was reached (Figure 5.28). This critical density of vesicles corresponds to the maximal liposomes adsorption during membrane formation process and relates to the minimum in frequency shift (~ -50 Hz for POPC, ~ -43 Hz for POPC/PazePC, ~ -24 Hz for POPC/PoxnoPC) and the maximum in dissipation (7.85×10^{-6} for POPC, 1.37×10^{-6} POPC/PazePC, 1.92×10^{-6} POPC/PoxnoPC). As described by others, the vesicle rupture usually starts at this point [102, 119]. Once a critical density of adsorbed vesicles is reached, the fusion of vesicles into planar membranes could be detected by an increase in Δf_7 and a decrease in ΔD, where the water from the inner space of the vesicles is released. Finally, both Δf_7 and ΔD reach saturation levels at $\Delta f_7 \sim -24 \pm 1$ Hz and $\Delta D \sim 0.14 \times 10^{-6}$ upon rinsing with buffer, demonstrating the formation of a stable bilayer [119].

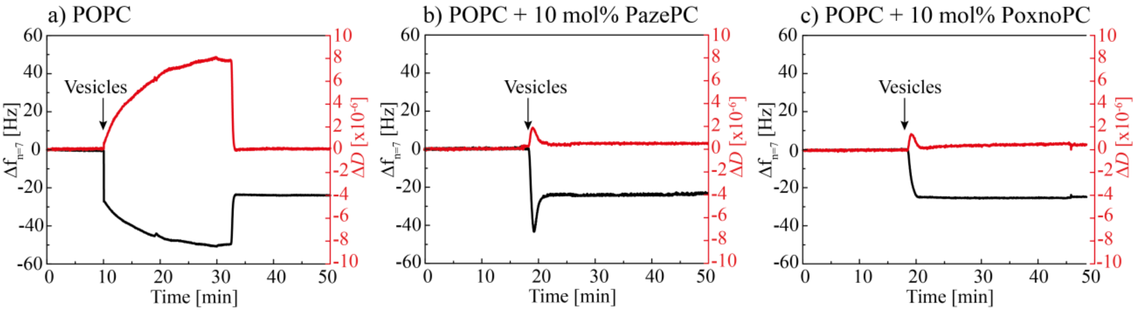

Figure 5.28 Changes in resonant frequency Δf (black) and dissipation ΔD (red) monitored at 35 MHz ($n = 7$) during formation of solid-supported membrane on SiO_2 substrates of (a) pure POPC membrane (b) POPC/PazePC membrane and (c) POPC/PoxnoPC membrane.

The incorporation of OxPL into POPC altered significantly the vesicle rupture process. Similar findings were reported by Makky *et al.* [102]. Doping POPC with 10 mol% of PazePC, resulted in a maximal change resonance frequency Δf_{max} (Δf_{max} = -43 Hz) which was significantly smaller compared to pure POPC. This finding indicates, that the onset of the bilayer formation occurs at lower surface coverage with vesicles. In case of POPC/PoxnoPC (10 mol%) membrane formation, no distinct minimum in Δf could be observed, indicating that the vesicles rupture immediately upon the contact to the solid surface without reaching a critical coverage level. The effects of PoxnoPC onto the membrane formation was reported to be similar to PazePC, but less enhanced and the trend (shown in Figure 5.28c) was observed at a doping ratio of 20 mol% [102]. This result indicates that the effective doping ratio of the POPC/PoxnoPC vesicles was higher as expected (between 10 mol% and 20 mol%). Nevertheless, it should be noted, that that the resonant frequency values after the membrane formation were comparable in the presence and absence of OxPL (Table 5.21).

Table 5.21 Maximal change in resonant frequency Δf_{max}, the difference in frequency Δf_{mem} and energy dissipation ΔD_{mem} before and after membrane formation monitored by QCM-D.

Vesicle Composition	Δf_{max} [Hz]	Δf_{mem} [Hz]	ΔD_{mem} [$\times 10^{-6}$]
POPC	-50.4	-23.7	0.02
+ PazePC 10 mol%	-43.0	-23.1	0.35
+ PoxnoPC 10 mol%	-24.0	-25.2	0.04

In the second step, the membranes were rinsed with PBS-buffer and EO6 was injected (c = 10 µg/ml) for 10 min, followed by 30 min of incubation time for 2 injection cycles (Figure 5.29). However, neither in the presence, nor in the absence of OxPL, a binding of EO6 could be detected in terms of a remarkable change in both Δf ($\Delta f_{change} < 2$ Hz) or ΔD.

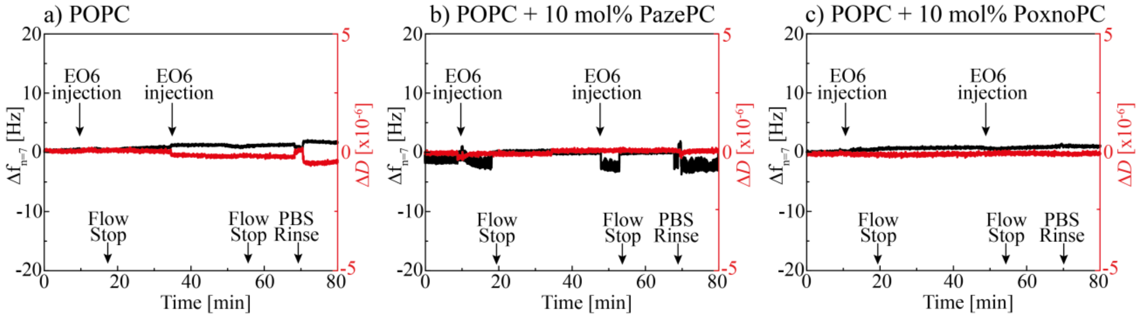

Figure 5.29 Changes in resonant frequency Δf (black) and dissipation ΔD (red) monitored at 35 MHz (n = 7) during two injections of EO6 onto the membranes of (a) pure POPC, (b) POPC/PazePC and (c) POPC/PoxnoPC. For none of the membranes, a binding of EO6 could be detected.

5.2.2.2 Characterization of EO6 Adsorption Strength to Phospholipid Monolayers

The work with model systems based on supported membrane formation was limited by the doping ratio of OxPL. There was hardly any vesicle formation if the molar ratio was higher than 20 mol%. With Langmuir film balances, it was possible to form phospholipid monolayers at the air-water interphase even with pure OxPL to create a highly disturbed model system (section 3.2.2.1).

In this surface tension study, pure POPC and pure OxPL were utilized to form model systems, based on a phospholipid monolayer formed at the air-water interphase. At a stable surface pressure of ~ 20 mN/m, EO6 was injected ($c = 100$ µg/ml) into the buffer subphase (Kibron film balance µ Trough S) underneath the lipid monolayers and the change in the surface tension and the surface potential was monitored simultaneously over time. In Figure 5.30, the change in surface pressure (π) as a function of time t is depicted, which was obtained from the difference of the surface tension of the air-buffer interface γ_o and the surface tension γ of the lipid monolayer.

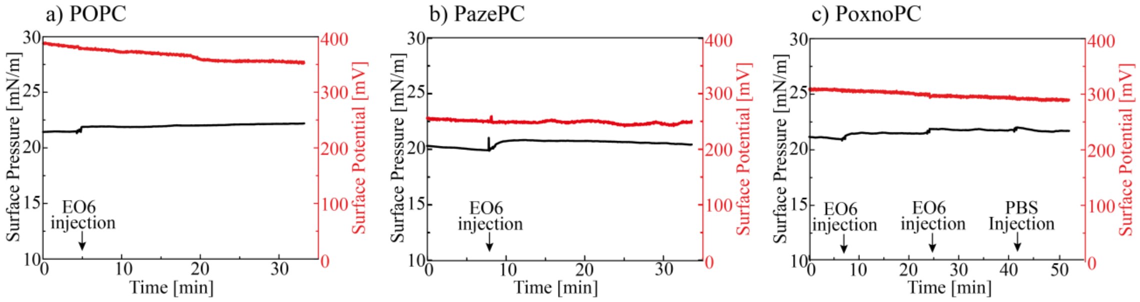

Figure 5.30 Changes in surface potential (red) and surface tension shown as a change in surface pressure (black) after EO6 injection into the subphase of (a) POPC, (b) PazePC and (c) PoxnoPC membrane. For each membrane, no significant increase after EO6 injection could be detected.

In each membrane system, the surface pressure increased by ~ 1 mN/m which is not significant. In case of PoxnoPC membrane two EO6 injections were carried out (Figure 5.30c) as well as a control injection of PBS-buffer with the same volume. There, it was obvious that the increase of ~ 1 mN/m came from the effect of the injected volume and that EO6 did not form any homogenous layer which could then interact with lipid membranes.

5.2.3 Summary

In this section, the potential binding of the monoclonal antibody EO6 to different species of oxidatively modified moieties, which were either incorporated into supported membrane model systems or displayed at the surface of apoptotic cancer cells from glioblastoma multiforme (GBM), were investigated.

The intermolecular binding of EO6 to model membranes in the presence or absence (as control) of OxPL were not monitored by neither QCM-D nor surface tension measurements. In contrast to the binding of EO6 to the surface of apoptotic cancer cells were detected by immunofluorescent convocal microscopy, showing the presence of oxidative modified moieties in the blebs of apoptotic cells.

The differential response of EO6 to the membrane model system and cancer cells is not surprising considering the difference in the molecular components of both systems. The main simplifications of the supported membrane model systems compared to the *in vitro* system are (i) the use of just two species of OxPL and (ii) the planarity of the supported lipid membrane. The obtained results imply that EO6 binding requires either the curvature of the cell (creating an additional disorder in the hydrocarbon chain of the cell membrane) or a more complex composition of the lipid membrane. So far, as no other studies working on model membranes with EO6 have been reported, it would be of particular importance to improve the *in vitro* cell model by utilizing for example a system with higher complexity. Such model systems would allow the selective and detailed investigation of specific ligand-receptor interactions by the combination of complementary physical techniques, which is not possible in any *in vivo* studies.

6 Conclusions

In this thesis, the impact of oxidative damage on structures and functions of biological membranes was investigated by the fabrication of precisely defined model systems of biological membranes (Langmuir monolayers, vesicles, supported membranes and multilamellar membranes) incorporating two stable oxidized phospholipids bearing either aldehyde (PoxnoPC) or carboxyl (PazePC) groups at the end of the truncated *sn*-2 acyl chain. The combination of various experimental methods enabled the quantitative determination of the impact of chain oxidization on physical properties of membranes (e.g. lateral cooperativity, fine-structures perpendicular to membrane planes, electrostatics). Moreover, the specific interactions of EO6 peptide and the acute immune response C-reactive protein (CRP) with oxidized phospholipids (OxPL) were studied.

In chapter 4, in the first step, the influence of oxidized phospholipids (OxPL) on the thermodynamics and electrostatics of lipid monolayers were investigated using Langmuir film balance at the air-water interface. The pressure-area (π-A) isotherms and surface potential ($\Delta\psi$-A) measurements implied that both OxPLs lead to a decrease in the isothermal compression modulus ($\Delta\kappa$ = 30 – 50 mN/m) suggesting a less packed lipid state with increased fraction of OxPL. Moreover, an increase in the molar fraction of OxPL resulted in the loss of lipid molecules into bulk water, which seems consistent with the destabilization of cell membranes under oxidative stress. Changes in the orientation of oxidized moieties and thus a decrease in the lateral cooperativity were suggested by surface potential measurements. At the same molecular area (70 Å²), both pure OxPL decreased the surface potentials ΔV_{70} ~ 330 mV on K^+-buffer, ~ 365 mV on Ca^{2+}-buffer corresponding to a decrease in the surface dipole moment μ_n normal to the air-water interface by ~ 200 mD, which was obtained using the Helmholtz equation (3.7). However, the incorporation of OxPL into the OPPC monolayer reduced the surface potential (ΔV_{70} ~ 15 – 35 mV) as well as the surface dipole moment ($\Delta\mu_n$ ~ 5 – 30 mD) with increased content of OxPL. These results suggested the reorientation of the terminal oxidized moieties of the *sn*-2 hydrocarbon chain into the vicinity of the polar headgroup region, which was supported by the theory of Demchak-Fort (DF) using three-layer capacitor model. This model enabled the estimation of the contribution of the extended conformation of the alkyl chain bearing the oxidized moieties (carboxyl or carbonyl) to the normal components of the phospholipid dipole moment. PazePC showed a resulting difference in surface potential ΔV ~ 63 mV and ~ 80 mV on Ca^{2+}- and K^+-buffer, while PoxnoPC showed ΔV ~ 68 mV and ~ 98 mV on Ca^{2+}- and K^+-buffer, respectively. The obtained values were in good agreement with corresponding values from the terminal CH_3 group (63 mV) reported by Taylor *et al.* [83].

In the second step, the impact of lipid oxidization on the structures and electrostatics of membranes was examined by the combination of high-energy specular X-ray reflectivity (XRR) and grazing-incidence X-ray fluorescence (GIXF). Both OxPL were found to form thinner monolayers than pure OPPC on different buffers, which was more pronounced for PazePC as demonstrated by scattering length density profiles reconstructed from XRR. The OxPL monolayers were found to be thinner in hydrocarbon chains ($\Delta d_{\mathrm{A}} \sim 4$ Å) and head groups ($\Delta d_{\mathrm{H}} = -1.3$ Å) than OPPC monolayers on K^+-buffer. On Ca^{2+}-buffer, the monolayer became even thinner ($\Delta d_{\mathrm{A}} \sim -4.6$ Å and $\Delta d_{\mathrm{H}} = -1.8$ Å). The smaller values found for the hydrocarbon chain layer thickness can be interpreted in terms of reorientation of the oxidized chains towards the aqueous phase based on the decrease in the lateral cooperativity, which was also suggested by Langmuir isotherms (section 4.1.1). In fact, OxPL were found to increase the electron density of hydrocarbon chain ($\Delta\rho = 10 - 20\%$) as well as the interface roughness ($\Delta\sigma \sim 0.1 - 0.5$ Å).

By the unique possibility of GIXF to localize specific target elements within ± 5 Å accuracy strong specific effects of cations on the electrostatics of lipid monolayers incorporating OxPL have been revealed. A clear enrichment of Cs^+ ions in the vicinity of PazePC membranes implied $N = 1.2$ Cs^+ ions per one PazePC molecule while K^+ ions showed no sign of enrichment. In the presence of Ca^{2+} ions, it was found that (1) Ca^{2+} ions are accumulated near the head groups, and (2) the thicknesses and electron densities of hydrocarbon chains and head groups increased. PazePC with its carboxylic group pointing into the subphase showed the highest accumulation of $N = 2.1$ Ca^{2+} ions per PazePC lipid located in the polar head group regions. The obtained binding affinity ($Ca^{2+} > Cs^+ > K^+$) could be interpreted in terms of the solvation entropy (Hofmeister series) and was found to be in good agreement with obtained XRR results, where PazePC monolayer on Cs^+-buffer was thinner than that on K^+-buffer ($\Delta d \sim 1.9$ Å).

Furthermore, to unravel the impact of oxidization on the inter-membrane interactions, stacks of planar membranes were deposited on solid supports. Off-specular neutron scattering measured at different relative humidities (RH) suggested an increase in vertical correlation length ($\Delta\Lambda \sim 70 - 90$ Å) in addition to a decrease in the lamellar periodicity ($\Delta d \sim 2 - 4$ Å) when OxPLs were incorporated into POPC membranes at low and high RH. This can be explained by the displacement of water from the head group region due to the reorientation of the oxidized chains towards the vicinity of the head group region. In case of pure OxPL membranes, a more distinct increase in vertical correlation length was found: $\Delta\Lambda_{\mathrm{PoxnoPC}} \sim 126$ Å and $\Delta\Lambda_{\mathrm{PazePC}} \sim 136$ Å indicating a lower stability of OxPL membrane multilayers.

In chapter 5, the combination of experimental techniques was utilized to shed light on specific interactions of peptides and proteins with membrane incorporating OxPLs; C-reactive protein that is characteristic for the acute immune responses and monoclonal antibody EO6.

The interaction enthalpies were determined using isothermal titration calorimetry (ITC), suggesting that the incorporation of OxPL leads to a decrease in the enthalphy $\Delta H_{\text{PazePC}} = -73.7 \pm 2.5$ kcal/mol and $\Delta H_{\text{PoxnoPC}} = -57.4 \pm 2.9$ kcal/mol, which are clearly lower than that of pure POPC vesicles $\Delta H_{\text{POPC}} = -41.5 \pm 2.0$ kcal/mol. In combination with dynamic light scattering (DLS), it has been concluded that the affinity of CRP to vesicles becomes higher when OxPL molecules were incorporated into the membrane. Moreover, PazePC exhibited a higher affinity compared to PoxnoPC.

The incubation of CRP on pure POPC multilayers resulted in a small increase in lamellar spacing $\Delta d_{\text{POPC}} \sim 3$ Å. However, the incubation of CRP on multilayers incorporating OxPLs exhibited a more pronounced increase in the lamellar periodicity; $\Delta d_{\text{PoxnoPC}} \sim 21$ Å and $\Delta d_{\text{PazePC}} \sim 6$ Å. A clear difference in the periodicity change suggests the interaction of CRP with PoxnoPC is different from that with PazePC. To verify this hypothesis, dual polarized waveguide interferometry (DPI) was utilized as a complementary technique to determine the changes in mass density Δm_{DPI} and average density $\Delta \rho$. The membrane incorporating PazePC exhibited the increase in both mass and average densities, $\Delta m_{\text{DPI}} \sim 6$ ng/cm^2 and $\Delta \rho \sim 0.02$ g/cm^3, while the membranes doped with PoxnoPC showed a decrease in both mass and average densities, $\Delta m_{\text{DPI}} \sim 180$ ng/cm^2 and $\Delta \rho \sim 0.7$ g/cm^3.

To unravel how the interaction with CRP altered the fine structures of membranes perpendicular to the plane of membranes, planar lipid membranes were deposited on solid substrates (called supported membranes). High-energy specular X-ray reflectivity measured at the solid-liquid interface suggests that the interaction with CRP resulted in an increase in scattering length density ($\Delta SLD_{\text{PazePC}} \sim 1.0 \times 10^{-6}$ Å^{-2}) of the outer head groups, but the roughness of the most outer interface showed almost no change ($\Delta \sigma_{\text{Paze}} \sim 0.5$ Å). On the other hand, the interaction of CRP with membranes incorporating PoxnoPC resulted in a much more significant increase in *SLD* and roughness; $\Delta SLD_{\text{Poxno}} \sim 1.8 \times 10^{-6}$ Å^{-2} and $\Delta \sigma_{\text{Poxno}} \sim 2$ Å, respectively. Based on the obtained results, a binding model for CRP and the membranes incorporating OxPL was proposed: CRP molecules lay parallel to the surface of membranes incorporating PazePC, while CRP molecules in contact with membranes incorporating PoxnoPC take a random orientation, partially intercalating into the hydrocarbon chain region.

As the final step, the accumulation of OxPLs in the apoptotic blebs of glioblastoma multiforme (GBM) cells undergoing apoptosis was verified by fluorescence microscopy. Here, the specific binding of the monoclonal antibody EO6 to OxPL was utilized by *in vitro* model systems of a cell surface, where the intermolecular distance between the ligand molecules (CD95L) was regulated at the optimal distance for the induction of apoptosis ($< d > = 11$ nm). The specific binding of EO6, protects the host from inflammation, was found to bind to the surface of apoptotic cells. The presence of non homogenous fluorescent patterns is in good agreement with the study on endothelial cells by Huber *et al.* [124], reporting that blebs from apoptotic cells containing a wide range of OxPL interacting with different EO types.

To conclude, the obtained results demonstrated that the combination of well defined membrane models and unique physical techniques is a powerful strategy for the discrimination of generic and specific impacts of lipid oxidization on structures and functions of cell membranes, ranging from the lateral cooperativity, vertical fine-structures, electrostatics, and specific interactions with proteins in inflammation and apoptosis.

7 Appendix

7.1 The Interaction between Mucin Proteins and Phospholipids

7.1.1 Mucin

Mucus

Mucus, also called mucosa, is a viscous protecting layer, which is present in all organs that are exposed to external environment such as the respiratory and the gastrointestinal tract [125]. Its main function is to protect the epithelial cells from microorganisms, dehydration and physical and chemical violation, as well as to aid the passage of materials through the gastrointestinal tract. Moreover it often harbors protective and probiotic bacteria in the outer sphere of the protecting layer [126, 127].

The two major components of gastrointestinal mucus are phospholipids and glycoproteins which belong to the mucin family. The phospholipids consist of up to 90% phosphatidylcholine (PC) and lysophosphatidylcholine (LPC) and they are found as a continuous layer at the luminal and mucosal cell side of the mucus gel [128]. It was suggested that the interaction between PC head groups and mucins establishes a hydrophobic barrier which prevents invasion of bacteria through the mucus layer [129]. The phospholipid film at the outer surface of the mucus can be up to 10 bilayers thick. In general the phospholipids are located at both sides of the mucus layer and as lamellar bodies inside the mucus. Furthermore, salts, cholesterol and other proteins are present in the mucosa as well. The structure of the whole surface protection system is shown in Figure 7.1 [129, 130, 131].

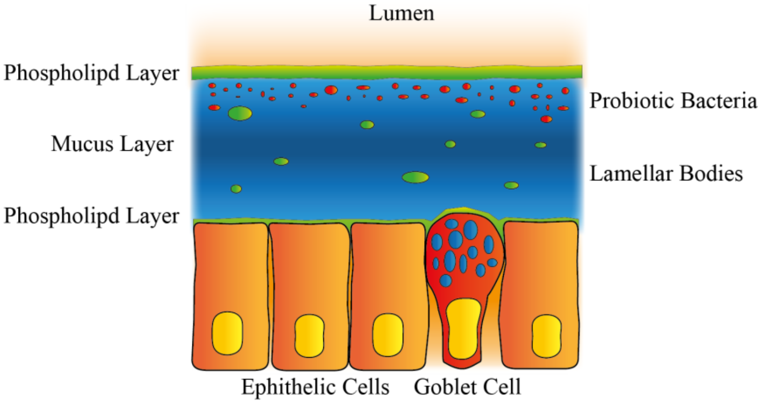

Figure 7.1 Simplified illustration of the surface protection system.

Mucin

Mucins are major glygoprotein components of the mucous, which can be grouped into two subclasses: membrane bound and secreted mucins. Members of the mucin family can differ considerably in size (0.5 – 20 MDa). Some are small and contain just a few hundred amino acid residues, whereas others contain several thousands of residues. However, 90 w% of the content are carbohydrates which are composed mainly of N-acetylgalactosamine, N-acetylglucosamine, fucose, galactose and sialic acid. Irrespective of size, the polypeptide chains have domains which are rich in serine and/or threonine and proline (STP) [125]. Most of the oligosaccharide chains are attached to the protein by an O-glyosidic linkage to the hydroxyl groups of these STP domains. This glycosylation just appears in a specific part of the protein, can make up to 60% of the protein core and it varies in number, length and sequence in different types of mucin [132].

The functions of mucins are dependent on their ability to form viscous gels. Thus, the assembly of the secreted porcine submaxillary mucin (PSM) was the target of different studies and is therefore well understood. As shown in Figure 7.2 the mucin monomer is N-glycosylated and disulfide bonds between the carboxyl terminal domains are formed to generate dimers. This dimerization occurs soon after the biosynthesis and folding in the endoplasmatic reticulum. In the next step the dimers are transported to the *cis*-Golgi compartment and the tandem repeats are O-glycosylated. The multimerization of the mucin dimers takes place in the *trans*-Golgi and is responsible for mucins ability to form gels [133].

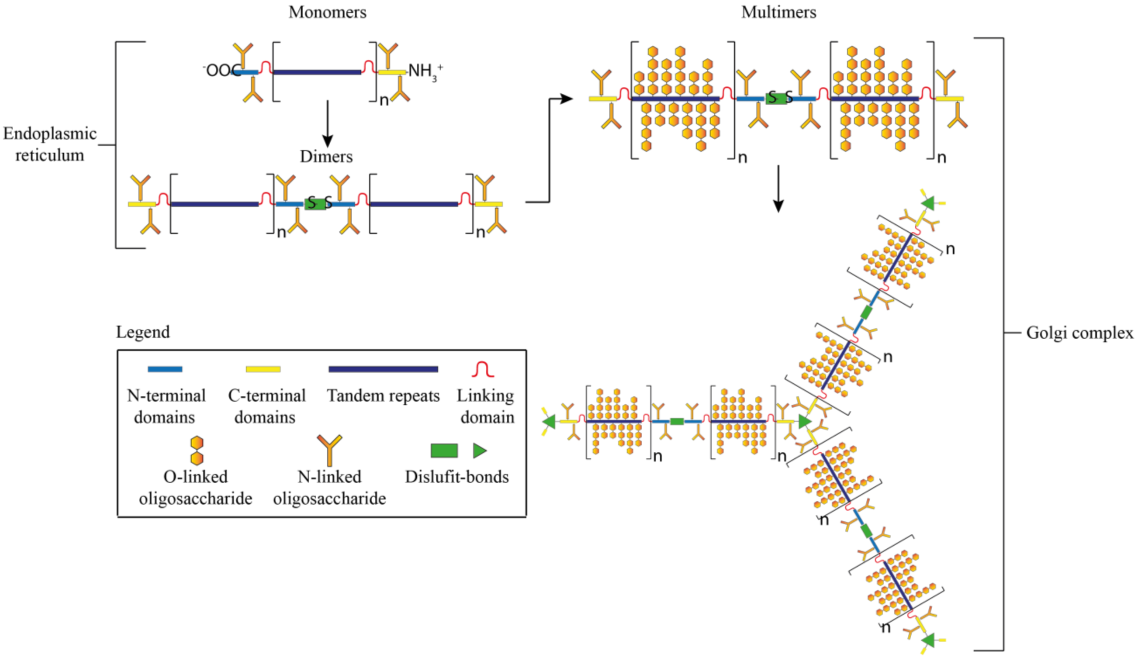

Figure 7.2 Schematic illustration of the stepwise multimerization of porcine submaxillary mucin (PSM).

Medical Relevance

Due to the protective role of the mucus layer on epithelial cells, mucus has a high medical relevance: alterations in its structure and quantity can cause inflammatory bowel diseases (IBD). IBD are chronic inflammations of the colon and small intestine and can be grouped into ulcerative colitis (UC) und Crohn's disease (CD). Both UC and CD can lead to colorectal cancer [134].

The amount of mucus in patient with IBD was observed to be reduced [135, 136]. Moreover, the glycosylation of mucins is changing during IBD[137]. This alteration in the amount and structure of the glycoproteins has huge influence on the whole protecting system, since mucins make up the largest part of the mucus. Interestingly, it was found by Stremmel *et al.* that the therapeutic replacement of PC in ulcerative colitis patient through a treatment with external PC can reduce the inflammatory activity in UC patients [128, 138].

However, although the mucus composition plays a key role in the protection of gut surfaces, the mechanism of interaction between the major components of mucus and the effect of ions is not fully understood. New knowledge about the role of phosphatidylcholine and mucin in the protection of gut surfaces can pave the way for the treatment of inflammatory bowel diseases.

The aim of this study is to model the surface protection system in the gastrointestinal tract to quantitatively determine how phospholipids interact with the large glycoproteins mucin 2 and mucin 3. The better understanding of the surface protection system could be used for the medical application of inflammatory bowel diseases in future. For this purpose the physical interaction of mucins with phospholipids was investigated by (i) light scattering techniques (**DLS**), (ii) isothermal titration calorimetry (**ITC**) and (iii) **Langmuir isotherms**. Prior to this, the physical properties of both mucins were investigated. To examine if the interaction of mucins with phospholipids is a matter of electrostatics, three different types of lipids were used: zwitterionic **DOPC**, negatively charged **DOPG** and positively charged **DOTAP**. In addition the interactions of the two zwitterionic lipids DOPC and **DOPE** were compared with each other. Stremmel *et al.* stated that the two particular types of gastric mucins, mucin 2 and mucin 3, showed strong physical interactions to the phospholipid head group phosphatidylcholine (unpublished results).

7.1.2 Characterization of Mucin 2 and Mucin 3 in Solution

Since mucin 2 and mucin 3 are commercially available fractions of a purification process of porcine mucin, their properties in solution are not well known. To gain more information about the characteristics of mucin 2 and mucin 3 in aqueous solution, size and ζ potential measurements were performed, in the first step (for more details see section 3.2.2.5).

Figure 7.3 demonstrates different options in representation of size distributions of mucin 2 and illustrates the sensitive dependence of light scattering to the presence of large particles. The DLS results reveal that mucin 2 consists mainly of monomers with an average diameter of 28 ± 7 nm (Figure 7.3c). In addition, there are also multimers (pentamers) with an average diameter of ~ 105 nm and larger aggregates (~ 800 - 900 nm) visible if volume or intensity is plotted versus the size (Figure 7.3a, b). However, the monomer fraction is predominantly present (Σ > 99%).

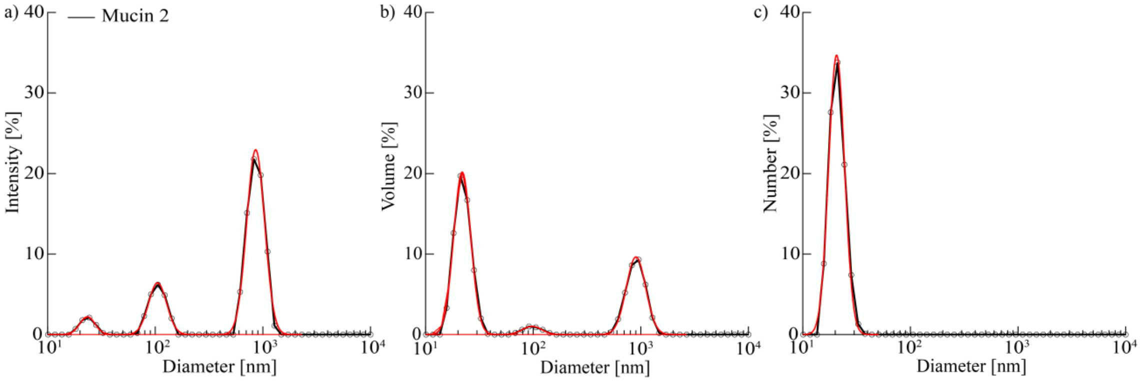

Figure 7.3 Size distribution of mucin 2 (black) together with the multi-lognormal fitting results (red) plotted as (a) intensity, (b) volume and (c) number versus the diameter.

The mucin 3 monomer fraction has a diameter of 46 ± 11 nm (Figure 7.4c) while there are also larger aggregates (~ 650 nm) present (Figure 7.4a, b). However, the monomer fraction is predominantly present (Σ > 99%). The obtained monomer sizes are in good agreement with reported hydrodynamic diameter of ~ 65 nm for gallbladder mucin [139] and ~ 50 – 100 nm for several fractions of ovine salivary mucins in dilute solutions (< 2 mg/ml) [140].

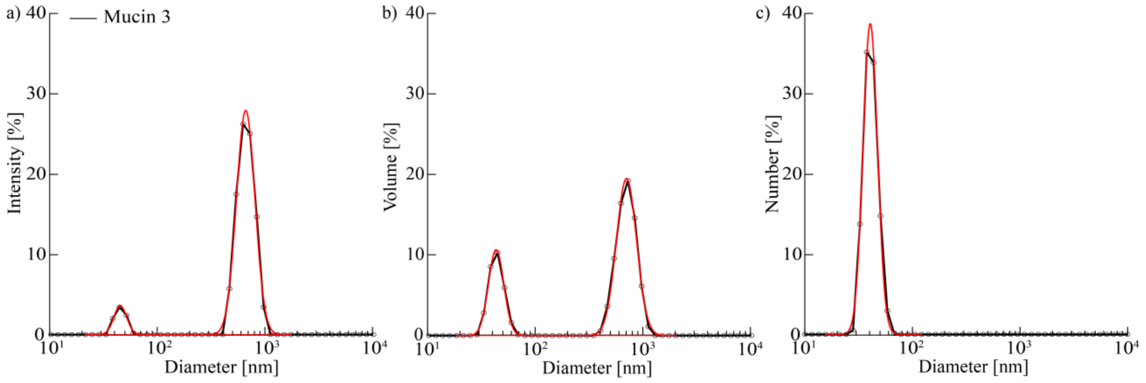

Figure 7.4 Size distribution of mucin 3 (black) together the multi-lognormal fitting results (red) plotted as (a) intensity, (b) volume and (c) number versus the diameter.

In the next step, the influence of mucin 3 concentration on the formation of aggregates was investigated (Figure 7.5). Within this context, the focus lies on mucin 3 aggregates where the peak position of the size distribution lies between 300 - 1000 nm (Figure 7.5b and Table 7.2). The size of aggregates increase with higher concentration, until a saturation in size of aggregates was reached ($c \geq 2.5$ mg/ml). Fitting the sizes of aggregates according to the Hill equation yields the transition, where small aggregates become large, which is found to be at $c_{Half} \sim 1.3$ mg/ml.

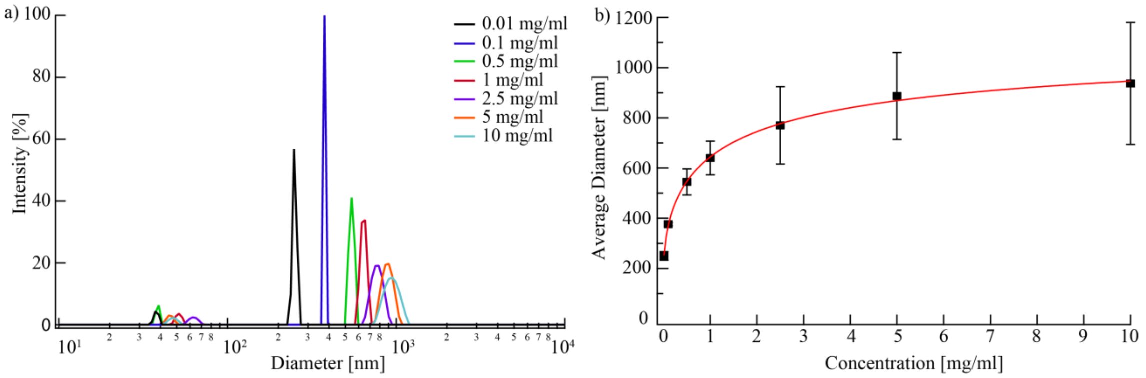

Figure 7.5 (a) Size distribution of mucin 3 at different concentrations. The first peak corresponds to the monomeric form of mucin 3, while the size of aggregates increases with higher concentrations (b). The data was fitted with the Hill equation (red).

The formation of larger aggregates and their increased size and broad distribution with higher mucin 3 concentrations are in good agreement with the characteristic property of mucins to form a gel on a typical aerodigestive epithelial surface. There, the complex gel layer acts as an interface with air, food, enzymes, bacteria and acidic pH [141]. Aggregation of most mucins can be observed by DLS at concentrations above 4 mg/ml [142]. DLS studies performed with pig gastric mucin identify native mucin and small aggregates even in dilute solutions of 1 mg/ml [143].

Table 7.1 Fitting results of experimental DLS data of the peak position and full width at half maximum (FWHM) of mucin 3 aggregates at different concentrations.

Concentration [mg/ml]	Diameter [nm]	FWHM [nm]
0.01	250	17
0.1	376	6
0.5	545	52
1	640	67
2.5	770	154
5	887	173
10	937	243

The mean value of the zeta (ζ) potentials is negative for both filtered mucins. Monomeric mucin 3 shows an average ζ potential of (-10.8 ± 0.9) mV and mucin 2 (-8.6 ± 0.5) mV. Table 7.1 gives an overview of the obtained hydrodynamic sizes (nm) and ζ potentials (mV) for mucin 2 and mucin 3. The negative ζ potentials lead to the assumption that in the structure of monomeric mucins the acidic carbohydrates sidechains of the glycoprotein are intact. There, the high charge density is based on sialic acid ($pK_a \sim 2.6$) and sulfated glucosamine ($pK_a \sim 1$) and galactoamines ($pK_a \sim 1$), which are negatively charged at neutral pH [142].

Table 7.2 Results for hydrodynamic diameter (nm) and zeta (ζ) potential of mucin 2 and mucin 3 together with the corresponding standard deviation.

Protein	Diameter [nm]	Zeta (ζ) Potential [mV]
Mucin 2	28 ± 7	-8.6 ± 0.5
Mucin 3	46 ± 11	-10.8 ± 0.9

In the second step, the unknown molar masses of mucin 2 and mucin 3 is determined by SLS from at least three measurements, respectively. The measurement of the excess intensity of scattered light caused by the mucin solution with respect to solvent at different concentrations and angles yields the so-called Debye plot, which gives the weight–average molecular weight by extrapolating to zero angle and zero concentration (section 3.2.2.5). Figure 7.6 shows the Debye plots for (a) mucin 2 and (b) mucin 3.

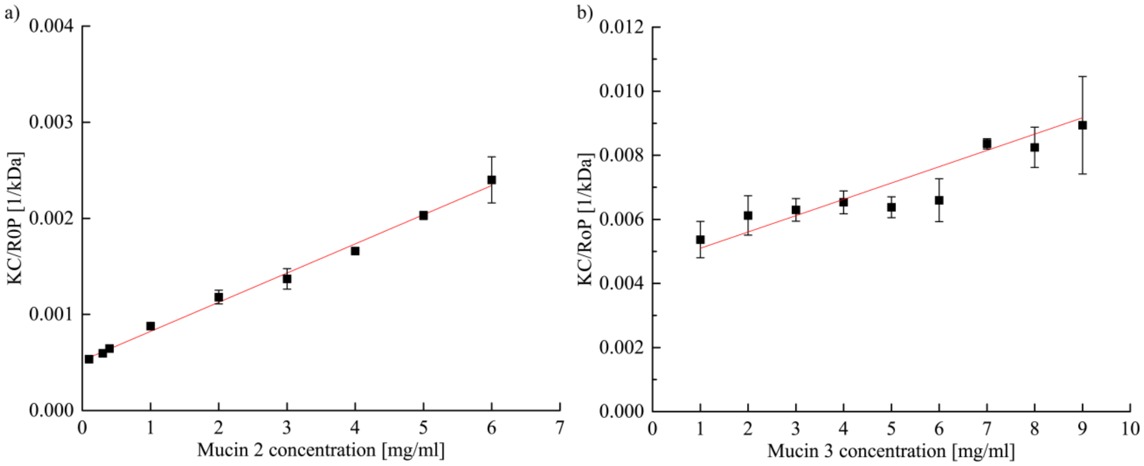

Figure 7.6 Debye plots of (a) mucin 2 and (b) mucin 3 together with the best linear fit (red), which yield the molecular mass from the extrapolation of the scattering intensity to both, zero angle and infinite dilution, and the reciprocal value of the y-axis according to the simplified Rayleigth equation (3.18).

Table 7.3 gives the obtained molecular masses for mucin 2 (left) and mucin 3 (right) together with the average results. Here, the average molecular masses of (2543 ± 346) kDa of mucin 2 and (204 ± 23) kDa of mucin 3 were obtained, which are in the range of the molecular weights reported for stomach mucins (200 kDa - 16 MDa) [144].

Table 7.3 Molecular masses M_W of mucin 2 (left) and mucin 3 (right) obtained from SLS measurements. Values were extracted from the linear fits of the measured Debye plots.

	Mucin 2	**Mucin 3**
Measurement	**M_w [kDa]**	**M_w [kDa]**
1)	2950 ± 845	204 ± 28
2)	2686 ± 257	203 ± 23
3)	1996 ± 65	205 ± 17
4)	2538 ± 216	-
Average	**2543 ± 346**	**204 ± 23**

Although the measurements look quite promising, the obtained values should be taken with caution, because the exact change in refractive index of increment of mucin solutions usually must be known. For mucin, values of the refractive index increment were reported to range between 0.10 ml/g – 0.14 ml/g depending on the mucine type that has been used [145, 146, 147]. Therefore, 10% error in the refractive index increment is used in the calculation of the M_W. For highly accurate numbers, measurement of *dn/dc* with a differential refractometer for the mucin samples prior the SLS measurements should be performed. However, the obtained molecular masses for mucin 2 and mucin 3 are good estimations and are used in the following sections.

7.1.2.1 Dynamic Properties of Mucin Proteins in Solution

The critical micelle concentration (CMC) of mucin 2 (Figure 7.7a) and mucin 3 (b) was obtained by surface tension measurements of three samples each. The concentration of surfactants in the bulk at which the micelle formation starts was found to be at ~ 2.8 µM (≈ 7 mg/ml) for mucin 2 and ~ 10 µM (≈ 2 mg/ml) for mucin 3, which is in good agreement with the transition concentration of c_{Half} ~ 1.3 mg/ml for mucin 3 obtained by DLS (previous section).

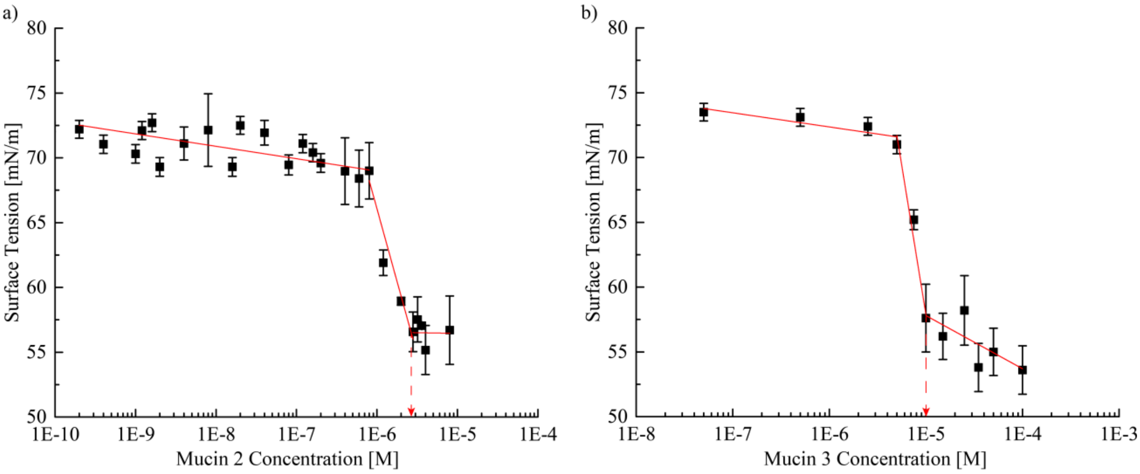

Figure 7.7 Results for surface tension measurements of (a) mucin 2 and (b) mucin 3.

Another parameter which describes the entanglement of monomers is the overlap concentration c*. At concentrations c < c* the mucin molecules can be treated as high molecular weight polymer solutions which are considered dilute and where the individual chains do not overlap with each other. At concentrations c > c* the solutions exhibits transient entanglements with viscoelastic properties. If such polymer can form noncovalent interactions, then semi-dilute and concentrated solutions will also display rheological behavior characteristics of aggregates and eventually of reversible gelation [148]. For porcine stomach mucin for example, it was found by rheological data that four regimes are present: dilute (< 3 mg/ml), semidilute (3 – 34 mg/ml), interpenetrated brush (> 34 mg/ml) and entangled liquid crystalline (> 479 mg/ml) [144].

The theoretical concentration where mucin 3 can be close to the overlap concentration can be calculated assuming that the monomers will occupy ~ 70% of a given volume (like packed lattice). By assuming the monomers to have a spherical volume (with the radius of $r_{Mucin\ 3} \approx 20$ nm) and the molecular weight M_W of ~ 200 kDa, the theoretical overlap concentration can be estimated to be ~ 7 mg/ml (and ~ 10 mg/ml in case of mucin 2, respectively). This demonstrates that mucin samples used in this section are below or close to the overlap concentrations reported for dilute and semidilute regimes, but far below the entangled regimes. The obtained CMC of 2 mg/ml for mucin 3 is below the concentration reported for the dilute regime (< 3 mg/ml).

However, from DLS results a transition concentration from small aggregates to larger aggregates was found to be c_{Half} = 1.3 mg/ml which is close to the CMC value (previous section).

7.1.3 Interaction of Mucin 2 and Mucin 3 with Phospholipid Monolayers

The interaction of mucin 2 and mucin 3 with phospholipids was investigated by Langmuir isotherms (for more details see section 3.2.2.1). Four different lipids were used which have the same hydrophobic chains but show differences in the polar head group: DOPC (zwitterionic), DOPE (zwitterionic), DOPG (anionic) and DOTAP (cationic).

In the first step, π-A isotherms for all lipids were recorded. Figure 7.8 shows (a) the π-A isotherms and (b) the compressional modulus κ which was calculated according to equation 3.4 for DOPC (black), DOPE (red), DOPG (green) and DOTAP (blue).

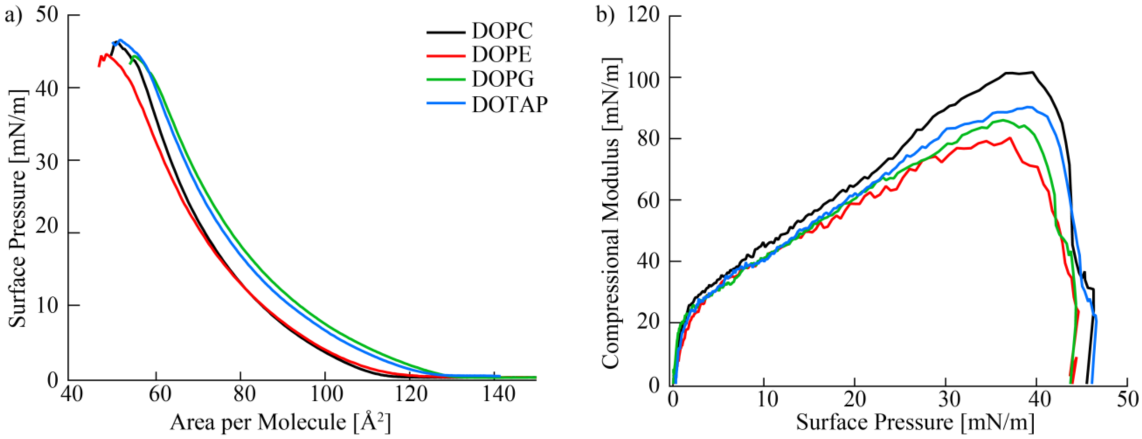

Figure 7.8 (a) Pressure-Area (π-A) isotherms and (b) the compressional modulus κ of the lipid monolayers of DOPC (black), DOPE (red), DOPG (green) and DOTAP (blue) on Hepes buffer.

The molecular areas at surface pressures of 20 mN/m and 30 mN/m are in good agreement with the literature values [149, 150, 151, 152]. The shape of the π-A isotherms for the different lipids is almost identical since they exhibit same hydrocarbon chains, which are the major determinant of the molecular area. However, the DOPG and DOTAP isotherms are slightly less compacted than DOPC and DOPE, most probably due to the coulomb repulsion that occurs in charged lipids like DOPG and DOTAP. However, all lipids reside in the liquid expanded phase L_e.

Figure 7.9 shows the recorded π-A isotherms of (a) DOPC (black) and (b) DOPE (red) with mucin 2 (blue), and mucin 3 (green) together with the compressional modulus κ (calculated according to equation 3.4) as insets. In both cases, the shape of the isotherms with mucin 2 and mucin 3 differs from that of the lipids alone. The injection of mucins (at low concentrations of

~ 50 ng/ml) leads to an expansion of the isotherms, leading to the assumption of a high affinity between mucins and the lipids at the air-water interface.

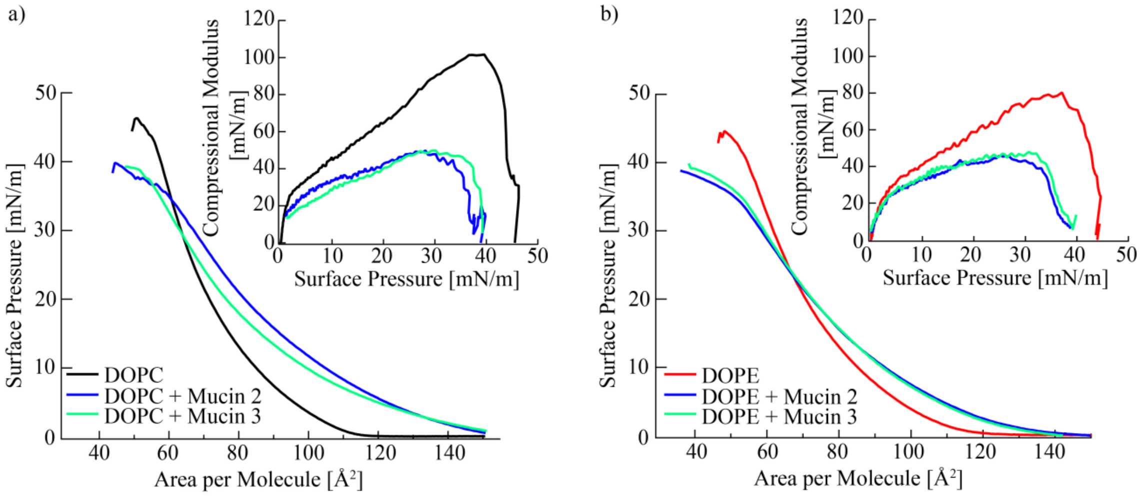

Figure 7.9 Pressure-Area (π-A) isotherms of (a) DOPC (black) and (b) DOPE (red) with mucin 2 (blue), and mucin 3 (green) together with the compressional modulus κ as insets.

The compressional modulus κ (Figure 7.9 insets) for both lipids, reveal a smaller maximal compressional modulus κ_{max} value when mucin is present ($\leq$ 50 mN/m), which represents a significantly less rigid monolayer. This leads to the conclusion that the interactions between the lipids are weaker. At low surface pressure mucin molecules presumably bind between the lipids and thereby expand the lipid monolayer.

Figure 7.10 shows the recorded π-A isotherms of (c) the negatively charged DOPG (black) and (d) the positively charged DOTAP (red) with mucin 2 (blue), and mucin 3 (green) together with the compressional modulus κ as insets. In both cases the shape of the isotherms with and without mucins are nearly identical. In addition, the calculated compressional modulus (Figure 7.10 insets) are also nearly the same, leading to the assumption of a weak interaction between mucin 2 and mucin 3 to DOPG and DOTAP. This is surprising, because mucin 2 and mucin 3 are both negatively charged and for that a strong electrostatic interaction at least with the positively charged DOTAP was expected. As the subphase contains 160 mM salt concentration which corresponds to a Debye screening length of ~ 1 nm, it is obvious that the affinity of ions to DOTAP is larger than the affinity of mucins to DOTAP. That is why the electrostatic interactions are not significant for the interaction between mucins and phosholipids.

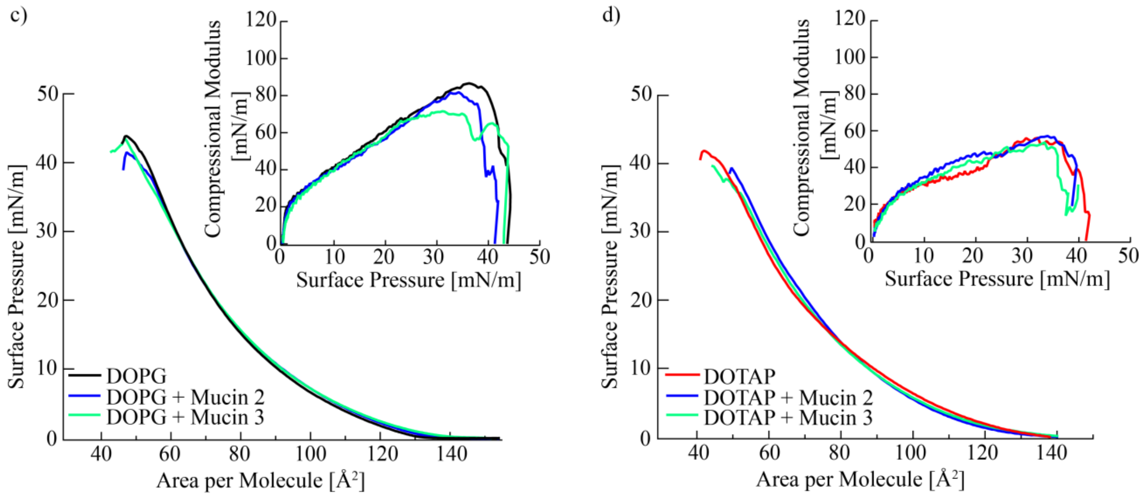

Figure 7.10 Pressure-Area (π-A) isotherms of (c) DOPG (black) and (d) DOTAP (red) with mucin 2 (blue), and mucin 3 (green) together with the compressional modulus κ as insets.

The results of the pressure-area isotherms can be summarized as follows:

(i) Both zwitterionic lipids DOPC and DOPE show physical interaction with mucin 2 and mucin 3 by changing the compressional modulus κ.

(ii) Electrostatic interactions do not play a significant role in mucin interactions, since the positively charged lipid DOTAP and the negatively charged lipid DOPG show both no interaction with mucin 2 and mucin3 (Figure 7.11).

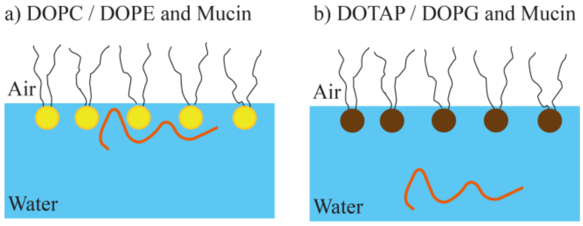

Figure 7.11 Schematic illustration of the interaction between (a) the zwitterionic lipids DOPC and DOPE (yellow) and (b) the charged lipids DOTAP and DOPG (brown) with mucin 2 or mucin 3 (orange).

7.1.4 Interaction of Mucin 2 and Mucin 3 with Phospholipid Liposomes

7.1.4.1 Adsoprtion Effects of Mucin on Liposome Sizes studied by Dynamic Light Scattering (DLS)

To get a better understanding of the medical application for the treatment of inflammatory bowel diseases, the surface protection system, more precisely the phospholipid containing lamellar bodies in the mucus layer, was mimicked by the use of phospholipid liposomes interacting with mucin. Since the monolayer study in the previous section showed that the interaction between zwitterionic phospholipids is more pronounced, **mucin 2** or **mucin 3** were mixed with the respective liposome solutions of **DOPC** or **DOPE** and the change in size of the liposomes was measured by DLS over time for at least 1 h.

Interaction of Mucin with DOPC Liposomes

Figure 7.12 presents the size distribution of pure DOPC liposomes (a, black) and the changes in size distribution after the addition of mucin 2 (a) within 60 min and (b) between 60 and 115 min. The biggest changes of DOPC size distribution in terms of peak position, shape and the appearance of big aggregates occur within the first 60 min, while the changes are less pronounced for the size distributions recorded from 60 – 115 min. The size distributions of DOPC liposomes after the addition of mucin 2 exhibit two populations with maxima at 100 nm and 200 nm. The former population represents the interaction of DOPC liposomes with mucin monomers, while the later represents the adsorption of DOPC liposomes to mucin 2 multimers.

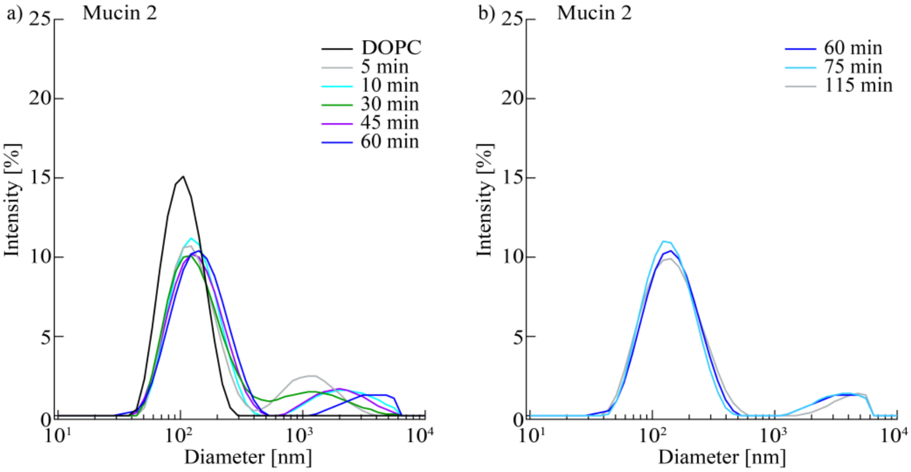

Figure 7.12 Changes in size distributions of DOPC liposomes (a, black) before and after the addition of mucin 2 (a) within 60 min and (b) between 60 and 115 min.

Figure 7.13 presents the size distribution of pure DOPC liposomes (a, black) and the changes in size distribution after the addition of mucin 3 within 60 min. The size distribution of DOPC liposomes after the addition of mucin 3 exhibits only one population.

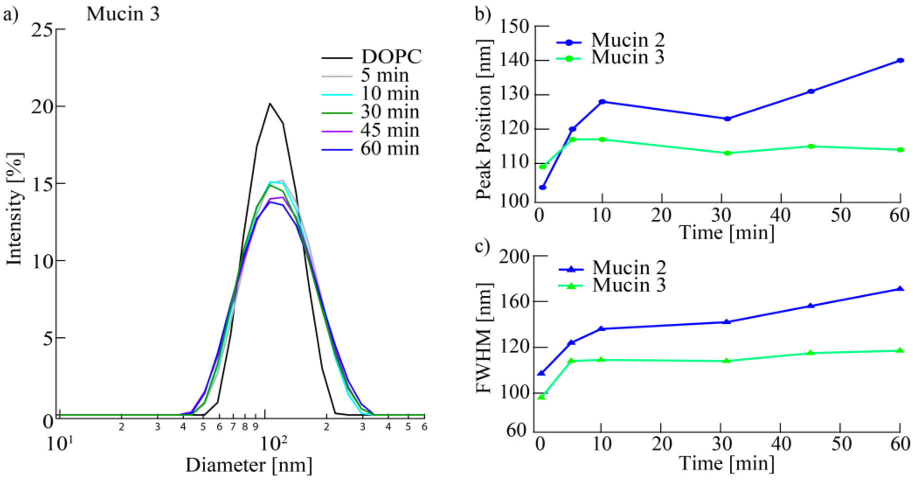

Figure 7.13 (a) Changes in size distributions of DOPC liposomes (black) before and after the addition of mucin 3 within 60 min. (b) Comparison of the changes in peak position and (c) FWHM of DOPC liposomes with mucin 2 (blue) and mucin 3 (green) within 60 min.

In the following lines, the focus lies on the interaction of DOPC with the mucin monomers. Therefore, peak position of the maximum and full width at half maximum (FWHM) were extracted by fitting the distribution of DOPC with mucin 2 or mucin 3 for the first 60 min with a lognormal distribution. Figure 7.13 demonstrates a comparison between the change in (b) peak position and (c) FWHM of the size distributions of DOPC with mucin 2 (blue) and mucin 3 (green) within 60 min, and the fitted values for the changes in diameter and FWHM with time are shown in Table 7.4.

Table 7.4 Peak position and FWHM of the size distribution of DOPC liposomes with mucin 2 (left) and mucin 3 (right) within 60 min, with respect to pure DOPC liposomes (at t = 0 min).

	Mucin 2		**Mucin 3**	
Time [min]	**Diameter [nm]**	**FWHM [nm]**	**Diameter [nm]**	**FWHM [nm]**
0	**103**	**97**	**109**	**76**
5	120	124	117	108
10	128	136	117	109
30	123	142	113	108
45	131	156	115	115
60	140	171	114	117

The interaction of DOPC liposomes with mucin 2 leads to a continuous shift and broadening of size distribution. The peak position and FWHM of the distribution show an increase by 37 nm in average diameter and 74 nm in FWHM (≈ 76%) after 60 min (Table 7.4, left), respectively. The impact of mucin 3 seems to be weaker, because the changes are less pronounced: the size increases by 10% and stayed stable over time, while FWHM increases continuously by 40 nm (≈ 50%) after 60 min.

It should be noted that both mucin samples were used in the same molar concentration (based on the obtained molecular masses by SLS) for a justified comparison of interaction. Because the SLS results include errors for big proteins due to the aggregations, another experiment was performed, to probe any contributions in the interaction that comes from variations in mucin concentrations (Figure 7.14). In this control experiment a comparable size increase of 10% was obtained as with lower mucin 3 concentrations used, while the FWHM increased less by 24 nm (Table 7.5). However, this control experiment with ~ ten times higher mucin 3 concentration showed, that the strength of interaction could not reach the level as that of mucin 2.

Table 7.5 (left) Peak position and FWHM of the size distributions of DOPC liposomes after the addition of mucin 3 within 60 min, with respect to pure DOPC liposomes (at t = 0 min).

	Mucin 3	
Time [min]	**Diameter [nm]**	**FWHM [nm]**
0	**115**	**108**
5	124	135
10	122	139
30	124	138
45	134	138
60	120	132

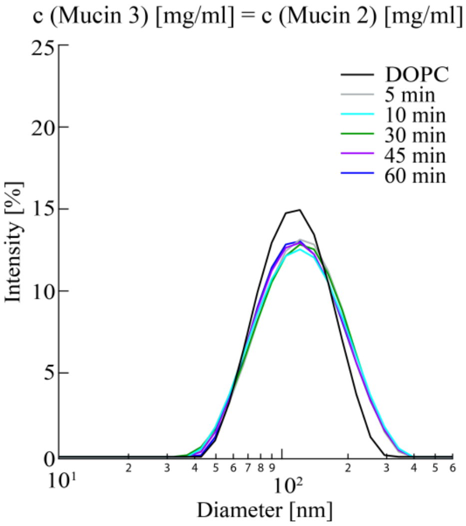

Figure 7.14 (right) Changes in size distributions of DOPC liposomes (black) after the addition of mucin 3 within 60 min, when mucin 3 is used in the same concentration (mg/ml) as mucin 2.

From the DLS results it can be concluded, that (i) the interaction of DOPC liposomes with mucin 3 is independent of mucin 3 concentration (in the range of 1 mg/ml – 10 mg/ml) and (ii) the interaction strength follows the trend:

DOPC + Mucin 2 > DOPC + Mucin 3.

The higher affinity of mucin 2 to DOPC liposomes can be explained by the difference in assumed structures and thus accessibilities of mucin 2 and mucin 3 to the phospholipid head group. Since mucin 2 has smaller (~ 28 nm) diameter of monomers while the molecular weight M_W is ~ 14 times larger than that of mucin 3, the structure of mucin 2 is assumed to be compact while that of mucin 3 is rather a random coil. Thus, due to its smaller size, mucin 2 is more accessible to the phospholipid head group and shows stronger interaction with DOPC liposomes than the more stretched mucin 3.

Interaction of Mucin with DOPE Liposomes

Figure 7.15 demonstrates the DLS results of the interaction of DOPE with mucin 2 (a, b) and mucin 3 (c, d) witin the first 5 min (upper panel) and within 60 min (lower panel). The size distributions were fitted with multi-peak lognormal distribution to extract the average diameter and FWHM of the different distributions. The obtained parameters resulted from the best fits are presented in Table 7.6.

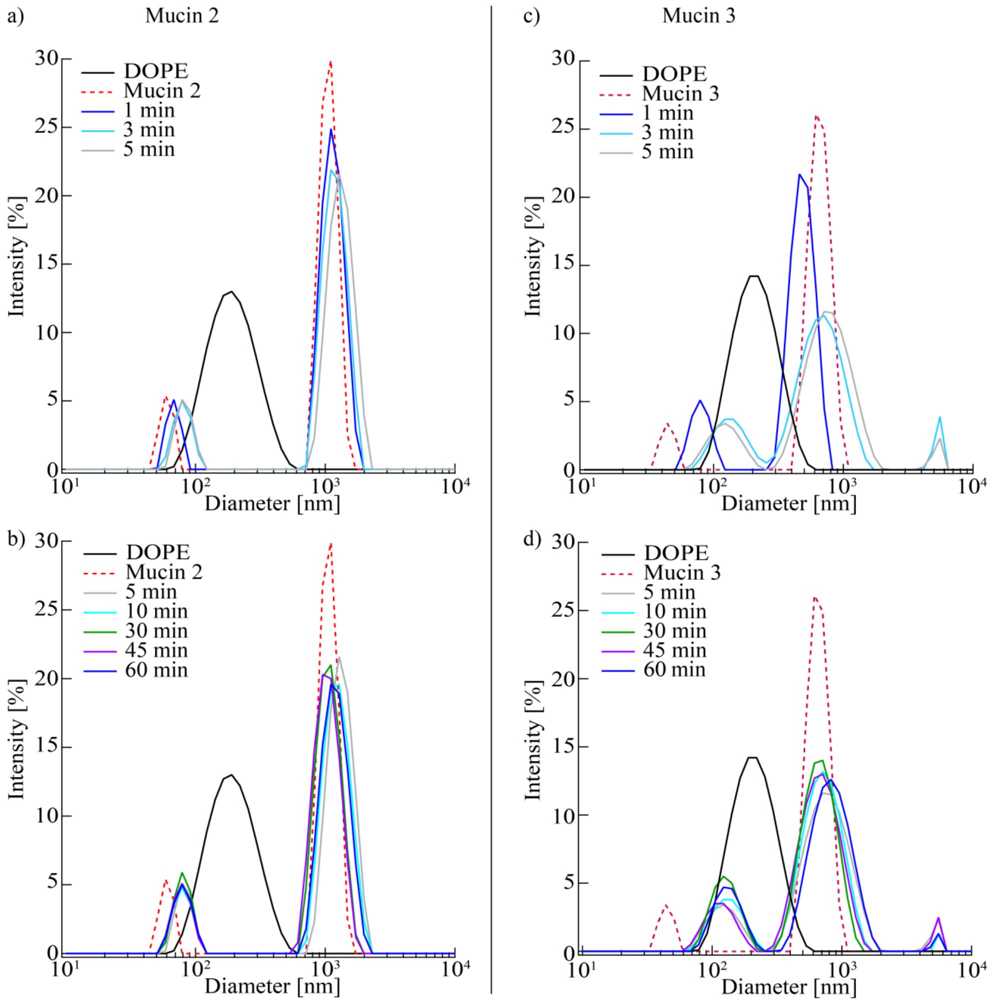

Figure 7.15 Changes in size distributions of DOPE liposomes (black) after the addition of mucin 2 (left) and mucin 3 (right) within 5 min (upper panel) and 60 min (lower panel).

On the one hand, the interaction of DOPE liposomes with mucin 2 (left) leads to an increase in size and FWHM (by the factor of 2) of the first peak within 3 min and stays stable over 60 min. On the other hand, the size distribution of mucin multimers (~ 1000 nm) shows similar peak position and width after 60 min.

The interaction of DOPE vesicels with mucin 3 seems completed after 3 min like with mucin 2. Unlike in the interaction with mucin 2, here, the size increases by the factor of ~ 3 and FWHM by the factor of ~ 6. In addition, big aggregates (~ 5000 nm) are formed after 3 min.

Table 7.6 Peak position and FWHM of the size distributions of DOPE liposomes after the addition of mucin 2 (left) and mucin 3 (right) within 60 min, with respect to pure DOPE liposomes (at t = 0 min) and mucin samples.

	Mucin 2		**Mucin 3**	
Time [min]	**Diameter [nm]**	**FWHM [nm]**	**Diameter [nm]**	**FWHM [nm]**
0 (DOPE)	**187**	**203**	**206**	**204**
0 (Mucin)	**60**	**18**	**44**	**14**
1	68	21	79	34
3	79	31	131	91
5	82	30	120	83
10	79	32	126	82
30	80	30	125	75
45	78	32	114	73
60	79	33	130	80

To investigate how strong DOPE liposomes interact with mucin monomers when multimers are absent, mucin 3 was filtered through a polycarbon filter (poresize 200 nm). Unfortunately, it was not possible to gain only monomers, instead a second fraction ($d_{\text{pentamer}} \approx 153$ nm) is present. However, the obtained DLS results are in good aggreement to the former results, as the diameter increases by ~ 90 nm and FWHM by 80 nm (Figure 7.16, Table 7.7). The second size distribution represents the interaction between DOPE liposomes and mucin 3 pentamers. The maximum diameter of this second peak increases by the factor of ~ 2 within 5 min and stays stable over time while FWHM increases. After 30 min the first size distribution becomes a shoulder and big aggregates are formed ($d \approx 6000$ nm), which underlines here as well the strong interaction between DOPE and mucin 3 multimers.

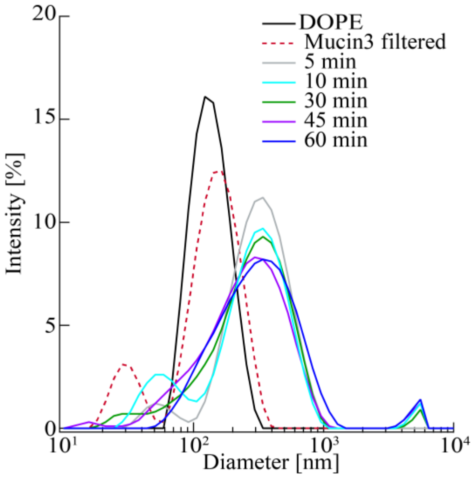

Figure 7.16 Changes in size distributions of DOPE liposomes (black) after the addition of filtered mucin 3 within 60 min.

Table 7.7 Peak position and FWHM of the size distributions of DOPE liposomes after the addition of filtered mucin 3 within 60 min, with respect to pure DOPE liposomes (at t = 0 min) and mucin 3.

	Filtered Mucin 3			
	Peak 1		**Peak 2**	
Time [min]	**Diameter [nm]**	**FWHM [nm]**	**Diameter [nm]**	**FWHM [nm]**
0 (DOPE)	**132**	**113**	**-**	**-**
0 (Mucin)	**30**	**18**	**153**	**149**
5	52	30	328	401
10	56	48	324	396
30	40	75	316	458
45	80	91	301	438
60	115	102	346	522

From the DLS results it can be concluded, that DOPE interacts with mucin 2 and mucin 3 in a different way. In case of mucin 2, DOPE liposomes interact more strongly with aggregates than with monomers. Thus, there is a small amount of DOPE liposomes left, which are available for interaction with mucin 2 monomers and just a small change in size and FWHM of the first peak is visible.

In the interaction with mucin 3, on the one hand, the DOPE liposomes also prefer the interaction with multimers, because bigger aggregates are formed after a short time. On the other hand, the interaction with monomers is strong as well. It can be assumed, that DOPE interacts strongly with both, monomers and multimers, which leads to different structures of vesicle-mucin formations (and even huge aggregates) which is visible in a distinct broadening of size distributions. However, the changes in size and FWHM shows that the interaction of DOPE liposomes follows the trend:

DOPE + Mucin 3 > DOPE + Mucin 2

7.1.4.2 Discussion

Studying the interaction of mucin 2 and mucin 3 with phospholipid liposomes (DOPC, DOPE), it was shown that (i) the interaction strength depends on the mucin type used and (ii) the interaction mechanism depends on the phospholipid used.

First, it can be concluded from the changes in peak position and FWHM of the size distributions within 60 min after the addition of mucin to the liposome suspensions, that in dependence of the lipid, one type of mucin shows stronger interaction than the other. Here the following trends for the strength of interaction were found for each phospholipid liposomes:

DOPC + Mucin 2 > DOPC + Mucin 3 and **DOPE + Mucin 3 > DOPE + Mucin 2**.

The affinity of mucins to DOPC liposomes can be explained by the different structures of mucins. Since the diameter of mucin 3 monomers is larger (~ 46 nm) with a smaller molecular weight M_W (~ 200 kDa) than that of mucin 2 (~ 28 nm and ~ 2500 kDa, respectively), the structure is assumed to be a random coil in case of mucin 3 and a compact structure in case of mucin 2. Thus, a smaller size enables mucin 2 to be more accessible to the phospholipid head group than the more stretched mucin 3.

The affinity of mucins to DOPE liposomes can be explained by different adsorption mechanisms of DOPC and DOPE liposomes to mucins revealed in this DLS study. The interaction of DOPC liposomes with mucins led to a small change in the features of the size distributions of pure liposomes. This leads to the assumption that DOPC liposomes predominantly interact with mucin monomers. In contrary to this, the overall shape of size distributions of DOPE liposomes was altered completely after the addition of mucin (2 or 3). Here, it can be assumed that the interaction of DOPE liposomes with mucin multimers is more prevalent than with monomers, which can lead to the formation of big aggregates as in case of mucin 3. Figure 7.17 gives an overview of the suggested and the dominant interactions of DOPC and DOPE liposomes with mucin 2 and mucin 3.

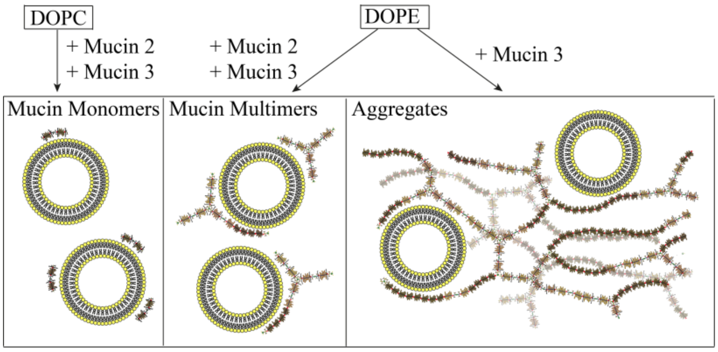

Figure 7.17 Schematic illustration of the dominant interaction between the DOPC and DOPE liposomes with mucin 2 and mucin 3.

7.1.4.3 Thermodynamic Properties of Mucin Interaction with Phospholipid Liposomes studied by Isothermal Titration Calorimetry (ITC)

To investigate the thermodynamic aspects and the influence of the charge on the interaction between mucin 2 and mucin 3 with phospholipid liposomes, ITC measurements were performed. In the experiments the liposomes solutions of DOPC, DOPE as well as DOPC + DOTAP (20 mol%) and DOPC + DOPG (20 mol%) were stepwise titrated into the protein solution and the released heat was measured. The fit of the raw data yields the changes in enthalpy (ΔH) (in respect to the heat of dilution (ΔH_d)), the binding constant K_b, the change in entropy ΔS as well as the binding stoichiometry n (for more information see section 3.2.2.7).

Interaction of Mucin 3 with DOPC Liposomes

Figure 7.18 demonstrates an ITC measurement with DOPC liposomes and mucin 3 and the resulting graph. The average change of enthalpy (ΔH) was calculated from the best three measurements and was found to be (-14.2 ± 1.6) kcal/mol (Table 7.8) which is in good agreement with the enthalpy value reported for the single binding site of 2'CMP to ribonuclease which is -15 kcal/mol.

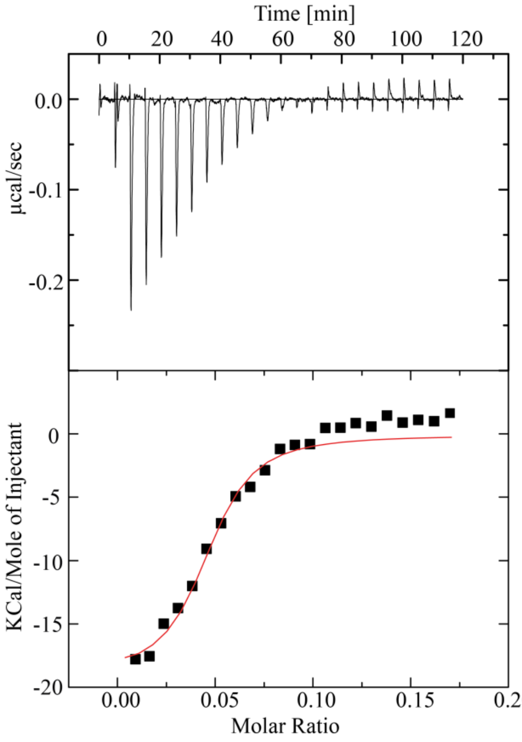

Figure 7.18 ITC measurement and the resulting graph including the fitting results (red) of mucin 3 and DOPC liposomes.

The low number of points in the first plateau indicates that the reaction saturates quickly. Thus, the change in enthalpy is difficult to be determined in some measurements. In addition, the binding constant (K_b) of the studied interaction may differ significantly from the position of the first plateau, because it plays an enormous role in the applied fitting function which is nothing but the slope at the inflection of the resulting graph. Decreasing the liposome concentration in the range from 20 µM to 10 µM and 5 µM could not solve this issue. However, the obtained results allow to estimate the range for the interaction strength of mucin 3 with DOPC liposomes.

Table 7.8 Obtained results from four ITC measurements of mucin 3 and DOPC liposomes.

Mucin 3 +	**ΔH [kcal/mol]**	**K_b [L/mol]**	**ΔS [cal/(mol*K)]]**	**n**
1) DOPC	-12.1 ± 1.3	(1.64 ± 0.39)E+07	-147.0 ± 17.9	(15.6 ± 0.8)E-02
2) DOPC	-16.1 ± 1.1	(0.19 ± 0.05)E+07	-6.1 ± 3.5	(5.4 ± 1.7)E-02
3) DOPC	-14.3 ± 1.0	(2.33 ± 1.76)E+07	-14.3 ± 4.8	(1.1 ± 0.2)E-02
average	**-14.2 ± 1.6**	**(1.38 ± 0.90)E+07**	**-55.8 ± 79.1**	**(7.5 ± 6.1)E-02**

One crucial phenomenon during the ITC measurements with mucin is the appearance of a baseline shift during the experiments (Figure 7.19). This could be indicative for the tendency of mucin 3 to stick to the wall of the sample cell, making it unavailable for interaction with the titrated phospholipid liposomes and varying the heat capacity of the cell. Thus, even at low concentrations of liposome solutions, the system is saturated quite fast. This might explain why a variation of concentrations of DOPC liposomes did not improve the presence of a more distinct plateau at the beginning.

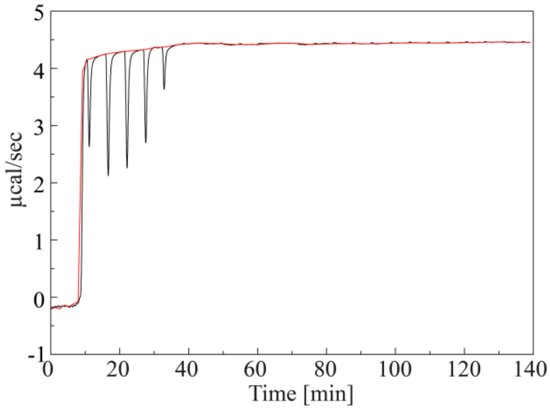

Figure 7.19 Shift of the baseline (red) during an ITC measurement (black) with mucin 3 and DOPC liposomes.

Interaction of Mucin 2 with DOPC Liposomes

To compare wether the interaction of DOPC liposomes with mucin 2 is more pronounced that with mucin 3, one ITC measurement was performed (Figure 7.20). The calculated change of enthalpy (Δ*H*) was found to be (-60.0 ± 10.3) kcal/mol (Table 7.9) which is ~ 4 times bigger than in the interaction with mucin 3. Silimar to mucin 3, mucin 2 shows sticking to the walls of the sample cell during the measurements. This behavior of mucin 2 makes it hard to gain reliable numbers. However, the outcome of this experiment supports the trend of the interaction of DOPC liposomes with mucin 2 to be stronger than with mucin 3 which was found in the previous DLS experiments.

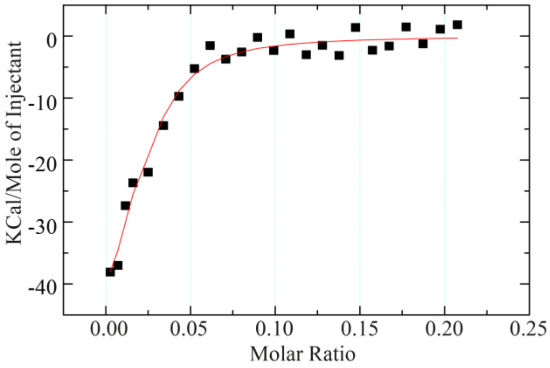

Figure 7.20 Resulting graph of the ITC measurement including the fit (red) of DOPC liposomes with mucin 2.

Table 7.9 Obtained results from ITC measurement of mucin 2 with DOPC liposomes.

Mucin 2 +	**Δ*H* [kcal/mol]**	**K_b [L/mol]**	**Δ*S* [cal/(mol*K)]]**	***n***
DOPC	-60.0 ± 10.3	(2.36 ± 0.73)E+07	-166 ± 50	(2.0 ±0.1)E-02

Interaction of Mucin 3 with DOPE Liposomes

To investigate if the strength of interaction is dependent upon the zwitterionic lipids used, one ITC measurement was performed with DOPE liposomes (Figure 7.21). It was found that the change in enthalpy (Δ*H*) is (-87.6 ± 7.4) kcal/mol (Table 7.10) which is ~ 6 times higher than in the interaction of DOPC liposomes with mucin 3. In addition, the change in enthalpy (Δ*H*) found for DOPC liposomes with mucin 2 (-60.0 ± 10.3) kcal/mol is also lower than in this experiment. Together with the results obtained by DLS measurements (previous section), it can be concluded that the high change in enthalpy is based on the interaction of DOPE liposomes mainly with mucin multimers, which releases much more heat during interaction than the DOPE interaction with single mucin molecules.

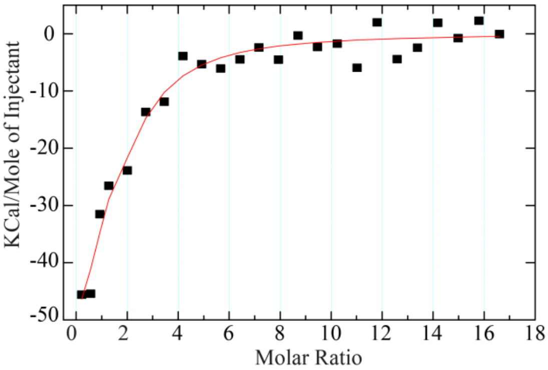

Figure 7.21 Resulting graph of the ITC measurement including the fit (red) of DOPE liposomes with mucin 3.

Table 7.10 Obtained results from ITC measurements of mucin 3 with DOPE liposomes.

Mucin 3 +	Δ*H* [kcal/mol]	K_b [L/mol]	Δ*S* [cal/(mol*K)]]	*n*
DOPE	-87.6 ± 7.4	(1.87 ± 0.39)E+07	-260 ± 80	1.3 ± 0.9

Interaction of Mucin 3 with DOTAP and DOPG incorporated Liposomes

To investigate wether the interaction of mucin 3 with phospholipid liposomes is a matter of electrostatics, one ITC measurements was performed with DOPC liposomes incorporated with 20 mol% of positively charged DOTAP or negatively charged DOPG. The same experimental conditions as with pure DOPC liposomes (5 µM) were used. The experimental results and the resulting thermodynamic constants are shown in Figure 7.22 and Table 7.11.

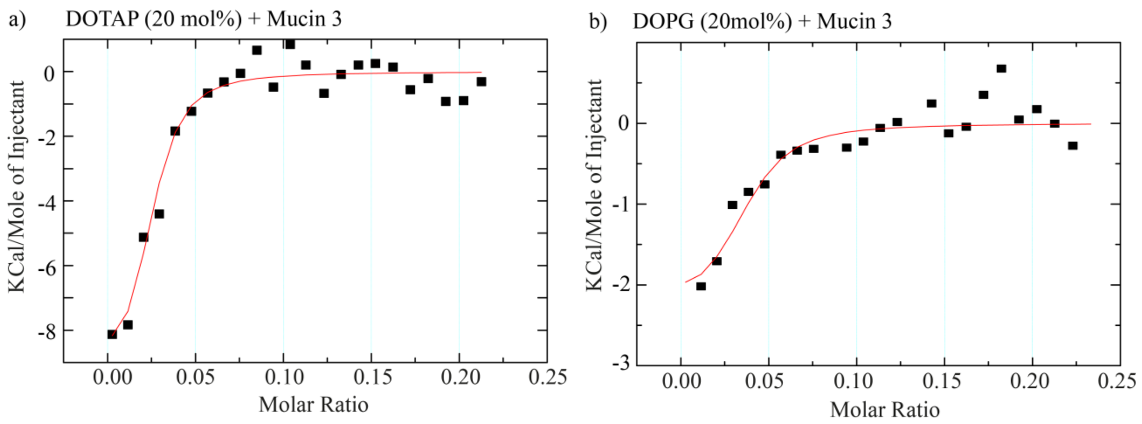

Figure 7.22 Resulting graphs of ITC measurements including the fits (red) of the interaction of mucin 3 with DOPC liposomes doped with 20 mol% of (a) DOTAP and (b) DOPG.

Table 7.11 Obtained results from ITC measurements of mucin 3 with DOPC liposomes doped with 20 mol% of DOTAP or DOPG.

Mucin 3 +	**ΔH [kcal/mol]**	**K_b [L/mol]**	**ΔS [cal/(mol*K)]**	***n***
DOTAP	-7.9 ± 0.9	(0.65 ± 0.31)E+07	-1.2 ± 0.7	(3.3 ± 0.4)E-02
DOPG	-4.0 ± 0.2	(0.45 ± 0.11)E+07	33.0 ± 9.4	(2.5 ± 0.3)E-02

The enthalpy changes (ΔH) for the protein-lipid interactions are in both cases smaller than the obtained enthalpy change for pure DOPC ($\Delta H = -18.1 \pm 4.5$ kcal/mol) while binding constants (K_b) and stoichiometry (n) are approximately in the same range. These results are in good agreement with the monolayer study (section 7.1.3). In addition, they support the conclusion that the interaction between mucin 3 and phospholipids is not a matter of electrostatics in the first place, but it is dependent upon the structure of the polar headgroup. The larger absolute value for the enthalpy change in case of DOTAP doped liposomes compared to DOPG doped liposomes can be explained by the electrostatic attraction between the positively charged DOTAP head groups and the negatively charged mucin 3.

7.1.5 Summary

The first main goal of this study was to investigate the physical properties of the glycoproteins mucin 2 and mucin 3 by light scattering techniques (SLS, DLS, zeta (ζ) potential) and surface tension measurements. The overview of the obtained results is presented in Table 7.12.

It was found, that both mucins show different populations of size distributions while the monomers were predominantly present ($\Sigma \approx 100$). It was shown, that in case of mucin 3 the size of aggregates increased with the concentration. A transition concentrations from small aggregates to larger aggregates was obtained to be c_{Half} = 1.3 mg/ml which is close to the critical micelle concentration (CMC) of 2 mg/ml found for mucin 3 by surface tension measurements. The CMC of mucin 2 was found to be 7 mg/ml. The theoretical overlap concentrations estimated to be ~ 7 mg/ml for mucin 3 and ~ 10 mg/ml for mucin 2 demonstrate that mucin samples used in this section are below or close to the overlap concentrations reported for dilute (< 3 mg/ml) and semidilute (3 – 34 mg/ml) regimes, but far below the entangled regimes of interpenetrated brushes (> 34 mg/ml) [144].

A high charge density of mucin monomers was found, confirming that both fractions of mucins have intact negatively charged carbohydrates side chains such as sialic acid (pK_a ~ 2.6), sulfated glucosamine (pK_a ~ 1) and galactoamines (pK_a ~ 1), which are negatively charged at neutral pH [142]. ζ potentials were obtained to be (-8.6 ± 0.5) mV for mucin 2 and (-10.8 ± 0.9) mV for mucin 3.

The average molecular masses were found to be (2543 ± 346) kDa for mucin 2 and (204 ± 23) kDa for mucin 3 determined by SLS measurements. From the larger diameter of monomeric mucin 3 (of ~ 46 nm) and a 14 times smaller molecular mass M_W compared to mucin 2, it was assumed that mucin 3 does not have a very compact structure but rather is a random coil or stretched chain, while mucin 2 has a compact structure.

Table 7.12 Overview of the obtained results for mucin 2 and mucin 3.

	Mucin 2	**Mucin 3**
Diameter [nm]	28 ± 7	46 ± 11
ζ potential [mV]	-8.6 ± 0.5	-10.8 ± 0.9
M_w [kDa]	2543 ± 346	204 ± 23
CMC [mg/ml]	7	2

The second main goal of this section was to investigate the interaction of mucin 2 and mucin 3 with different phospholipids by the use of different membrane models such as phospholipid monolayers and phospholipid liposomes. The interaction of mucins with the membrane models mimic the protecting function of the gel like mucus layer in the gastrointestinal tract maintained by the outer layer covered with PC lipids. Gaining information about the mechanical interactions of mucins with phospholipids will improve the medical treatment of inflammatory bowel diseases.

To examine if the interaction is a matter of electrostatics, different types of lipids were used in the membrane model systems: zwitterionic DOPC, negatively charged DOPG and positively charged DOTAP. In addition, the interaction of mucins with the two zwitterionic DOPC and DOPE were compared with each other.

It was found, that the interaction with mucin 2 and mucin 3 is not a matter of electrostatics since the zwitterionic lipids DOPC and DOPE showed a much stronger adsoprtion than the charged lipids DOTAP and DOPG in both, Langmuir isotherm and ITC experiments. In addition, the interaction between liposomes and mucin was found to be exothermic by ITC measurements. There, the enthalpy change (Δ*H*) of each interaction was obtained; leading to the conclusion that mucin 3 interacts with phospholipids following the trend (Table 7.13):

DOPE > **DOPC** > DOPC + **DOTAP** (20 mol%) > DOPC + **DOPG** (20 mol%).

Table 7.13 Overview of the obtained thermodynamic results for the interaction of each lipid liposomes with mucin 3.

Mucin 3 +	**Δ*H* [kcal/mol]**	**K_b [L/mol]**	**Δ*S* [cal/(mol*K)]]**	***n***
DOPE	-87.6 ± 7.4	(1.87 ± 0.39)E+07	-260 ± 80	1.3 ± 0.9
DOPC	-14.2 ± 1.6	(1.38 ± 0.90)E+07	-55.8 ± 79.1	(7.5 ± 6.1)E-02
DOTAP	-7.9 ± 0.9	(0.65 ± 0.31)E+07	-1.2 ± 0.7	(3.3 ± 0.4)E-02
DOPG	-4.0 ± 0.2	(0.45 ± 0.11)E+07	33.0 ± 9.4	(2.5 ± 0.3)E-02

Moreover, the zwitterionic lipids DOPE and DOPC and their interaction with mucin 2 and mucin 3 were compared to each other. Here a higher enthalpy change (Δ*H*) was found for DOPE than for DOPC which can be explained with the assumed affinity mechanism supported by DLS results (Figure 7.17). The change in peak position and FWHM of the size distributions led to the assumption that DOPC mainly interacts with the mucin monomers, while DOPE predominantly interacts with mucin multimers. This can lead to the formation of big aggregates as found in case of mucin 3. Amongst the zwitterionic lipids, the following trend for the interaction with mucin 2 or mucin 3 was found to be:

DOPC + Mucin 2 > DOPC + Mucin 3 and **DOPE + Mucin 3 > DOPE + Mucin 2**.

Bibliography

1. Kinnunen, P. K., On the Principles of Functional Ordering in Biological Membranes. *Chemistry and physics of lipids* **1991,** *57*, 375-399.

2. Kinnunen, P. K.; Kõiv, A.; Lehtonen, J. Y.; Rytömaa, M.; Mustonen, P., Lipid Dynamics and Peripheral Interactions of Proteins with Membrane Surfaces. *Chemistry and physics of lipids* **1994,** *73*, 181-207.

3. Mouritsen, O. G., *Life-as a Matter of Fat*. Springer: 2005.

4. Singer, S. J.; Nicolson, G. L., The Fluid Mosaic Model of the Structure of Cell Membranes. *Science* **1972,** *175*, 720-731.

5. Alberts, B.; Johnson, A.; Lewis, J.; Raff, M.; Roberts, K.; Walter, P., B Cells and Antibodies. **2002**.

6. Karp, G., *Cell Biology*. Wiley Online Library: 2010.

7. Wood, L.; Gibson, P.; Garg, M., Biomarkers of Lipid Peroxidation, Airway Inflammation and Asthma. *European Respiratory Journal* **2003,** *21,* 177-186.

8. Ames, B. N.; Shigenaga, M. K.; Hagen, T. M., Oxidants, Antioxidants, and the Degenerative Diseases of Aging. *Proceedings of the National Academy of Sciences* **1993,** *90*, 7915-7922.

9. Domingues, M. R. M.; Reis, A.; Domingues, P., Mass Spectrometry Analysis of Oxidized Phospholipids. *Chemistry and physics of lipids* **2008,** *156*, 1-12.

10. Kinnunen, P. K., Amyloid Formation on Lipid Membrane Surfaces. *Open Biol J* **2009,** *2*, 163-175.

11. Kinnunen, P. K., Fusion of Lipid Bilayers: A Model Involving Mechanistic Connection to H II Phase Forming Lipids. *Chemistry and Physics of lipids* **1992,** *63*, 251-258.

12. Mattila, J.-P.; Sabatini, K.; Kinnunen, P. K., Interaction of Cytochrome C with 1-Palmitoyl-2-Azelaoyl-Sn-Glycero-3-Phosphocholine: Evidence for Acyl Chain Reversal. *Langmuir* **2008,** *24*, 4157-4160.

13. Khandelia, H.; Mouritsen, O. G., Lipid Gymnastics: Evidence of Complete Acyl Chain Reversal in Oxidized Phospholipids from Molecular Simulations. *Biophysical Journal* **2009,** *96*, 2734-2743.

14. Berliner, J. A.; Heinecke, J. W., The Role of Oxidized Lipoproteins in Atherogenesis. *Free Radical Biology and Medicine* **1996,** *20*, 707-727.

15. Halliwell, B.; Gutteridge, J., Role of Free Radical and Catalytic Metal Ions in Human Disease: An Overview. **1990**.

16. Zhang, X. Y.; Tan, Y. L.; Cao, L. Y.; Wu, G. Y.; Xu, Q.; Shen, Y.; Zhou, D. F., Antioxidant Enzymes and Lipid Peroxidation in Different Forms of Schizophrenia Treated with Typical and Atypical Antipsychotics. *Schizophrenia research* **2006,** *81*, 291-300.

17. Cejas, P.; Casado, E.; Belda-Iniesta, C.; De Castro, J.; Espinosa, E.; Redondo, A.; Sereno, M.; García-Cabezas, M. Á.; Vara, J. A.; Domínguez-Cáceres, A., Implications of Oxidative Stress and Cell Membrane Lipid Peroxidation in Human Cancer (Spain). *Cancer Causes & Control* **2004,** *15*, 707-719.

18. Mahalka, A. K.; Maury, C. P. J.; Kinnunen, P. K., 1-Palmitoyl-2-(9′-Oxononanoyl)-Sn-Glycero-3-Phosphocholine, an Oxidized Phospholipid, Accelerates Finnish Type Familial Gelsolin Amyloidosis in Vitro. *Biochemistry* **2011,** *50*, 4877-4889.

19. Uhlson, C.; Harrison, K.; Allen, C. B.; Ahmad, S.; White, C. W.; Murphy, R. C., Oxidized Phospholipids Derived from Ozone-Treated Lung Surfactant Extract Reduce Macrophage and Epithelial Cell Viability. *Chemical research in toxicology* **2002,** *15*, 896-906.

20. Chang, M.-K.; Bergmark, C.; Laurila, A.; Hörkkö, S.; Han, K.-H.; Friedman, P.; Dennis, E. A.; Witztum, J. L., Monoclonal Antibodies against Oxidized Low-Density Lipoprotein Bind to Apoptotic Cells and Inhibit Their Phagocytosis by Elicited Macrophages: Evidence That Oxidation-Specific Epitopes Mediate Macrophage Recognition. *Proceedings of the National Academy of Sciences* **1999,** *96*, 6353-6358.

21. Koppaka, V.; Axelsen, P. H., Accelerated Accumulation of Amyloid Β Proteins on Oxidatively Damaged Lipid Membranes. *Biochemistry* **2000,** *39*, 10011-10016.

22. Roentgen, W., Ueber Eine Neue Art Von Strahlung., Aus Den Sitzungsberichten Der Wuerzburger Physik. *Medic. Gesellschaft, Wuerzburg* **1895**.

23. Compton, A. H., A Quantum Theory of the Scattering of X-Rays by Light Elements. *Physical review* **1923,** *21*, 483.

24. Tolan, M., Reflectivity of X-Rays from Surfaces. *X-Ray Scattering from Soft-Matter Thin Films: Materials Science and Basic Research* **1999**, 5-31.

25. Als-Nielsen, J.; McMorrow, D., *Elements of Modern X-Ray Physics*. John Wiley & Sons: 2011.

26. Russell, T., X-Ray and Neutron Reflectivity for the Investigation of Polymers. *Materials science reports* **1990,** *5*, 171-271.

27. Parratt, L. G., Surface Studies of Solids by Total Reflection of X-Rays. *Physical review* **1954,** *95*, 359.

28. Abelès, F., Recherches Théoriques Sur Les Propriétés Optiques Des Lames Minces. *J. Phys. Rad* **1950,** *11*, 307.

29. Novikova, N. N.; Yurieva, E. A.; Zheludeva, S. I.; Kovalchuk, M. V.; Stepina, N. D.; Tolstikhina, A. L.; Gaynutdinov, R. V.; Urusova, D. V.; Matkovskaya, T. A.; Rubtsov, A. M., X-Ray Fluorescence Methods for Investigations of Lipid/Protein Membrane Models. *Journal of synchrotron radiation* **2005,** *12*, 511-516.

30. Ohta, K.; Ishida, H., Matrix Formalism for Calculation of Electric Field Intensity of Light in Stratified Multilayered Films. *Applied optics* **1990,** *29*, 1952-1959.

31. Abuillan, W.; Schneck, E.; Korner, A.; Brandenburg, K.; Gutsmann, T.; Gill, T.; Vorobiev, A.; Konovalov, O.; Tanaka, M., Physical Interactions of Fish Protamine and Antisepsis Peptide Drugs with Bacterial Membranes Revealed by Combination of Specular X-Ray Reflectivity and Grazing-Incidence X-Ray Fluorescence. *Physical Review E* **2013,** *88*.

32. Schneck, E.; Schubert, T.; Konovalov, O. V.; Quinn, B. E.; Gutsmann, T.; Brandenburg, K.; Oliveira, R. G.; Pink, D. A.; Tanaka, M., Quantitative Determination of Ion Distributions in Bacterial Lipopolysaccharide Membranes by Grazing-Incidence X-Ray Fluorescence. *Proceedings of the National Academy of Sciences* **2010,** *107*, 9147-9151.

33. Boggs, P. T.; Donaldson, J. R.; Schnabel, R. B., Algorithm 676: Odrpack: Software for Weighted Orthogonal Distance Regression. *ACM Transactions on Mathematical Software (TOMS)* **1989,** *15*, 348-364.

34. Sinha, S.; Sirota, E. B.; Garoff, S.; Stanley, H., X-Ray and Neutron Scattering from Rough Surfaces. *Physical Review B* **1988,** *38*, 2297.

35. Lei, N.; Safinya, C.; Bruinsma, R., Discrete Harmonic Model for Stacked Membranes: Theory and Experiment. *Journal de Physique II* **1995,** *5*, 1155-1163.

36. Kern, W.; Puotinen, D., Rca Review, Vol. 31rca Laboratories. *Princeton, NJ and RCA Solid-State Division, Sommerville, NJ* **1970**, 187.

37. Oliveira, R. G.; Schneck, E.; Quinn, B. E.; Konovalov, O. V.; Brandenburg, K.; Seydel, U.; Gill, T.; Hanna, C. B.; Pink, D. A.; Tanaka, M., Physical Mechanisms of Bacterial Survival Revealed by Combined Grazing-Incidence X-Ray Scattering and Monte Carlo Simulation. *Comptes Rendus Chimie* **2009,** *12*, 209-217.

38. Abuillan, W.; Schneck, E.; Körner, A.; Brandenburg, K.; Gutsmann, T.; Gill, T.; Vorobiev, A.; Konovalov, O.; Tanaka, M., Physical Interactions of Fish Protamine and Antisepsis Peptide Drugs with Bacterial Membranes Revealed by Combination of Specular X-Ray Reflectivity and Grazing-Incidence X-Ray Fluorescence. *Physical Review E* **2013,** *88*, 012705.

39. Langmuir, I.; Schaefer, V. J., Properties and Structure of Protein Monolayers. *Chemical Reviews* **1939,** *24*, 181-202.

40. Dynarowicz-Łątka, P.; Kita, K., Molecular Interaction in Mixed Monolayers at the Air/Water Interface. *Advances in colloid and interface science* **1999,** *79*, 1-17.

41. Rideal, E.; Davies, J., Interfacial Phenomena. Academic Press, New York: 1963.

42. Davies, J.; Rideal, E., Interfacial Phenomena. 1961. New York: Academic Press.

43. Costin, I.; Barnes, G., Two-Component Monolayers. I. Experimental Procedures and Selection of a System. *Journal of Colloid and Interface Science* **1975,** *51*, 94-105.

44. Brockman, H., Dipole Potential of Lipid Membranes. *Chemistry and physics of lipids* **1994,** *73*, 57-79.

45. Vogel, V.; Möbius, D., Local Surface Potentials and Electric Dipole Moments of Lipid Monolayers: Contributions of the Water/Lipid and the Lipid/Air Interfaces. *Journal of colloid and interface science* **1988,** *126*, 408-420.

46. Vogel, V.; Möbius, D., Hydrated Polar Groups in Lipid Monolayers: Effective Local Dipole Moments and Dielectric Properties. *Thin Solid Films* **1988,** *159*, 73-81.

47. Demchak, R. J.; Fort, T., Surface Dipole Moments of Close-Packed Un-Ionized Monolayers at the Air-Water Interface. *Journal of Colloid and Interface Science* **1974,** *46*, 191-202.

48. Nelson, A., Co-Refinement of Multiple-Contrast Neutron/X-Ray Reflectivity Data Using Motofit. *Journal of Applied Crystallography* **2006,** *39*, 273-276.

49. Miller, C. E.; Majewski, J.; Gog, T.; Kuhl, T. L., Characterization of Biological Thin Films at the Solid-Liquid Interface by X-Ray Reflectivity. *Physical review letters* **2005,** *94*, 238104.

50. Novakova, E.; Giewekemeyer, K.; Salditt, T., Structure of Two-Component Lipid Membranes on Solid Support: An X-Ray Reflectivity Study. *Physical Review E* **2006,** *74*, 051911.

51. Tolan, M.; from Soft-Matter, X.-r. S., Thin Films: Materials Science and Basic Research. *Springer Tracts in Modern Physics (Springer, Berlin, 1999)* **1999,** *148*.

52. Schneck, E.; Rehfeldt, F.; Oliveira, R. G.; Gege, C.; Demé, B.; Tanaka, M., Modulation of Intermembrane Interaction and Bending Rigidity of Biomembrane Models Via Carbohydrates Investigated by Specular and Off-Specular Neutron Scattering. *Physical Review E* **2008,** *78*, 061924.

53. Schneck, E.; Oliveira, R. G.; Rehfeldt, F.; Demé, B.; Brandenburg, K.; Seydel, U.; Tanaka, M., Mechanical Properties of Interacting Lipopolysaccharide Membranes from Bacteria Mutants Studied by Specular and Off-Specular Neutron Scattering. *Physical Review E* **2009,** *80*, 041929.

54. Clark, N. A.; Lunacek, J. H.; Benedek, G. B., A Study of Brownian Motion Using Light Scattering. *Am. J. Phys* **1970,** *38*, 575-585.

55. Zasloff, M., Antimicrobial Peptides of Multicellular Organisms. *Nature* **2002,** *415*, 389-395.

56. Krasnici, S.; Werner, A.; Eichhorn, M. E.; Schmitt-Sody, M.; Pahernik, S. A.; Sauer, B.; Schulze, B.; Teifel, M.; Michaelis, U.; Naujoks, K., Effect of the Surface Charge of Liposomes on Their Uptake by Angiogenic Tumor Vessels. *International journal of cancer* **2003,** *105*, 561-567.

57. Domingues, M. M.; Santiago, P. S.; Castanho, M. A.; Santos, N. C., What Can Light Scattering Spectroscopy Do for Membrane-Active Peptide Studies? *Journal of Peptide Science* **2008,** *14*, 394-400.

58. McLaughlin, S., The Electrostatic Properties of Membranes. *Annual review of biophysics and biophysical chemistry* **1989,** *18*, 113-136.

59. Epand, R. M., Do Proteins Facilitate the Formation of Cholesterol-Rich Domains? *Biochimica et Biophysica Acta (BBA)-Biomembranes* **2004,** *1666*, 227-238.

60. Falla, T. J.; Hancock, R., Improved Activity of a Synthetic Indolicidin Analog. *Antimicrobial agents and chemotherapy* **1997,** *41*, 771-775.

61. Cross, G. H.; Ren, Y.; Freeman, N. J., Young’s Fringes from Vertically Integrated Slab Waveguides: Applications to Humidity Sensing. *Journal of applied physics* **1999,** *86*, 6483-6488.

62. Cross, G. H.; Reeves, A.; Brand, S.; Swann, M. J.; Peel, L. L.; Freeman, N. J.; Lu, J. R., The Metrics of Surface Adsorbed Small Molecules on the Young's Fringe Dual-Slab Waveguide Interferometer. *Journal of Physics D: Applied Physics* **2004,** *37*, 74.

63. Swann, M. J.; Peel, L. L.; Carrington, S.; Freeman, N. J., Dual-Polarization Interferometry: An Analytical Technique to Measure Changes in Protein Structure in Real Time, to Determine the Stoichiometry of Binding Events, and to Differentiate between Specific and Nonspecific Interactions. *Analytical biochemistry* **2004,** *329*, 190-198.

64. Cross, G. H.; Reeves, A. A.; Brand, S.; Popplewell, J. F.; Peel, L. L.; Swann, M. J.; Freeman, N. J., A New Quantitative Optical Biosensor for Protein Characterisation. *Biosensors and Bioelectronics* **2003,** *19*, 383-390.

65. Mashaghi, A.; Swann, M.; Popplewell, J.; Textor, M.; Reimhult, E., Optical Anisotropy of Supported Lipid Structures Probed by Waveguide Spectroscopy and Its Application to Study of Supported Lipid Bilayer Formation Kinetics. *Analytical chemistry* **2008,** *80*, 3666-3676.

66. Lee, T.-H.; Hall, K. N.; Swann, M. J.; Popplewell, J. F.; Unabia, S.; Park, Y.; Hahm, K.-S.; Aguilar, M.-I., The Membrane Insertion of Helical Antimicrobial Peptides from the N-Terminus of Helicobacter Pylori Ribosomal Protein L1. *Biochimica et Biophysica Acta (BBA)-Biomembranes* **2010,** *1798*, 544-557.

67. Hammond, D. J.; Singh, S. K.; Thompson, J. A.; Beeler, B. W.; Rusiñol, A. E.; Pangburn, M. K.; Potempa, L. A.; Agrawal, A., Identification of Acidic Ph-Dependent Ligands of Pentameric C-Reactive Protein. *Journal of Biological Chemistry* **2010,** *285*, 36235-36244.

68. Seelig, J., Titration Calorimetry of Lipid-Peptide Interactions. *Biochimica et biophysica acta* **1997,** *1331*, 103-16.

69. Leavitt, S.; Freire, E., Direct Measurement of Protein Binding Energetics by Isothermal Titration Calorimetry. *Current Opinion in Structural Biology* **2001,** *11*, 560-566.

70. Curie, J.; Curie, P., An Oscillating Quartz Crystal Mass Detector. *Rendu* **1880,** *91*, 294-297.

71. Höök, F., *Development of a Novel Qcm Technique for Protein Adsorption Studies*. Chalmers University of Technology: 1997.

72. Sauerbrey, G., Verwendung Von Schwingquarzen Zur Wägung Dünner Schichten Und Zur Mikrowägung. *Zeitschrift für physik* **1959,** *155*, 206-222.

73. Bingen, P.; Wang, G.; Steinmetz, N. F.; Rodahl, M.; Richter, R. P., Solvation Effects in the Quartz Crystal Microbalance with Dissipation Monitoring Response to Biomolecular Adsorption. A Phenomenological Approach. *Analytical chemistry* **2008,** *80*, 8880-8890.

74. Rodahl, M.; Höök, F.; Krozer, A.; Brzezinski, P.; Kasemo, B., Quartz Crystal Microbalance Setup for Frequency and Q-Factor Measurements in Gaseous and Liquid Environments. *Review of Scientific Instruments* **1995,** *66*, 3924-3930.

75. Rodahl, M.; Kasemo, B., On the Measurement of Thin Liquid Overlayers with the Quartz-Crystal Microbalance. *Sensors and Actuators A: Physical* **1996,** *54*, 448-456.

76. Rodahl, M.; Kasemo, B., A Simple Setup to Simultaneously Measure the Resonant Frequency and the Absolute Dissipation Factor of a Quartz Crystal Microbalance. *Review of Scientific Instruments* **1996,** *67*, 3238-3241.

77. Domack, A.; Prucker, O.; Rühe, J.; Johannsmann, D., Swelling of a Polymer Brush Probed with a Quartz Crystal Resonator. *Physical Review E* **1997,** *56*, 680.

78. Voinova, M. V.; Rodahl, M.; Jonson, M.; Kasemo, B., Viscoelastic Acoustic Response of Layered Polymer Films at Fluid-Solid Interfaces: Continuum Mechanics Approach. *Physica Scripta* **1999,** *59*, 391.

79. Sackmann, E., Supported Membranes: Scientific and Practical Applications. *Science* **1996,** *271*, 43-48.

80. Körner, A.; Deichmann, C.; Rossetti, F.; Köhler, A.; Konovalov, O.; Engler, A. J., Cell Differentiation of Pluripotent Tissue Sheets Immobilized on Supported. **2013**.

81. Lipowsky, R.; Sackmann, E., *Structure and Dynamics of Membranes: I. From Cells to Vesicles/II. Generic and Specific Interactions*. Elsevier: 1995.

82. Tsukanova, V.; Grainger, D. W.; Salesse, C., Monolayer Behavior of Nbd-Labeled Phospholipids at the Air/Water Interface. *Langmuir* **2002,** *18*, 5539-5550.

83. Taylor, D., Developments in the Theoretical Modelling and Experimental Measurement of the Surface Potential of Condensed Monolayers. *Advances in colloid and interface science* **2000,** *87*, 183-203.

84. Majewski, J.; Kuhl, T.; Kjaer, K.; Smith, G., Packing of Ganglioside-Phospholipid Monolayers: An X-Ray Diffraction and Reflectivity Study. *Biophysical Journal* **2001,** *81*, 2707-2715.

85. Weygand, M.; Wetzer, B.; Pum, D.; Sleytr, U. B.; Cuvillier, N.; Kjaer, K.; Howes, P. B.; Lösche, M., Bacterial S-Layer Protein Coupling to Lipids: X-Ray Reflectivity and Grazing Incidence Diffraction Studies. *Biophysical Journal* **1999,** *76*, 458-468.

86. Vogel, M.; Münster, C.; Fenzl, W.; Salditt, T., Thermal Unbinding of Highly Oriented Phospholipid Membranes. *Physical review letters* **2000,** *84*, 390.

87. Sabatini, K.; Mattila, J.-P.; Megli, F. M.; Kinnunen, P. K., Characterization of Two Oxidatively Modified Phospholipids in Mixed Monolayers with DPPC. *Biophysical Journal* **2006,** *90*, 4488-4499.

88. Cwiklik, L.; Jungwirth, P., Massive Oxidation of Phospholipid Membranes Leads to Pore Creation and Bilayer Disintegration. *Chemical Physics Letters* **2010,** *486*, 99-103.

89. Wong-Ekkabut, J.; Xu, Z.; Triampo, W.; Tang, I.; Peter Tieleman, D.; Monticelli, L., Effect of Lipid Peroxidation on the Properties of Lipid Bilayers: A Molecular Dynamics Study. *Biophysical Journal* **2007,** *93*, 4225-4236.

90. Huster, D.; Jin, A. J.; Arnold, K.; Gawrisch, K., Water Permeability of Polyunsaturated Lipid Membranes Measured by ^{17}O NMR. *Biophysical Journal* **1997,** *73*, 855-864.

91. Oliveira, R. G.; Schneck, E.; Quinn, B. E.; Konovalov, O. V.; Brandenburg, K.; Gutsmann, T.; Gill, T.; Hanna, C. B.; Pink, D. A.; Tanaka, M., Crucial Roles of Charged Saccharide Moieties in Survival of Gram Negative Bacteria against Protamine Revealed by Combination of Grazing Incidence X-Ray Structural Characterizations and Monte Carlo Simulations. *Physical Review E* **2010,** *81*, 041901.

92. Makino, M.; Yoshikawa, K., Dynamic Properties of a Phospholipid Thin Film at an Air/Water Interface with a Periodic Change in Surface Area. *Langmuir* **1997,** *13*, 7125-7134.

93. Huster, D.; Arnold, K.; Gawrisch, K., Strength of Ca^{2+} Binding to Retinal Lipid Membranes: Consequences for Lipid Organization. *Biophysical Journal* **2000,** *78*, 3011-3018.

94. Böckmann, R. A.; Grubmüller, H., Multistep Binding of Divalent Cations to Phospholipid Bilayers: A Molecular Dynamics Study. *Angewandte Chemie International Edition* **2004,** *43*, 1021-1024.

95. Jurkiewicz, P.; Cwiklik, L.; Vojtíšková, A.; Jungwirth, P.; Hof, M., Structure, Dynamics, and Hydration of POPC/Pops Bilayers Suspended in Nacl, Kcl, and Cscl Solutions. *Biochimica et Biophysica Acta (BBA) - Biomembranes* **2012,** *1818*, 609-616.

96. Sabatini, K.; Mattila, J.-P.; Megli, F. M.; Kinnunen, P. K. J., Characterization of Two Oxidatively Modified Phospholipids in Mixed Monolayers with DPPC. *Biophysical Journal* **2006,** *90*, 4488-4499.

97. Jurkiewicz, P.; Olżyńska, A.; Cwiklik, L.; Conte, E.; Jungwirth, P.; Megli, F. M.; Hof, M., Biophysics of Lipid Bilayers Containing Oxidatively Modified Phospholipids:

Insights from Fluorescence and Epr Experiments and from Md Simulations. *Biochimica et Biophysica Acta (BBA)-Biomembranes* **2012,** *1818*, 2388-2402.

98. Haverd, V. E.; Warr, G. G., Cation Selectivity at Air/Anionic Surfactant Solution Interfaces. *Langmuir* **2000,** *16*, 157-160.

99. Seelig, J., Interaction of Phospholipids with Ca< Sup> 2+</Sup> Ions. On the Role of the Phospholipid Head Groups. *Cell biology international reports* **1990,** *14*, 353-360.

100. Salditt, T., Structure and Fluctuations of Highly Oriented Phospholipid Membranes. *Current opinion in colloid & interface science* **2000,** *5*, 19-26.

101. Schneck, E.; Demé, B.; Gege, C.; Tanaka, M., Membrane Adhesion Via Homophilic Saccharide-Saccharide Interactions Investigated by Neutron Scattering. *Biophysical journal* **2011,** *100*, 2151-2159.

102. Makky, A.; Tanaka, M., Impact of Lipid Oxidization on Biophysical Properties of Model Cell Membranes. *The Journal of Physical Chemistry B* **2015**.

103. Hofmeister, F., Zur Lehre Von Der Wirkung Der Salze. *Archiv für experimentelle Pathologie und Pharmakologie* **1888,** *25*, 1-30.

104. Thompson, D.; Pepys, M. B.; Wood, S. P., The Physiological Structure of Human C-Reactive Protein and Its Complex with Phosphocholine. *Structure* **1999,** *7*, 169-177.

105. Pepys, M. B.; Hirschfield, G. M., C-Reactive Protein: A Critical Update. *Journal of Clinical Investigation* **2003,** *111*, 1805.

106. Vigushin, D. M.; Pepys, M. B.; Hawkins, P. N., Metabolic and Scintigraphic Studies of Radioiodinated Human C-Reactive Protein in Health and Disease. *Journal of clinical investigation* **1993,** *91*, 1351.

107. Chang, M.-K.; Binder, C. J.; Torzewski, M.; Witztum, J. L., C-Reactive Protein Binds to Both Oxidized Ldl and Apoptotic Cells through Recognition of a Common Ligand: Phosphorylcholine of Oxidized Phospholipids. *Proceedings of the National Academy of Sciences* **2002,** *99*, 13043-13048.

108. Volanakis, J. E.; Wirtz, K. W., Interaction of C-Reactive Protein with Artificial Phosphatidylcholine Bilayers. **1979**.

109. Mattila, J.-P.; Sabatini, K.; Kinnunen, P. K., Oxidized Phospholipids as Potential Novel Drug Targets. *Biophysical Journal* **2007,** *93*, 3105-3112.

110. Pepys, M.; Baltz, M. L., Acute Phase Proteins with Special Reference to C-Reactive Protein and Related Proteins (Pentaxins) and Serum Amyloid a Protein. *Advances in immunology* **1982,** *34*, 141-212.

111. Kushner, I.; Kaplan, M. H., Studies of Acute Phase Protein I, an Immunohistochemical Method for the Localization of C-Reactive Protein in Rabbits, Association with Necrosis in Local Inflammatory Lesions. *The Journal of experimental medicine* **1961,** *114*, 961-974.

112. Gershov, D.; Kim, S.; Brot, N.; Elkon, K. B., C-Reactive Protein Binds to Apoptotic Cells, Protects the Cells from Assembly of the Terminal Complement Components, and Sustains an Antiinflammatory Innate Immune Response Implications for Systemic Autoimmunity. *The Journal of experimental medicine* **2000,** *192*, 1353-1364.

113. Đorđević, V.; Ristić, T.; Ćosić, V.; Vlahović, P.; Zvezdanović, L.; Đorđević, G., Inflammatory and Apoptotic Markers in Ischemic Heart Disease Patients. *Journal of Medical Biochemistry* **2008,** *27*, 154-160.

114. Koller, D.; Hackl, H.; Bogner-Strauß, J. G.; Hermetter, A., Effects of Oxidized Phospholipids on Gene Expression in Raw 264.7 Macrophages: A Microarray Study. **2014**.

115. Cowsill, B. J.; Coffey, P. D.; Yaseen, M.; Waigh, T. A.; Freeman, N. J.; Lu, J. R., Measurement of the Thickness of Ultra-Thin Adsorbed Globular Protein Layers with Dual-Polarisation Interferometry: A Comparison with Neutron Reflectivity. *Soft Matter* **2011,** *7*, 7223-7230.

116. Stottrup, B. L.; Keller, S. L., Phase Behavior of Lipid Monolayers Containing DPPC and Cholesterol Analogs. *Biophysical journal* **2006,** *90*, 3176-3183.

117. Kinnunen, P. K.; Kaarniranta, K.; Mahalka, A. K., Protein-Oxidized Phospholipid Interactions in Cellular Signaling for Cell Death: From Biophysics to Clinical Correlations. *Biochimica et Biophysica Acta (BBA)-Biomembranes* **2012,** *1818*, 2446-2455.

118. Ducharme, D.; Max, J. J.; Salesse, C.; Leblanc, R. M., Ellipsometric Study of the Physical States of Phosphatidylcholines at the Air-Water Interface. *Journal of Physical Chemistry* **1990,** *94*, 1925-1932.

119. Keller, C.; Glasmästar, K.; Zhdanov, V.; Kasemo, B., Formation of Supported Membranes from Vesicles. *Physical Review Letters* **2000,** *84*, 5443.

120. Ji, S.-R.; Wu, Y.; Potempa, L. A.; Qiu, Q.; Zhao, J., Interactions of C-Reactive Protein with Low-Density Lipoproteins: Implications for an Active Role of Modified C-Reactive Protein in Atherosclerosis. *The international journal of biochemistry & cell biology* **2006,** *38*, 648-661.

121. Volanakis, J. E., Human C-Reactive Protein: Expression, Structure, and Function. *Molecular immunology* **2001,** *38*, 189-197.

122. Palinski, W.; Hörkkö, S.; Miller, E.; Steinbrecher, U. P.; Powell, H. C.; Curtiss, L. K.; Witztum, J. L., Cloning of Monoclonal Autoantibodies to Epitopes of Oxidized Lipoproteins from Apolipoprotein E-Deficient Mice. Demonstration of Epitopes of Oxidized Low Density Lipoprotein in Human Plasma. *Journal of Clinical Investigation* **1996,** *98*, 800.

123. Shaw, P. X.; Hörkkö, S.; Chang, M.-K.; Curtiss, L. K.; Palinski, W.; Silverman, G. J.; Witztum, J. L., Natural Antibodies with the T15 Idiotype May Act in Atherosclerosis, Apoptotic Clearance, and Protective Immunity. *The Journal of clinical investigation* **2000,** *105*, 1731-1740.

124. Huber, J.; Vales, A.; Mitulovic, G.; Blumer, M.; Schmid, R.; Witztum, J. L.; Binder, B. R.; Leitinger, N., Oxidized Membrane Vesicles and Blebs from Apoptotic Cells Contain Biologically Active Oxidized Phospholipids That Induce Monocyte-Endothelial Interactions. *Arteriosclerosis, thrombosis, and vascular biology* **2002,** *22*, 101-107.

125. Perez-Vilar, J.; Hill, R. L., The Structure and Assembly of Secreted Mucins. *Journal of Biological Chemistry* **1999,** *274*, 31751-31754.

126. Allen, A.; Pain, R. H.; Robson, T. R., Model for the Structure of the Gastric Mucous Gel. *Nature* **1976,** *264*, 88-89.

127. Allen, A.; Snary, D., The Structure and Function of Gastric Mucus. *Gut* **1972,** *13*, 666-672.

128. Schneider, H.; Braun, A.; Fullekrug, J.; Stremmel, W.; Ehehalt, R., Lipid Based Therapy for Ulcerative Colitis-Modulation of Intestinal Mucus Membrane Phospholipids as a Tool to Influence Inflammation. *Int J Mol Sci* **2010,** *11*, 4149-64.

129. Lichtenberger, L. M., The Hydrophobic Barrier Properties of Gastrointestinal Mucus. *Annu Rev Physiol* **1995,** *57*, 565-83.

130. Bengmark, S.; Jeppsson, B., Gastrointestinal Surface Protection and Mucosa Reconditioning. *Journal of Parenteral and Enteral Nutrition* **1995,** *19*, 410-415.

131. Kao, Y. C.; Lichtenberger, L. M., A Method to Preserve Extracellular Surfactant-Like Phospholipids on the Luminal Surface of Rodent Gastric Mucosa. *Journal of Histochemistry & Cytochemistry* **1990,** *38*, 427-431.

132. Gendler, S. J.; Spicer, A. P., Epithelial Mucin Genes. *Annual review of physiology* **1995,** *57*, 607-34.

133. Perez-Vilar, J.; Hill, R. L., The Structure and Assembly of Secreted Mucins. *The Journal of biological chemistry* **1999,** *274*, 31751-4.

134. Feagins, L. A.; Souza, R. F.; Spechler, S. J., Carcinogenesis in Ibd: Potential Targets for the Prevention of Colorectal Cancer. *Nature Reviews Gastroenterology and Hepatology* **2009,** *6*, 297-305.

135. Heazlewood, C. K.; Cook, M. C.; Eri, R.; Price, G. R.; Tauro, S. B.; Taupin, D.; Thornton, D. J.; Png, C. W.; Crockford, T. L.; Cornall, R. J.; Adams, R.; Kato, M.; Nelms, K. A.; Hong, N. A.; Florin, T. H.; Goodnow, C. C.; McGuckin, M. A., Aberrant Mucin Assembly in Mice Causes Endoplasmic Reticulum Stress and Spontaneous Inflammation Resembling Ulcerative Colitis. *PLoS medicine* **2008,** *5*, e54.

136. Braun, A.; Treede, I.; Gotthardt, D.; Tietje, A.; Zahn, A.; Ruhwald, R.; Schoenfeld, U.; Welsch, T.; Kienle, P.; Erben, G.; Lehmann, W. D.; Fuellekrug, J.; Stremmel, W.; Ehehalt, R., Alterations of Phospholipid Concentration and Species Composition of the Intestinal Mucus Barrier in Ulcerative Colitis: A Clue to Pathogenesis. *Inflamm Bowel Dis* **2009,** *15*, 1705-20.

137. Corfield, A.; Myerscough, N.; Longman, R.; Sylvester, P.; Arul, S.; Pignatelli, M., Mucins and Mucosal Protection in the Gastrointestinal Tract: New Prospects for Mucins in the Pathology of Gastrointestinal Disease. *Gut* **2000,** *47*, 589-594.

138. Stremmel, W.; Merle, U.; Zahn, A.; Autschbach, F.; Hinz, U.; Ehehalt, R., Retarded Release Phosphatidylcholine Benefits Patients with Chronic Active Ulcerative Colitis. *Gut* **2005,** *54*, 966-71.

139. Smith, B. F.; Peetermans, J. A.; Tanaka, T.; LaMont, J. T., Subunit Interactions and Physical Properties of Bovine Gallbladder Mucin. *Gastroenterology* **1989,** *97*, 179-87.

140. Shogren, R.; Jamieson, A.; Blackwell, J.; Cheng, P.; Dearborn, D.; Boat, T., Solution Properties of Porcine Submaxillary Mucin. *Biopolymers* **1983,** *22*, 1657-1675.

141. Hollingsworth, M. A.; Swanson, B. J., Mucins in Cancer: Protection and Control of the Cell Surface. *Nature Reviews Cancer* **2004,** *4*, 45-60.

142. Bansil, R.; Stanley, E.; LaMont, J. T., Mucin Biophysics. *Annual Review of Physiology* **1995,** *57*, 635-657.

143. Bhaskar, K.; Gong, D.; Bansil, R.; Pajevic, S.; Hamilton, J. A.; Turner, B. S.; LaMont, J. T., Profound Increase in Viscosity and Aggregation of Pig Gastric Mucin at Low Ph. *American Journal of Physiology-Gastrointestinal and Liver Physiology* **1991,** *261*, G827-G832.

144. Waigh, T.; Papagiannopoulos, A.; Voice, A.; Bansil, R.; Unwin, A.; Dewhurst, C.; Turner, B.; Afdhal, N., Entanglement Coupling in Porcine Stomach Mucin. *Langmuir* **2002,** *18*, 7188-7195.

145. Carlstedt, I.; Lindgren, H.; Sheehan, J., The Macromolecular Structure of Human Cervical-Mucus Glycoproteins. Studies on Fragments Obtained after Reduction of Disulphide Bridges and after Subsequent Trypsin Digestion. *Biochem. J* **1983,** *213*, 427-435.

146. Chace, K. V.; Naziruddin, B.; Desai, V. C.; Flux, M.; Sachdev, G. P., Physical Properties of Purified Human Respiratory Mucus Glycoproteins: Effects of Sodium Chloride Concentration on the Aggregation Properties and Shape. *Experimental lung research* **1989,** *15*, 721-737.

147. Shogren, R.; Gerken, T. A.; Jentoft, N., Role of Glycosylation on the Conformation and Chain Dimensions of O-Linked Glycoproteins: Light-Scattering Studies of Ovine Submaxillary Mucin. *Biochemistry* **1989,** *28*, 5525-5536.

148. Burchard, W.; Stadler, R.; Freitas, L.; Möller, M.; Omeis, J.; Mühleisen, E., Covalent, Thermoreversible and Entangled Networks: An Attempt at Comparison. In *Biological and Synthetic Polymer Networks*, Springer: 1988; pp 3-38.

149. Park, J.-W., Individual Leaflet Phase Effect on Nanometer-Scale Surface Properties of Phospholipid Bilayers. *Colloids and Surfaces B: Biointerfaces* **2009,** *71*, 128-132.

150. Bordi, F.; Cametti, C.; De Luca, F.; Gili, T.; Gaudino, D.; Sennato, S., Charged Lipid Monolayers at the Air–Solution Interface: Coupling to Polyelectrolytes. *Colloids and Surfaces B: Biointerfaces* **2003,** *29*, 149-157.

151. Yuan, C.; Furlong, J.; Burgos, P.; Johnston, L. J., The Size of Lipid Rafts: An Atomic Force Microscopy Study of Ganglioside Gm1 Domains in Sphingomyelin/Dopc/Cholesterol Membranes. *Biophysical journal* **2002,** *82*, 2526-2535.

152. Shapovalov, V. L.; Brezesinski, G., Breakdown of the Gouy-Chapman Model for Highly Charged Langmuir Monolayers: Counterion Size Effect. *The journal of physical chemistry B* **2006,** *110*, 10032-10040.